N° d'ordre NNT: 2019LYSEC48

THÈSE DE DOCTORAT DE L'UNIVERSITÉ DE LYON

opérée au sein de

l'Ecole Centrale de Lyon

Spécialité: **"Génie Électrique"**

préparée dans le laboratoire **Ampère**

dans le cadre de l'École Doctorale EEA de Lyon **(ED160)**

par : **Maria Roberta Longhitano**

Electromagnetic devices modelling with material constitutive laws adapted to high temperature/frequency

Modélisation de dispositifs électrotechniques avec des modèles de matériaux adaptés pour les hautes températures/fréquences

---

Soutenue publiquement le 18 décembre 2019 devant le jury composé de :

Président	
M. Laurent Daniel	Professeur, Centrale Supélec, Laboratoire GEEPS, Gif sur Yvette
Rapporteurs	
Mme Ruth V. Sabariego	Professeure, KU, Leuven, Belgique
M. Ermanno Cardelli	Professore, Univ. degli Studi di Perugia, Italie
Autres membres	
M. Christophe Geuzaine	Professeur, Univ. de Liège, Belgique
M. Riccardo Scorretti	CR CNRS, ECL, Laboratoire Ampère
M. Laurent Krähenbühl	DR CNRS, ECL, Laboratoire Ampère
M. Fabien Sixdenier	MCF HDR, UCB Lyon 1, Laboratoire Ampère
M. François Henrotte	Assistant de recherche et chargé de cours, UCLouvain, Belgique

Abstract

Magnetic materials play a central role in electromagnetic energy conversion applications. The actual trend of power electronics is to stress these materials at higher temperatures and higher frequencies. Therefore from an engineer's point of view it is crucial to have reliable and accurate models able to predict the behaviour of such materials at various temperatures.

This thesis is devoted to the modeling of static hysteresis in magnetic materials by using Henrotte's energy-based model which, among other nice features, is inherently vectorial. In particular, three points are highlighted: 1) the characterization of the model from experimental data, 2) the usage of this model in a Finite Element software to simulate electrical devices, 3) the influence of the temperature on the material.

A large number of measurements have been executed by using original experimental setups. Measurements have been performed at different temperatures (spanning from 223 K to 448 K) and for several excitation signals. By using these measurements, an original model of a 3C90 soft ferrite which takes into account the temperature has been found. In particular, we propose a scaling law which allows to predict the behaviour of the material at different temperatures. The approaches developed in this thesis allowed to take into account the effects of temperatures with success, i.e. the accuracy is satisfying in all the temperature range with the same number of parameters. This model has been validated by using uniaxial excitation with simple and complex signals. A benchmark to check the capability of our model to take into account vectorial excitation has been developed. This benchmark, which consists in a three-leg transformer excited by two coils with independent voltage sources, has been designed, manufactured and simulated in 2D by using the Finite Element software Gmsh/GetDP. Experimental measurements and numerical simulations are reasonably close, and demonstrate the reliability of our modeling. Starting from these results, future developments can be foreseen. In particular, two points of paramount interest are the extension of the model to be able to work at higher frequencies and the link between the micro-structure of the material and the properties of our model.

Keywords:
Magnetic losses; Static hysteresis; Dynamic hysteresis; Temperature; Soft ferrite Mn-Zn; Magnetic measurements; Finite Element simulations; Electromagnetic devices.

Résumé

Les efforts de recherche pour améliorer la compacité des composants magnétiques pour des applications en électrotechnique et surtout en électronique de puissance ont conduit à augmenter la densité de flux ou/et la fréquence. Ajoutons que les signaux d'alimentation sont chargés en harmoniques. Consécutivement, les matériaux magnétiques, dans ces applications, sont soumis à des fréquences et températures élevées. Du point de vue de l'ingénieur, il est donc crucial d'avoir à disposition des modèles robustes et suffisamment précis pour prédire le comportement de ces matériaux à de hautes fréquences/températures.

Dans cette thèse, la modélisation de l'hystérésis statique des matériaux magnétiques a été faite avec le modèle énergétique de Henrotte. Ce modèle a ensuite été étendu pour prendre en compte la température à travers plusieurs de ses paramètres. Trois points de méthode sont mis en lumière : 1) la caractérisation magnétique spécifique pour extraire les données d'entrée nécessaires au protocole d'identification 2) L'extension du modèle à la température et l'analyse de sa précision et de sa robustesse, notamment à travers le nombre de cellules nécessaires pour avoir une précision satisfaisante. 3) L'implantation du modèle dans un logiciel éléments finis pour simuler le comportement d'un démonstrateur instrumenté pour vérification expérimentale.

Les approches menées dans cette thèse, ont permis de prendre en compte avec succès la température, dans le sens où la précision du modèle est satisfaisante sur toute la plage de température mesurée avec un même nombre de paramètres. Des comparaisons avec des signaux ou/et des températures ne faisant pas partie des données d'entrée ont été menées et ont permis de montrer une bonne robustesse du protocole d'identification et de la manière dont la température était prise en compte. De premières propriétés concernant l'évolution des paramètres du modèle avec la température ont pu être dégagées, ce qui ouvre des perspectives intéressantes pour l'établissement d'une loi de prédiction complète.

Sur un cas test dédié (type transformateur), mis en place lors de cette thèse, les simulations éléments finis et les résultats de mesure ont été en bon accord pour des signaux d'excitation pouvant mener à des champs alternatifs, avec harmoniques et produisant des champs tournants. Les résultats sur les grandeurs globales étaient globalement satisfaisants malgré un grand nombre d'hypothèses simplificatrices.

Enfin un certain nombre de travaux débutés, mais non finalisés sont présentés en tant que perspectives. On peut citer :

- la prise en compte des effets dynamiques à travers les paramètres du modèle énergétique.
- le(s) lien(s) existant entre la distribution des paramètres du modèle (extraits à partir de mesures globales macroscopiques) et les propriétés de la microstructure du matériau (mesurables à échelle microscopique).

Mots clés:
Pertes magnétiques ; Hystérésis statique ; Hystérésis dynamique ; Températures ; Ferrite doux Mn-Zn ; Mesures magnétiques ; Simulations aux Elements Finis ; Dispositifs électromagnétiques.

Contents

Nomenclature

ϵ	Electrical permittivity (F/m)
ϵ_0	Electrical permittivity of vacuum (F/m)
ϵ_r	Relative electrical permittivity (F/m)
Ω	Bounded open set of the three-dimensional oriented Euclidean space
$\partial\Omega$	Boundary of Ω
Φ	Magnetic flux (Weber)
curl	Curl
div	Divergence
grad	Gradient
A_e	Effective area
C_1	Sensor coil
C_2	Sensor coil
f	Frequency
l_a	Axial length (along z-axis)
l_e	Effective length
N	Number of cells
N_1	Measurement winding
N_3	Excitation winding
N_4	Excitation winding
N_b	Secondary winding
N_h	Primary winding
R_{N_3}	Coil_{N_3} resistance
R_{N_4}	Coil_{N_4} resistance
R_{series}	Series resistance
R_{shunt}	Shunt resistance

T	Temperature
t	Time instant
V_e	Effective volume
1D	One-dimensional
2D	Two-dimensional
3D	Three-dimensional
$\mathbf{a}$	Magnetic vector potential (Wb/m)
$\mathbf{b}$	Magnetic flux density (T)
$\mathbf{d}$	Electric flux density (C/m^2)
$\mathbf{e}$	Electric field (V/m)
$\mathbf{h}$	Magnetic field (A/m)
$\mathbf{J}$	Magnetic polarisation (T)
$\mathbf{j}$	Current density (A/m^2)
$\mathbf{M}$	Magnetisation (A/m)
χ_m	Magnetic susceptibility
μ	Magnetic permeability (H/m)
μ_0	Magnetic permeability of vacuum (H/m)
μ_r	Relative magnetic permeability
σ	Electric conductivity (S/m)
v	Electric scalar potential (V)
AUX	Identification method based on an AUXiliary function
D.U.T.	Device Under Test
DLang	Double Langevin function
DSF	Dynamical with Static Feedback
DWM	Dynamical with Wall Motion
EB	Energy-Based
FE	Finite Element
GO	Grain-Oriented
GSE	Generalised Steinmetz Equation
HA	High Amplitude

HypTang	Hyperbolic Tangent function
iGSE	improved Generalised Steinmetz Equation
JA	Jiles-Atherton
LA	Low Amplitude
MSE	Modified Steinmetz equation
NO	Non-Oriented
NRMSE	Normalised Root Mean Square Error
OPT	OPTimisation method
PWM	Pulse Width Modulation
RD	Rolling Direction
SE	Steinmetz Equation
SMMs	Soft Magnetic Materials
TD	Transverse Direction
TEAM	Test Electromagnetic Analysis Methods

List of Figures

List of Tables

Part I

English version

Introduction

Context and Motivation of this work

Magnetic materials play a central role in the current and future development of electromagnetic energy conversion applications. We can find magnetic components in plenty of appliances, from the transportation, automotive, digital, biomedical systems to many more high technology and domotic applications.

The electromagnetism is strongly bound to electronic and power electronic sciences. These applications are looking for systems with high power and efficiency for a lowest cost and minor volume. In order to achieve such high targets, the development of precise physical and numerical models for magnetic components and materials is mandatory.

In particular, transformers are considered an essential element of modern power electronic circuits. They are typically required to possess small volume and high reliability. According to the theory of electromagnetics, the electromotive force induced in a transformer winding is proportional to the operating frequency and the magnetic flux. So, smaller magnetic flux is required if the operating frequency is higher [12]. Hence, increasing switching frequencies of power electronic systems can lead to a considerable reduction of the volume and weight of transformers. In fact, with the evolution of power electronic technology, the operational switching frequencies in power electronic systems have been extended to the megahertz (MHz) region.

The trends of high frequency (HF) applications and miniaturisation of power electronic systems significantly enhance the development of low power losses, high permeability magnetic materials. Soft magnetic materials are commonly used as the core materials of the transformers and inductors, due to their outstanding magnetic properties. They play a key role in designing high performance power electronic systems. For example, soft ferrites are included into this group.

The variety of applications of such materials require to assess the magnetic material on a large range of environmental conditions. For instance, at high frequencies, a number of factors, such as magnetic core loss, thermal effects on magnetic properties of core materials, skin effects in both magnetic cores and windings, and the effects of stray capacitances and inductances, become significant and cannot be neglected [12].

For this purpose, throughout the chapters of the thesis, these problematics are addressed.

The most important variables are the temperature and use frequency, according to the dependence of these environmental specifications to the volume and the efficiency of systems. The willingness of manufacturers to develop scientific knowledge on magnetic materials comes from the high impact of the magnetic components on the losses, the volume or the thermal management of an electronic device. Limiting or decreasing this impact on the volume and the efficiency means pushing over the critical parameters of the magnetic material, such as the maximal operating temperature, the coercive magnetic field, the eddy current response in the material.

Furthermore, HF power converters rarely use purely sinusoidal signals to drive the magnetic components. Rather, an active switching circuit modifies the input signal using pulse width modulation (PWM) [13]. Fourier analysis outlines this modulated signal as the superposition of many frequencies, hence optimally conceived soft magnetic materials shall have broadband functionality.

These factors should be considered for a proper design and numerical simulation of electromagnetic devices. In this context, the estimation of magnetic losses (also called iron losses) is fundamental and difficult, in view of the sophistication of the magnetic material behaviour, considering their hysteretic nature. Moreover, the high harmonic content in the magnetic waveforms, the increased induction levels in electromagnetic devices exacerbate the development of appropriate methods for effectively predicting the magnetic losses.

The complexity of hysteresis and temperature dependence, as well as its dynamical behaviour: all these aspects are not taken into account in a unique hysteresis model. In the view of a very high accuracy, the numerical integration of magnetic losses in the field solution by means of a complete temperature-frequency dependent hysteresis model is necessary. To this end, several hysteresis models have been studied in literature, among whom the most famous are the Preisach and Jiles-Atherton models. Both have some advantages, but also some drawbacks. In particular, in their basic formulation they are scalar models, and their physical background is somehow incomplete, especially for Preisach model. Indeed, for practical applications, it is crucial to respect thermodynamic foundation in order to accurately compute losses.

Henrotte's Energy-Based (EB) model is coherent with the thermodynamic principles, it is a quasi-static model and intrinsically vectorial. One of the important features consists in the possibility to built the hysteresis loop as a superposition of several cell contributions, which can be properly chosen, increasing their number, for achieving the desired accuracy.

The global objective of this thesis is to develop efficient methods for the accurate prediction of the behaviour of soft magnetic materials composing magnetic components, considering two important variables in the EB hysteresis model: temperature and frequency.

Outline

This thesis is divided into five chapters, wherein Chapter 1 provides a brief introduction to the topic, the major physical phenomena associated with magnetism of materials and basic quantities involved in magnetic hysteresis. The properties of ferromagnetic materials, particularly soft magnetic materials, are reviewed. Particular attention is paid to the quasi-static and also dynamic hysteresis models present in the literature.

The metrological characterisation of materials is the subject of Chapter 2, where the measuring instruments and principles are introduced.

Chapter 3 proposes an extension to the existing EB model, so as to take into account the effect of temperature, in the light of the parameter variation as function of this external quantity. Parameters are identified via a suitable method based on standard measurements. Then, the hysteresis model is validated on quasi-static measurements at different temperatures, assessing its predictive power.

Chapter 4 is devoted to a practical application for testing the EB model in different cases of unidirectional and rotational loadings. A test-case transformer is built, in order to validate the model in such configurations.

Chapter 5 presents the conclusion and outlook of the dissertation and introduces some work already begun on possible directions to explore : 1) the possibility to take into

account dynamics in the EB model; 2) comparison of two different identification strategies for the material parameters; 3) correlation between such parameters and microstructure of materials.

Original contributions

The main original contributions of this thesis have been presented in the following peer-reviewed journals and conference proceedings.

Journals or Proceedings

- M. R. Longhitano, F. Sixdenier, R. Scorretti, L. Krähenbühl, C. Geuzaine, "Temperature-dependent hysteresis model for soft magnetic materials", COMPEL - The International Journal of Computations and Mathematics in Electrical and Electronic Engineering, vol. 38, no. 5, pp. 1595–1613, 2019. (https://doi.org/10.1108/COMPEL-12-2018-0535).

- M. R. Longhitano, F. Sixdenier, R. Scorretti, C. Geuzaine and L. Krähenbühl, "Comparison of identification protocols of a static hysteresis model", *2019 22nd International Conference on the Computation of Electromagnetic Fields (COMPUMAG)*, Paris, France, 2019, pp. 1-4.
(DOI: 10.1109/COMPUMAG45669.2019.9032825).

- M. R. Longhitano, F. Sixdenier, R. Scorretti, C. Geuzaine and L. Krähenbühl, "Test-case transformer for the energy-based vector hysteresis model", *2019 22nd International Conference on the Computation of Electromagnetic Fields (COMPUMAG)*, Paris, France, 2019, pp. 1-4.
(DOI: 10.1109/COMPUMAG45669.2019.9032728).

Conferences

- M. R. Longhitano, F. Sixdenier, R. Scorretti, L. Krähenbühl, C. Geuzaine, F. Henrotte, "Comparison of identification protocols of a static hysteresis model", Compumag 2019, Jul 2019, Paris, France.

- M. R. Longhitano, F. Sixdenier, R. Scorretti, C. Geuzaine, L.Krähenbühl, "Test-case transformer for the energy-based vector hysteresis model", Compumag 2019, Jul 2019, Paris, France.

- M. R. Longhitano, F. Sixdenier, R. Scorretti, L. Krähenbühl, C. Geuzaine, "Exploring new solutions for temperature dependent hysteresis models", 18th IGTE, Sep 2018, Graz, Austria. (https://hal.archives-ouvertes.fr/hal-01899461)

- M. R. Longhitano, F. Sixdenier, R. Scorretti, L. Krähenbühl, "Les paramètres d'un modèle d'hystérésis statique peuvent-ils renseigner sur la microstructure d'un matériau ?", Symposium de Génie Electrique, Jul 2018, Nancy, France. (https://hal.archives-ouvertes.fr/hal-01875941).

Chapter 1

State of the art

A general framework introducing the state of the art is presented. It mainly concerns the fundamental principles of the theory of magnetism, focusing in particular on the ferromagnetism and a specific class of materials belonging to this category, the soft magnetic materials (SMMs). The main properties of the hysteresis phenomena are described. Particular attention is paid to the modelling of hysteresis losses, considering both static and dynamic hysteresis models.

Magnetic materials modelling can be studied at different scales length levels. The fundamental physical mechanisms can be approached by means of the quantum mechanics, at the atomic level. Other methods, the so-called micromagnetic models, have been investigated at the submicrometer length scale. They are inspired by the physical nature of the material, but are not fully employable in practice to model the hysteresis property at the macroscopic (ultra-millimeter) scale length, which is important for real engineering applications, such as power converters, electrical machines, etc [14]. Firstly, it is difficult to model bulk macroscopic magnetic materials particularities, such as the presence of defects, mainly due to impurities and inhomogeneities of the crystal lattice. Secondly, taking into account their dimension, the behaviour of practical applications requires a significant amount of computing time and memory allocation [14].

In this chapter, most popular macroscopic magnetic material models are reviewed, including mathematical and phenomenological approaches. Differently from purely physical models, phenomenological models do not rely on a deep understanding of the physical nature of materials. They can be rather considered as adaptable tools able to mimic input-output relations, that can be experimentally observed [14]. A more physical approach is introduced with Henrotte's Energy-Based (EB) model. Due to its appealing features, such as the energy consistence and the fact that it is inherently vectorial, this work focuses on the EB hysteresis model. Its extensions to high temperatures and frequencies are the main topics investigated in this thesis.

1.1 Origins of Magnetism

The history of magnetic materials and magnetism dates back to antiquity. The word *magnet* means "the stone from Magnesia" and derives from the ancient town Magnesia, in Greece. Here, it was discovered the presence of some lodestone, consisting of magnetite (iron oxide Fe_3O_4) attracting iron. Until the beginning of the XIX century, this phenomenon was mainly used only for the production of compasses. It is only in the twentieth century that scientists have begun to deeply understand this phenomenon, and develop theories and technologies relying on its interpretation.

In 1800, Alessandro Volta invented the electric battery and thus improved the way

electric currents could be studied. The first decisive experience was attributed to Hans Christian Ørsted in 1820, who discovered that a magnetic field could be generated with an electric current. This opened the way to the electromagnetism, one of the mainstay of physics. In the weeks following Ørsted's discovery, André-Marie Ampère laid the basis of electrodynamics. Magnetism results from the presence of electrical currents, in other words from the motion of electric charges. We owe him the terms "current" and "voltage" to indicate these electrical quantities. William Sturgeon successfully used this knowledge to produce the first electromagnet in 1824. Next, Michael Faraday stated the famous law of electromagnetic induction. In 1831 he showed that a moving magnet generates an electrical current in a nearby conductor wire.

James Clerk Maxwell specified the concepts of electric and magnetic fields, in particular, with the introduction of the electric displacement field. He published his theory in 1864, and deduced from it in 1865 the theoretical existence of electromagnetic waves. In his famous Treaty (1873), he simplified his theory, but the modern writing in the form of four equations, the well-known Maxwell's equations, is the contribution of Oliver Heaviside. In the following years, Heinrich Hertz demonstrated experimentally the presence of electromagnetic waves, verifying the theoretical studies of Maxwell.

Later, Pierre Curie and Pierre Weiss studied the phenomenon of spontaneous magnetisation and its temperature dependence. The existence of magnetic domains was hypothesised by Weiss to explain how a material could be magnetised. The properties of the walls of such magnetic domains were studied in detail by Felix Bloch and Louis Néel.

1.1.1 Basic concepts

In a general manner, there are two possible presentations for the electromagnetism in substances [15].

The true understanding of the origin of magnetism has come with quantum mechanics, born in the twentieth century. Quantum theory describes nature at the smallest scales of atoms and is related to their structure and behaviour. In this context, the first interpretation considers substances consisting of particles located in free space and microscopic electrical quantities, defined at the subatomic scale. Macroscopic quantities are then obtained through the calculation of averages. These principles, however, go beyond the focus of this work.

The second presentation considers directly the macroscopic variables, where the term *macroscopic* indicates that substances are explored by means of volume elements, very small on our scale, but still containing a very high number of atoms.

Essentially, the magnetic properties of materials arise from the motion of electrons. Two types of motions are associated with electrons: the motion of electrons in an orbit within the nucleus and the spin of electrons around its axis (Figure 1.1). Both have a magnetic moment (in $\mathrm{A} \cdot \mathrm{m}^2$) associated with them. The net magnetic moment $\mathbf{m}_0$ of an atom is the vector sum of its orbital and spin magnetic moments. The spin of the electron generates a magnetic field with a direction dependent on the quantum number [3]. For their part, electrons, orbiting around the nucleus, create a magnetic field around the atom. The magnetic moment of an electron circulating around the nucleus of an atom is called the Bohr magneton $\mu_B = 9.274 \times 10^{-24} \mathrm{A} \cdot \mathrm{m}^2$.

The study of the magnetic properties of materials begins by defining macroscopic field quantities. The fundamental concepts are the magnetic field $\mathbf{h}$ and magnetic flux density (or induction) $\mathbf{b}$. Both of them are vector quantities. In some cases, the induction and the field are collinear (parallel), so that it is possible to treat them as scalar quantities, b and h.

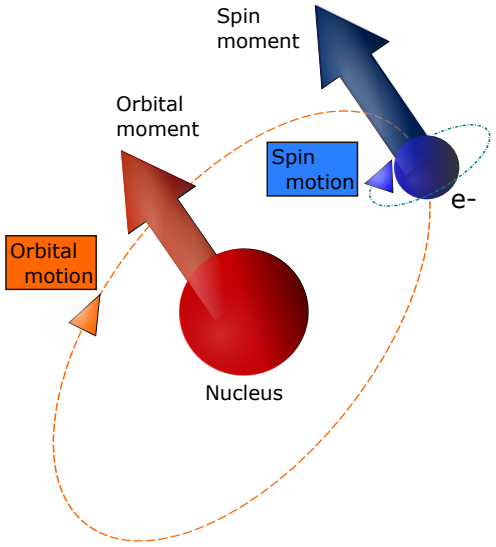

Figure 1.1: Orbital and spin motions.

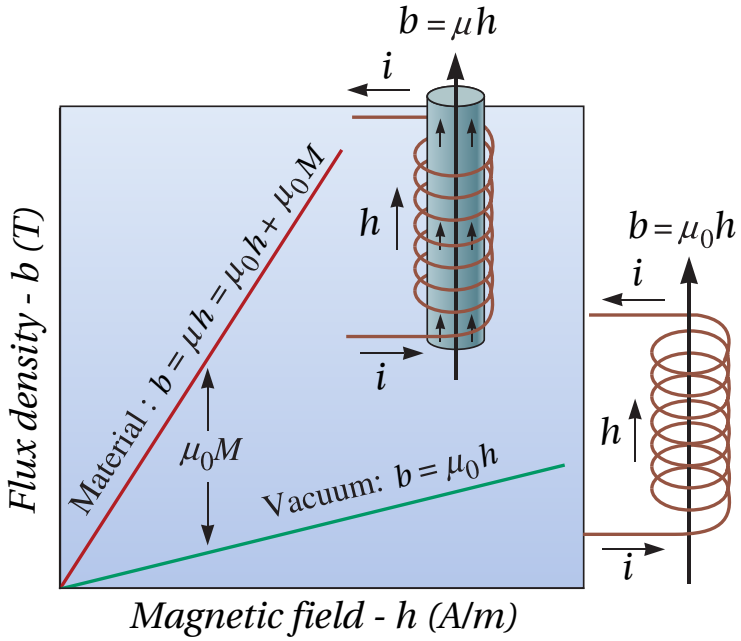

Figure 1.2: A magnetic field h is created by a current i passing through a coil, in the presence, or not, of a medium. Flux density b results being higher when a magnetic core is placed within the coil [1].

Figure 1.2 shows a coil with n turns. When an electric current is passed through the coil, a magnetic field h is generated:

$$h = \frac{ni}{l} \tag{1.1}$$

in which i is the current (in amperes, A) and l the length of the coil (in meters, m). Hence, the units of h are A/m (ampere per meter). When h is applied in free space, lines of magnetic flux are induced. The magnetic flux density, or induction, b (in tesla, T) is correlated to the imposed magnetic field by

$$b = \mu_0 h \tag{1.2}$$

where $\mu_0 = 4\pi \times 10^{-7}$ H/m (henry per meter) is the permeability of vacuum. Flux density b can be defined by the mechanical force which it exerts on a moving charged particle [16]. When a material is placed within the magnetic field, the flux density is determined on the basis of the interaction between the induced and permanent magnetic dipoles and the magnetic field. So, one has $b = \mu h$, where μ is the permeability of the material. If the magnetic moments intensify the applied field, then $\mu > \mu_0$, a greater flux is produced and the magnetic field is amplified. In the other case, when the magnetic moments oppose the field, $\mu < \mu_0$.

In order to quantify the influence of the magnetic material, the relative permeability μ_r is introduced:

$$\mu_r = \frac{\mu}{\mu_0} \tag{1.3}$$

A large value of μ_r suggests that the material magnifies the effect of the applied magnetic field and will carry magnetic flux more readily [1].

The magnetisation $\mathbf{M}$ (A/m) can be defined as the vector sum of the magnetic moments m_0 of all the atoms in a small volume V of the material, divided by the volume V: $M = \frac{\sum m_0}{V}$ [16]. Magnetisation indicates the variation in the induction, due to the presence of the core material (cf. Figure 1.2). Thus, in presence of materials, the equation (1.2) writes:

$$b = \mu_0 h + \mu_0 M \tag{1.4}$$

The first term corresponds to the effect of the imposed magnetic field, the second one represents the effect of the magnetic material that is present and contributes to the total flux density b. At the macroscopic level, M is considered as a quantity resulting from spatial averaging over the whole sample under test.

Another quantity is the magnetic polarisation $\mathbf{J}$ (T), linked to the magnetisation by $\mathbf{J} = \mu_0 \mathbf{M}$. So, b is related to M, J and h by the equation:

$$b = \mu_0 h + \mu_0 M = \mu_0 h + J \tag{1.5}$$

For soft magnetic materials (SMMs), the approximation $b \approx J$ is valid. However, the difference between these two quantities becomes important in case of high excitation levels or for permanent magnets [16].

The magnetic susceptibility χ_m provides the amplification created by the material and is the ratio between the magnetisation and the magnetic field

$$\chi_m = \frac{M}{h} \tag{1.6}$$

Similarly to μ_r, χ_m refers to the degree to which the material strengthens the magnetic field. They are related by

$$\mu_r = 1 + \chi_m \tag{1.7}$$

In conclusion, the orbital and spin motions of electrons and the manner in which the electrons interact with one another are at the basis of the origin of magnetism. The main difference is that, in some materials, there is no collective interaction of atomic magnetic moments, whereas in other materials there is a strong interaction between atomic moments. In sum, when a magnetic field is applied to a material, several kinds of behaviour can be observed.

1.1.2 Different types of behaviour in magnetic materials

Magnetism can be classified into different categories introduced hereafter: diamagnetism, paramagnetism, antiferromagnetism, ferrimagnetism and ferromagnetism (cf. Figure 1.3).

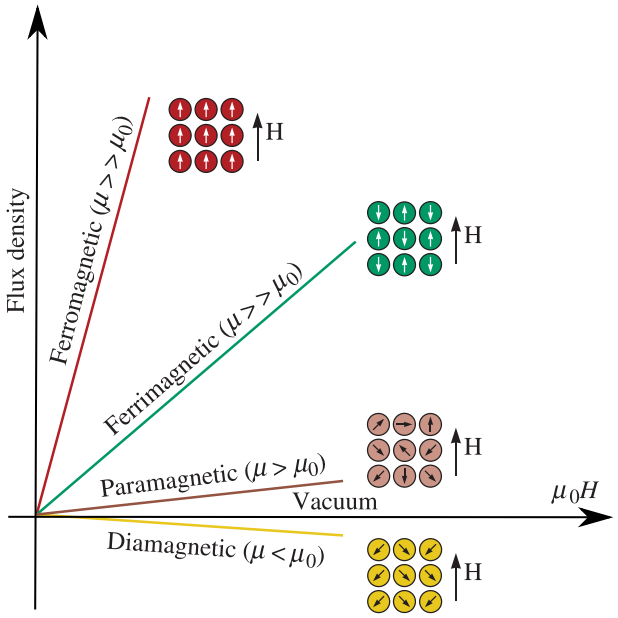

Figure 1.3: Effect of the core material on the flux density [1].

Diamagnetism

This type of magnetism is characterised by a negative susceptibility, with an order of magnitude of about 10^{-5} or 10^{-6}. By acting on each atom, a magnetic field has an effect on magnetic moments. These oppose the imposed magnetic field, causing the magnetisation to be less than zero. The magnetisation direction is opposite to the direction of applied field (cf. Figure 1.4). Examples of diamagnetic materials are copper, silver, gold, bismuth and berylium.

Paramagnetism

In materials having unpaired electrons, each atom has a magnetic moment, due to electron spin. Under the influence of a magnetic field, these moments tend to rotate and align themselves along the field direction (cf. Figure 1.5), resulting in a small net magnetisation. Very high magnetic fields are needed to align all dipoles, due to the fact that they do not interact. In addition, the effect is lost once the magnetic field is removed, since the impact of the thermal motion, randomly orienting the magnetic moments, prevails. Thus, they do not retain any magnetisation in the absence of an externally imposed magnetic field. Paramagnetic materials include iron oxide, aluminium, oxygen, titanium. Above the

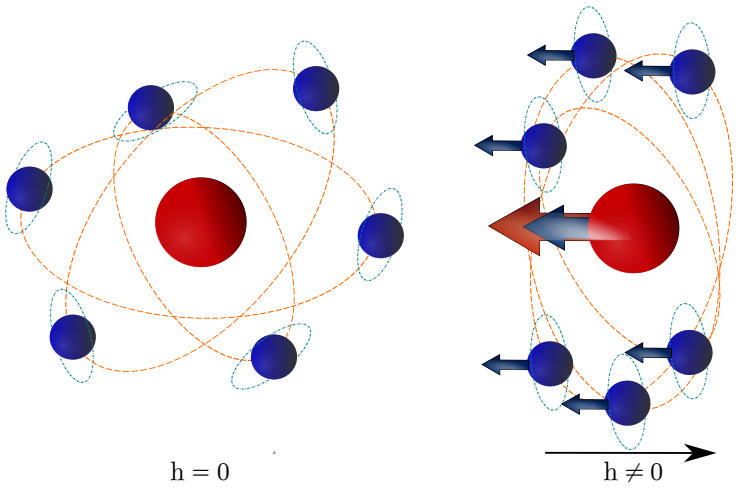

Figure 1.4: Diamagnetic behaviour.

Curie temperature, ferromagnetic and ferrimagnetic materials also manifest paramagnetic behaviour.

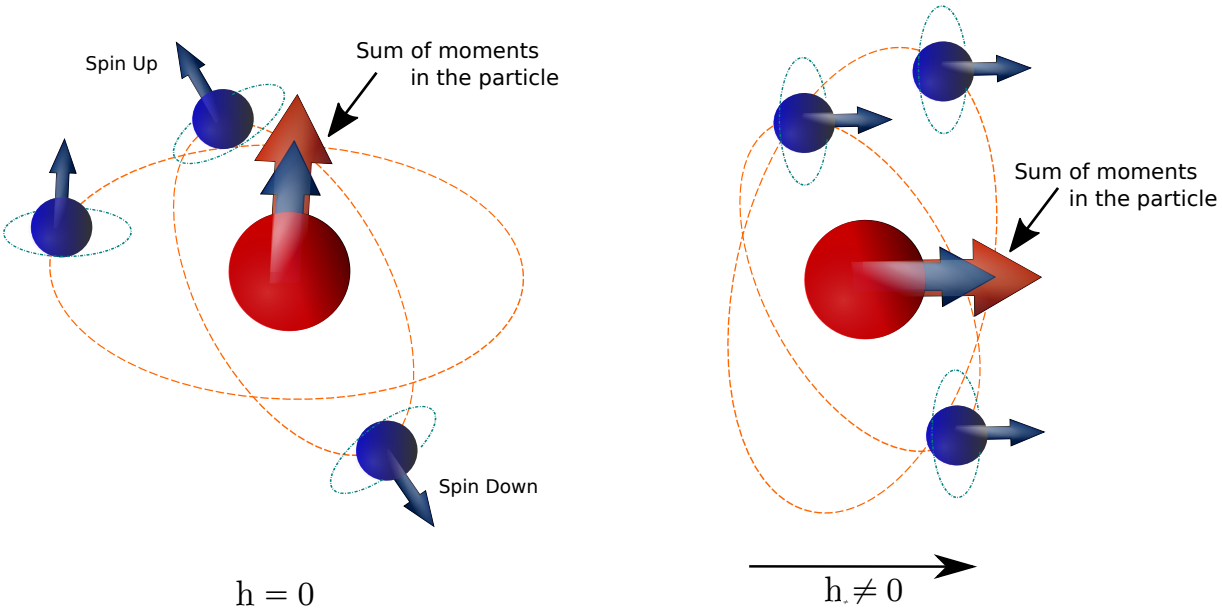

Figure 1.5: Paramagnetic behaviour.

Antiferromagnetism

In this kind of magnetism, the exchange interaction between neighboring atoms determines an antiparallel alignment of the atomic magnetic moments. Antiferromagnetic materials are characterised by electron spins, associated with atoms, oriented with respect to each other in such a way as their net magnetisation is equal to zero. Their susceptibility is tipically low ($\approx 10^{-6}$). As for ferromagnetic materials, these materials become paramagnetic above a transition temperature (Néel temperature).

Ferrimagnetism

Ferrimagnetic materials can supply good amplification of the applied field. In ceramic materials, several ions have different magnetic moments which may align or not with the

field, so a net magnetisation is obtained. A group of ceramics, the ferrite materials, used in power electronics, are ferrimagnetic. Most of them are good insulators of electricity, thus eddy current losses do not appear significant, compared to those in metallic ferromagnetic materials. For this reason, ferrites are commonly used in several high frequencies applications.

Ferromagnetism

Iron, nickel, cobalt and some of the rare earths (gadolinium, dysprosium) belong to this category, with a $\chi_m \gg 1$ (typically $\chi_m \approx 10 - 10^7$). For ferromagnetic materials, the susceptibility is function of h and of the temperature T. The characteristics of materials, in a magnetic field, are then represented by the curves $J(h,T)$, $M(h,T)$, $b(h,T)$. At the atomic scale, these materials show a long-range ordering phenomenon, which induces the unpaired electron spins to arrange parallel with each other. The magnetic moments are spontaneously magnetised into regions of uniform magnetisation, called *domains*, separeted by walls (cf. Weiss domains, Bloch walls) and oriented in such a manner that the net magnetisation of the medium is zero. The magnetic domains are induced to align with each other under the influence of an externally imposed magnetic field. Then, the material is considered magnetised (cf. Figure 1.6). The limiting value of the magnetisation acquired by the material in larger fields is called the saturation magnetisation, M_{sat}. Ferromagnetic materials show a spontaneous magnetisation M_s in the absence of an imposed magnetic field and will tend to remain partially magnetised after being subjected to an imposed magnetic field. This phenomenon is called *hysteresis* and is deeply discussed in this thesis. Moreover, ferromagnetic materials have a maximum temperature above which the ferromagnetic property sharply disappears, as a result of random thermal fluctuations, becoming paramagnetic. This maximal temperature value is called the Curie temperature (or point) T_C.

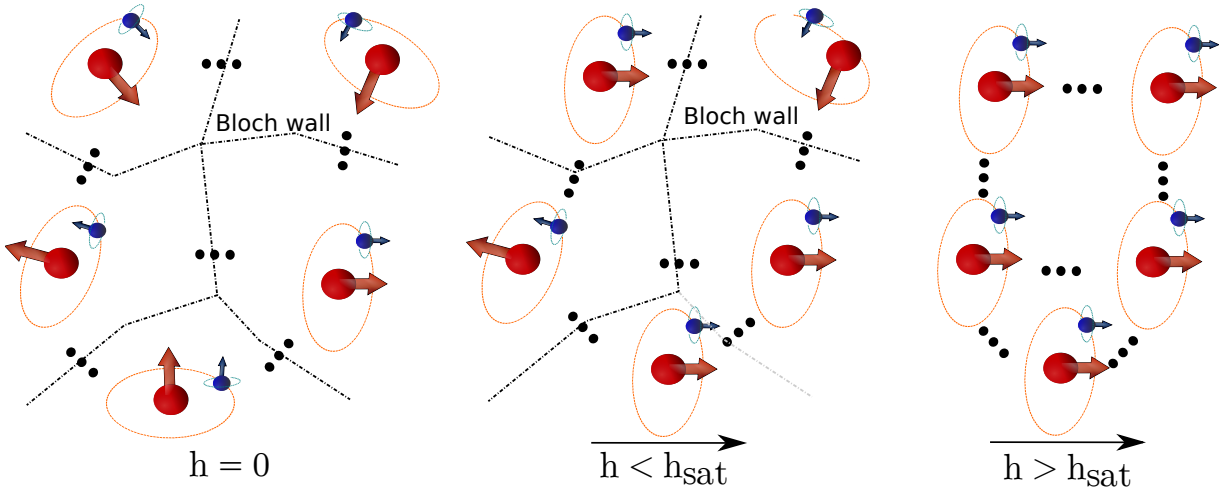

Figure 1.6: Ferromagnetic behaviour.

1.2 Ferromagnetism: from mesoscopic to macroscopic scale

The microscopic properties of ferromagnetic materials arise at the macroscopic scale. Especially, the hysteresis phenomenon is the outcome of sophisticated magnetisation

processes on a microscopic level. Moreover, it depends on the nature of lattice defects that constitute the microstructure of materials.

These materials are aggregates of crystal grains, characterised by a particular orientation and size. For the purpose of minimising the magnetic energy, they split spontaneously into several structures with homogeneous magnetisation. These structures are called domains, separated by transition zones, in which the direction of the magnetisation is smoothly modified. Thus, the modification of the averaged magnetisation over a sample is due to the motion of these walls. This movement is however influenced by the presence of *pinning sites* in the lattice, particularly dislocations, impurities and inclusions, resulting in the Barkhausen effect, a stair-step like increase of magnetisation at the microscopic level. This dissipation phenomenon shows an irreversible nature and represents the microscopic origin of the magnetic hysteresis.

Basically, the most relevant characteristics [7] of a ferromagnetic material are:

- dependence of permeability on the magnetic field and on the previous magnetic history (hysteresis);
- approach of the magnetisation to a maximum, once the magnetic field is indefinitely increased (saturation);
- the presence of magnetised regions (domains) including many atoms and having magnetic moments similar to the saturation moments, even if the material is unmagnetised (spontaneous magnetisation);
- disappearance of these features when the temperature is raised to a certain value (Curie point).

All these phenomena are the result of a complex interplay of smaller scale length levels, as seen in Figure 1.7. In the *atomic* scale, the physical mechanisms behind the magnetic behaviour are defined. The following step is the grain structure of the polycrystalline material at the *microscopic* level ($\approx 10^{-6}$). The representative elementary volume represents the *mesoscopic* (millimeter) scale and, finally, the *macroscopic* (ultra-millimeter) level, which is attractive for final users of electromagnetic devices [14], [2]. Therefore, the microscopic and mesoscopic scale mechanisms are at the heart of the observed phenomena at the macroscopic level and depend on the inner material architecture. Thus, it is of great interest to develop adequate approaches that examine the real multiscale nature of materials, in order to understand and accurately predict the magnetic properties of such materials [2].

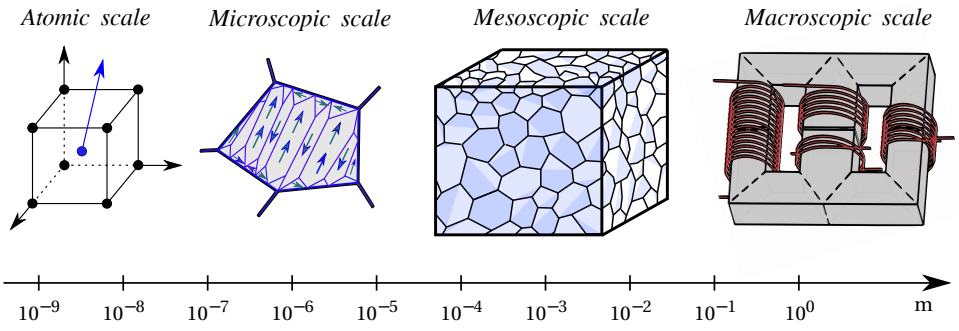

Figure 1.7: Different observation scales, from the atomic to the macroscopic level, adapted from [2].

The next sections present the multiscale origins of ferromagnetism, from the mesoscopic to the macroscopic level.

1.2.1 Mesoscopic scale

Several kind of observation methods (for example, the Kerr effect) allow to detect the distribution of magnetisation in materials. The spontaneous alignment of atomic magnetic moments, parallel to each other, is one of the characteristic properties of ferromagnetic materials. This orientation is a local phenomenon [3]. Bulk systems are generally divided in several magnetised areas, the orientation of which varies from one region to another (cf. Figure 1.8). These regions of parallel magnetisation are the so-called *magnetic (or*

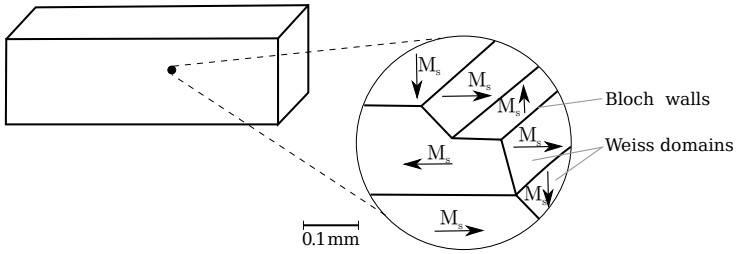

Figure 1.8: Division of a sample in magnetic domains [3].

Weiss) domains, characterised by different shapes. For most materials, their size ranges from fews μm up to 100 μm. In every magnetic domain of a homogeneous material, with a uniform temperature, the module of the spontaneous magnetisation $\mathbf{M}_s$ has the same value. Each domain is separated from its neighbour by a transition zone in which the orientation of magnetic moments gradually changes, from the current magnetisation direction to the one existing in the adjacent domain. This transition regions are named *domain (or Bloch) walls*. The magnetic moment m_0 of a sample, having volume V, is included in the following limits [3]:

$$0 \leq m_0 = \int M_s dV \leq M_s V \tag{1.8}$$

It can vary from 0 to $M_s V$ under the effect of an applied magnetic field $\mathbf{h}$, which involves a modification of the distribution of the Weiss domains. Magnetic properties of materials depend on the variation of this structure under the influence of an external field.

The domain structure, in particular the orientation and configuration of the magnetic moments, is a result of the intricate balance of different energy contributions. It corresponds to the configuration minimising the total energy W_{tot} of a system. This energy can be decomposed in the sum of two terms:

$$W_{tot} = W_{in} + W_{ze}, \tag{1.9}$$

where W_{ze}, the Zeeman energy, represents the potential energy of a magnetised body in an external field, and W_{in} is the internal energy.

In a ferromagnetic material, the main terms contributing to the internal energy W_{in} are W_{an} (anisotropy energy), W_{ms} (magneto-static energy), W_{ex} (exchange energy) and W_{me} (magneto-elastic energy):

$$W_{in} = W_{an} + W_{ms} + W_{ex} + W_{me}. \tag{1.10}$$

The influence of each term is considered in the case of an ideal perfect monocrystalline sample, called *reference crystal*, in which the crystalline axes are parallel to the edges of the sample [3]. Hereafter, each contribution is examined in detail.

Anisotropy energy W_{an}

Figure 1.9 describes the preference for the magnetisation to be oriented along certain crystallographic directions. For example, in single crystalline samples, it can be noticed that magnetisation curves, along specific crystallographic directions, differ from each other. In iron, the magnetisation curve along the [100][1] direction is steeper and reaches saturation at lower values of external field than along [110] or [111]. Therefore, it is the easy axis of magnetisation, i.e. the direction in which the anisotropy energy W_{an} is minimum. This contribution measures the intensity of the interaction of magnetic moments, resulting in parallel orientation.

In absence of an external field, the spontaneous magnetisation lies preferably along one of the easy axes. Under the influence of the anisotropy energy alone, spontaneous magnetisation tends to align in parallel to the edges of the reference crystal (cf. Figure 1.10).

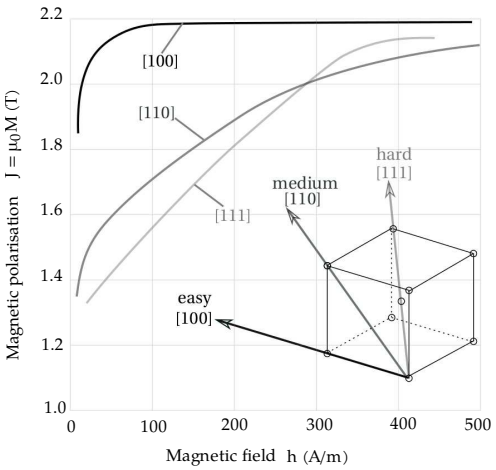

Figure 1.9: Initial magnetisation curve for α-Fe single crystals in three crystallographic directions. Inset: crystal structure of body centered cubic iron, with easy, medium and hard axis of magnetisation [3].

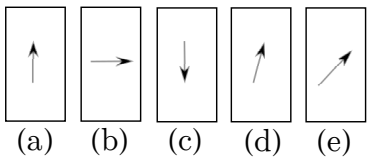

Figure 1.10: Five cases of magnetisation of a reference crystal. W_{an} is minimum in the cases (a), (b), (c), then it increases successively in cases (d) and (e) [3].

Magneto-static energy W_{ms}

The magneto-static energy represents the potential energy of the self-created magnetic moments in the magnetic field, due to their long-range magnetic dipolar interaction. This kind of energy results in a splitting of the reference crystal into many lamellar domains, since W_{ms} is inversely proportional to the number of lamellae (cf. Figure 1.11). A large external magnetic field is generated in the first configuration (Figure 1.11(a)). The second one (Figure 1.11(b)) reduces that field at the expense of the formation of domains, separated by 180°-walls, but it induces the increase of the wall energy (cf. Figure 1.11(c)).

[1]Here, square brackets designate a direction in the crystal lattice (crystallographic zones).

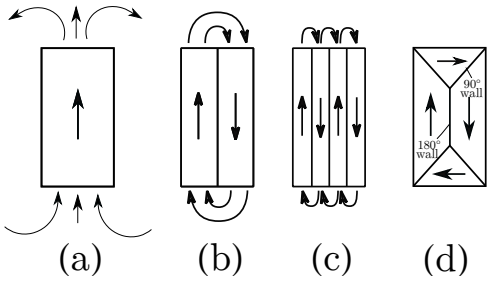

Figure 1.11: Lamellar structure at decreasing W_{ms}.

The last configuration introduces the so-called closure domains by forming 90°-walls (cf. Figure 1.11(d)). This modification remove the external field almost completely [3]. In this case, the arrangement of domains is such that the sample does not generate any appreciable external field.

Exchange energy W_{ex}

The contribution W_{ex} is the energy resulting from the interaction of two magnetic moments. It depends on the distance separating these moments as well as their orientation. Conversely to the case of W_{ms}, this term accounts for short-range interactions between close neighbours. In most cases, it favours parallel alignment of neighbours moments. In a ferromagnetic material, the exchange energy favours moments with same direction and therefore uniform magnetisation. It tends to keep adjacent magnetic moments parallel to each other. W_{ex} passes through a minimum when the magnetic moments are parallel. Both W_{an} and W_{ex} arise inside a Bloch wall. Their sum represents the energy associated with the Bloch wall itself, which has the effect to limit the total area of domain walls.

Particularly, the subdivision of the reference crystal into increasingly more lamellar domains (cf. Figure 1.11 (a)-(c)) will stop when the decrease of the resultant W_{ms} will be compensated by the rise of energy in the Bloch walls. Considering once more Figure 1.11, in the saturated state (a), the spontaneous magnetisation is aligned parallel to an easy axis of magnetisation. In this situation, the magneto-static energy W_{ms} has a great value due to the discontinuities in magnetisation changes. It is subsequently reduced by the formation of two domains of opposite magnetisation (b). The field lines close at the ends of the adjacent domains, causing the decrease of W_{ms} outside the sample. This mechanism endures until (c) and is limited by the energy stored in the 180°-walls. This is due to the increase of W_{ex} and W_{an} in the Bloch wall, resulting from the progressive modification of the orientation of magnetic moments. Hence, by over-simplifying, one can generally write:

$$\text{number of lamellar domains } \uparrow \qquad W_{ms} \downarrow \qquad W_{an} \uparrow \qquad W_{ex} \uparrow$$

Closure domains might be formed at the end surfaces (d), which encloses the flux paths within the sample, hence the W_{ms} disappears. The appearance of closure domains is affected by the associated magneto-elastic energy.

Magneto-elastic energy W_{me}

The magneto-elastic energy is associated to deformations and constraints, the origin of which is magnetostriction. The latter consists in a dimensional change related to the magnetisation. Magnetostriction is said positive when the sample elongates in the direction of $\mathbf{M}$, negative when it contracts in the $\mathbf{M}$ direction (cf. Figure 1.12).

In the reference crystal, this energy varies according to the structure of magnetic domains (cf. Figure 1.13). Configurations (a)-(b) correspond to a weak value of W_{me},

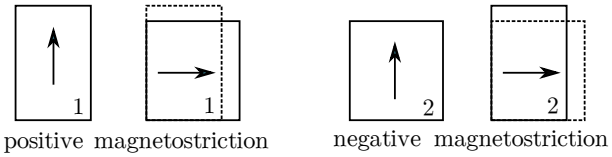

Figure 1.12: Magnetostriction [3].

since this one is a result only of the deformation of the crystal along the direction of polarisation. In (c), W_{me} is increased, due to the action of the stresses exerted by the four domains one upon the other.

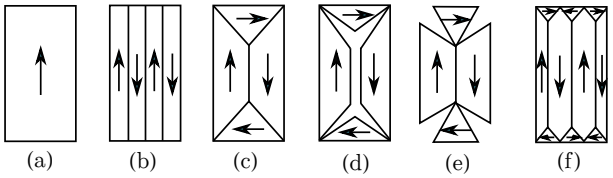

Figure 1.13: Structure of magnetic domains subject to W_{me} [3].

These constraints ideally cut the crystal along the domain walls. If the magnetostriction is positive, the case (d) is obtained. The configuration (e) corresponds to a negative magnetostriction. In case (f), in which the size of the closure domains is reduced, W_{me} is weaker than in (c).

External field (Zeeman) energy W_{ze}

Until now, the case of a magnetic medium subject to no field has been considered. When a magnetic field **h** is applied, the interaction between the magnetisation and the applied magnetic field results in the external field energy W_{ze}, also called Zeeman energy. In the presence of such a magnetic field, the magnetic moments will align themselves such that they are parallel to it [8].

Polycrystalline material: magnetic domains structure

In case of a polycrystalline material, the overall concept according to which magnetic domains structure corresponds to a minimum of the internal energy of a sample is still valid. However, this minimum cannot be obtained by reducing separately the internal energy of every grain considered as isolated from the other. For example, for each grain, the W_{ms} depends significantly on the environment in which it is located. In each grain, the subdivision in domains will tend to follow the same procedures of the crystal reference. In the case of a monocrystal, the effect of the sample shape is preponderant. Actually, for a polycrystal, this effect is neglected, since it is important to consider the grain structure.

For instance, Figure 1.14 depicts the domain configuration of a polycrystalline material. The presence of grain boundaries and various orientations of easy axis in the grains have significant impact on the magnetisation distribution and domain structure. Polycrystalline materials are characterised by complicated grain structures endowed with presence of defects, such as cavities, inclusions, precipitates, magnetic texture. These defects hinder the motion of Bloch walls by a pinning process and give rise to secondary structures, such as the knife-edged structure (cf. Figure 1.15). Hence, domain walls become building blocks for more complex descriptions involving the superposition of many contributions.

Figure 1.15(a) shows that the inclusion produces a W_{ms} associated to the presence of magnetic masses + and -. This energy is reduced by the presence of a Bloch wall passing

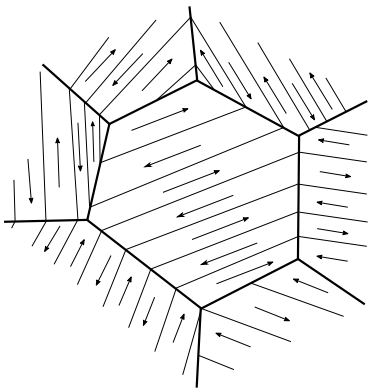

Figure 1.14: Domain configuration of a polycrystalline material, adapted from [4].

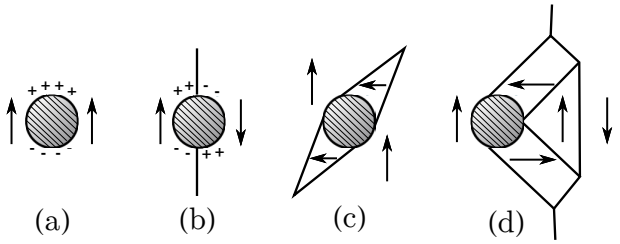

Figure 1.15: Examples of possible effects of an inclusion on the local structure of magnetic domains [3].

through the inclusion causing a decrease of the average distance between the masses + and - (Figure 1.15(b)). Hence, the Bloch wall tends to be retained by the inclusion, this phenomenon is called *pinning effect*. Such effect is of great physical relevance, since it influences directly the shape of the hysteresis diagram *b-h*. In absence of a pre-existing Bloch wall close to the defect, the W_{ms} is usually decreased by the creation of secondary knife-edged domains (Figure 1.15(c)). The decreasing of W_{ms} is often obtained by an indirect pinning of a wall by means of several secondary domains (Figure 1.15(d)).

In conclusion, the motion of the Bloch walls is irreversible, impeded by the interaction of the moving domain walls with grain boundaries, precipitates, surface roughness and residual stresses. Figure 1.16 shows a magnetisation process on a sample of polycrystalline hot-pressed Mn-Zn ferrite.

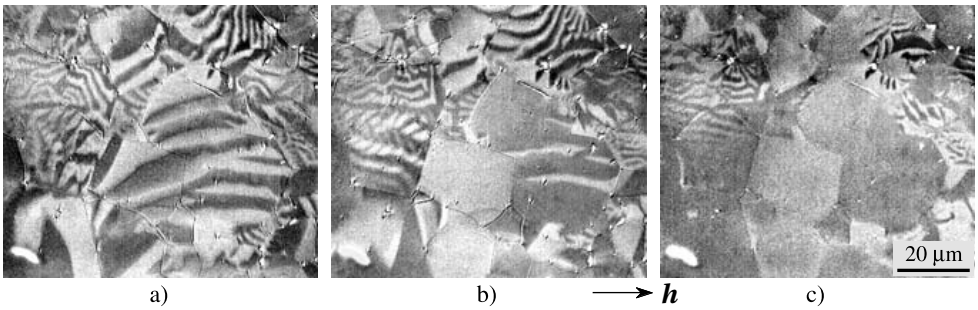

Figure 1.16: Magnetisation process observed on the surface of a piece of hot-pressed Mn-Zn ferrite. (a) Demagnetised state. With the application of a magnetic field (b, c) strong reorientation processes are observed [5].

1.2.2 Macroscopic scale: the hysteresis cycle

The term *hysteresis cycle*, or *magnetisation curve*, denotes the relationships *M(h)*, *J(h)* or, generally, *b(h)*, with b and J related to M by means of (1.5). Hence, the macroscopic magnetic properties of a ferromagnetic sample can be described by a family of *b-h* diagrams, which represent the response of magnetic materials, determining the magnetic constitutive laws. Figure 1.17 depicts the typical shape of a hysteresis cycle.

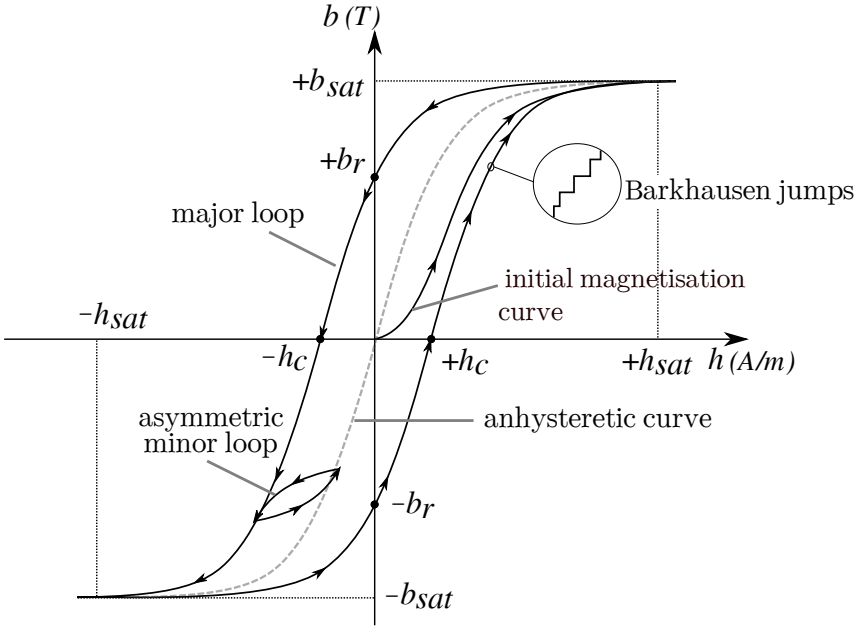

Figure 1.17: Typical hysteresis cycle of polycrystal and representation of the most important features, adapted from [6].

For ferromagnetic materials subject to an unidirectional time-varying magnetic field $h(t)$, the macroscopic constitutive law is non-linear and hysteretic. For instance, increasing *h(t)* from an initial value $h(t_0)$ at time t_0 to a new value $h(t_1)$ and decreasing back to the initial value, so that $h(t_2) = h(t_0)$, the magnetic induction $b(h(t_2))$ commonly no longer returns to the initial value $b(t_0)$. The new point $(h(t_2), b(t_2))$ depends on the actual value of the magnetic field strength $h(t_2)$ and also on its previous history [17]. Under periodic conditions, the function *b(h)* assumes the shape of a hysteresis cycle. When a slow sinusoidal variation of h leading to saturation occurs, the cycle is named *major hysteresis loop*. A cycle with field peak value with lower intensity than the major loop is called *minor hysteresis loop*.

Figure 1.18 illustrate the steps of a magnetisation process in a typical domain structure of an iron single crystal. In Figure 1.18(a), it is shown the domain structure without

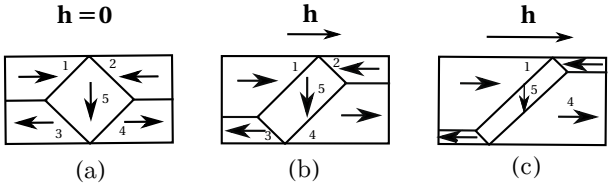

Figure 1.18: Magnetisation process [3].

defects. When a magnetic field is applied, the magnetic moments energy increases in domains 2 and 3, to a lesser extent in domain 5. The fulfilment of the condition of minimal energy in the sample results in a decrease of volume of these domains. When

the magnetic field increases, the structure of domains will become successively as seen in Fig.1.18(b) and (c). Finally, a single domain oriented along **h** will remain. In this ideal example, the motion of Bloch walls is perfectly free. By turning off **h**, one can find back the configuration (a), in other words, the magnetisation process is reversible.

Crystalline defects have an important impact on the shape of $b(h)$ curve. In Figure 1.19, the action of punctual defects on the motion of Bloch walls inside a single crystal and its correspondence with *initial magnetisation curve* are described.

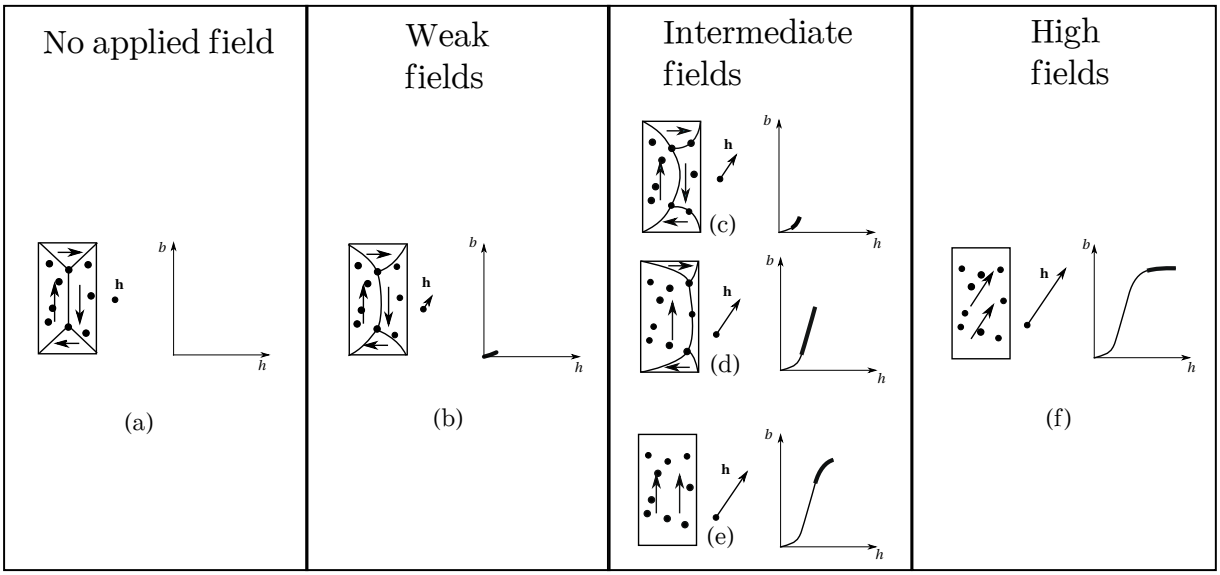

Figure 1.19: Evolution of the magnetisation in a single crystal in the presence of pinning sites, adapted from [3].

Figure 1.19(a) shows a typical domain structure, where the Bloch walls are pinned by two defects and appear rectilinear. Such configuration corresponds to a minimum of the wall energy. When a weak field is applied (cf. Figure 1.19(b)), a reversible deformation of Bloch walls occurs. These behave as elastic membranes, and there is no change in the pinning sites position. This zone is characterised by a quasi-linear behaviour of the material, as well as moderate permeabilities. Magnetisation evolves in accordance to the Rayleigh law [18], [7]. At intermediate strength fields (cf. Figure 1.19(c)), the stress on the walls makes the pinning sites give up. Bloch walls move in a series of jumps highlighted by the Barkhausen's experience (see Figure 1.17). These wall motions are irreversible and the $b-h$ slope is maximum, namely the permeability passes through its maximum value, as it can be seen in Figure 1.19(d). Then, the increase of magnetisation by irreversible motions of Bloch walls is terminated (cf. Figure 1.19(e)). Finally, Figure 1.19(f) shows the saturation zone, where higher fields cause the magnetisation to deviate from the easy magnetisation direction to align with the applied magnetic field. This phenomenon is reversible, the permeability decreases and tends asymptotically to the vacuum permeability μ_0.

When a magnetic material is magnetised with a monotonically increasing field, the initial magnetisation curve is obtained. Starting from the neutral state ($h = 0$, $b = 0$) up to the saturation of the material (b_{sat}).

Typically, the neutral state is accessible via demagnetisation after the application of an AC field with progressively reducing amplitude. In case of thermal demagnetisation, the neutral state is reached by heating the material beyond the Curie temperature and, then, the *virgin curve* is obtained. The *normal magnetisation curve* is the locus of the tips of the minor hysteresis loops, which are gradually enlarged with increasing excitation [16].

The *saturation state* is obtained by applying a field of amplitude large enough to sweep away the domain structure, leaving the material in quite uniform magnetisation, the subsequent evolution of which will be independent of its history prior to saturation [7]. This is why the saturation hysteresis loop, obtained by cycling the field between opposite large values, is usually used to characterise magnetic materials. The descending branch of the hysteresis loop leads from saturation $+b_{sat}$ to negative saturation $-b_{sat}$, the ascending branch leads back to positive saturation $+b_{sat}$.

The equation $\mathbf{b} = \mu_0\mathbf{h} + \mathbf{J}$ indicates that, theorically, there is no saturation value for b. The accessible limit values of b derive from the impossibility of generating magnetic field strengths as high as wished [7]. However, practically, the expression b_{sat} can be used to denote the saturation induction field, which corresponds in theory to the magnetic polarisation, as

$$b_{sat} = \lim_{h\to\infty}(b - \mu_0 h) \tag{1.11}$$

Considering a sample subject to a magnetic field strength h greater than h_{sat}, the *residual flux density* b_r, also named *remanent induction field* or *retentivity*, represents the flux density remaining in the sample after the decrease of h to zero. b_r represents the maximal induction that may be present after the disappearance of a magnetic field.

The *coercive field* h_c, or *coercivity*, is the magnetic field required to cancel the residual flux density. It provides a measure of the magnetic hardness/softness of the material, its value typically differing by many order of magnitude in SMMs and in permanent magnets (see Section 1.3). Both b_r and h_c are specific properties of the material and included in the main hysteresis loop.

The *anhysteretic curve* constitutes the "ideal" magnetisation curve of the material if it were perfect, in the sense that it has no defects that hinder the magnetisation and demagnetisation process. The so-called *demagnetised state* is obtained by applying an oscillating field of amplitude slowly decreasing from a high initial value to zero. The same procedure can be generalised by considering a given constant field h_0, and by superimposing to it an oscillating field of slowly decreasing amplitude (Figure 1.20). The result is an anhysteretic state and the curve connecting these states, generated under different bias field h_0, is named the anhysteretic curve. It is independent of prior history and represents the skeleton around which hysteresis manifests itself [7].

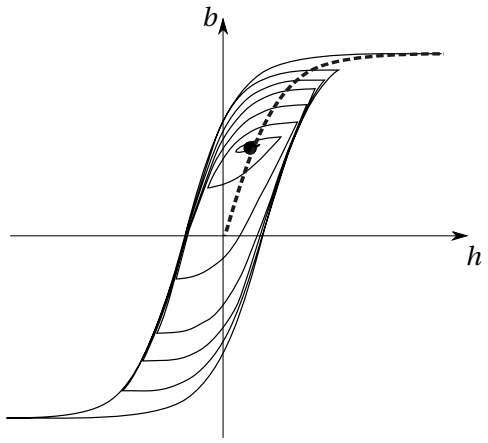

Figure 1.20: Example of field history generating a point of the anhysteretic curve. The field oscillates around a constant bias value, with an amplitude slowly decreasing from infinity to zero. By repeating the same procedure under different bias fields, one generates the anhysteretic curve, represented by the dashed line [7].

1.3 Classification of ferromagnetic materials

The hysteresis loop represents the main magnetic properties and, by the value of its parameters, a classification of the materials can be investigated.

Ferromagnetic materials have a wide variety of applications in various engineering fields. Depending on their characteristic parameter values, they may be classified as *hard* and *soft* ferromagnetic materials. Coercivity is assumed as the main criterion, and IEC Standard 60404-1 [19] recommends the coercive force of 1000 A/m as a value to distinguish both groups (cf. Figure 1.21). Magnetically, soft materials are easier to demagnetise after saturation, traditionally they provide a coercive field of less than 1000 A/m, while hard materials have high coercivity (greater than 10000 A/m).

Hard magnetic materials have broad, quite square hysteresis loops and, usually, they are applied for permanent magnets production and magnetic recording/memory devices.

SMMs have very narrow loops. They are temporary magnets, readily losing their magnetisation as soon as the field is removed. We may find them in transformers and motor cores, in order to minimise the energy dissipation due to the alternating fields associated with AC electrical applications.

This work focuses mainly on the study of SMMs, further described below.

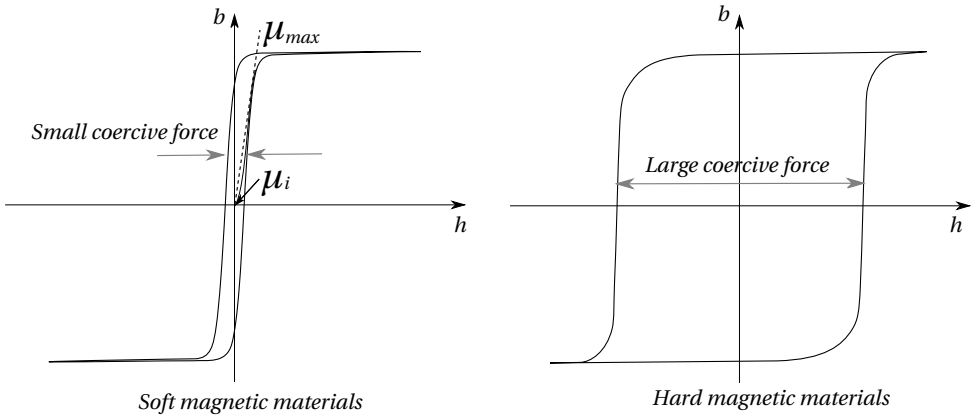

Figure 1.21: Typical hysteresis loop of soft and hard magnetic materials.

Soft magnetic materials

The choice of SMMs is a trade-off between polarisation, permeability, losses and cost. An overview of the global market of magnetic materials and the relative contributions of the different types of soft magnets is shown in Figure 1.22.

It would be desirable to be able to find the SMM endowed of excellent properties, such as high saturation polarisation, small losses, small coercivity, good mechanical properties, etc. [20]. However engineers have to accept always some compromises, i.e. high permeability at the cost of saturation polarisation, small power loss at the cost of saturation polarisation, better magnetic parameters at the price of mechanical properties, etc.

For transformers and electromagnetic devices, electrical steels are prevalent. For a given excitation field, the magnetic polarisation should be as high as possible. Iron losses must be acceptable at the operating frequency. Alloy steels with C, Si or Al, which reduce losses and increase permeability, also decrease the saturation polarisation and have a major impact on cost. This kind of ferromagnetic materials are widely used in practical applications, as a result of their ability to enhance the flux produced by an electrical current.

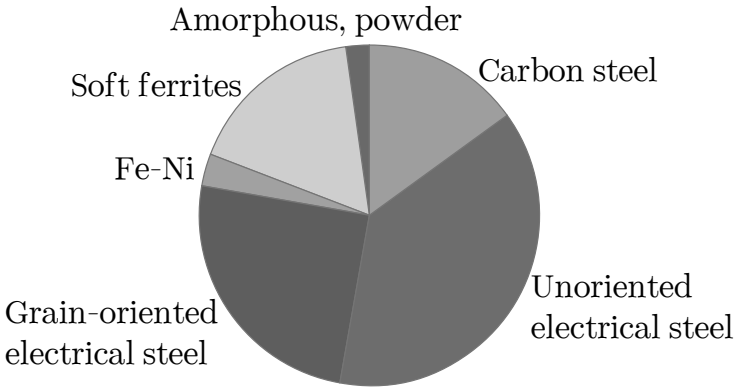

Figure 1.22: Global market for SMMs [8].

An SMM exhibits minimal hysteresis, high polarisation and the largest possible permeability. The latter represents one of the most important parameter, since it indicates the amount of magnetic flux density generated by the material in a given magnetic field. In some range of magnetic field, the $b(h)$ response is linear, $b = \mu h$. At the origin of the hysteresis loop, the initial permeability μ_i is smaller than the slope b/h in slightly larger fields, where it attains its maximum value μ_{max}. The distinction between magnetic induction b and polarisation J is insignificant in applications where high permeability of the soft material ensure that the magnetic fields h involved are very small [8].

SMMs may be employed both for DC and AC applications. For instance, one of the main static and low-frequency AC applications consists in flux concentration in magnetic circuits, including cores for transformers and inductors operating at fundamental main frequency (50 Hz). Among the most important DC uses, there are relays and electromagnets. For high power applications, silicon-iron (*Fe-Si*) alloys are widely used.

In a grain-oriented (GO) steel, the iron crystals have the best magnetic properties in "easy" direction, due to its anisotropic properties. These materials are well-suited for transformers, where the axis of b is fixed, hence it is advantageous to use crystallographically oriented sheet with an easy axis to further reduce losses. This material was developed by Norman Goss in 1934. GO silicon steel with the *Goss texture* is produced by a long process of rolling and annealing which favours secondary crystallisation. The thickness of GO silicon steel laminations is about $200 - 350\ \mu m$. At higher frequencies, thinner laminations are useful, also for reducing losses in case of non-sinusoidal waveforms with a high harmonic content.

Non-oriented (NO) Fe-Si alloys are appropriate in motors and generators, where, during operation, the direction of flux continually changes.

Fe-Ni alloy possesses useful magnetic properties as concerns the permeability, in particular *permalloys* with composition close to $Ni_{80}Fe_{20}$ have the highest permeability.

The *Fe-Co* alloys are used, for example, in generators for aircrafts or in electromagnetic pumps working at high temperatures. They are much less versatile and more expensive.

More and more power electric and power electronic devices use higher frequency signals, up to MHz. In the high frequency range, electrical steel exhibits prohibitively high power loss and should be substituted by other materials, such as ferrites.

Ferrites are non-conductive, isotropic ceramic compounds derived from iron oxides, as well as oxides of other metals [21]. *Ni–Zn* and *Mn–Zn* are the two basic families of soft ferrites, widely used as core materials for high frequency inductors and transformers in miniaturised power supply applications. Since they have higher resistivity than other magnetic materials, eddy current losses that can be large at high frequencies in metal-core inductors are reduced. Soft ferrites have low values of polarisation ($0.2 - 0.5$ T) compared

to metallic ferromagnets, nevertheless their insulating feature is an outstanding advantage at high frequencies. Mn-Zn ferrites are used up to about 1 MHz, Ni–Zn ferrites from 1 to 300 MHz or more. The latter have lower polarisation, but higher resistivity [8] than Mn-Zn ferrites, and are therefore more suitable for frequencies above 1 MHz. Mn-Zn have a comparably high permeability and saturation induction.

An overview of some physical and magnetic properties of the main SMMs used in applications is presented in Table 1.1 [9], [22].

Table 1.1: Representative SMMs and typical values of some basic magnetic parameters at room temperature.

	h_c (A/m)	b_{sat} (T)	T_C (°C)	Cost (€/kg)	Application domain
Fe-Si NO	$30-80$	$1.96-2.12$	$735-765$	1	Low frequencies
Fe-Si GO	$4-15$	2.02	750	2	(50 Hz – 1 kHz)
					Transformers,
					electric machines,...
Ferrite Mn-Zn	$5-20$	$0.4-0.55$	$130-280$	$5-40$	High frequencies
Ferrite Ni-Zn	$20-200$	$0.2-0.35$	$110-400$		(1 – 500 kHz, ≈ MHz)
Fe-Ni	4	$0.8-1.60$	450	$10-40$	Power
Amorphous	$0.5-1$	0.62	320	$40-160$	electronics
(Co-based)					

1.4 Iron loss modelling

Up to now, it was implicitly assumed that, during the Barkhausen jumps, the magnetic system evolution takes place so quickly that it is not influenced by the rate at which the external field changes during the jump. Therefore, the role of the external field is to bring the magnetic medium to the instability threshold at which the Barkhausen jumps occur. Under this hypothesis, a Barkhausen jump appears as an instantaneous event. The term *rate-independent hysteresis* is referred to magnetisation curves independent of the field rate (frequency).

However, magnetisation processes are influenced by the rate of change of the field. A system requires a certain time to react to varying external actions. This is the case, in ferromagnetic materials, where the magnetisation changes are damped by the production of eddy currents around moving domain walls. When the spontaneous evolution of the system through the Barkhausen jumps and the forced evolution driven by the external field take place on comparable time scales, rate-independent approximations are no longer valid. Since the frequency of the magnetic field is increased, the hysteresis phenomena start to be *rate-dependent*.

The *iron losses* in magnetic components are also named *core losses* or *magnetic losses*. For conducting ferromagnetic materials, the iron losses are often separated into *hysteresis losses* and *eddy current losses*. The former describes the losses due to the hysteresis properties of the magnetic material. Currents directly induced by the variation of the external magnetic field are named eddy currents. They originate from the variation of magnetic field in the machine cores. This creates (microscopic and macroscopic) eddy currents, which, in their turn, create Joule losses and heating. They depend on the geometry of the sample and on the rate of variation of the external field. Microscopic currents are induced locally because of the motion of domain walls.

The loop area has an important physical meaning, because it represents the energy density, for each cycle, irreversibly transformed into heat. The term $h\mathrm{d}b$ is the infinitesimal energy per unit of volume injected in a magnetic sample, during the magnetisation process. The integral

$$W = \frac{p}{f} = \oint_{loop} h \ \mathrm{d}b \tag{1.12}$$

represents the amount of work per unit volume performed by the external source and irreversibly transferred as heat. p is the *power loss density* ($\mathrm{W/m^3}$), p/f is known as the *energy loss per cycle*, where f is the frequency, in Hz, of the magnetic field h.

The loss processes are generated by the motion of domain walls, associated with a magnetisation change in the material. According to the Faraday's law, such variation induces eddy currents leading to a magnetic field counteracting the changes (time and direction) of magnetic fields (Lenz's law).

With increasing frequency, the intensity of eddy currents raises leading to an increase of the loop area and the change in the cycle shape (raise of the magnetic coercivity h_c), as observed in the dynamic hysteresis loops depicted in Figure 1.23.

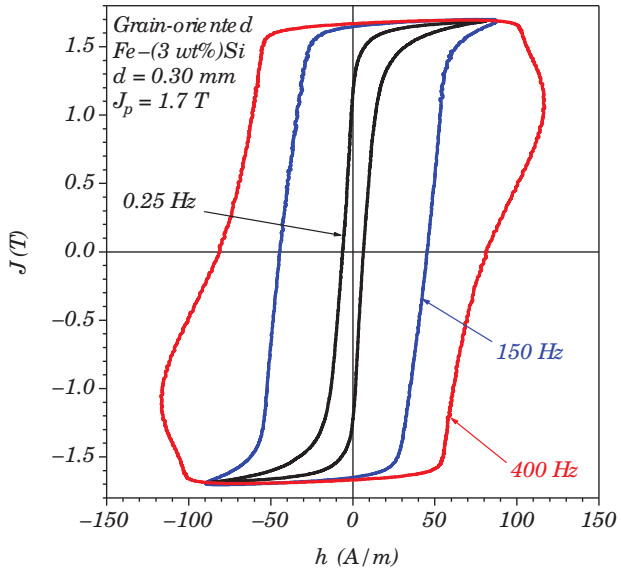

Figure 1.23: Hysteresis loops in a GO 0.30 mm thick Fe–Si steel sheet measured under sinusoidal polarisation of peak value $J_p = 1.7$ T at different frequencies [9].

In magnetic cores, iron losses can be reduced by means of thinner lamination sheet material. Eddy current losses increase proportional with the square of the lamination sheet thickness. Typically, thinner lamination sheets are used in high-speed machines. Iron losses can become the factor that contributes mostly in applications with increasing speed and run by power electronics inverters with varying switching frequencies.

1.4.1 Empirical approaches

This section shows an overview [23]- [24] of the most used approaches, based on Steinmetz equation, for calculating iron losses in electrical devices.

One method for determining iron losses relies on the *Steinmetz equation* (SE) :

$$p_{Fe} = C_{SE} \cdot f^{\alpha} \cdot b_p^{\beta} \tag{1.13}$$

It is only valid for purely sinusoidal inductions. The peak value of the flux density in the material is b_p, coefficients C_{SE}, α, β are determined by fitting the loss model to the measurement data.

Several extensions of the SE have been investigated also for other cases, such as non-sinusoidal waveform of flux densities. In the *Modified Steinmetz equation* (MSE) loss calculations with arbitrary waveforms of flux density are considered. MSE introduces an equivalent frequency f_{eq} depending on the remagnetisation rate dm/dt. Since the latter is proportional to the rate of change of the flux density db/dt, the equivalent frequency is defined as:

$$f_{eq} = \frac{2}{\Delta b^2 \cdot \pi^2} \int_0^T \left(\frac{db}{dt}\right)^2 dt \tag{1.14}$$

Thus,

$$p_{Fe} = C_{SE} \cdot f_{eq}^{\alpha-1} \cdot b_p^{\beta} \cdot f_r \tag{1.15}$$

corresponds the specific time-average magnetic loss, where f_r is the remagnetisation frequency ($T_r = 1/f_r$), $\Delta b = b_{max} - b_{min}$. This method becomes less precise in case of waveforms with a small fundamental frequency part.

In the *Generalised Steinmetz equation* (GSE), the magnetic loss is a single-valued function of b and db/dt, without taking into account the history of the flux density waveform:

$$p_{Fe} = \frac{1}{T} \int_0^T C_{SE} \cdot \left|\frac{db}{dt}\right|^{\alpha} \cdot |b(t)|^{\beta-\alpha} \, dt \tag{1.16}$$

The accuracy of GSE is limited, due to the presence of the minor loops in the hysteresis curve in case of higher harmonics. In order to overcome this problem, the *improved Generalized Steinmetz equation* (iGSE) was developed. In this case, the waveform is divided in one major and one or more minor loops. For each loop, iron losses are calculated separately with:

$$p_{Fe} = \frac{1}{T} \int_0^T C_{SE} \cdot \left|\frac{db}{dt}\right|^{\alpha} \cdot |\Delta b|^{\beta-\alpha} \, dt \tag{1.17}$$

in which Δb is the peak-to-peak magnetic induction of the major or minor loop of the waveform.

On the other hand, the *Natural Steinmetz Extension* (NSE) is applied to the waveform of the whole period and examines the impact of rectangular switching waveform, for example pulse width modulation (PWM):

$$p_{Fe} = \left(\frac{\Delta b}{2}\right)^{\beta-\alpha} \frac{C_{SE}}{T} \int_0^T \left|\frac{db}{dt}\right|^{\alpha} dt \tag{1.18}$$

In summary, the introduced approaches offer a fast way to predict the iron losses without requiring previous loss measurements. Moreover, the Steinmetz coefficients may be obtained by curve fitting from the curves in the datasheet or directly provided by the manufacturers. Nonetheless, the drawbacks consist in the fact that coefficients vary with temperature and, overall, these approaches are less accurate compared to the hysteresis loss models, especially at low frequency.

1.4.2 Bertotti's loss decomposition

Other approaches elaborated for determining iron losses include an extension to (6.1), proposed by Jordan [25]. This method presents a separation of iron losses into static hysteresis losses and dynamic eddy current losses. Additionally, an empirical correction factor, the excess loss factor was introduced in [26]. Due to the existence of magnetic domains, the eddy current loss is divided in two components due to the global and local eddy currents, known as the eddy current loss and excess (or anomalous) loss, respectively.

Then, Bertotti proposed a loss separation theory [7]. It decomposes the total power loss p_{tot} at the frequency f into a sum of three contributions: the hysteresis loss p_h, the classical loss p_{cl} and the excess loss p_{exc}:

$$p_{tot} = p_h + p_{cl} + p_{exc} = C_0 b_m^2 f + \frac{\sigma \pi^2 d^2}{6 m_v} \cdot (b_m f)^2 + C_1 b_m^\alpha f^\beta \quad (1.19)$$

where σ is the electrical conductivity (siemens per meter, S/m), d (m) is the thickness of lamination and m_v is the volumetric mass density (kg/m^3), b_m the maximal flux density. Quantities α, β, C_0 and C_1 are material related parameters fitted based on the loss measurements under sinusoidal flux conditions.

Figure 1.24 shows the behaviour of the three contributions as a function of frequency. The decomposition of losses into these parts reflects the coexistence of three dominant space-time scales in the magnetisation process: fast and localised Barkhausen jumps give rise to p_h; large-scale eddy current patterns controlled by the system geometry is associated to p_{cl}; intermediate-scale losses due to the existence of regions of dimensions controlled by the microstructure (e.g., grain size) is related to p_{exc} [27].

More particularly, p_h results from the discontinuous nature of the magnetisation process. Domain wall pinning is manifested as a result of the existence of inclusions and imperfections in the crystal structure, thus it is linked to the static (rate-independent) hysteresis loss. In the sample geometry, global induced currents develop due to changes in magnetisation. It is a rate-dependent phenomenon which influences the shape of hysteresis loop with increasing frequency. Finally, the magnetic domain level is linked to the excess loss. The associated eddy currents arise from the motion of domain walls in dynamic states, under the influence of the external field.

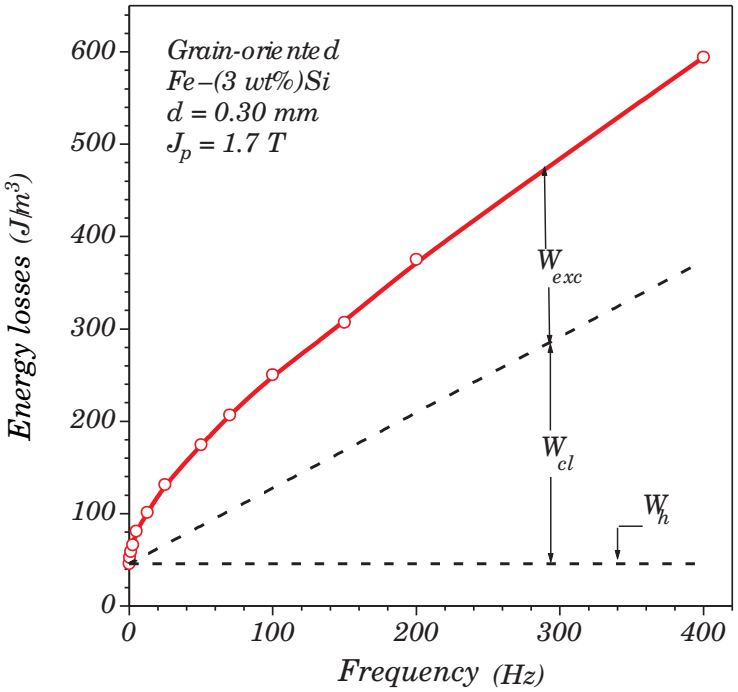

Figure 1.24: Corresponding behaviour of the energy loss per cycle and unit volume $W(f)$ (area of the hysteresis loop) and its decomposition in the quasi-static W_h , classical W_{cl} , and excess W_{exc} components. [9].

For a given flux density $b(t)$, Bertotti's formulation separates the total excitation field h into three contributions:

$$h_{tot}(t) = h_s(b(t)) + h_{class} + h_{exc} \quad (1.20)$$

in which $h_s(b(t))$ is the quasi-static contribution, frequency independent, related to the hysteresis losses. The contribution h_{class} is linked to macroscopic eddy currents. It is the product of γ to the time derivation of the magnetic induction field:

$$h_{class} = \gamma \frac{\partial b}{\partial t} \qquad \gamma = \frac{\sigma d^2}{12} \tag{1.21}$$

where γ depends on the conductivity σ and on the geometry of the sample. The term h_{exc} is linked to the dynamic of the magnetic domain walls (microscopic eddy currents). It is equal to the product of a constant α, the sign of the time derivation of the magnetic flux density and the square root of the absolute value of the time derivation of the magnetic induction.

$$h_{exc} = \alpha \delta \left| \frac{\partial b}{\partial t} \right|^{1/2} \qquad \alpha = \sqrt{\sigma G V_0 S} \qquad \delta = \text{sign}\left(\frac{\partial b}{\partial t} \right) \tag{1.22}$$

where S is the cross sectional area of the lamination sample, G a dimensionless coefficient of the eddy current damping, V_0 characterises the statistical distribution of the local coercive fields and take into account the grain size [28].

1.5 Hysteresis models

Iron losses include two intertwined phenomena, hysteresis and eddy current losses. In order to obtain a better accuracy of the iron loss prediction, hysteresis models are essential. However, conventional hysteresis models, such as the well-known Preisach and Jiles-Atherton, consider only one term (hysteresis) independently on the other. Even so, a large number of experimental data is required to fit parameters. Compared to the Steinmetz models, hysteresis models give better results in terms of accuracy. The disadvantage is a higher computational cost. Generally, the main objectives in hysteresis modelling are the ability to reproduce the shape of the hysteresis loop and determining the associated energy loss (i.e. the area of the loop).

Several hysteresis models are evaluated and discussed in more detail in this section, subdividing the review in static and dynamic modelling.

1.5.1 Static hysteresis models

In a magnetic material subjected to a complex signal (i.e. with high harmonic content), the magnetic field $\mathbf{h}(t)$ at a given time t is function of the flux density $\mathbf{b}(t)$, and also of the history of the material, that is $(\mathbf{h}(t'), \mathbf{b}(t'))_{t' \in]-\infty;t)}$. When history is considered, a static or quasi-static hysteresis model is necessary. This section will present a review of the most commonly employed models of hysteresis in electrical engineering. Up to now, the two dominant ones are the classical Preisach [29], [30], [14], [31], [32] and Jiles-Atherton (JA) models [33], some of which are implemented in several commercial softwares (among others, Flux, Maxwell 3D and Comsol).

Extensions of such models in order to account for the temperature are considered in [34], [35] for Preisach and [36] for JA model. Some extensions adjusting the original scalar models into their vectorial versions have been proposed in order to take into account rotational processes. They include the vector Preisach models [37], [38], [39], [40], [41] and vector JA models [42], [43], [44], [45].

More physical approaches include the energy-based models, in which the non-linear vector behaviour of ferromagnetic material is described by means of a pseudo-particles and a friction-like representation of hysteresis [10], [46]. This kind of model provides a

more intrinsic physical description of the complex nature of hysteresis, which explains its increasingly large popularity in ferromagnetic hysteresis modelling [47].

1.5.1.1 The Preisach model

The Preisach model [29], [30] is a phenomenological model characterised by the presence of *hysterons*, an assembly of elementary hysteretic particles. Each of them has a rectangular hysteresis loop, represented by an elementary hysteresis operator $\hat{\gamma}_{\alpha,\beta}$.

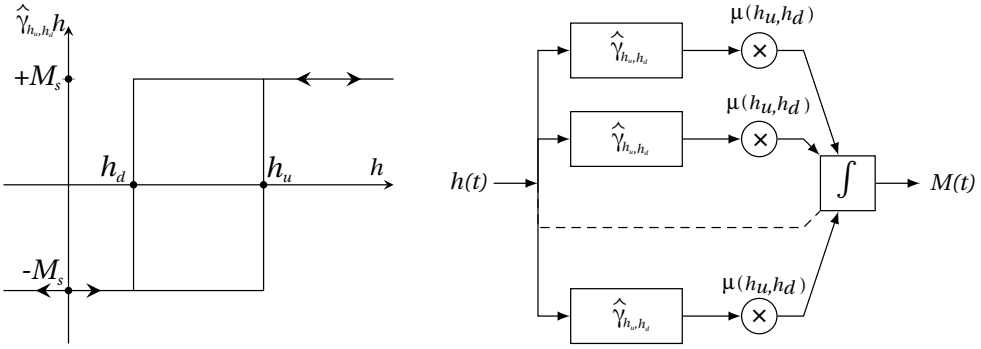

Figure 1.25: Preisach elementary hysterons (left) and lock representation of the classical Preisach model (right).

A typical loop is illustrated in Figure 1.25 (left). The input of the model is the magnetic field h. Quantities h_u and h_d correspond to "up" and "down" switching values of input, respectively. Outputs of the elementary hysteresis operators may assume two values, $+M_s$ and $-M_s$, where M_s represents the local magnetisation. These operators can be interpreted as two-position relays with "up" and "down" positions corresponding to $\hat{\gamma}_{h_u,h_d}h(t) = +M_s$ and $\hat{\gamma}_{h_u,h_d}h(t) = -M_s$, respectively. The Preisach model can then be defined as [31]:

$$M(t) = \hat{\Gamma}h(t) = \iint_{h_u \geq h_d} \mu(h_u, h_d)\hat{\gamma}_{h_u,h_d}h(t)dh_u dh_d \tag{1.23}$$

where $\mu(h_u \geq h_d)$ is a weight function called the Preisach density function (PDF). The operator $\hat{\Gamma}$ is used to denote the Preisach hysteresis operator.

The Preisach model may be considered as a system of parallely connected two-position relays, as depicted by the block diagram in Figure 1.25 (right). The same input is applied to each of two-position relays. Every output is multiplied by the PDF $\mu(h_u, h_d)$ and integrated with respect of variables h_u and h_d. Consequently, the magnetisation $M(t)$ is obtained. The PDF $\mu(h_u, h_d)$ is a non-negative weight function indicating the weights of each hysteron in the Preisach plane S:

$$S = \{(h_u, h_d) : h_u \geq h_d,\ h_u \leq H_u,\ h_d \geq H_d\}$$

where H_u and H_d refer to the highest and lowest values for h_u and h_d respectively. The Preisach plane S can be divided into two subregions, S^+ corresponding to relays with output value $+M_s$ and S^- which corresponds to output values $-M_s$.

A working example of Preisach model is illustrated in Figure 1.26. It is assumed that the input is $h(t_0) = h_0 < H_d$ at an initial time t_0. Hence, all delayed relay elements have $-M_s$ as output value. Firstly, the input is increased monotonically until some maximum at time t_1 up to a value $h(t_1) = h_1$, that is:

$$h([t_0; t_1]) = h_0 \rightarrow h_1$$

The corresponding Preisach plane is shown in Figure 1.26 (left), in which the boundary between S^+ and S^- is the horizontal line $h_u = h_1$. Each element below the memory curve is turned on, namely they are characterised by a h_u value lower than h_1, in the same way, all hysterons with $h_u > h_1$ are turned off. Next, the input is decreased monotonically until some input h_2 at time t_2:

$$h([t_1; t_2]) = h_1 \rightarrow h_2$$

All hysterons with h_d value higher than h_2 will be switched off (see staircase memory curve in Figure 1.26 (right)). The output $M(t)$ can be rewritten as

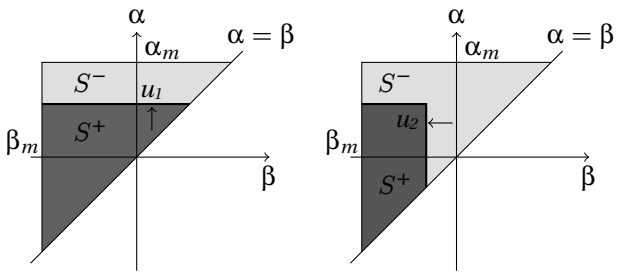

Figure 1.26: Preisach elementary hysterons (left) and lock representation of the classical Preisach model (right), where $\alpha = h_u$, $\beta = h_d$, $u_1 = h_1$, $u_2 = h_2$.

$$M(t) = \iint_{S^+} \mu(h_u, h_d) dh_u dh_d - \iint_{S^-} \mu(h_u, h_d) dh_u dh_d \tag{1.24}$$

Hence, an instantaneous value of output depends on the subdivision of the plane into positive and negative sets, defined by the past sequence of local maxima and minima of the input.

In the magnetic interpretation, it would be desirable to relate the operators to some real physical objects, such as magnetic particles, their distribution, etc. Nevertheless, there are several issues concerning this interpretation. Even if the model refers to magnetic particles, it does not take into account their geometric shape and spatial location, influencing the magnetisation. For this reason, it may be considered as a mathematical tool, rather than a physical model. Furthermore, the Preisach model laid the foundations of other hysteresis models such as the Stop- and Play-type models, further detailed in [48], [49].

Due to the contribution of several hysterons, the model requires a high computational cost (i.e. every state has to be reassessed if one of the operators changes state).

Moreover, in order to be used in practical context, the PDF $\mu(h_u, h_d)$ must be identified. Often, the identification procedure relies on a fit of analytical functions, such as Lorentzian, Gauss-Gauss or Lognormal-Gauss distributions [7], which in turns requires a significant amount of experimental data and is generally rather complicated [50]- [51]- [52].

1.5.1.2 The Jiles-Atherton model

The JA model [53], [54], [55] is one the most popular hysteresis models, due to some advantages, such as small number of parameters and quite easy implementation.

The model decomposes the magnetisation M into a reversible component M_{rev}, corresponding to domain wall bending during the magnetisation process, and an irreversible component M_{irr} related to domain wall movement over the pinning sites.

Thus the total magnetisation is $M = M_{rev} + M_{irr}$. The differential equation modelling the irreversible component of M is:

$$\mathrm{d}M_{irr} = \frac{M_{an} - M_{irr}}{k\delta - \alpha(M_{an} - M_{irr})}\mathrm{d}h \tag{1.25}$$

in which α is the coupling between magnetic domain moments. The coefficient k represents a factor of proportionality between the energy dissipated when a domain wall crosses a pinning site, and the variation of the magnetisation as an effect of this movement. Finally, δ corresponds to a directional variable corresponding to the sign of the derivative $\frac{\mathrm{d}h}{\mathrm{d}t}$. That is $\delta = 1$ when h is increasing and $\delta = -1$ when h is decreasing.

The anhysteretic magnetisation M_{an} is the magnetisation of an ideal ferromagnet which does not possess pinning sites and thus, its magnetisation curve does not present hysteresis, the magnetisation being made only through the rotating mechanism of the magnetic moments. It is described using the Langevin function $L(x)$, in which an effective field h_e replaces the magnetic field h:

$$M_{an} = M_{sat}L\left(\frac{h_e}{a}\right) = M_{sat}\left(\coth\frac{h_e}{a} - \frac{a}{h_e}\right) \tag{1.26}$$

where M_{sat} is the saturation magnetisation and the parameter a is a measure of the coupling between the adjacent magnetic domains.

The field $h_e = h + \alpha M$ is introduced to take into account the effective field seen by the magnetic domains, similar to the molecular field by the Weiss theory [56]. The reversible component of the magnetisation c is a fraction of the difference of the anhysteretic magnetisation and the irreversible one:

$$M_{rev} = c(M_{an} - M_{irr}) \tag{1.27}$$

The differential equation which gives the dependence between the magnetisation of a magnetic sample and the applied magnetic field is:

$$\frac{\mathrm{d}M}{\mathrm{d}h} = \frac{(1-c)\frac{\mathrm{d}M_{irr}}{\mathrm{d}h_e} + c\frac{\mathrm{d}M_{anh}}{\mathrm{d}h_e}}{1 - (\alpha c)\frac{\mathrm{d}M_{anh}}{\mathrm{d}h_e} - \alpha(1-c)\frac{\mathrm{d}M_{irr}}{\mathrm{d}h_e}} \tag{1.28}$$

Hence, in order to use the JA model, five parameters α, a, M_{sat}, c and k (Table 1.2) have to be identified from experimental data. Many researchers have proposed stochastic

Table 1.2: Physical properties of JA model parameters.

Parameters	**Physical property**
a (A/m)	shape parameter for M_{an}
c	reversibility coefficient
k (A/m)	linked to hysteresis losses
α	linked to domain interaction
M_{sat} (A/m)	saturation magnetisation

optimisation methods, such as the genetic algorithm [57], [58] and population-based search algorithms, like particle swarm optimisation [59].

The implementation is relatively simple and requires few memory storage [60], [61]. Nevertheless, there are some shortcomings in case of distorted hysteresis loops, leading to inaccurate predictions. Experience has demonstrated that the model does not accurately

approximate the measured minor loops with the same parameters as those identified from major loops [62]. Most importantly, the original JA model sometimes does not ensure the closure of minor loops in a physical adequate manner. For this reason, several modifications have been formulated in order to overcome this problematic [63], [64] [65], [66], [67]. However, these attempts to eliminate the unphysical behaviour of the model rest on artificial corrections, aiming to match simulated and measured loops, lacking a real physical explanation. Furthermore, the concepts underlying the JA model have been critically analysed in [61], for instance its decomposition of magnetisation into reversible and irreversible parts.

1.5.1.3 Henrotte's Energy-Based model

The so-called Vector Play Model, relying on a description of ferromagnetic hysteresis as a set of elementary pseudo-particles was firstly presented in [10], then extended to its current form, such Energy-Based (EB) model in [68], [46], [69], [70], [71]. Inspired by the Preisach and JA models, Bergqvist [10] presented a quasi-static magnetic vector hysteresis model based on thermodynamic principles. Namely, it considers the magnetisation as the superposition of a number of pseudo-particles. The notion of dry-friction force is used to model the domain wall pinning to describe the physical origin of hysteresis.

In this section, the basic concepts of the EB model are presented, focusing on its readily vectorial nature and thermodynamic foundation. As a first step, thermodynamics relations will be introduced in case of systems in equilibrium, described by the anhysteretic curve. Then, a dry-friction like pinning force will be introduced to depict the deviation of the magnetisation process from the anhysteretic curve, so accounting for the complexity of the non-equilibrium thermodynamics associated to hysteresis phenomena.

Thermodynamic foundation and energy conservation The formulation of the model is based on the following assumptions [69]:

- hysteresis losses and eddy current losses can be treated separately [7].
- The magnetic flux density $\mathbf{b}$ is represented as a sum (1.29) of two components: an empty space magnetic polarisation $\mathbf{J}_0 = \mu_0 \mathbf{h}$, always linear and reversible, and a material magnetic polarisation $\mathbf{J}$, related to the presence of microscopic moments attached to the atoms of the material body, and that is both non-linear and irreversible.

$$\mathbf{b} = \mathbf{J}_0 + \mathbf{J} \tag{1.29}$$

  Focusing only on the relevant magnetic energy contribution in a magnetic body, the work of the electromagnetic field is given by (1.30).

$$\dot{W} = \mathbf{h} \cdot \dot{\mathbf{J}} = \mu_0 \mathbf{h} \cdot \dot{\mathbf{M}} \tag{1.30}$$

  where the notation $\dot{\square} = \partial_t$ means derivation with respect to time.
- Hysteresis losses can be interpreted as the power delivered by a generalised force parallel to the variation of the magnetisation, i.e. the magnetic equivalent of a dry friction force [68]. The physical origin of this force is the pinning effect that opposes the motion of Bloch walls [7].

In a ferromagnetic material, the local form of first law of thermodynamics, which states conservation of energy, writes:

$$\dot{U} = \dot{W} + \dot{Q} = \mathbf{h} \cdot \dot{\mathbf{J}} - \operatorname{div} \mathbf{q} \tag{1.31}$$

where U is the internal energy, W and Q are respectively the amounts of work and heat supplied to the system, and $\mathbf{q}$ is the heat flux.

It can be demonstrated that (1.31) can be rewritten as:

$$\dot{U} + D = \mathbf{h} \cdot \dot{\mathbf{J}} + T\dot{S} \tag{1.32}$$

where D is a dissipation functional defined as:

$$D = T\dot{S} + \text{div } \mathbf{q} \tag{1.33}$$

In order to get rid of the term $\dot{S}$, we use the Helmoltz free energy:

$$F = U - TS \qquad \Longrightarrow \qquad \dot{F} = -D + \mathbf{h} \cdot \dot{\mathbf{J}} + T\dot{S} - \dot{T}S - T\dot{S} \tag{1.34}$$

Therefore, by assuming that transformations are isotherm (that is: $T = const$, hence $\dot{T} = 0$) we can write:

$$D = \mathbf{h} \cdot \dot{\mathbf{J}} - \dot{F} \geq 0 \tag{1.35}$$

The fact that the dissipation functional is positive comes from the second principle of thermodynamic.

Reversible contribution In case of a reversible transformation there is no dissipation ($D = 0$) thus:

$$\dot{U} = \dot{F} = \mathbf{h} \cdot \dot{\mathbf{J}} = \mu_0 \mathbf{h} \cdot \dot{\mathbf{M}} \tag{1.36}$$

One observes that in this case the magnetic field can be expressed by the derivative of the free energy at fixed temperature[2]:

$$\mathbf{h} = \frac{1}{\mu_0} \left(\frac{\partial F}{\partial \mathbf{M}} \right)_T \tag{1.37}$$

Since there is no dissipation, $\mathbf{M}$ and $\mathbf{h}$ are linked by a one-to-one anhysteretic function:

$$\mathbf{M} = \mathbf{M}_{an}(\mathbf{h}) \tag{1.38}$$

accordingly to (1.36), we define the reversible part of the magnetic field $\mathbf{h}_r$ as:

$$\mathbf{h}_r = \frac{1}{\mu_0} \left(\frac{\partial F}{\partial \mathbf{M}} \right)_T = \left(\frac{\partial U}{\partial \mathbf{J}} \right)_T \tag{1.39}$$

Consequently, from (1.35) D is given by

$$D = (\mathbf{h} - \mathbf{h}_r) \cdot \dot{\mathbf{J}} \geq 0 \tag{1.40}$$

Irreversible contribution The irreversible part is introduced in the model by pinning forces. In this respect, it is recalled that Weiss domains are separated by Bloch walls, in which the orientation of magnetic moments varies gradually from the orientation of the domain on the one side to the one of the domain on the other side. Magnetisation of a ferromagnetic material involves the motion of these walls. The reversibility of this process depends on the presence of defects, inclusions or impurities, in the crystal structure (Figure 1.27).

[2]In thermodynamics it is customary to explicitly write fixed quantities (T in this case) together with derivatives.

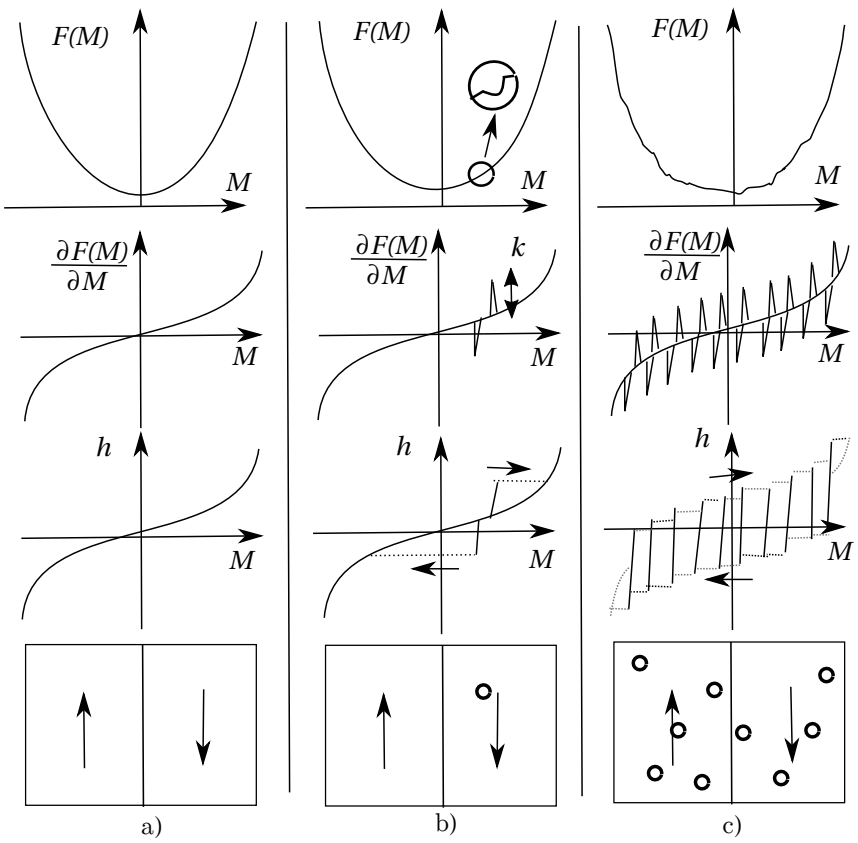

Figure 1.27: Illustration of $h - M$ relation in a) the presence of no potential drops, b) one potential drop and c) several drops. First row shows free energy F as function of magnetisation, second row $\frac{\partial F}{\partial M}$, third row the resulting $h - M$ relation and fourth row a schematic domain configuration with the small circles representing inclusions [10].

In a perfect crystal, the walls move freely whereas the magnetisation goes smoothly. As a result, there is no dissipation associated with a quasi-static variation of the applied field. Without inclusions and when $\mathbf{h} = 0$, the Helmholtz free energy density has a "regular" (non-rippled) shape like in Figure 1.27(a) with a unique minimum at $\mathbf{M} = 0$.

Considering a real material with defects, the system is disrupted by a small potential well around some M, so the energy density looks like the rippled curve in Figure 1.27 (b, c) [72]. Indeed, such defects represent small magnetic voids in the crystal lattice which pin Bloch walls at fixed positions and prevent them from moving under the effect of an external magnetic field. When a wall crosses a defect, each configuration with a pinned wall corresponds to a local minimum of the magnetic energy. When the latter becomes higher than the energy barrier due to this pinning force, Bloch walls suddenly rearrange and the energy corresponding to the jump is dissipated [10], hence the irreversibility and the hysteresis behaviour.

By means of a mechanical analogy, hysteresis losses can be interpreted as the power delivered by a force parallel to the variation of the magnetisation, that is the magnetic equivalent of a mechanical friction force κ [10], [68]. Basing on this analogy, the input is the magnetic field $\mathbf{h}$, which can be decomposed in a reversible part $\mathbf{h}_r$ and an irreversible part $\mathbf{h}_{ir}$ (1.41) acting respectively as spring force and friction force [68].

$$\mathbf{h} = \mathbf{h}_r + \mathbf{h}_{ir} \tag{1.41}$$

The magnetic work delivered by the reversible magnetic field $\mathbf{h}_r$, under a variation of the magnetisation, is fully converted into internal energy. Hence, the vector $\mathbf{h}_r$ is linked with the magnetic polarisation of the material, whereas, the dissipation functional D is associated with the dry-friction force and writes:

$$D = \mathbf{h}_{ir} \cdot \dot{\mathbf{J}} = \kappa \left|\dot{\mathbf{J}}\right| \qquad \Rightarrow \qquad \mathbf{h}_{ir} = \frac{\partial D}{\partial \dot{\mathbf{J}}} = \kappa \frac{\dot{\mathbf{J}}}{\left|\dot{\mathbf{J}}\right|} \tag{1.42}$$

Thus, D represents the power density delivered by the irreversible magnetic field $\mathbf{h}_{ir}$, κ (in A/m) is a material characteristic called *pinning field*, that opposes the motion of domains walls and it is proportional to the pinning site energy that determines the coercivity h_c of the hysteresis loop.

If the distance between drops in the system is small, the situation can be represented by approximating the sequence of small jumps by a continuous relation between h and M, as shown in Figure 1.28. Along the ascending and descending branches of the saturation loop, respectively, $h = \frac{\partial F}{\partial M} \pm \kappa$ or equivalently $M = M_{an}(h \mp \kappa)$ [10]. Minor loops corresponds to the horizontal lines connecting the branches of the major loop. This determines the relation between magnetisation and field for the scalar case.

Now, by combining (1.39)-(1.42) one obtains:

$$\mathbf{h} - \mathbf{h}_r - \mathbf{h}_{ir} = 0 \qquad \Rightarrow \qquad \mathbf{h} - \frac{\partial U}{\partial \mathbf{J}} - \kappa \frac{\dot{\mathbf{J}}}{\left|\dot{\mathbf{J}}\right|} = 0 \tag{1.43}$$

The functional D is not differentiable in $\dot{\mathbf{J}} = 0$, thus $\mathbf{h}_{ir}$ can be defined by means of a *subgradient* of the functional D, which is the set defined as:

$$\mathbf{h}_{ir} \in \left\{ \mathbf{h}_{ir}, |\mathbf{h}_{ir}| \leq \kappa \;\text{ if }\; \dot{\mathbf{J}} = 0, \quad \mathbf{h}_{ir} = \kappa \frac{\dot{\mathbf{J}}}{\left|\dot{\mathbf{J}}\right|} \;\text{ otherwise} \right\} \tag{1.44}$$

Since real ferromagnetic materials are characterised by a statistical distribution of pinning fields [10], [73], [70], a multi-cell model has been elaborated. It relies on the fact that

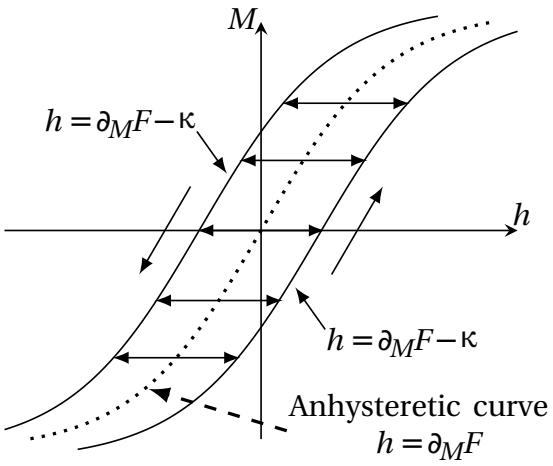

Figure 1.28: Magnetization curve when the well density goes to infinity [10].

the material, homogeneous at the macroscopic scale, is composed of N heterogeneous microscopic abstract subregions (also called *cells*), defined by a specific pinning force κ^k. The reversible magnetic field $\mathbf{h}_r$ is computed as the weighted sum of contributions $\mathbf{h}_r^k$ of a number of cells N:

$$\mathbf{h}_r = \sum_{k=1}^{N} \omega_k \mathbf{h}_r^k \tag{1.45}$$

In this sum, ω_k are the weights associated to cells, namely they highlight the relative importance of each contribution and must verify the condition $\sum_{k=1}^{N} \omega_k = 1$. Basing on the knowledge of the magnetic field $\mathbf{h}$, independent equations can be solved for each cell:

$$\mathbf{h} - \mathbf{h}_r^k - \mathbf{h}_{ir}^k = 0 \tag{1.46}$$

The number of cells in which the EB model is discretised depends on the required accuracy: models with higher number of cells will be more accurate, but also more time consuming from the computational point of view. The resolution of the non-linear differential equations (1.46) is proposed in [68]. It is called the *simplified differential approach*. An approximate solution is obtained on the basis of the explicit update rule, in which the terms $\mathbf{h}_r^k$ are upgraded as a function of the applied magnetic field $\mathbf{h}$ and of their previous value $\mathbf{h}_{r0}^k$ according to:

$$\mathbf{h}_r^k = \begin{cases} \mathbf{h}_{r0}^k & \text{if } \left|\mathbf{h} - \mathbf{h}_{r0}^k\right| < \kappa^k \\ \mathbf{h} - \kappa^k \cdot \frac{\mathbf{h} - \mathbf{h}_{r0}^k}{\left|\mathbf{h} - \mathbf{h}_{r0}^k\right|} & \text{otherwise} \end{cases} \tag{1.47}$$

where κ in A/m is a material characteristic called *pinning field*, that opposes the motion of domains walls. It is proportional to the pinning site energy that determines the coercivity h_c of the hysteresis loop. In Figure 1.29 a pictorial representation of the update rule is shown.

The sphere of radius κ is centered in $\mathbf{h}_r$. The tip of applied magnetic field $\mathbf{h}$ is either inside the sphere or on its surface. If the tip of $\mathbf{h}$ moves inside the sphere, then the condition

$$\left|\mathbf{h} - \mathbf{h}_{r0}^k\right| < \kappa^k \tag{1.48}$$

is fulfilled and the sphere remains fixed, $\mathbf{h}_r$ is unmodified and $\dot{\mathbf{J}} = 0$, since the two vectors are in a one-to-one relationship. If $\mathbf{h}$ tends to go beyond the sphere, the latter has to shift to comply with the condition (1.48), i.e. the center of the sphere moves according to (6.12), so that $\mathbf{h}$ remains on the boundary of the shifted sphere.

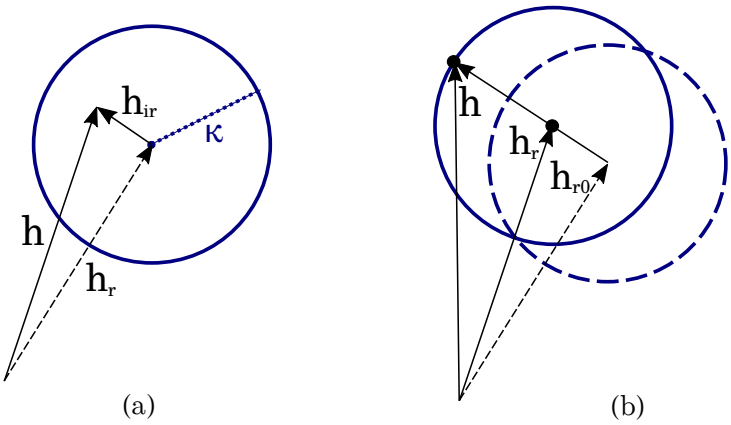

Figure 1.29: Vector diagram of $\mathbf{h} = \mathbf{h}_r + \mathbf{h}_{ir}$.

Then, the magnetization $\mathbf{M}$ is computed as:

$$\mathbf{M} = M_{an}(|\mathbf{h}_r|)\frac{\mathbf{h}_r}{|\mathbf{h}_r|} \tag{1.49}$$

where M_{an} is a scalar, monotone increasing anhysteretic magnetization function. Finally, the magnetic flux density is given by

$$\mathbf{b} = \mu_0(\mathbf{M} + \mathbf{h}) \tag{1.50}$$

The EB model is completely characterised by the anhysteretic curve M_{an} and by the couples of parameters $(\omega_k, \kappa^k)_{k=1...N}$. M_{an} can be represented by analytical expressions, i.e. Langevin or double Langevin functions [68] or interpolated from experimental measurements [74].

1.5.1.4 Static hysteresis and temperature

The objective of a temperature-dependent model is twofold:

1. to predict the device performance at a given external temperature,
2. to determine the equilibrium temperature for a given operating mode, in a specific operating environment, in order to optimize components in their design phase.

So as to be useful in practical engineering applications, hysteresis models must consider the effect of temperature. The well known JA and Preisach hysteresis models were widely used during the last decades to predict hysteresis curves or magnetic losses. Despite the wide number of users of these models, very few authors tried to take into account the temperature. For example, analytical empirical laws of variation of the JA model parameters versus temperature are used in [36] to predict hysteresis loops. In [75], several approaches (analytical, numerical, and mixed) were compared in order to identify each parameter variations.

As regards Preisach models, [34] used a double well potential distribution. Static and dynamic interactions were taken into account in order to simulate various magnetisation processes, such as field-cooled, zero field-cooled, thermo-remanent magnetisation, magnetic relaxation in applied field, and the major hysteresis loop as a function of temperature.

The authors of [76] assumed that the Preisach distribution function was a factorised product of a Gaussian coercive field distribution, and a Gaussian interaction field

distribution both with some dispersion coefficients. Those last two approaches are rather complicated to implement in engineering softwares such as Finite Element (FE) or circuit-type (SPICE) ones.

The EB model presents several advantages in modelling magnetic hysteresis. Firstly, it is inherently vectorial and is defined by an adjustable precision according to the choice of the number of cells to represent the magnetic material. Secondly, as a result of its thermodynamic foundations, the model is particularly suitable to accurately predict the complex material response in compliance with the physics of magnetic systems. Moreover, it provides an energy balance, so that the stored and dissipated energies can be computed at any moment in time, not only at the end of closing hysteresis loops.

The EB model has been tested and implemented in Finite Elements [68], [69], [77] and been improved in the case of rotating fields [78]. In [79] a method is proposed, in which linear variations of saturation magnetisation and coercive field are considered to take into account the temperature for permanent magnets. Variations of some parameters of the EB model were identified by means of methods described in [36], [80], [81]. The EB model showed suitability to the temperature dependence, by allowing some parameters to change their values. The thermal behaviour was qualitatively well identified, loops expanded or shrank themselves in function of temperature showing the ability of the model to qualitatively retrieve the Hopkinson effect [82], [74]. Empirical laws are used in order to predict the thermal behaviour, considering both temperature and the complex inductions waveforms influence on soft ferrites. A temperature-dependent hysteresis model based on a vectorial elemental operator with thermal-sensitive spontaneous magnetisation and biaxial anisotropy for the soft ferrites is introduced in [83].

Due to all its desiderable features, the EB model was chosen as preferred hysteresis model. Therefore, its magnetic behaviour and its temperature dependent magnetic hysteresis property, in a large temperature range is studied in this thesis. Particularly, to accommodate the thermal effects on the material constitutive law, recent developments on the dependence of the EB model on temperature are presented in this work, with the final object to propose a temperature-dependent model for SMMs (Chapter 3).

Figure 1.30 shows a short summary of the main features of three hysteresis models, the Preisach, Jiles-Atherton and Energy-Based models.

	Preisach model	Jiles-Atherton model	Energy-Based model
Description	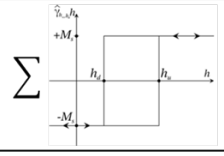	Based on a differential equation with five parameters to identify	Accurate energy-balance Intrinsically vectorial Arbitrary number of parameters 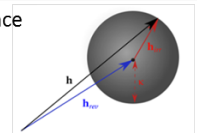
Identification	Interpolation method	Iterative and optimization procedures	Anhysteretic curve $h_c(h_p)$ curves
Experimental data	Large amount of measurements: first order reversal curves	Set of hysteresis loops	Set of hysteresis loops
Asymmetric minor loops	Accurate	Not guaranteed	Accurate
Implementation	Difficult High computational cost and memory	Simple and fast	Simplified Differential approach Variational approach Full Differential approach

Figure 1.30

1.5.2 Dynamic hysteresis models

Up to this point, the described models were considered independent of time, namely the rate at which the magnetic quantities h or b vary is sufficiently low, so that the fields are not affected in time. These models are valid at very low frequency (for instance, $f < 1$ Hz for metallic materials, $f < 1$ kHz for ferrites) and this type of hysteresis is rate-independent.

However, in real industrial applications, magnetic materials are mostly stressed at higher frequencies. In fact, with the advance of power electronics, supplying electromagnetic devices becomes no more limited to the frequencies distributed by electric networks. As the rate of change of the flux density b or of the applied field h increases, the hysteresis loops change their size and shape. The magnetisation curves are influenced by the field rate and this kind of hysteresis is considered as rate-dependent. Therefore, h or b will depend on the rate of change of the magnetic quantities, giving rise to additional phenomena, such as the skin effect.

Among the existing hysteresis models in literature, some improvements have been investigated to adapt these models to be used in dynamic conditions, accounting for eddy-current losses. For instance, several studies were proposed on the dynamic version of Preisach model [84], [85], [86], [87], [41] and Jiles-Atherton model [88], [89], [90], [91], [45].

The next sections will present some models developed at the Ampère laboratory, École Centrale Lyon (Dynamical with Static Feedback (DSF) [92]- [93] and Dynamical with Wall Motion (DWM)) [92]- [94], and finally the Loss Surface (LS) [95]- [96] model developped in the G2Elab, Grenoble INP.

1.5.2.1 Dynamical with Static Feedback model

The DSF model [92], [93] points out the dynamical behaviour of the material and considers a simple geometry (flux tube with a constant cross-section). It allows to obtain the dynamic behaviour of a magnetic circuit with a constant cross-section, where the anisotropy of the material is neglected. Dynamic effects developped in the circuit (wall motion, macroscopic eddy currents) are considered in this model by a single representation.

The dynamic behaviour of the circuit is described by a first order differential equation:

$$\frac{\mathrm{d}b_a(t)}{\mathrm{d}t} = \frac{1}{\gamma}\left[h_{dyn}(t) - h_{stat}(b(t))\right] \tag{1.51}$$

in which b_a is the average flux density in the cross-section, h_{dyn} is the excitation applied field at the surface and $h_{stat}(b_a)$ is a static excitation field which corresponds to a given value of b_a. The magnetisation history of the material can be considered by means of a hysteretic static model for $h_{stat}(b_a)$. Parameter γ is a dynamic behavioural parameter, the value of which has to be fitted by comparing simulated and measured dynamic loops.

The main assumption of this model is to consider the homogeneity of the phenomena in the cross-section of the flux tube. DSF model has some advantages, especially it requires only one parameter γ independent of the waveform and velocity of the excitation, the calculation time is short, it is reversible $b_a(h_{dyn})$ or $h_{dyn}(b_a)$. Equation (1.51) can be compared with the expression (1.52) defined in the case of a magnetic lamination if the skin effect, saturation and edge effects are negligible.

$$h_{tot} = h_{stat}(b_a) + \frac{\sigma d^2}{12} \cdot \frac{\partial b_a}{\partial t} \tag{1.52}$$

where h_{tot} is the excitation field in the lamination surface when eddy currents are induced in the cross-section, d is the thickness of the lamination, σ is the conductivity of the

material, b_a the averaged magnetic flux density over the thickness. In both cases, it is assumed the homogeneity of magnetic data. An analogy between (1.51) and (1.52) allows to estimate the value of the parameter γ, given by:

$$\gamma = \frac{\sigma d^2}{12} \tag{1.53}$$

1.5.2.2 Dynamical with Wall Motion model

Dynamic modelling of the material can be performed using the DWM model [92], [94] in case of more stringent dynamic sollicitations. The magnetic diffusion equation results from Maxwell's equations and a law describing the conductive property of the material

$$\text{curl}(\text{curl } \mathbf{h}) = -\sigma \frac{\partial \mathbf{b}}{\partial t} \tag{1.54}$$

Since the magnetic field is always perpendicular to the cross section, then div $\mathbf{h} = 0$, thus (1.54) becomes

$$\frac{\partial^2 h(y,t)}{\partial y^2} = \frac{\sigma}{\beta} \frac{\partial b(y,t)}{\partial t} \tag{1.55}$$

where β is representative of the domain structure of the material and associated to domain walls. It differs from the parameter γ, in the DSF model, where it includes macroscopic eddy currents and motion of domain walls. This model includes the excess dynamic effects by means of a dynamical material law implemented into the magnetic diffusion equation.

Furthermore, these dynamic models (DSF and DWM) have been employed and adapted to take into account another variable parameter, the temperature in [97] and [11].

1.5.2.3 Loss Surface model

The LS model [95], [96] is a dynamic and scalar hysteresis model. The magnetic field h is determined as a characteristic surface function

$$S = h(b, \frac{\mathrm{d}b}{\mathrm{d}t}) = h_{stat}(b) + h_{dyn}(\frac{\mathrm{d}b}{\mathrm{d}t}) \tag{1.56}$$

separated into static and dynamic parts. The model links the magnetic field on the sheet surface with the flux density in the thickness of the sheet. The static part is modeled by a rate-independent hysteresis model, the dynamic part is built by two linear analytical equations describing the low and high values of the flux density derivatives after subtracting the static part h_{stat}. The LS model has been also implemented in the Finite Element software Flux from Altair Group, France.

1.5.3 Dynamic-thermal problematics

During a dynamic process, electromagnetic energy losses in ferromagnetic materials are dissipated in the form of heat, which results in an increase of temperature. With rising temperature in magnetic components, the atoms in the material possess stronger vibrations, which weakens the alignment of magnetic moments and magnetisation. This is more emphasised at higher frequencies, where the fast oscillating external field rotates and consistently re-aligns the magnetic moments. This produces frictions of magnetic moments leading to an increased hysteresis loss [98]. Moreover, when the temperature of the material overcomes the Curie point, the alignment of the magnetic moments is destroyed. Therefore, the magnetic field produced by the magnetic material disappears,

which results in the failure of magnetic devices. Temperature increment associated to the energy loss is tipically one of the most important limiting factors to the performance of magnetic devices. Hence, adopting an accurate temperature-dependent dynamic hysteresis model is fundamental to the engineering design of more reliable devices and systems. For this reason, in this thesis, an attempt to account for temperature and frequency dependence in a fully-fledged hysteresis model is studied and investigated.

Chapter 2

Magnetic Measurements

This chapter presents the magnetic measurement methods for the characterisation of SMMs that provide the groundwork for the measurement setups used in the present work. The magnetic characterisation of materials has two major aims:

- the measurement of some intrinsic magnetic parameters, such as the saturation magnetisation, the Curie temperature, etc...;
- the determination of the constitutive law of the material $b(h)$.

The magnetic characterisation relies on the combined determination of two variables, the magnetic field strength and the magnetic induction. For unidirectional excitations, there exists two methods to determine the relation $b(h)$: the *field-metric* and *current-metric* methods. The former identifies $h(t)$ through direct measurement of the surface magnetic field strength. On the contrary, the latter provides an indirect determination of the magnetic field strength using the excitation current. For isotropic materials, the magnetisation vector is always aligned with the applied magnetic field. Especially, for soft ferrites considered in this thesis, the adoption of a scalar relationship between the magnetic induction $b(t)$ and the magnetic field $h(t)$ is valid. The experimental approach taken during this work is based upon the current-metric method, under the condition of unidirectional quasi-static and dynamic excitation, with the aim to determine the macroscopic scalar relation between the magnetic field $h(t)$ and the induction $b(t)$ of the sample, i.e. a toroidal powder core.

This chapter presents the methods employed during the experimental phase (Section 2.1) and results concerning temperature-dependent magnetisation curves measured in quasi-static conditions (Section 2.2) and measurements at high frequencies (Section 2.3). Finally, Section 2.4 deals with a systematic parameter identification method for the EB model and describes how to obtain the material parameters starting from standard measurements.

2.1 Characterisation by ring method

The main elements of the experimental setup are a closed magnetic circuit, enclosing the SMMs, and two windings around the material under test. Ring-shaped cores are recommended by IEC 60404-4 [99] and IEC 60404-6 [100]. This method is particularly appropriate for high permeability materials. In such geometry, there are no air gaps associated, so the magnetic circuit comprises only the material to measure. Two layers of windings are wrapped around the sample, the inner one is the secondary winding N_2. It should be placed as closely as possible around the material surface, so as to limit the effect

of air flux, enclosed between the core and the winding [16]. The objective is to determine the secondary voltage and, consequently, the magnetic induction $b(t)$. The time-varying magnetic field $h(t)$ is produced by means of an excitation winding, the primary winding with N_1 turns.

For accurate measurements, an important issue to consider is that the applied magnetic field decreases as function of the diameter of the ring core. In fact, the related magnetic path length is $l(D) = \pi D$ (cf. Figure 2.1).

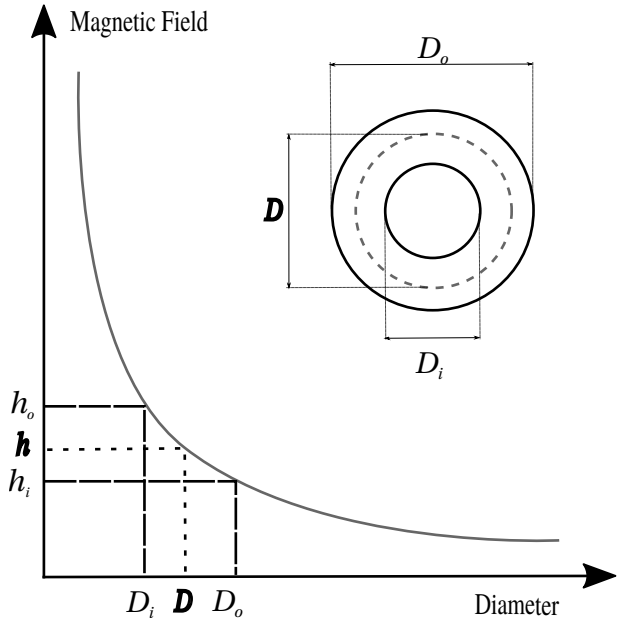

Figure 2.1: Magnetic field dependence on toroidal diameter.

In order to approach a good uniformity of the magnetisation over the sample cross-section, a general rule is established to consider the ratio between outer and inner diameters $D_o/D_i \leq 1.1$. Thus, the effective magnetic path length is $l_e = \pi D_e$, with $D_e = (D_i + D_o)/2$. In order to deal with the quite high values of the ratio D_o/D_i in samples, l_e is usually referred to as $l_e = \pi(D_o - D_i)/\ln(D_o/D_i)$ [101]. The effective area is $A_e = H_t \cdot (D_o - D_i)/2$ (cf. Figure 2.2), where H_t is the core height [16]. The effective

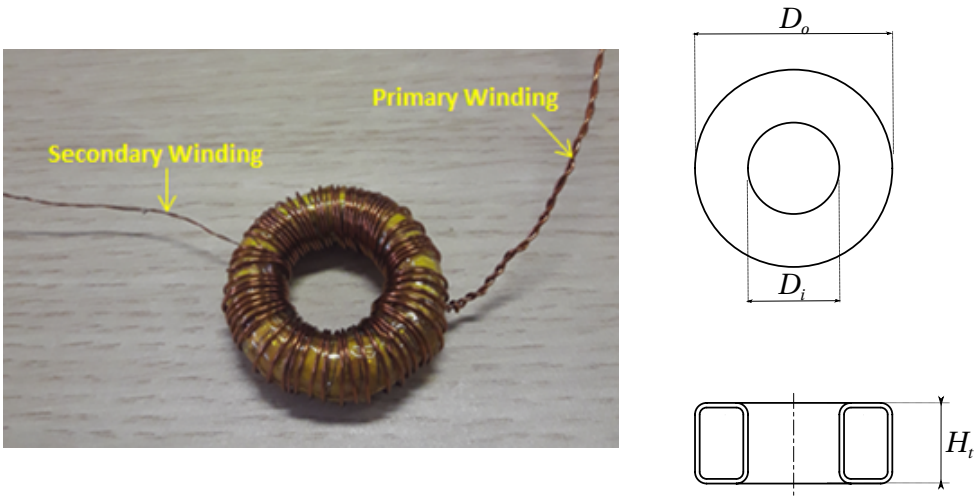

Figure 2.2: Device under test (D.U.T.): a soft ferrite Mn-Zn ring sample, with primary (excitation) $N_1 = 60$ turns and secondary (measurement) $N_2 = 39$ turns.

magnetic field h is determined by means of the Ampère law using the measured excitation

current, namely a time-dependent current $i_1(t)$ in the primary (excitation) winding with N_1 turns. In a ring core, assuming a constant magnetic path length l_e, one has

$$\oint_{l_e} \mathbf{h}(t) \cdot \mathrm{d}\mathbf{l} = N_1 i_1(t) \tag{2.1}$$

Thus, the magnetic field $h(t)$ can be determined as

$$h(t) = \frac{N_1 i_1(t)}{l_e} \tag{2.2}$$

The magnetic induction $b(t)$ is determined basing on the Maxwell-Faraday equation,

$$\oint_{\partial S_{mc}} \mathbf{e}(t) \cdot \mathrm{d}\mathbf{l} = -\frac{\partial}{\partial t} \int_{S_{mc}} \mathbf{b}(t) \cdot \mathrm{d}\mathbf{S} = -\frac{\partial}{\partial t} \Phi_{mc}(t) \tag{2.3}$$

where S_{mc} is the cross-section of the measuring coil, ∂S_{mc} is the closed countour enclosing S_{mc} and $\Phi_{mc}(t)$ is the time-dependent flux passing throug S_{mc}. The induced voltage in the measuring coil, with number of turns N_2, is given by

$$V_2(t) = -N_2 \frac{\partial \Phi_{mc}(t)}{\partial t} \tag{2.4}$$

So, the magnetic flux Φ_{mc} at a time t_1 is determined as

$$\Phi_{mc}(t_1) = -\frac{1}{N_2} \int_0^{t_1} V_2(t) \mathrm{d}t \tag{2.5}$$

Actually, the whole flux consists of two contributions [17]: the flux $\Phi_{mat}(t)$ inside the material, with cross-section A_e and the flux in the air surrounding the sample $\Phi_{air}(t)$,

$$\Phi_{mc}(t) = \Phi_{mat}(t) + \Phi_{air}(t) = \int_{A_e} \mathbf{b}(t) \cdot \mathrm{d}\mathbf{S} + \int_{S_{mc}-A_e} \mu_0 \mathbf{h}(t) \cdot \mathrm{d}\mathbf{S} \tag{2.6}$$

The second term can be neglected in most of the practical cases, especially for materials with high permeability [101]. Then, the magnetic induction of the material $b_{mat}(t_1)$ is determined as follows:

$$b_{mat}(t_1) = \frac{1}{A_e} \int_{A_e} \mathbf{b}(t_1) \cdot \mathrm{d}\mathbf{S} \approx \frac{\Phi_{mc}(t_1)}{A_e} = -\frac{1}{N_2 A_e} \int_0^{t_1} V_2(t) \mathrm{d}t \tag{2.7}$$

It is assumed that the magnetic field h in the excitation coil, in the material and in the surrounding air, is uniform. The resulting magnetic flux density $b_{mat}(t)$ or polarisation $J_{mat}(t)$ is an average value over the whole cross-section of the sample, namely $b_{mat}(t) = \bar{b}(t)$ or $J_{mat}(t) = \bar{J}(t)$.

2.2 Quasi-static measurements

This section describes the experimental systems that enable to perform measured data in quasi-static conditions. The objective is to measure the quasi-static (DC) hysteresis loops of magnetic materials. These represent the rate-independent $b(h)$ behaviour, related only to the sequence of values attained by the applied field and not to its rate of change. The magnetisation process occurs so slowly that the hysteretic behaviour is independent on the rate of change of the magnetic induction. As a result, time-dependent and dynamic effects, such as eddy currents, are supposed to be irrelevant. It has to be remarked that for low amplitude excitation fields, the measured signal is weak. Therefore, the signal/noise ratio is proportionally higher. Tipically, under quasi-static conditions, there are two approaches to determine the magnetization curves:

1. *Point-by-point (or ballistic) procedure*: the magnetising field strength is changed in a step-like fashion and the resulting change in the magnetic induction is measured by integration of the voltage induced on a secondary winding, integrated over a time interval sufficient to ensure a complete decay of eddy currents.

2. *Hysteresigraph method*: the magnetising field is controlled in an appropriate continuous fashion, as slowly as properly to avoid eddy currents effects. The magnetic field is continuously and monotonically increased from zero to its maximum value, in order to define the initial magnetisation curve. Optionally, h is constantly cycled from the maximum positive value to the maximum negative value and back, with the aim of determining the DC hysteresis cycles. The related change of the magnetic flux is continuously detected [16].

It should be pointed out that values obtained from the curves produced by any hysteresigraph with its characteristic slow flux changes may not be identical to those found with the point-by-point method, with its abrupt changes or reversals of flux. Ideally, these two experimental approaches should bring about the same results, in fact most materials show little or no difference between the two test methods. However, some materials can show wide discrepancies because of the complicated definition of DC magnetization curve and hysteresis [101], due to domain wall motion, eddy current effects, etc. [102]. In this work, measurements have been performed by means of the hysteresigraph method.

2.2.1 Temperature-dependent measurements

In the measurement setups, the hysteresigraph (or continuous recording) method is applied to characterise a toroidal core (cf. Figure 2.2), made of soft ferrite Mn-Zn 3C90 [103]. The 3C90 ferrite consists of an isotropic material, the parameters of which are listed in Table 7.1.

This section presents the structure of the measurement systems used to characterise the toroidal core shown in Figure 2.2. The hysteresis loops have been measured in quasi-static conditions at various temperatures (cf. Table 7.2) in case of:

- **simple excitation waveforms** (unidirectional alternating measurements) by means of the automatic measuring system depicted in Figure 2.3;

- **complex excitation waveforms** (unidirectional with addition of harmonics) using the experimental setup presented in Figure 2.4.

Each quantity is provided in Table 7.3.

2.2.1.1 Simple excitation waveforms

Measurements of magnetisation curves have been conducted using a hysteresisgraph manufactured by Laboratorio Elettrofisico Walker LDJ Scientific (Nerviano, Italy) [104]. It allows for measurements of rings and strips up to 1 MHz [104], according to the International Standards IEC 60404-4 [99], IEC 60404-6 [100].

The experimental setup is detailed in Figure 2.3. The sample has to be prepared with a primary set of turns N_1 for excitation and a secondary set of turns N_2 to detect the magnetic flux. The D.U.T is then placed in the thermal chamber. An excitation signal (in V) is sent to the Arbitrary Function Generator (AFG) by means of a PC. Therefore, a voltage at the desired frequency is generated and amplified by a power amplifier, in order to reach a suitable level of excitation current. The excitation winding is connected

Table 2.1: Core parameters for 3C90 ferrite material.

Symbol	**Value**	**Description**	**Conditions**
μ_i	$2300 \pm 20\%$	initial permeability	25 °C; $\leqslant$ 10 kHz; 0.25 mT
μ_a	$5500 \pm 25\%$	amplitude permeability	100 °C; 25 kHz; 200 mT
b	470 mT	magnetic induction	25 °C; 10 kHz; 1200 A/m
	380 mT		100 °C; 10 kHz; 1200 A/m
ρ	4800 kg/m^3	density	
T_c	$\geqslant$ 493 K	Curie temperature	
l_e	73.2 mm	effective length	
A_e	36.9 mm^2	effective area	
V_e	2700 mm^3	effective volume	
D_o	29.7 ± 0.7 mm	external diameter	
D_i	18.2 ± 0.6 mm	internal diameter	
H_r	8.1 ± 0.5 mm	height	

Table 2.2: Range of measured temperatures (K).

Simple excitation	223	248	273	293	323	348	373	398	423	448
Complex excitation				293	323		373			

Table 2.3: Symbols and description of each quantity.

Symbol	**Simple signals**	**Complex signals**	**Description**
N_1	60	60	excitation winding
N_2	39	39	secondary winding
R_{shunt}	1.795 Ω	2 Ω	shunt resistance
Rheostat	60 Ω	176 Ω	rheostat

to the rheostat resistance and the shunt resistance to measure the current flowing in it. A general requirement is that b must change as a sinusoidal function with respect to time, $b(t) = b_0 \cdot \sin(2\pi f t)$. Due to the non-linearity of magnetic materials, generally this condition is achieved only by a feedback control by the software, that drives the AFG to supply the suitable voltage $v(t)$ to reach the required condition. The $h(t)$ field is determined measuring the current $i(t)$ in the primary winding (2.2). The current is obtained by measuring the voltage across a low-inductance resistance R_{shunt}. A digital fluxmeter utilises the sense coil (N_2) to measure average flux density and total flux.

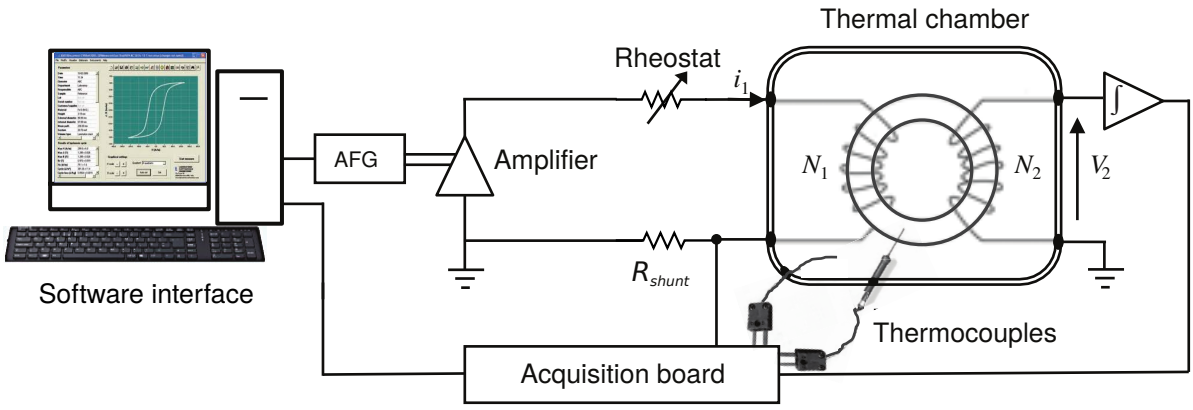

Figure 2.3: Block diagram, adapted from [11], of the bench for characterising SMM in the Ampère laboratory.

The question on how low the frequency should be in order to obtain quasi-static hysteresis loops is linked to the control of the magnetisation rate. In the hysteresigraph method, the latter is controlled to be low and constant, allowing to minimise eddy current effects.

2.2.1.2 Complex excitation waveforms

In light of the impossibility to add harmonics in the hysteresigraph made by Laboratorio Elettrofisico [104], we have built the experimental setup presented in Figures 2.4. We made that in order to generate waveforms as close as possible to realistic excitations. The D.U.T. is placed in a laboratory oven (SNOL 30/1100) used to heat up the sample at various temperatures $T = 293\ \text{K}, 323\ \text{K}, 373\ \text{K}$.

The AFG is programmed by a PC with the help of the software Waveform Manager Plus, suitable for the creation, editing and management of arbitrary waveforms. The amplified signal is then transmitted to the primary winding connected to a series resistance and a shunt resistance. This assembly allows to create a pseudo-current source to perform current-driven measurements, in which R_{shunt} is used to measure the current flowing in it. The magnetic field h is then deduced by this current from (2.2). At the secondary winding, the output voltage is measured to provide access to the magnetic flux density b by means of (7.6). Finally, the image signals of h and b are processed in order to plot the hysteresis loops $b(h)$.

2.2.2 Measurement results

In detail, for each case, the input voltages set in the AFG are:

1. *simple signals*: sinusoidal excitation waveform ($f = 50$ Hz) for different levels of v_p:

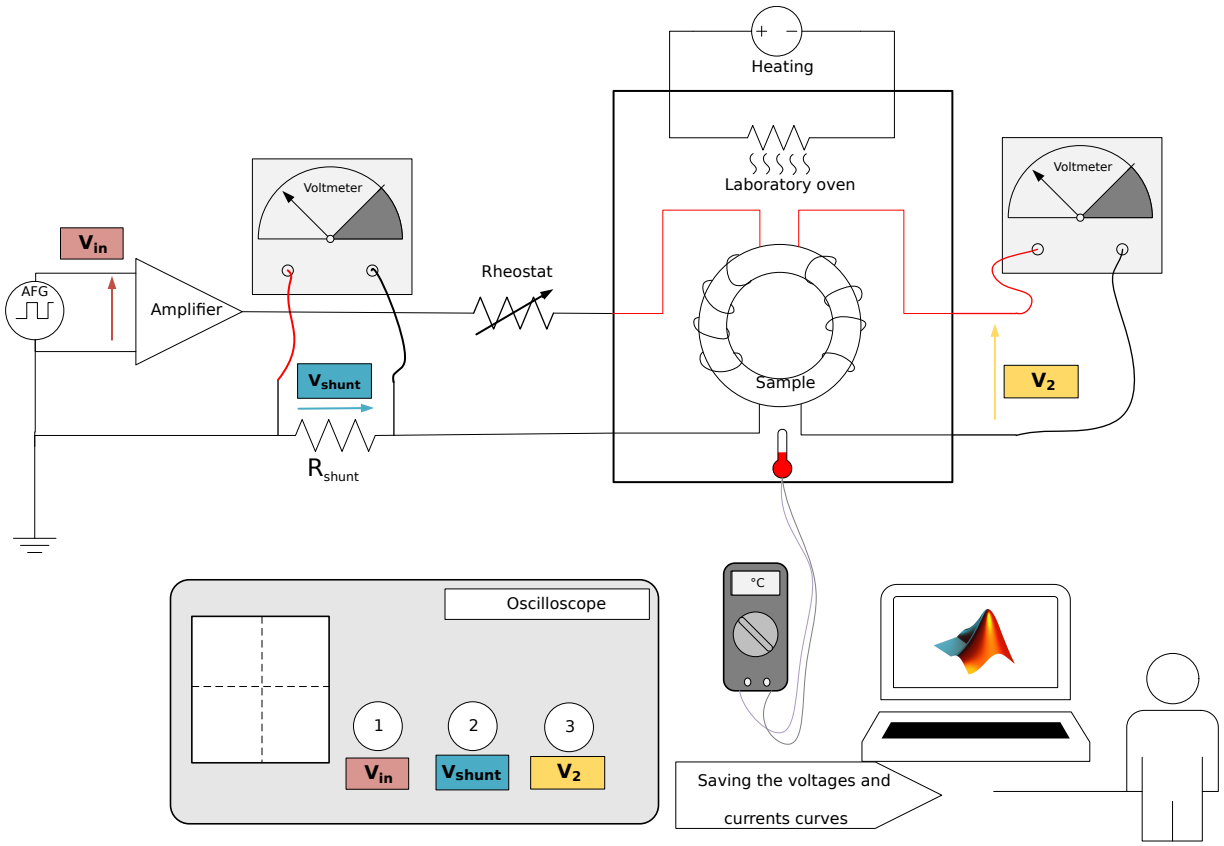

Figure 2.4: System for measuring complex magnetic hysteresis loops $b(h)$.

$$v(t) = v_p \cdot (\sin(2\pi f t)) \tag{2.8}$$

2. *complex signals*:

   - sinusoidal excitation waveform ($f = 50$ Hz) with superimposed higher harmonic ($3f = 150$ Hz), $T = 293$ K (cf. Figure 2.5):

$$v(t) = v_p \cdot (\sin(2\pi f t) + \sin(6\pi f t)) \tag{2.9}$$

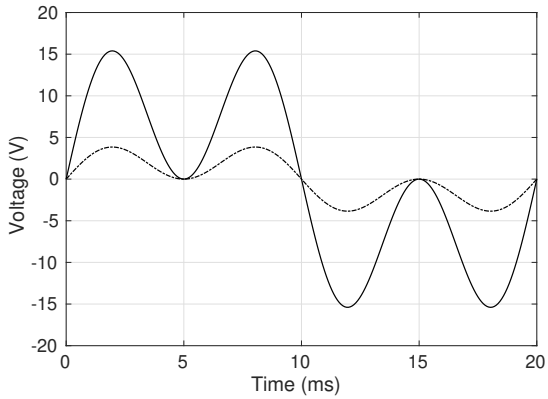

Figure 2.5: Complex signal variation over time (dotted line: $v_p = 1$ V; full line: $v_p = 5$ V).

   - pulse-width modulation (PWM) excitation (fundamental $f = 1$ kHz) at $T = 323$ K (cf. Figure 2.6a) and $T = 373$ K (cf. Figure 2.6b).

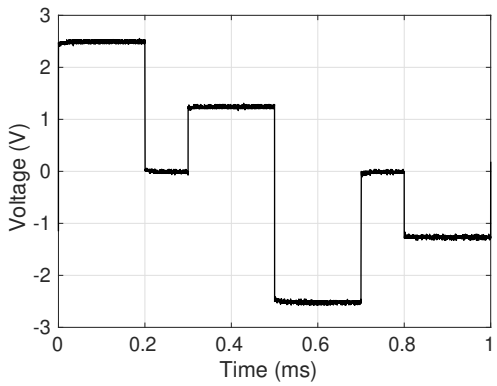

(a) PWM excitation ($T = 323$ K).

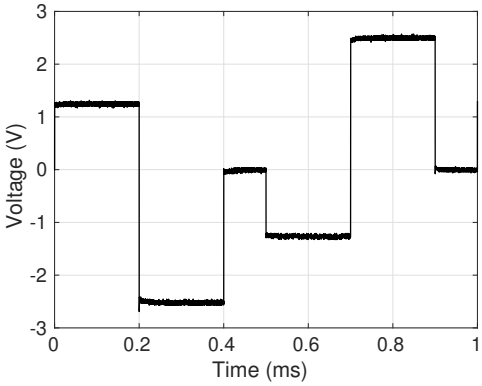

(b) PWM excitation ($T = 373$ K).

Figure 2.6: Complex excitation waveforms.

In order to illustrate the obtained measurements, hysteresis loops are plotted in Figure 2.7 for several excitation waveforms and several temperatures (Appendix A.1). As concerns hysteresis loops derived from simple excitation waveforms, several cycles at different field strengths have been measured at same temperature (cf. Figures 2.7a-2.7c-2.7e). On the other hand, the addition of harmonics gives rise to closed small loops at the tips of each loop at a given temperature, the so-called minor loops within the major cycle (cf. Figures 2.7b-2.7d-2.7f).

Globally, we may observe that saturation induction and the coercive field decrease as temperature raises. The obtained results will be discussed in more detail in Chapter 3.

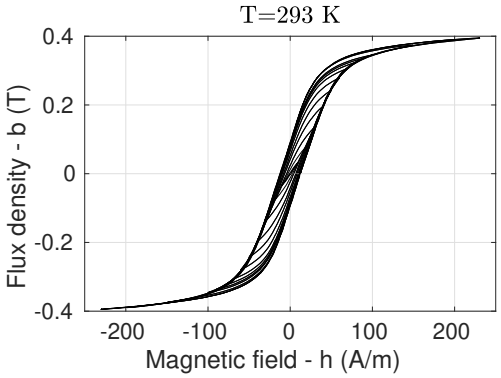

(a) Simple waveforms, $T = 293$ K.

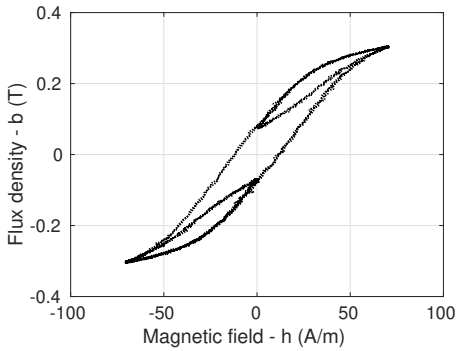

(b) Complex waveform, $T = 293$ K.

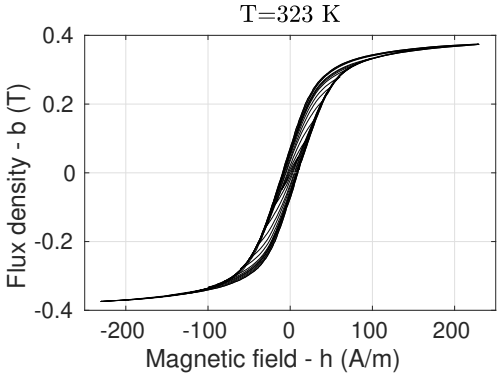

(c) Simple waveforms, $T = 323$ K.

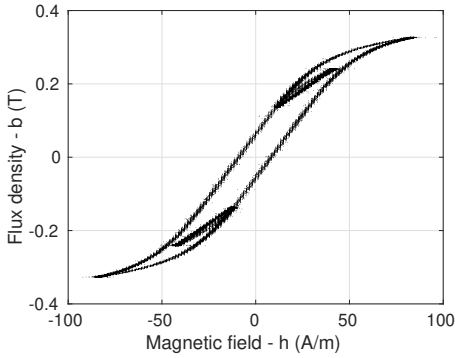

(d) Complex waveform, $T = 323$ K.

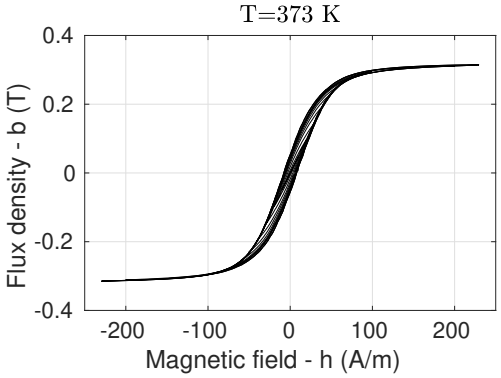

(e) Simple waveforms, $T = 373$ K.

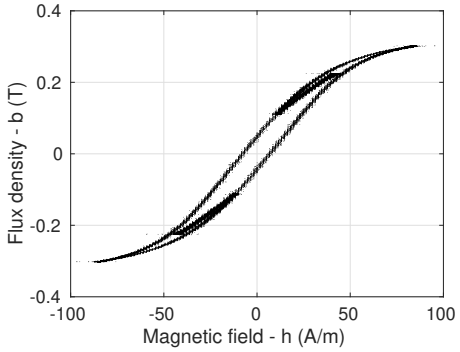

(f) Complex waveform, $T = 373$ K.

Figure 2.7: Hysteresis cycles $b(h)$ measured in different conditions.

2.3 High Frequency (HF) measurements

Characterisation of SMMs in the kHz range and beyond is essential, especially in power electronics, where the miniaturisation of power converters requires magnetic components operating at higher and higher frequencies, between 10 kHz and 1 MHz. Higher switching frequencies lead to smaller passive components and this reduces the material cost and allows to comply with space requirements more easily.

If the frequency of the alternating field increasing the rate of magnetisation increases, dynamic effects increase, superimposed on the strictly static behaviour of the material. In HF measurements, the temperature of the sample can drastically increase. For instance, in a Mn-Zn ferrite ring sample tested at 1 MHz and peak polarisation $J_p = 0.1$ T, sample heating can proceed at a rate higher than 2 K/s [101]. Thus, it is necessary to let the temperature stabilise and perform measurements in a short period so that temperature increment can be neglected. Furthermore, stray inductances and capacitances begin to have an important role with the increase of the magnetising frequency above the kHz range.

In this work, the 3C90 ferrite material has been characterised by means of the AMH-1M Permeameter suited for HF (cf. Figure 2.3), at different exciting frequencies, ranging from 10 kHz up to 1 MHz (cf. Table 2.4) magnetising the sample with a sinusoidal h field. At such frequencies, the impact of eddy current losses cannot be neglected any more. Usually, eddy current losses are split up into losses due to skin and proximity effects. The skin effect describes the eddy currents due to the magnetic field created by the current in the conductor itself, whereas the proximity effect characterises eddy currents that originate from an external magnetic field. The impact of losses due to these effects need to be mitigated for an efficient design of inductors or transformers. This is usually achieved by HF Litz wires [105]- [106]- [107]- [108], which allow for low losses and great flexibility in the design of the magnetic component. HF Litz wires are composed of multiple insulated strands, as shown in Figure 2.8. This has the effect of distributing the current equally among the wire strands, reducing the increase in wire resistance that takes place at higher frequencies.

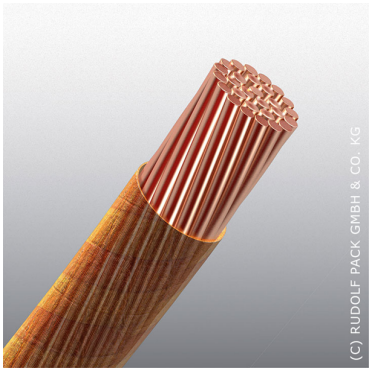

Figure 2.8: Litz wires.

Specifically, Litz wires have been used at the primary winding in order to reduce skin effect and proximity effect losses.

Table 2.4: Range of measured frequencies.

10 kHz	20 kHz	50 kHz	70 kHz	100 kHz	200 kHz	500 kHz	1 MHz

Measurement results

Measurements results are shown in Figure 2.9 and Appendix A.2, with maximal flux density ranging from 0.02 to 0.4 T.

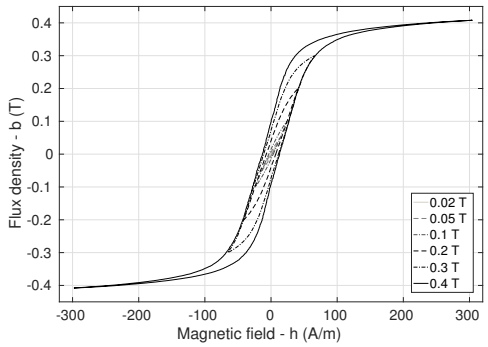

(a) $f = 10$ kHz.

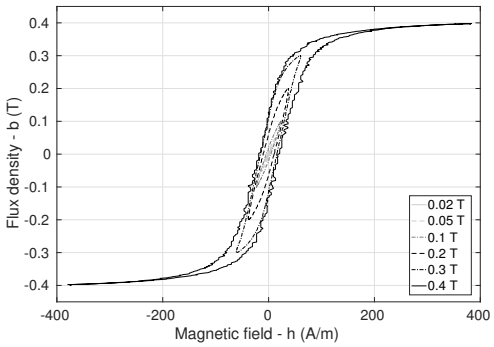

(b) $f = 100$ kHz.

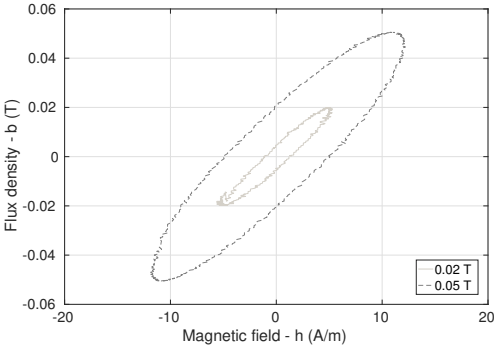

(c) $f = 500$ kHz.

Figure 2.9: Measured $b(h)$ loops at different frequencies.

In Figure 2.10, two hysteresis loops measured at the same magnetic induction $b = 0.02$ T, but at different frequencies (10 kHz and 1 MHz) are shown. The $b(h)$ loops broaden, as well as the coercive field h_c, which increases for higher frequencies. It can be noticed that measurements at 100 kHz (cf. Figure 5.11b) is more affected by noise, compared to data measured at 10 kHz (cf. Figure 5.11a). The noise mainly relates to the measuring of h. This is due to the fact that the parasitic induced voltages are not negligible at high frequencies. This effect is mainly visible on the major ascending and descending branches.

2.4 Identification of the Energy-Based model

The aim of this section is to describe how the material parameters ω and κ of the EB hysteresis model can be identified starting from standard measurements (Section 2.2). This identification protocol is based on a auxiliary function, so hereafter, one can refer to it as AUX method [109].

In the EB hysteresis model, the memory of the material is represented by the values of $\mathbf{h}_r^k$ and the demagnetized state, the irreversible part of the model corresponds to $\mathbf{h}_{irr}^k$. As the loading is always unidirectional in standard measurements, in this section we shall take into account the modulus of the field $h = |\mathbf{h}|$.

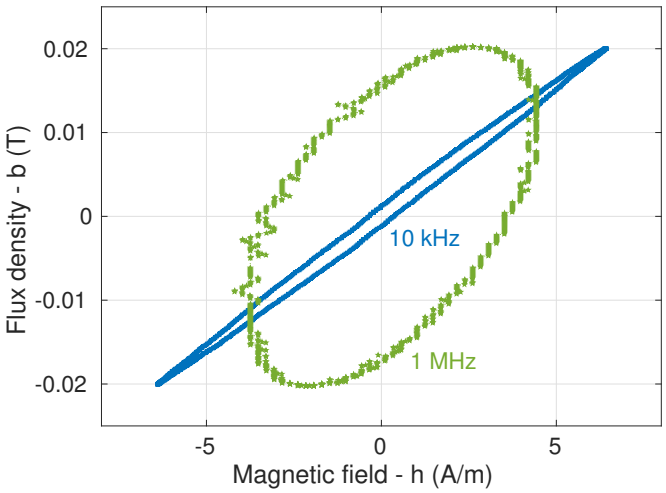

Figure 2.10: Measurements at $f = 10$ kHz and 1 MHz.

In order to avoid ambiguities, in this paragraph the reversible magnetic field (which was formerly indicated by $\mathbf{h}_r$) will be noted by the symbol H_r. As excitation is uniaxial, vector notation is dropped; that is, we will write h_r^k instead of $\mathbf{h}_r^k$.

The identification is taken on in two steps:

1. First, it is assumed that the model is composed of an infinite number of cells. Therefore, the pinning field of cells h_r^k and cells weights ω_k become continuous functions of a quantity κ homogeneous to a magnetic field:

   $$h_r^k \overset{N\to\infty}{\longrightarrow} h_r(\kappa) \qquad ; \qquad \omega_k \overset{N\to\infty}{\longrightarrow} \omega(\kappa)$$

   and the reversible magnetic field writes:

   $$H_r = \lim_{N\to\infty} \sum_{k=1}^{N} \omega_k h_r^k = \int_0^\infty h_r(\kappa)\omega(\kappa)d\kappa$$

   The continous pinning field probability density $\omega(\kappa)$ is identified.

2. In order to be used within realistic Finite Element simulations, this continous model is discretized into a model composed of a "small" number of cells N (in practice, $N < 10$).

2.4.1 Identification of the continuous pinning field probability density

According to [109], starting from the demagnetized state, $h = 0$, an unidirectional loading until $h = h_A$ is first considered. The subregions κ involved in this loading are those such that $\kappa < h_A$, so, at the end, $h_r(\kappa) = h_A - \kappa$, the other $h_r(\kappa)$ remaining zero, that is:

$$h_r(\kappa)|_{h:0\to h_A} = \begin{cases} h_A - \kappa & \text{if } \kappa \leq h_A \\ 0 & \text{otherwise} \end{cases} \tag{2.10}$$

The reversible field H_r is

$$H_r(0 \to h_A) = \int_0^\infty \max(h_A - \kappa, 0)\omega(\kappa)\ \mathrm{d}\kappa = F(h_A) \tag{2.11}$$

where the auxiliary function $F(h)$ is defined as:

$$F(h) = \int_0^h \omega(\kappa)(h-\kappa)\ \mathrm{d}\kappa \tag{2.12}$$

and the first and second derivatives given by[1]:

$$\partial_h F(h) = \int_0^h \omega(\kappa)\ \mathrm{d}\kappa \tag{2.13}$$

$$\partial_h^2 F(h) = \omega(\kappa)|_{\kappa=h} \tag{2.14}$$

Starting from the h_A state, the material is now unloaded until the magnetic field reaches $-h_B$, with $0 \leq h_B \leq h_A$. The κ-cells involved in the unloading are those such that $-h_B + \kappa < h_A - \kappa$, i.e. $\kappa < (h_A + h_B)/2$, that is:

$$h_r(\kappa)|_{h:0\to h_A\to h_B} = \begin{cases} -h_B + \kappa & \text{if } \kappa \leq \frac{h_A+h_B}{2} \\ h_A - \kappa & \text{if } \frac{h_A+h_B}{2} \leq \kappa \leq h_A \\ 0 & \text{otherwise} \end{cases} \tag{2.15}$$

At the end of the process, the reversible field H_r is

$$\begin{aligned} H_r(0 \to h_A \to -h_B) &= \int_0^\infty \min(-h_B + \kappa, \max(h_A - \kappa, 0))\ \mathrm{d}\kappa \\ &= \int_0^{\frac{h_A+h_B}{2}} \omega(\kappa)(-h_B+\kappa)\ \mathrm{d}\kappa + \int_{\frac{h_A+h_B}{2}}^{h_A} \omega(\kappa)(h_A-\kappa)\ \mathrm{d}\kappa \\ &= \int_0^{h_A} \omega(\kappa)(h_A-\kappa)\ \mathrm{d}\kappa - 2\int_0^{\frac{h_A+h_B}{2}} \omega(\kappa)\left(\frac{h_A+h_B}{2} - \kappa\right)\ \mathrm{d}\kappa \\ &= F(h_A) - 2F\left(\frac{h_A+h_B}{2}\right) \end{aligned} \tag{2.16}$$

The auxiliary function F plays an important role in the parameters identification. By knowing the anhysteretic curve, the first magnetization (virgin) curve of the material is the composition of the anhysteretic curve with F:

$$J_{virgin}(h) = J_{an}(H_r(0 \to h)) = J_{an}(F(h)) \tag{2.17}$$

Figure 2.11 depicts the virgin (initial) and anhysteretic magnetisation curves. On the basis of hysteresis loop measurements, the initial magnetisation curve can be determined (see 1.2.2). To identify the anhysteretic curve, there exist several strategies, as it is not part of standard magnetic measurement procedure.

The anhysteretic saturation law can be deduced from a fitting on measurements or it can be computed by considering the median line of the major loop, interpolated from experimental measurements [74].

[1] Remind that in the case of integrals depending upon a parameter (in this case h), when a parameter is present in the extrema the following integration rule holds:

$$\frac{d}{dh}\int_0^{v(h)} f(h,\kappa)d\kappa = v'(h)f(h,v(h)) + \int_0^{v(h)} \frac{\partial f(h,\kappa)}{\partial h} d\kappa$$

In this case we have $v(h) = h$, hence the first term vanishes because:

$$v'(h)f(h,v(h)) = 1 \cdot \omega(h)(h-h) = 0$$

It can be matched with analytical expressions, such as the hyperbolic tangent function (2.18) [10]- [77]- [110], Langevin (2.19) [72] or Double Langevin functions, such as (2.20) [68]:

$$J_{an}(h) = J_a \tanh\left(\frac{h}{h_a}\right) \tag{2.18}$$

$$J_{an}(h) = J_a L\left(\frac{h}{h_a}\right) \tag{2.19}$$

$$J_{an}(h) = J_a L\left(\frac{h}{h_a}\right) + J_b L\left(\frac{h}{h_b}\right) \tag{2.20}$$

with $L(x) = \coth x - \frac{1}{x}$ is the Langevin function. The term indexed with a represents the magnetic polarisation, at high field intensity, associated with the rotation of the magnetic moments relative to their preferred easy-magnetisation axis. Whereas, the term indexed with b represents the magnetic polarisation due to the motion of Bloch walls.

Based on the virgin curve measurement and the knowledge of the auxiliary function F, it is possible to deduce the anhysteretic curve by application of (2.17). Once the function F is known for a material, parameters J_a, h_a, J_b, h_b can be determined by matching the measured virgin curve $J_{virgin}(h)$ with $J_{an}(F(h))$, in order to verify (2.17) [47].

Therefore, it is useful to consider an identification protocol independent of J_{an}, relying on the coercive fields h_c which are already known from the measurements of symmetrical hysteresis loops of increasing amplitude h_p.

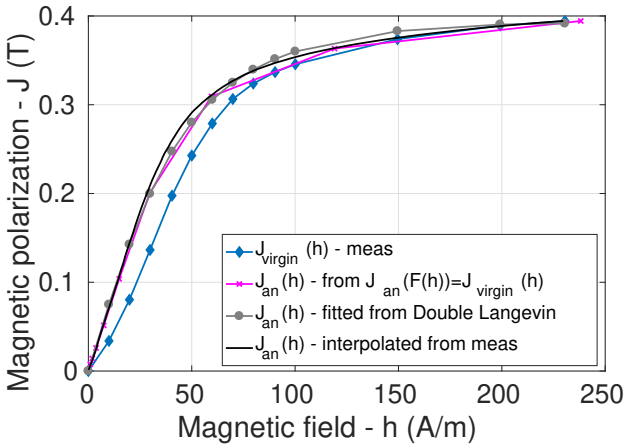

Figure 2.11: Virgin and anhysteretic magnetisation curves for the 3C90 ferrite material at $T = 293$ K.

The AUX method [109] focuses on the experimental curve $h_c(h_p)$, in which h_c is detected on a cycle, for which the applied magnetic field amplitude is h_p (as an example, see Figure 2.12). The coercive field is characterised by

$$J_{an}(H_r(0 \to h \to -h_c)) = 0 \tag{2.21}$$

which implies

$$F(h) - 2F\left(\frac{h + h_c(h)}{2}\right) = 0 \tag{2.22}$$

The $h_c(h)$ curve has the following properties:

1. $h_c(0) = 0$, which implies $F(0) = 0$.

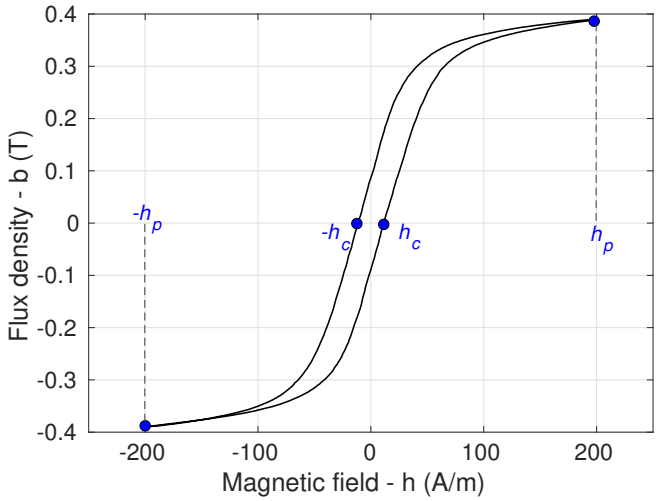

Figure 2.12: Identification of input data for the construction of the $h_c(h_p)$ curves.

2. For $h \geq h_s$ the material is completely saturated, hence one can rewrite (2.11) as:

$$F(h) = \int_0^h \omega(\kappa)(h-\kappa)\,d\kappa = \int_0^\infty \omega(\kappa)(h-\kappa)\,d\kappa$$

We can develop this expression as:

$$F(h) = \int_0^\infty \omega(\kappa)(h-\kappa)\,d\kappa = h\int_0^\infty \omega(\kappa)\,d\kappa - \int_0^\infty \omega(\kappa)\kappa\,d\kappa = h - h_{c_{max}}$$

where:

$$h_{c_{max}} = \int_0^\infty \omega(\kappa)\kappa\,d\kappa$$

3. $h_c(h) < h$, thereby the following inequality holds:

$$\frac{h_c(h)+h}{2} < h \tag{2.23}$$

Hereafter, it is explained the identification procedure. The $h_c(h_p)$ characteristic is interpolated in the range $[h_{p_{min}}, h_{p_{max}}]$ and it is extrapolated as follow for field values outside the measurement range (7.9):

$$h_c(h_p) = \begin{cases} h_c = h_{c_{max}} & \text{if } h_p > h_{p_{max}} \\ h_c = f(h_p) & \text{if } h_{p_{min}} < h_p < h_{p_{max}} \\ h_c = h_{c_{min}} \cdot \left(\frac{h_p}{h_{p_{min}}}\right)^2 & \text{if } h_p < h_{p_{min}} \end{cases} \tag{2.24}$$

where $f(h_p)$ is an interpolation function[2]. The quadratic extrapolation at low fields derives from Rayleigh law [18].

The next step is the definition of an auxiliary continuous function $F(h)$, based on the $h_c(h_p)$ curve. The curve $h_c(h_p)$ contains enough information to completely identify $F(h)$ [109]. For any magnetic field h which saturates the material ($h > h_{p_{max}}$) it is known that:

$$F(h) = h - h_{c_{max}} \tag{2.25}$$

[2]In principle, any interpolation method can be used. We used piecewise linear interpolation because this method ensures that no unphysical negative values are obtained.

For magnetic fields of lower magnitude, the function F satisfies:

$$F\left(\frac{h+h_c(h)}{2}\right)=\frac{F(h)}{2} \tag{2.26}$$

The procedure consists in selecting an arbitrary initial value $h^0 > h_{p_{max}}$. The subsequent terms of the series are recursively given by:

$$h^n=\frac{h^{n-1}+h_c(h^{n-1})}{2} \tag{2.27}$$

The values of function $F(h^n)$ can then be computed as:

$$F(h^n)=\begin{cases} h^n-h_{c_{max}} & \text{if } h^n > h_{p_{max}} \\ \frac{F(h^{n-1})}{2} & \text{otherwise} \end{cases} \tag{2.28}$$

By using (2.25)-(7.11), the curve $F(h)$ can be sampled in an arbitrary number of points. The first derivative and second derivatives of $F(h)$ can be evaluated at the series points x^k by finite differences with sufficient accuracy.

$$\partial_h F(x^j)=F(x^j)\frac{\Delta_2-\Delta_1}{\Delta_1\Delta_2}+F(x^{j+1})\frac{\Delta_1}{\Delta_2\Delta_3}-F(x^{j-1})\frac{\Delta_2}{\Delta_1\Delta_3} \tag{2.29}$$

$$\partial_h^2 F(x^j)=2\left(\frac{F(x^{j-1})}{\Delta_1\Delta_3}-\frac{F(x^j)}{\Delta_1\Delta_2}+\frac{F(x^{j+1})}{\Delta_2\Delta_3}\right) \tag{2.30}$$

where $\Delta_1=x^j-x^{j-1}$, $\Delta_2=x^{j+1}-x^j$ and $\Delta_3=x^{j+1}-x^{j-1}$.

The first derivative $\partial_h F(h)$ represents the pinning field cumulative distribution function. The pinning field (continuous) probability density $\omega(\kappa)$ is then deduced by derivating $F(h)$ twice:

$$\omega(\kappa)=\frac{\partial^2 F(h)}{\partial h^2}$$

By using this procedure, the continuous distribution $\omega(\kappa)$ can be numerically computed

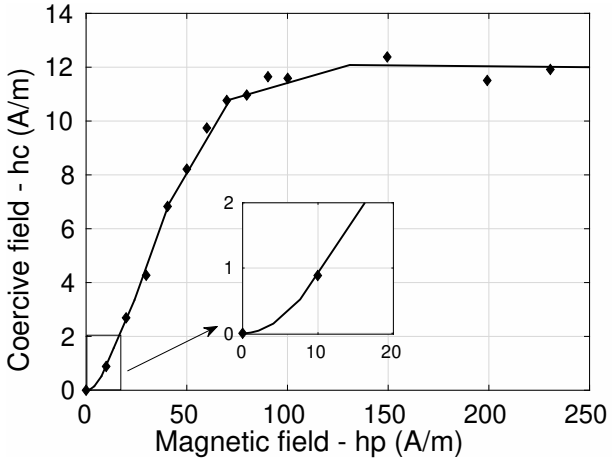

Figure 2.13: Curve $h_c(h_p)$ of symmetrical hysteresis loops measured for 3C90 ferrite material at $T = 293$ K. Measurement points are represented as diamonds.

in a very high number of points.

The identification procedure described above has been applied to the 3C90 ferrite material, for which all the steps are depicted in Figures 2.13, 2.14, 2.15 and 2.16 for $T = 293$ K.

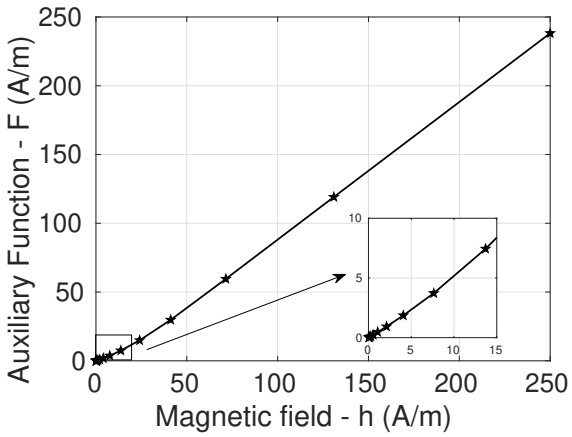

Figure 2.14: Identified $F(h)$ function for 3C90 ferrite material. The behaviour at low field is detailed in the zoom.

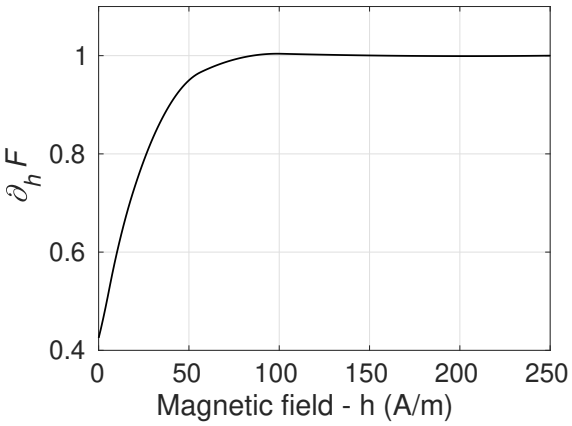

Figure 2.15: Identified cumulative weight distribution function $\partial_h F(h)$ as a function of pinning field.

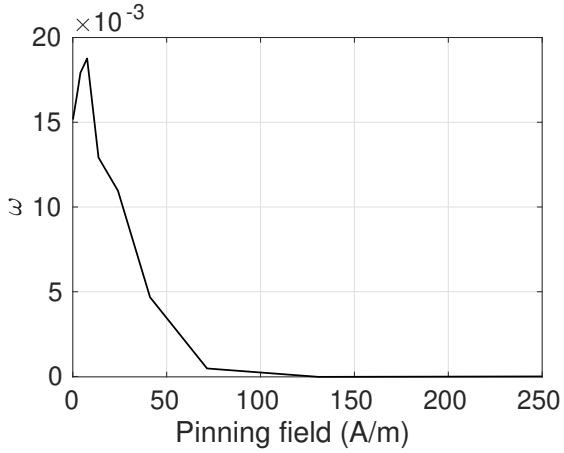

Figure 2.16: Identified pinning field distribution $\omega(\kappa)$.

2.4.2 Discretization of the model

In practice, a discrete approximation of the distribution $\omega(\kappa)$ is needed for Finite Element implementations (2.31), (2.32) [70]. For this reason, the discrete sets of parameters $(\omega_k, \kappa^k)_{k=1,...,N}$ are derived from the continuous distributions $\omega(\kappa)$ previously obtained, where the number N of cells is much lower (typically $N \leq 10$) compared to the number of points of $\omega(\kappa)$. Each region $k = 1, ..., N$ of the decomposition corresponds to a specific cell of the EB model. Each of them is characterized by its own weight ω_k (dimensionless) and own pinning strength κ^k (in A/m).

$$\omega_k = \int_{h^{k-1}}^{h^k} \omega(\kappa)\ \mathrm{d}\kappa = \partial_h F(h^k) - \partial_h F(h^{k-1}) \tag{2.31}$$

$$\kappa^k = \frac{\int_{h^{k-1}}^{h^k} \omega(\kappa)\kappa\ \mathrm{d}\kappa}{\int_{h^{k-1}}^{h^k} \omega(\kappa)\ \mathrm{d}\kappa} = \frac{[h\partial_h F(h) - F(h)]_{h^{k-1}}^{h^k}}{\omega_k} \tag{2.32}$$

A discretisation method, treated in [47], is adopted in order to find the best subdivision of the pinning field distribution. Specifically, the objective is to search for the best piecewise linear representation of the cumulative distribution function $\partial_h F(h)$ with N segments, which is equivalent to find the best partitioning of the area underneath the continuous distribution $\omega(\kappa)$ with N rectangles. In this respect, an increasing piecewise linear function composed of (x^k, y^k) points with $k = 0, 1, ..., N$ is considered, with $x^0 = h^0$ and $x^N = h^N$ fixed a priori. An optimization procedure enables to find the best location of the points (x^k, y^k) that approximates the curve $\partial_h F(h)$ by means of the least square fitting method. Then, the parameters ω_k and κ^k [47] related to each cell are given by (2.33) and (2.34).

$$\omega_k = y^k - y^{k-1} \tag{2.33}$$

$$\kappa^k = \frac{(x^k y^k - F(x^k)) - (x^{k-1}\ y^{k-1} - F(x^{k-1}))}{\omega_k} \tag{2.34}$$

For a proper discretisation, it is useful to introduce a specific cell for the reversible effect, which respects the constraints $\omega_1 = \partial_h F(0)$ and $\kappa^1 = 0$. This corresponds to the introducing of a Dirac delta function in the pinning field distributions. As an example, Figure 2.17 shows the discretisation method with 3 cells and one additional cell to represent the reversible response, resulting in 4 segments for the cumulative distribution function (cf. Figure 2.17a). This corresponds to 4 rectangles for the pinning field continuous distribution (cf. Figure 2.17b).

On the basis of the described identification method for the parameters of the EB hysteresis model, Chapter 3 will analyse the model by comparing the simulated response with measurement data on 3C90 ferrite material, both for standard (alternating sinusoidal) measurements and for non-standard measurements with addition of higher harmonics. In the latter case, the predictions of the material response are compared with measurements that have not been used for the parameter identification.

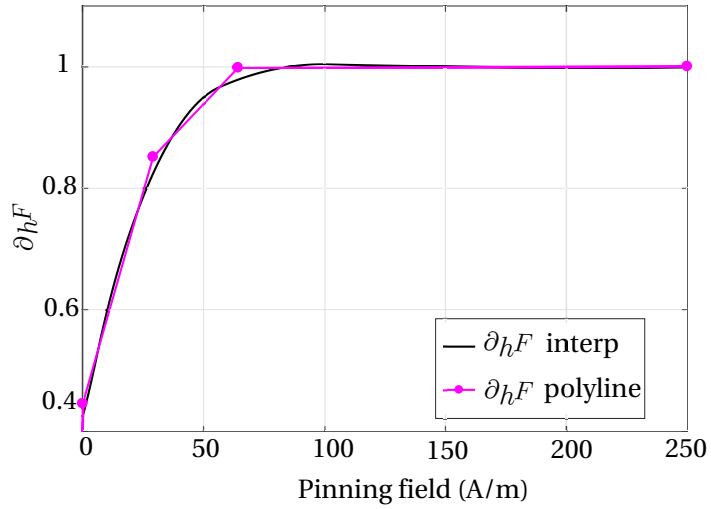

(a) Discrete representation with 4 cells (3+1 purely reversible) for the cumulative distribution function of 3C90 material.

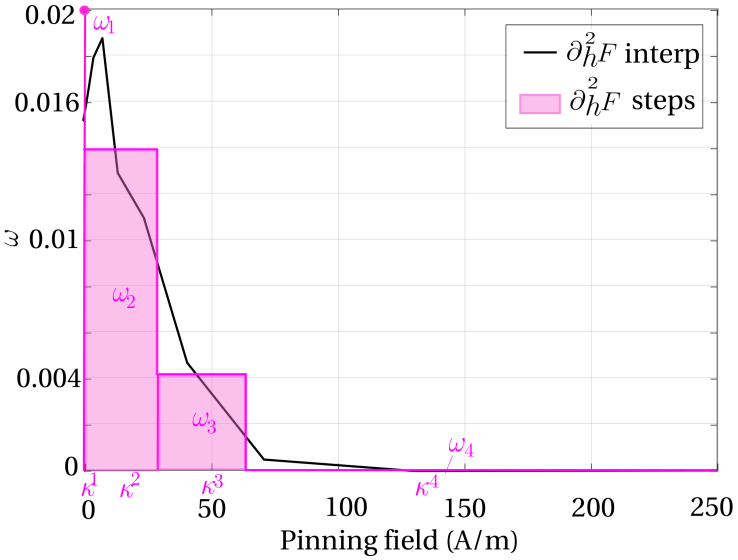

(b) Discrete representation with 4 cells (3+1 purely reversible) for the corresponding cumulative weight distribution function field distribution.

Figure 2.17: Discretisation procedure.

Chapter 3

Static modelling

This chapter deals with the validation of the EB hysteresis model for quasi-static unidirectional loadings. For this purpose, the applicability of the model to arbitrary unidirectional loads is analyzed.

The effect of temperature on magnetic properties of the 3C90 Mn-Zn ferrite material is described in Section 3.1. The material parameters are identified using the systematic parameter identification method introduced in Chapter 2 (Section 2.4) and results of this identification procedure are presented in Section 3.2.

Next, Section 3.3 compares model predictions with quasi-static measurements over a wide temperature range.

In this context, Section 3.4 deals with an accuracy analysis, namely the discretization of the pinning field distribution. The number of cells N is increased and the match between the simulated hysteresis loops and the measured data is examined.

Section 3.5 compares the predictions of the model with experimental data that have not been used for the parameter identification. This comparison enables to evaluate the predictive power of the EB hysteresis model in case of arbitrary magnetisation curves at different temperatures.

Finally, in Section 3.6 recent developments on the dependence of the EB model on temperature are presented. In practical applications, designers need to predict the behaviour of the material response at any temperature. For this reason, a parameter variation law in function of temperature is proposed for soft ferrites.

3.1 Effect of temperature on magnetic properties

The magnetisation processes in ferromagnetic materials are dependent on temperature. The influence of the temperature on the magnetic b-h characteristics of the 3C90 ferrite material is clearly noticeable, as it can be seen in the presented charts in Section 2.2.2 and in Figure 3.1. *Prima facie*, the temperature increasing has for effect to decrease the area of the hysteresis loops of the Mn-Zn ferrite.

Some parameters of the hysteresis loop vary with temperature. Particularly, it is observed that the saturation flux density b_{sat} decreases with increasing temperature (cf. Figure 3.2a). For the lowest temperatures, under 273 K, maximum induction at saturation reaches the highest values. As the temperature rises, maximum flux density values decreases. For the highest measured temperature (448 K), b_{sat} assumes a minimum value. A similar tendency is observed for coercivity (cf. Figure 3.2b) which decays with temperature, as expected [111].

This notable temperature dependence is caused by processes occurring in the atomic structure of such materials [112]. When the material is located in the magnetising field,

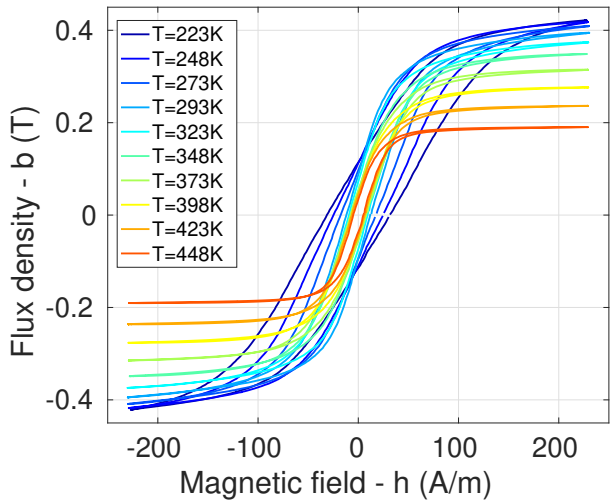

Figure 3.1: Measurements at maximal amplitude $h_p = 230$ A/m in the temperature range.

magnetic moments of atoms are organised in accordance with the direction of the magnetic field. If temperature raises, also the thermal energy of atoms increases. Magnetic moments easily can change their directions according to the direction of the applied field, since thermal vibration of atoms are reinforced. This results in a decrease of the coercive force of the material for higher temperatures. Simultaneously, extremely vibrating atoms hinder a complete arrangement of magnetic moments, when the magnetic field is close to saturation. This explains the fact that maximum value of flux density is lower at high temperatures.

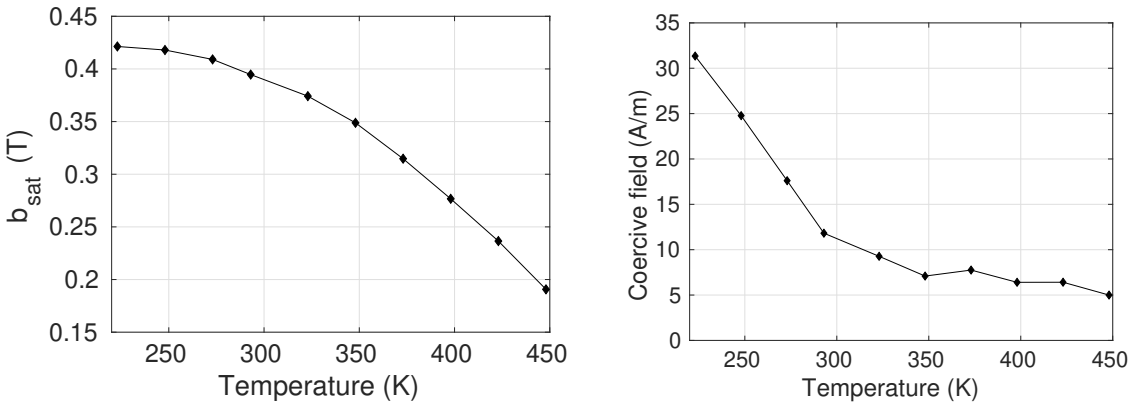

(a) Flux density at saturation versus temperature.

(b) Temperature dependence of the coercive field.

Figure 3.2: Variation of b_{sat} (left) and h_c (right) in function of temperature for 3C90 ferrite material.

An amplitude permeability μ_a and an initial permeability μ_i can be defined and measured experimentally. The amplitude permeability μ_a is the relative permeability determined by the slope of the straight line extending from the origin at $h = 0, b = 0$ to any point of the initial magnetisation curve [16]. That is, it is the ratio between the peak values of flux density b and magnetic field h for each loop:

$$\mu_a = \frac{1}{\mu_0} \cdot \frac{b_{peak}}{h_{peak}} \tag{3.1}$$

The initial permeability μ_i represents the relative permeability at the origin of the $b(h)$ curve described by the hysteresis cycle and involves reversible magnetisation processes, such as wall motion or rotation of magnetisation:

$$\mu_i = \lim_{h \to 0} \mu_a \tag{3.2}$$

We computed it as the ratio between the peak flux density b and the peak magnetic field h in the material measured for the smallest loop.

Figure 3.3a depicts the initial permeability μ_i, measured on the lowest measured loop, for each temperature. Three regions may be identified: in the domain of low fields, we find approximately the initial permeability for $h \simeq 0$. In the region of mean field, μ_i increases to reach a maximum. Finally, in the domain of high fields, it decreases significantly when approaching saturation. Figure 3.3b shows the variation of the amplitude permeability μ_a as function of the peak flux density b_p. Precisely, the figure represents the measured μ_a at 293 K and 323 K, for $f = 50$ Hz.

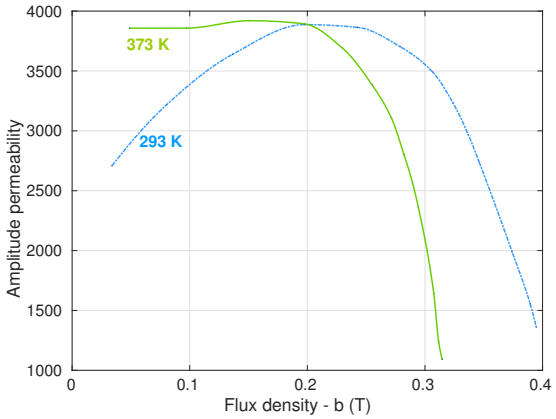

(a) Amplitude permeability at 293 K and 373 K as a function of peak flux density.

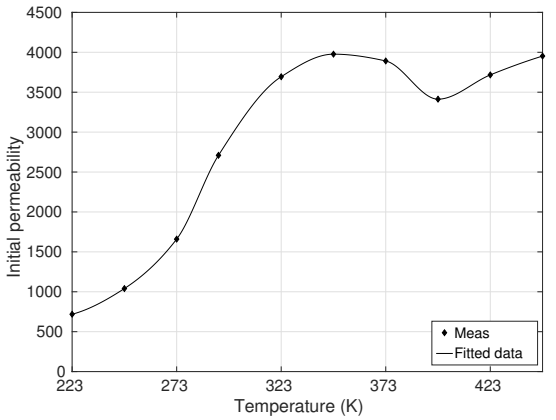

(b) Initial permeability μ_i as a function of temperature.

Figure 3.3: Amplitude and initial permeability of the 3C90 ferrite material.

3.2 Parameters identification in function of temperature

The protocol previously described in Section 2.4 has been applied to 3C90 ferrite in the measured temperature range.

The $h_c(h_p)$ characteristics have been measured for each series of hysteresis loops of increasing h_p, for each temperature. The variation of the $h_c(h_p)$ curves in function of temperature is shown in Figure 3.4. It is evident that the coercive field decreases as temperature raises, which is coherent with the loops depicted in Figure 3.1.

Next, Figures 3.5 and 3.6 illustrate the construction of auxiliary functions $F(h)$ and the corresponding pinning field cumulative weight distribution functions $\partial_h F(h)$. The estimated continuous distributions $\omega(\kappa|T)$ are depicted in Figure 3.7. The final step consists in discretizing the continuous distributions in N cells, in order to obtain the discrete sets of parameters $(\omega_k, \kappa^k)_{k=1,\dots,N}$.

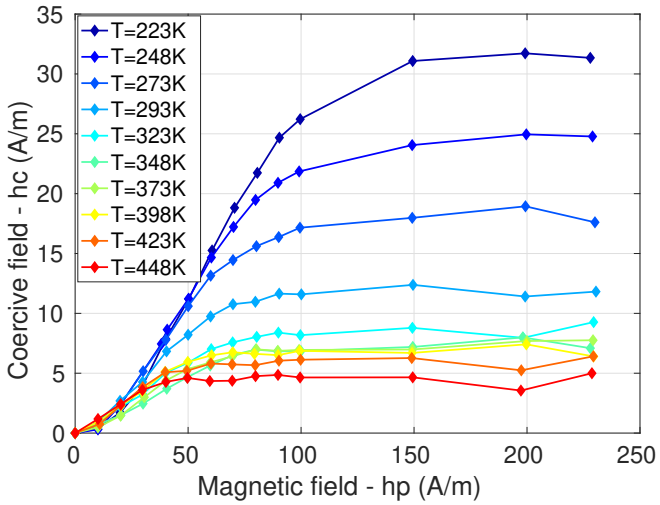

Figure 3.4: Curve $h_c(h_p)$ for 3C90 material in the temperature range.

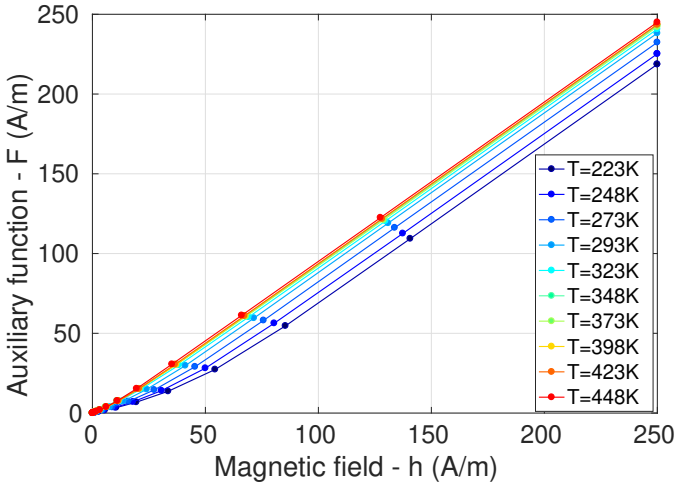

Figure 3.5: Function $F(h)$ for 3C90 material in the temperature range.

The average pinning field decreases, as the temperature increases. This could be linked to the fact that, for higher temperatures, thermal noise makes easier to overcome pinning

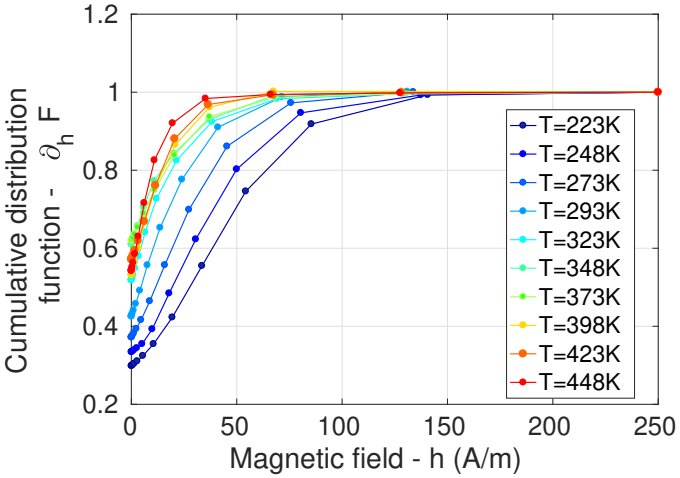

Figure 3.6: Corresponding cumulative weight distribution function $\partial_h F(h)$ as a function of pinning field, for 3C90 material in the temperature range.

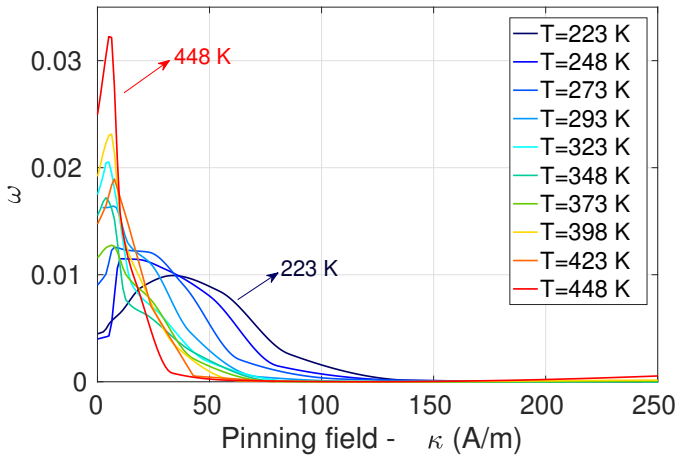

Figure 3.7: Continuous distributions $\omega(\kappa|T)$.

energy barriers, and therefore reduces the pinning field. On the other hand, it is reported in literature [113] that at the higher temperatures grain size increases. Therefore, the growth of grain size increases the distance of pinning points in the material and, consequently, decreases the coercive field.

3.3 Validation of temperature-dependent hysteresis

The EB model has been tested with simple measurements at various temperatures, by varying the number of cells from 2 to 8.

It is necessary to represent the anhysteretic curve in order to fully identify the EB hysteresis model. Here, it is computed by considering the median line of the measured major loop. The parameter identification can be done in two ways: 1) by minimizing the error between measurements and calculated hysteresis loops; 2) by means of the identification procedure described in Section 2.4. In this section, the latter method is applied and the validation is deliberately done with quasi-static standard measurements (cf. Section 2.2.1.1).

Comparisons of theoretical results with experimental data are provided for different loop amplitudes and temperatures. Figure 3.8 depicts measured and simulated $b(h)$ loops with the same amplitude ($h_p = 230$ A/m) for different temperatures (e.g. $T = 248$ K, 348 K and 448 K). In this particular case, simulations have been performed with 3 cells. Already with this number of parameters, measurements and computed hysteresis cycles, on the whole, are in good agreement.

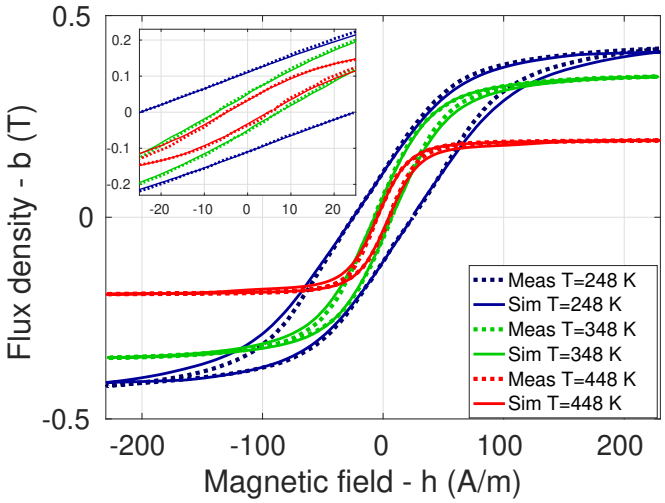

Figure 3.8: Measured and simulated major loops at $h_p = 230$ A/m for different temperatures (248 K, 348 K, 448 K). The number of cells is $N = 3$.

Measured and computed loops with different amplitudes ($h_p = 40$ A/m, 80 A/m, 150 A/m and 230 A/m) at the same temperature, e.g. $T = 273$ K, 323 K and 423 K are compared in Figures 3.9, 3.10 and 3.11 respectively. In this case, the EB model has been simulated with 4 cells. There exists some difference in the ascending and descending branches, especially for the lowest presented temperature $T = 273$ K (cf. Figure 3.9).

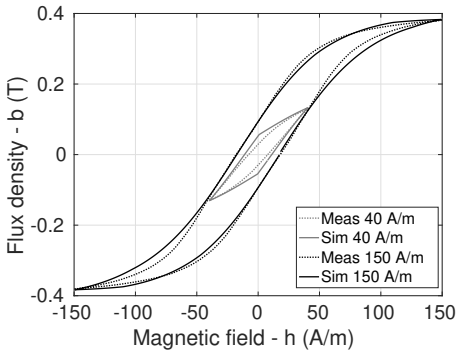

(a) Measured and simulated loops for amplitudes $h = 40$ A/m, 150 A/m.

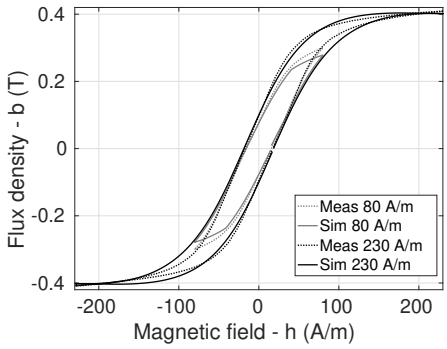

(b) Measured and simulated loops for amplitudes $h = 80$ A/m, 230 A/m.

Figure 3.9: Simulated and measured loops for simple excitation waveforms ($T = 273$ K). Dotted lines: measured values; full lines: simulated values. The number of cells is $N = 4$.

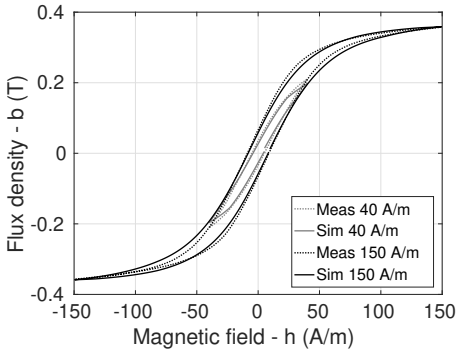

(a) Measured and simulated loops for amplitudes $h = 40$ A/m, 150 A/m.

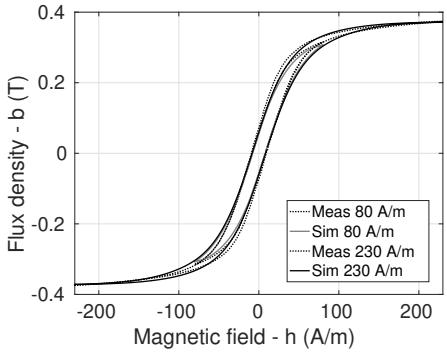

(b) Measured and simulated for amplitudes $h = 80$ A/m, 230 A/m.

Figure 3.10: Simulated and measured loops for simple excitation waveforms ($T = 323$ K). Dotted lines: measured values; full lines: simulated values. The number of cells is $N = 4$.

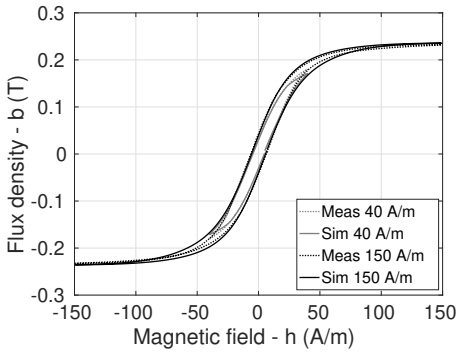

(a) Measured and simulated loops for amplitudes $h = 40$ A/m, 150 A/m.

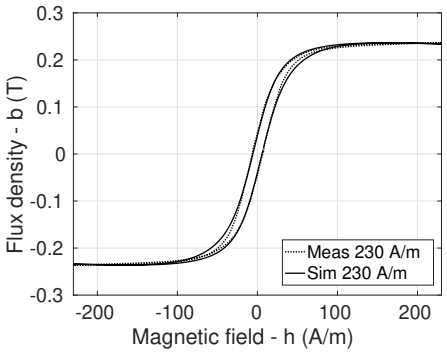

(b) Measured and simulated loops for amplitudes $h = 230$ A/m.

Figure 3.11: Simulated and measured loops for simple excitation waveforms ($T = 423$ K). Dotted lines: measured values; full lines: simulated values. The number of cells is $N = 4$.

3.4 EB model: accuracy and robustness analyses

The objective of this section is to examine the accuracy of the match between models response and measured data and to verify whether the precision can be improved by increasing the number of parameters in the model. This validation is purposely conducted with standard measurements, that is merely with alternating sinusoidal fields.

The accuracy of the EB model in predicting the measured cycles has been quantified by means of the relative normalised root mean square error (NRMSE) between simulated and measured flux density:

$$\text{NRMSE} = \frac{\sqrt{\sum_{n=1}^{N_{meas}} ||b_{sim,n} - b_{meas,n}||^2}}{\sqrt{\sum_{n=1}^{N_{meas}} ||b_{meas,n}||^2}} \times 100\% \tag{3.3}$$

where N_{meas} is the number of measurement points.

The following figures summarise the results of the convergence analysis, namely the NRMSE for a number of cells N spanning from 2 to 8.

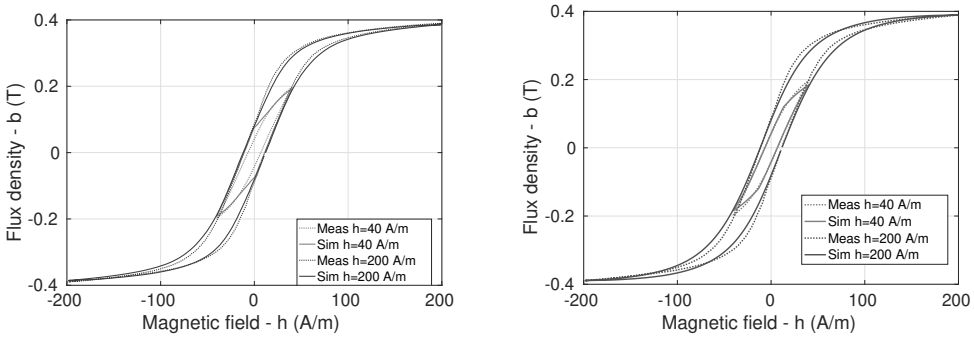

(a) $N = 3$ cells. (b) $N = 4$ cells.

Figure 3.12: Variation of hysteresis loop with magnetic field intensity, $h_p = 40$ A/m and $h_p = 200$ A/m.

Figure 3.12 shows hysteresis loops with variable magnetic field intensity, represented with $N = 3$ (Figure 3.12a) and 4 cells (Figure 3.12b). It is apparent that modelling with 3 cells, a quite accurate representation of the major loop is possible, whereas the internal loop appears almost parallelogram-shaped for the minor loop at 40 A/m (cf. Figure 3.12a). Increasing the number of cells to $N = 4$ (Figure 3.12b) significantly reduces the difference in loop area and the NRMSE (cf. Figure 3.13). The hysteresis loops at small and intermediate magnetic fields become more precise and approach the experimental loop shape. Difference between the measured and calculated major loops indeed exists, especially around the saturation knee.

Figure 3.14 represents the NRMSE versus temperature, for cycles of fixed amplitude $h_p = 230$ A/m. For major cycles, a quite good representation of hysteresis loops (NRMSE $< 5\%$) is generally obtained starting from 3 cells.

Figure 3.15 represents the NRMSE versus cycle amplitude, for temperatures $T = 248\text{ K}, 348\text{ K}, 448\text{ K}$. For cycles of lower amplitudes results are mixed. The global trend is that the error is proportionally lower for cycles of higher amplitude. This can be explained by the argument that for cycles of high amplitude all cells are activated simultaneously (apart from reversing points), and therefore one deduces from (6.12) that:

$$h_r^k = h - \kappa^k \cdot \text{sgn}(\dot{h}) \tag{3.4}$$

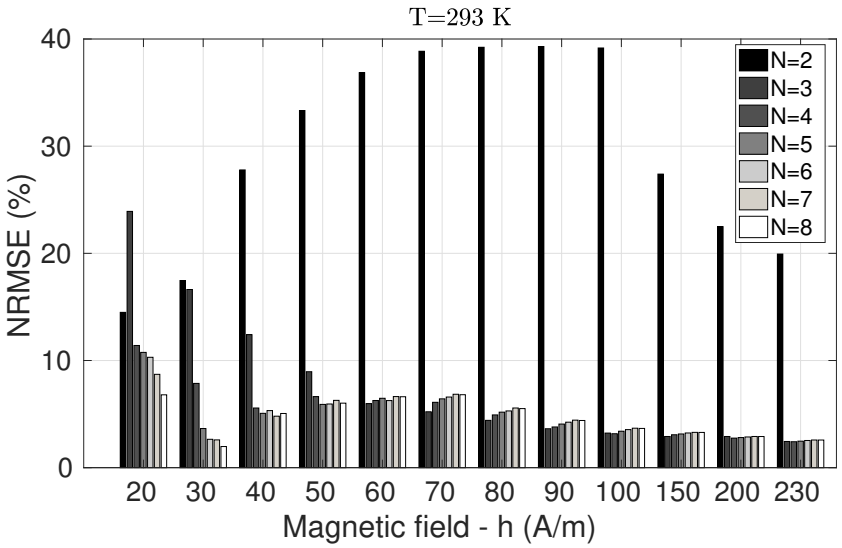

Figure 3.13: NRMSE at different amplitudes of applied field for $T = 293$ K by varying the number of cells N.

and therefore, by using (1.45) one obtains:

$$h_r = h - \mathrm{sgn}(\dot{h}) \cdot \sum_{k=1}^{N} \omega_k \kappa^k \tag{3.5}$$

Hence, the details of the pinning distribution play a less important role: the field h_r is determined by the sum in (3.5). Moreover, when the material is saturated, the field is determined by the saturation value of M_{an} more than by the exact value of h_r.

Conversely, at low fields not all cells are activated, and thus the details of the pinning distribution (ω_k, κ^k) play a much more important role. Nevertheless, the NRMSE stabilizes for $N \geq 3$, apart from very low-amplitude cycles ($h_p \leq 30$ A/m) for which usually a higher number of cells can be used in order to increase the accuracy, especially starting from $T = 293$ K.

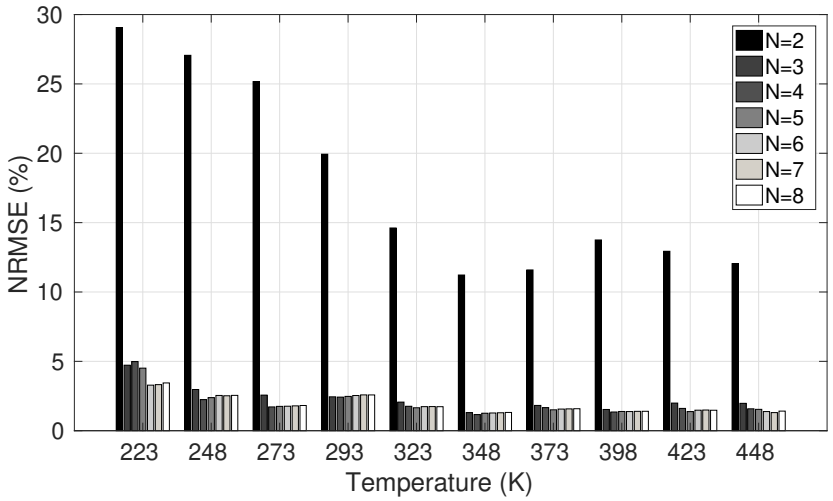

Figure 3.14: NRMSE at constant amplitude of applied field ($h_p = 230$ A/m) for different temperatures by varying the number of cells N.

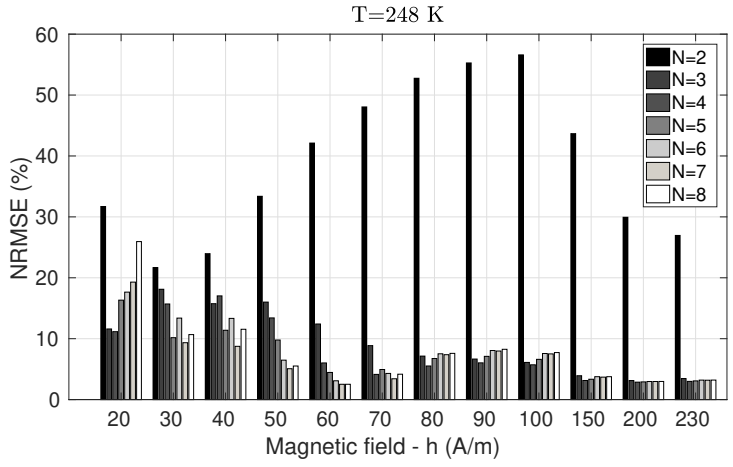

(a)

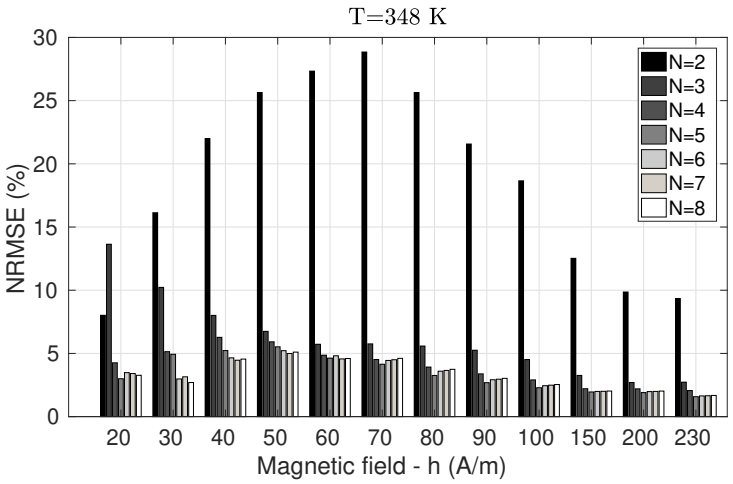

(b)

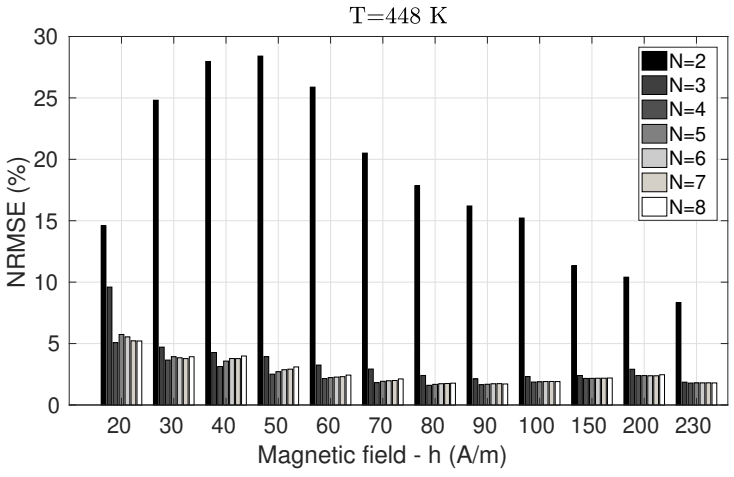

(c)

Figure 3.15: NRMSE at different amplitudes of applied field for three temperatures by varying the number of cells N.

3.5 Validation on complex waveforms

The same identified parameters have been employed to simulate complex magnetisation trajectories. Measurements have been performed for $T = 293$ K, 323 K and 373 K (cf. Measurement results). Comparisons of these non-standard measurements with those given by the EB model allow to fully assess its predictive power. In order to further evaluate the model, it is useful to compare its performances with the JA model as it concerns minor loops predictions.

To identify the JA parameters, optimisation methods are usually applied, so that the deviation between the simulated and measured hysteresis curves is minimised according to the objective function employed. For this purpose, an optimisation method (*fmincon*) of the Matlab Optimisation Toolbox is used, whereas the identification procedure of the EB model can be done without the need of least-square error minimisation. The identified material parameters at the three temperatures for the JA model are listed in Table 3.1.

Table 3.1: Parameters of JA model for 3C90 ferrite material.

Parameters	$T = 293$ K	$T = 323$ K	$T = 373$ K
a	13.42 A/m	86.99 A/m	107.04 A/m
c	0.0034	0.0025	0.0033
k	12.09 A/m	72.73 A/m	99.84 A/m
α	$2.70e^{-8}$	$8.80e^{-9}$	$1.64e^{-8}$
M_{sat}	$2.99e^{5}$ A/m	$1.08e^{6}$ A/m	$1.16e^{6}$ A/m

Parameters of the EB model identified at $T = 293$ K for $N = 4$ cells are illustrated in Table 3.2.

Table 3.2: Parameters of EB model for 3C90 ferrite material at $T = 293$ K.

ω	κ (A/m)
$\omega_1 = 0.43422$	$\kappa^1 = 0$
$\omega_2 = 0.41383$	$\kappa^2 = 13.53$
$\omega_3 = 0.14966$	$\kappa^3 = 42.37$
$\omega_4 = 0.00227$	$\kappa^4 = 115.61$

The cycles measured and simulated with JA and EB model ($N = 3$ and 4 cells) are depicted in Figure 3.16, for the signal with third harmonic at $T = 293$ K.

Results show that JA model deviates more in the minor loop region and overestimates the entire loop, not providing a good agreement with measurements. Conversely, the EB model reproduces satisfactorily experimental data already with $N = 3$ cells, complying with the correct closure of minor loops. Moreover, computed results are improved using a finer discretization, e.g. 4 cells. With the addition of one more cell, minor loops are well predicted, which is coherent with the study of the evaluation of the model's prediction, previously introduced. The model shows its ability in simulating signals with harmonics at a given temperature. It produces stable minor loops, namely it closes the loops in a more physically adequate manner, compared to the original JA model [65], [61], [62], [17].

When comparing measurements at the other temperatures (cf. Figure 3.17), results given by the JA model are even more overestimated, inaccurate, showing big deviations from experimental data.

On the contrary, the performance of the EB model (direct implementation [47]), makes it possible to adjust the accuracy of modelling by selecting adequate discretization,

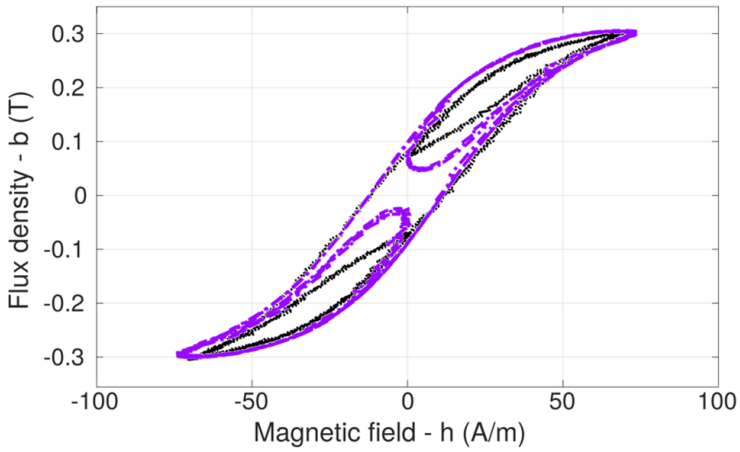

(a)

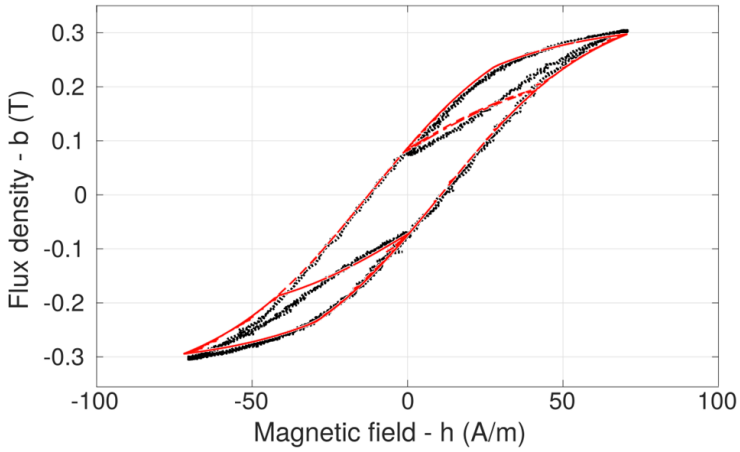

(b)

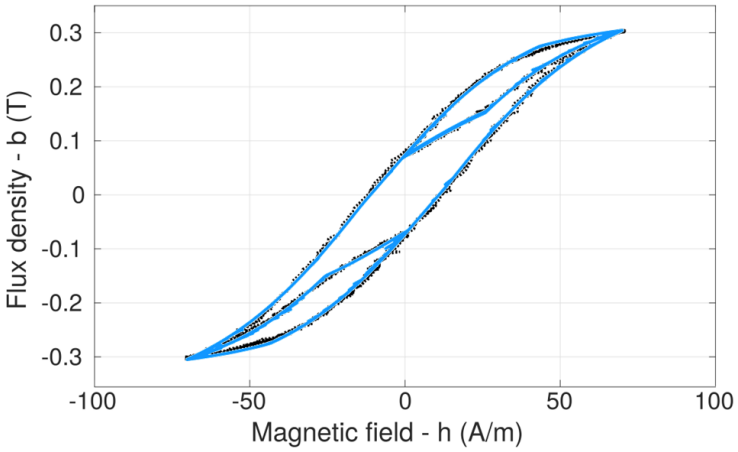

(c)

Figure 3.16: Measured loop with third harmonic at $T = 293$ K simulated with the (a) JA and EB models with (b) $N = 3$ and (c) $N = 4$ cells.

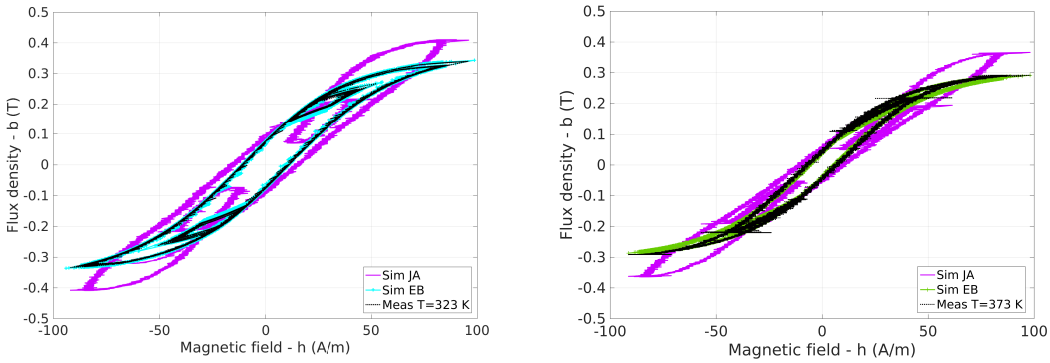

(a) (b)

Figure 3.17: Measured loops at $T = 323$ K (a) and $T = 373$ K (b) compared to simulations with JA model and the EB model (4 cells).

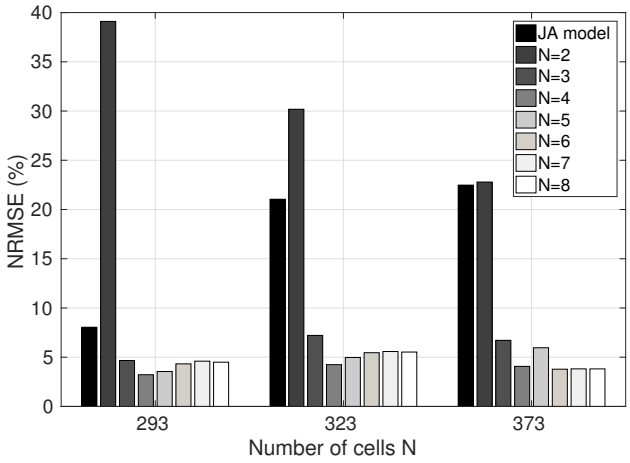

Figure 3.18: Estimated NRMSE for complex magnetisation curves at $T = 293$ K (3^{rd} harmonic), 323 K and 373 K (PWM) for the JA model and the EB model, with N ranging from 2 to 8.

as it can be noted in Figure 3.18, where the NRMSE between measurements and calculated loops for each measured temperature contributes to the evaluation of the models prediction. Note that the EB model has been applied with the same parameters identified with simple excitation waveforms. Simulated and measured results are globally in good agreement, showing that the EB model is able to predict complex loops [17] at any temperature, at least within the measured range. Finally, the EB model with parameters identified under sinusoidal conditions are able to give reasonably accurate results under non-standard conditions.

3.6 A first assessment

In this section, the analysis of the temperature dependence of magnetic properties of SMMs, especially soft Mn-Zn ferrites, has been examined.

This study puts in evidence how results of the systematic parameters identification procedure depend on this variable. The curves $h_c(h_p)$ decrease as temperature increases, which is coherent with the variation of the coercive field in function of temperature.

The observed trend in the continuous distributions $\omega(\kappa|T)$ is that the peak of the distribution shifts towards lower values when the temperature increases (Figure 3.7). This evidence could be explained by the argument that higher thermal noise reduces the energy required to overcome pinning energy barriers. In fact, when the temperature of a ferromagnetic or ferrimagnetic material is increased, the added thermal energy enhances the motion of domains, facilitating the alignment, as well as preventing them from remaining aligned when the field is removed [1]. As a result, for high temperatures, saturation magnetisation, remanance, and the coercivity are all reduced. Hence, at high temperatures, it is easier to demagnetise the material, but magnetic moments of atoms cannot attain full arrangement in saturation region of the hysteresis loop [112].

Moreover, the coercive field has a striking dependence on the grain size. In the literature, several work [114], [115], [116] have investigated the link between coercive field and grain size, that are inversely proportional. Therefore, the existence of a possible link between grain size, pinning force distribution and temperature deserves to be examined.

The static EB hysteresis model under simple and distorted sinusoidal magnetisation waveforms has been compared. From the analysis of the precision of the model, it is observed that the NRMSE is generally higher for low temperature (Fig. 3.14) and/or for low applied fields. These two facts could be linked, in that under low thermal noise and/or low applied field, cells corresponding to low pinning field are not simultaneously activated[1], and therefore the material exhibits a more complex behaviour. In the experimental phase, it has been impossible to completely saturate the material for low temperatures, due to the fact that h_p values have been fixed for all temperatures. Therefore, if one compares calculated and experimental loops for three temperatures (248 K, 348 K, 448 K), as in Figure 3.8, for $T = 248$ K the observed deviation could result from the fact that saturation is not fully attained in this case, thus the identified anhysteretic curve M_{an} may be less accurate. Moreover, since the protocol [109] requires that the material must be fully saturated, it is possible that the obtained parameters (ω_k, κ^k) are not so accurate for this particular temperature.

As one could expect, the global trend shows that NRMSE decreases as the number of cells N, used to model the material, increases. It is observed that three cells are generally enough to obtain a good result for not too complex signals, whereas a higher number of

[1]Cells which activate simultaneously are practically indistinguishable. This fact has been used in [74] to build simplified EB models.

cells is generally needed for signals with low amplitude harmonics.

A difficult task in the validation step is the comparison of the EB model predictions with experimental data not used for the parameter identification. The parameters identified under standardised conditions are able to give extremely accurate results also under complex conditions, proving that the material parameters express themselves already in simple measurements.

3.7 Proposed temperature extension

This section proposes an extension of the EB hysteresis model to take into account the temperature. This subject is part of a review article published in COMPEL [117]. In particular, it is discussed how this variable can be accounted for in the model, via an appropriate parameter identification and interpolation procedure.

Indeed, in practical applications, engineers need to predict the continuous distribution $\omega(\kappa)$ curves at any temperature and/or directly a discretized approximation (ω_k, κ^k).

3.7.1 Continuous $\omega(\kappa|T)$ curves interpolation

In order to assess the robustness of our approach, we have performed a cross-validation by comparing the original functions $\omega(\kappa|T)$ obtained for all available temperatures with interpolated curves obtained by using only half of the dataset. Namely, the distributions have been interpolated by having available only $\omega(\kappa|T)$ for a few temperatures (T = 223 K, 273 K, 323 K, 373 K and 448 K) with the final aim to reconstruct the five remaining curves (T = 248 K, 293 K, 348 K, 398 K, 423 K). Figure 3.19 shows the original curves (full lines), obtained by the AUX method, and the new computed ones. The interpolated and original curves are in good agreement. This suggests that the model could have been identified by using a reduced set of measurements.

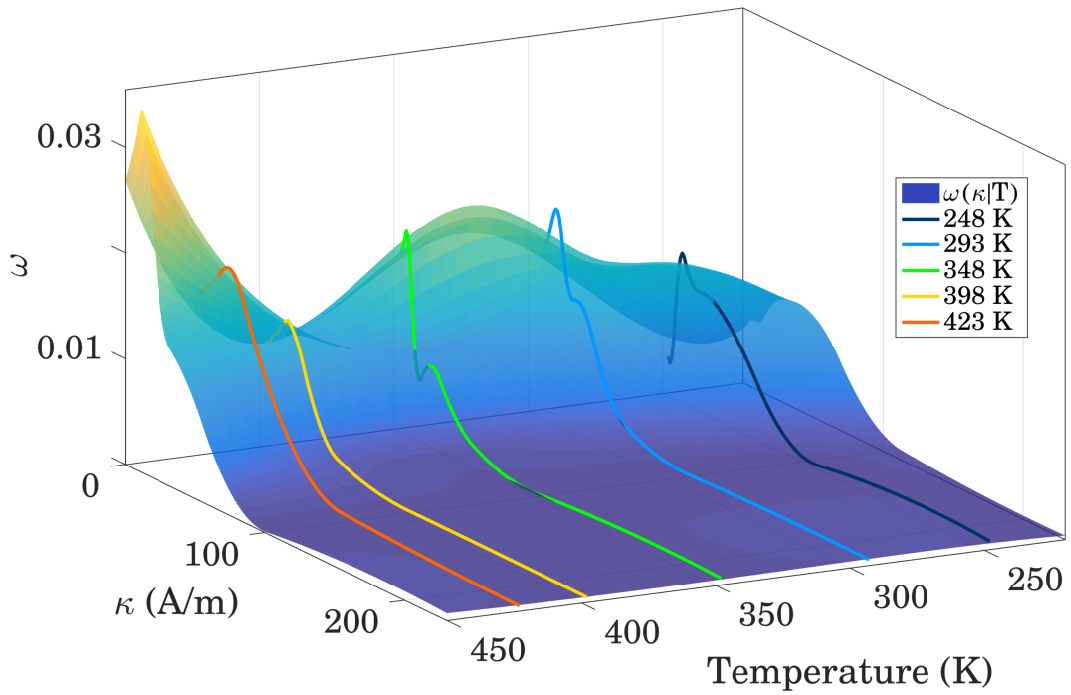

Figure 3.19: Reconstructed continuous distributions $\omega(\kappa|T)$ and original ones (248 K, 293 K, 348 K, 398 K, 423 K, in full lines).

3.7.2 Discrete (ω_k, κ^k) sets function of temperature

In this section, a first property of the variation law of parameters in function of temperature is proposed. The continuous distributions $\omega(\kappa|T)$ have been discretized in $N = 3$ cells, thus achieving discrete parameters $(\omega_k(T), \kappa^k(T))_{k=1,\dots,N}$, with temperature T ranging from 223 K to 448 K. As for parameters ω_k, the same property $\sum_{k=1}^{N} \omega_k = 1$

must hold at any temperature. Parameters κ^k are related to a local pinning force or a local coercive field. Therefore the variations of $(\omega_k(T), \kappa^k(T))_{k=1...N}$ as a function of temperature T could be obtained by the knowledge of the macroscopic coercive field $h_c(T)$, which has already been measured. More precisely, it has been hypothesised that, at any temperature, the products $\omega_k(T) \cdot \kappa^k(T)$ rescale as:

$$\frac{\omega_k(T) \cdot \kappa^k(T)}{\omega_k(T_0) \cdot \kappa^k(T_0)} = \frac{h_c(T)}{h_c(T_0)} \tag{3.6}$$

in which the ratio is known for a reference temperature T_0. Remark that this is consistent with [74].

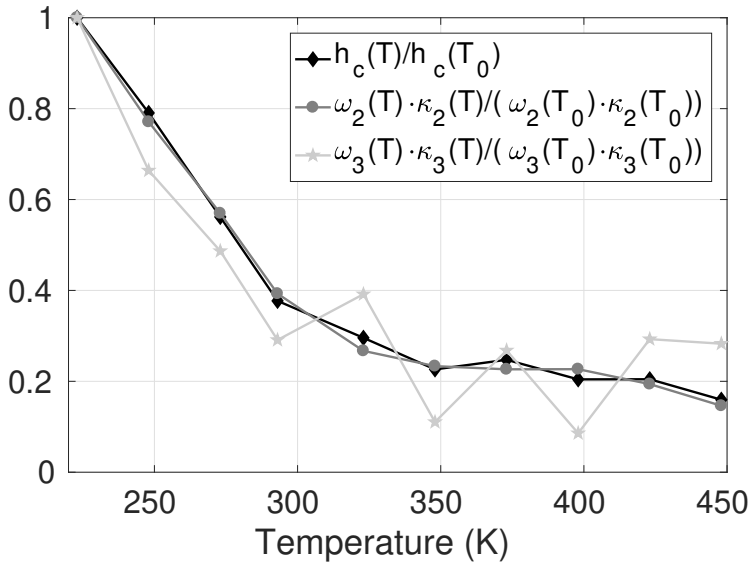

Figure 3.20: Variation law of parameters with temperature ($T_0 = 223$ K).

Figure 3.20 shows the curves of (8.2) for the second and third cell. The first cell $k = 1$ is not represented, since the constraint $\kappa^1 = 0$ is imposed, hence (8.2) is meaningless. Moreover, κ^1 takes into account the reversible part of the applied field and thus it is not related to the coercive field. Concerning the two irreversible cells, there is a fairly good agreement between the rescaled product of parameters for $k = 2$ and the coercive field. The third cell shows the same trend, but it may be noted the presence of erratic behaviour starting from $T = 293$ K. The same trend is observed for cells of order higher than 3 but with a much more erratic behaviour. A possible explanation is that starting from $k \geq 4$ the effect of cells is negligible (Figure 3.14): $\omega_k \ll 1$ for $k > 3$, henceforth the parameters of these cells cannot be identified accurately.

Finally, EB models identified at a reference temperature could be used to simulate the behaviour of magnetic materials at other temperatures, at the price of a few measurements to be performed in the desired range of temperature.

3.8 Conclusion

The EB hysteresis model has first been analysed under various magnetisation waveforms and at different temperatures. Globally, the results of measured and simulated hysteresis loops are in good agreement at any temperature. This reveals that the identification protocol used to obtain the model parameters is robust and stable, as the parameters

identified by simple excitation waveforms can be used to simulate hysteresis loops subject to complex magnetisation waveforms.

An extension to the existing EB model has then been proposed, so as to take into account the effect of temperature with only a few measurements, based on a 2D interpolation. A scaling law of the model parameters (ω_k, κ^k) with the temperature has been suggested and partially validated. This constitutes a first step toward predicting hysteresis loops for complex signals and for any temperature falling in the range of available measurements.

However, additional tools are required to separate the identification of $\omega_k(T)$ and $\kappa^k(T)$, in order to obtain a comprehensive variation law in function of temperature and proposing new ways and solutions.

On the other hand, methods to predict the behaviour of materials as a function of temperature are valuable tools for engineers. A possible way to obtain this information could be microscopic imaging. In fact, in some cases, several authors [114]- [115]- [116] reported in literature that the coercive field is inversely proportional to grain size. Therefore, the existence of a possible link between grain size, pinning force distribution and temperature deserves to be investigated.

Chapter 4

Validation with 2D FE Simulations

To test the accuracy of hysteresis models in FEA (Finite Element Analysis), simulation results can be compared to measurements on a test-case for the validation of magnetic field analysis. This chapter applies the EB hysteresis model to the FE simulation of a real transformer application [118] designed in the Ampère laboratory. This represents a test-case, inspired by [119], to benchmark the predictive capability of the hysteresis model, considering different current excitations of the transformer winding system, which are adapted to yield sinusoidal, phase-shifted, distorted or rotating magnetic flux density waveforms. Measured data are compared to the simulated ones for various excitation cases.

4.1 Experimental setup

The setup has been designed and built especially for this purpose. The geometry of the transformer is shown in Figure 4.1, for which the parameters are listed in Table 4.1. The D.U.T consists of a pair of E-cores made of the same material, which forms a closed magnetic flux path (cf. Figure 4.2). The material is a very common material (soft ferrite Mn-Zn 3C90 from Ferroxcube [103], previously characterised) used in power electronics. Two windings of 15 turns are placed on the external limbs. The windings can be connected in series or supplied by two independent controlled voltage sources. Unidirectional or rotating fields in some parts are then possible. For each configuration, both the applied voltage and the currents through the windings are measured. With the help of suitable supports built by means of a 3D printer, the sensor coils C_1 and C_2, consisting of 20 turns each, are used to estimate the flux going in the central leg from each winding.

This provides a test-case for the validation of a 2D magnetic field analysis as well as vector hysteresis and presence of multiple harmonic signals. Several test cases are defined depending on the supplied conditions of the windings (cf. Figure 4.3), with various maximal amplitude field value components v_p, and phase shifting angles ϕ. In that way, a set of different excitation source fields is built, made of two different amplitudes, $v_p = 1$ V (LA = low amplitude) or 5 V (HA = high amplitude), associated with two ϕ values, 0° (unidirectional case) and 90° (rotating case). The test-case has different configurations, but attention will be paid to following ones:

- Case 1 is tested to validate unidirectional waveforms.
- Case 2 is appropriate for checking vector hysteresis modelling, with rotational flux.
- Case 3 is convenient for checking distorted multi-harmonic signals under unidirectional or rotating fluxes.

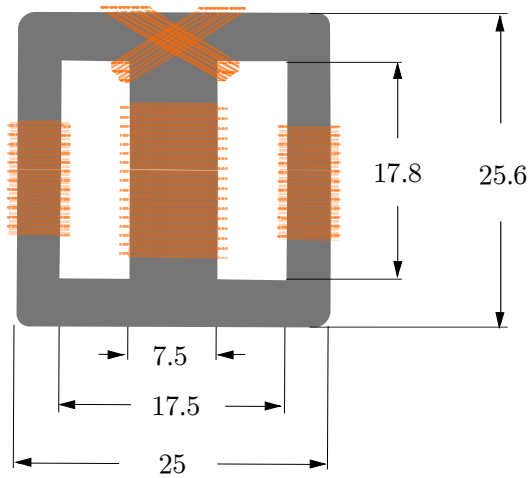

Figure 4.1: E-E core transformer (dimensions in mm) and the located windings.

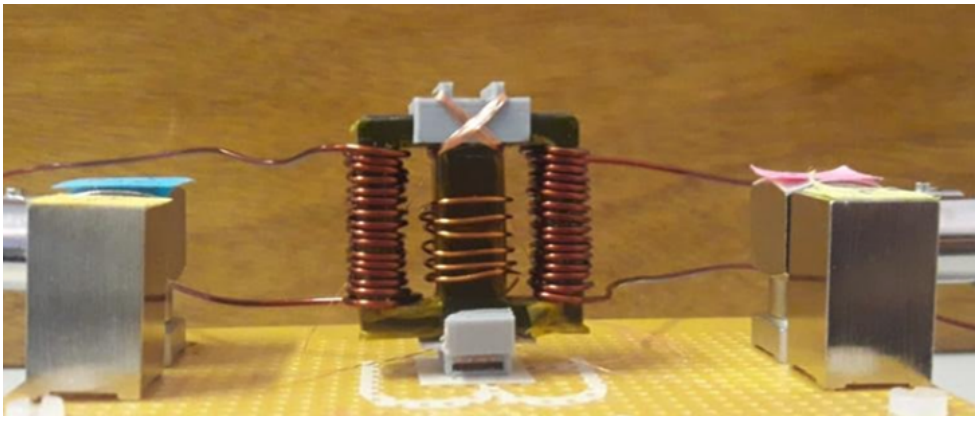

Figure 4.2: D.U.T built in the Ampère laboratory.

Table 4.1: Description of each quantity.

Symbol	**Value**	**Description**
l_e	58 mm	effective length
A_e	52 mm^2	effective area
V_e	2990 mm^3	effective volume
l_a	7.5 mm	axial length (along **z**-axis)
N_1	5 turns	Measurement winding
N_3	15 turns	Excitation winding
N_4	15 turns	Excitation winding
C_1	20 turns	Sensor coil
C_2	20 turns	Sensor coil
R_{series}	38.7 Ω	Series resistance
R_{shunt}	2 Ω	Shunt resistance
R_{N3}	0.20 Ω	Coil$_{N3}$ resistance
R_{N4}	0.20 Ω	Coil$_{N4}$ resistance

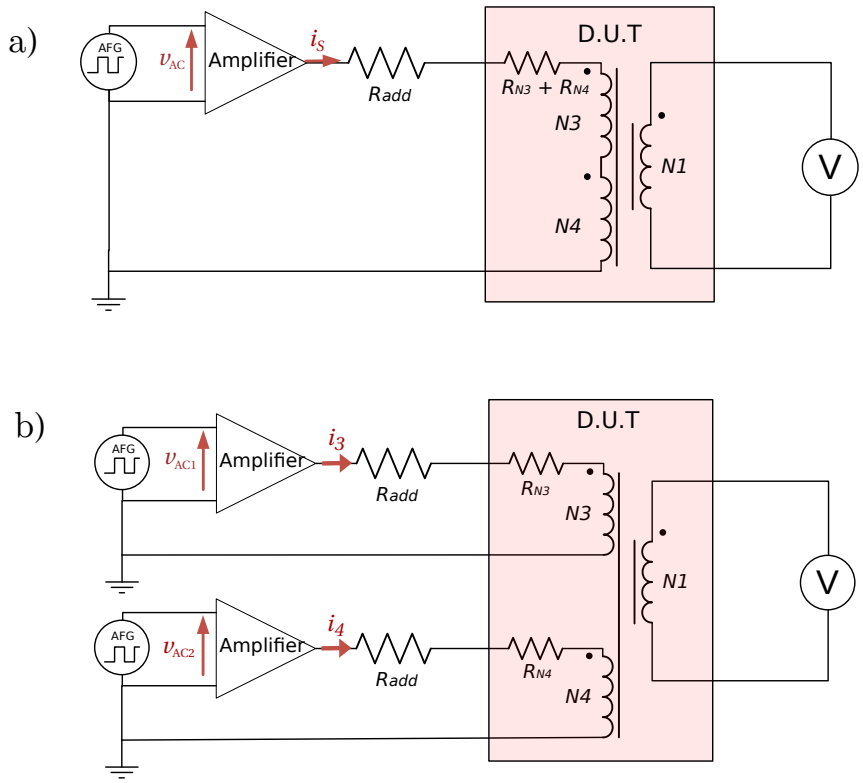

Figure 4.3: Circuit connections: a) series-aiding connected windings; b) two independent voltage supplies.

4.2 FE simulations

This section introduces the simulations built in the open source Gmsh/GetDP FE code [120] by means of the 2D FE magnetodynamic $\mathbf{a} - v$ formulation (Appendix B), in which the EB model (*simplified differential approach*) has been implemented [47]. Indeed, as ferrite is an insulator, and coils are modelled as stranded inductors, there are no eddy currents, hence in practice the formulation reduces to the simpler magnetostatic $\mathbf{a}-$formulation. This has been previously elaborated and tested on different cases of increasing geometrical complexity, such as the square case and the TEAM 32 transformer [47]- [120].

The windings are considered as stranded inductors and each of them is represented in the cross-section by two rectangle regions around a core leg. The electric global quantities are used in the definition of voltage sources and for the coupling with circuit equations. A coupling with external circuits in the FE software enables the imposition of voltage-driven sources. The test-case transformer can be considered as a 2D case, in which the fields $\mathbf{h}$ and $\mathbf{b}$ lie in the $\mathbf{xy}$-plane and the current density $\mathbf{j}$ is assumed perpendicular to the domain. Thanks to the 2D limitation, the $\mathbf{a} - v$ formulation is expressed in terms of a potential vector $\mathbf{a}$, where the component along the $\mathbf{z}$-axis, $\mathbf{a}_z$, represents the unknown of the problem.

Moreover, due to symmetry, only half of the transformer cross-section can be considered, as seen in Figure 4.4. The geometry is discretized using a mesh made of 4420 triangles with 2000 nodes. Points 1-2-3-4 have been fixed in order to calculate the vector potentials $\mathbf{a}_z(1)$, $\mathbf{a}_z(2)$, $\mathbf{a}_z(3)$ and $\mathbf{a}_z(4)$. The aim is to compute the magnetic flux distributions on the core region, in particular the flux going in the central leg from each external winding.

As concerns the model parameters choice, simulations are performed adopting $N = 4$

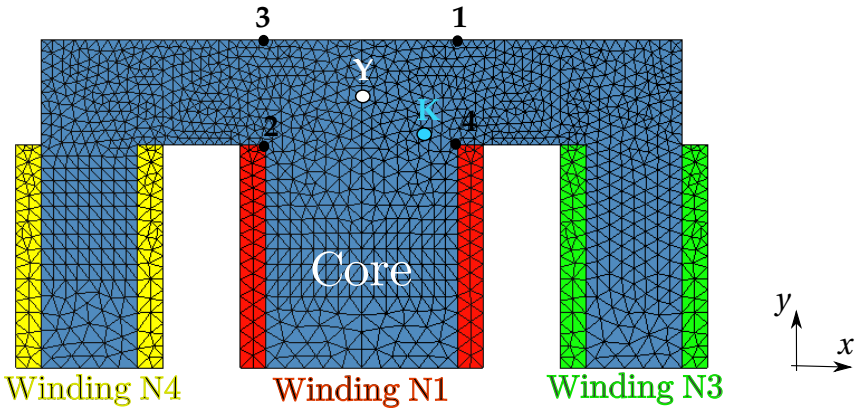

Figure 4.4: Geometry of the E-E transformer.

cells for the EB model, with the previously identified discrete parameters (ω_k, κ^k) for $T = 293$ K (cf. Table 9.1). The anhysteretic saturation law is firstly approximated by a hyperbolic tangent function such as (2.18) with saturation magnetic polarisation $J_a = 0.38$ T and $h_a = 53$ A/m, a parameter affecting the initial slope of the curve.

Table 4.2: Parameters for 3C90 ferrite material.

ω	κ (A/m)
$\omega_1 = 0.43422$	$\kappa^1 = 0$
$\omega_2 = 0.41383$	$\kappa^2 = 13.53$
$\omega_3 = 0.14966$	$\kappa^3 = 42.37$
$\omega_4 = 0.00227$	$\kappa^4 = 115.61$

Three periods with 1000 time steps each are computed, with a smooth start from the demagnetised state. Namely, as the simulations start, the voltage sources are smoothly increased in amplitude from 0 to v_p during the 50 first steps, and then reach their typical evolution regimes. Therefore, measurement and simulated data are compared on the basis of different quantities, in the steady state regime:

- voltage (in V) on the measurement winding N_1;
- magnetic fluxes (in weber, Wb) going in the central limb from each winding N_3 and N_4. To this aim, points $1, 2, 3, 4$ (cf. Figure 4.4) have been fixed to calculate the vector potentials $\mathbf{a}_z(1)$, $\mathbf{a}_z(2)$, $\mathbf{a}_z(3)$ and $\mathbf{a}_z(4)$ in order to compute the magnetic fluxes as

$$\Phi_{12,sim} = [\mathbf{a}_z(2) - \mathbf{a}_z(1)] \cdot l_a \tag{4.1}$$

$$\Phi_{34,sim} = [\mathbf{a}_z(4) - \mathbf{a}_z(3)] \cdot l_a \tag{4.2}$$

4.2.1 Case 1 (series)

In the configuration of Case 1, the two external windings are connected in series with the resistance $R_{add} = R_{series} + R_{shunt}$. The whole circuit is fed by a sinusoidal voltage source with different levels of peak value and frequency of 50 Hz.

$$v_{AC} = v_p \cdot \sin(2\pi f t) \tag{4.3}$$

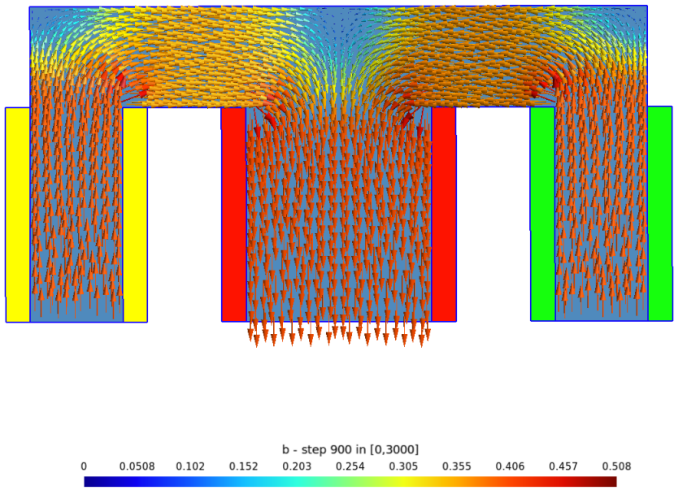

Figure 4.5: Case 1: field distribution result displayed for a given time step ($n = 900$).

Only unidirectional flux patterns are generated and no rotating fields are expected. Figure 4.5 illustrates the field distribution result displayed for a given time step ($n = 900$).

The currents obtained in the winding from the simulations and the measured ones are shown in Figure 4.6.

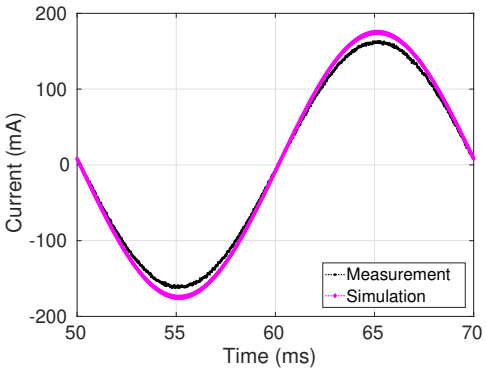

(a) LA: current in the winding.

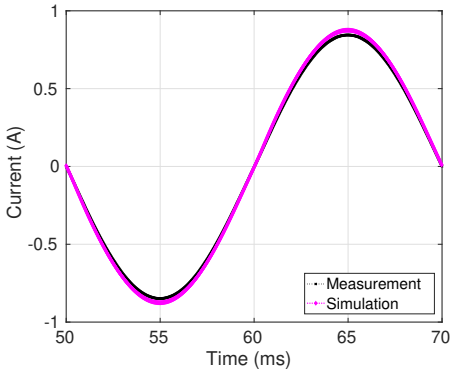

(b) HA: current in the winding.

Figure 4.6: Case 1 (series). Comparison of the measured currents in the winding with the simulation with the EB hysteresis model.

In Figures 4.7 the computed voltages are compared to the measured data obtained in the measurement winding (N_1) for LA and HA. The magnetic fluxes going in the central leg from the series-connected external windings are depicted in Figure 4.8. Simulated results are able to reproduce the shape of the experimental data, even if they tend to overestimate measurements.

4.2.2 Case 2 (rotating fields)

In this configuration, the two external windings are supplied with two sinusoidal voltage waveforms at the same frequency ($f_1 = f_2 = 50$ Hz) and a phase-shift of ϕ.

$$v_{AC1} = v_p \cdot \sin(2\pi f_1 t + \phi) \tag{4.4}$$

$$v_{AC2} = v_p \cdot \sin(2\pi f_2 t) \tag{4.5}$$

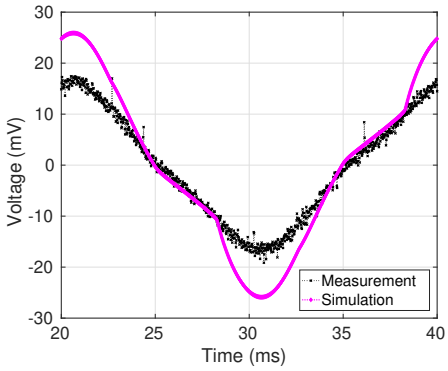

(a) LA.

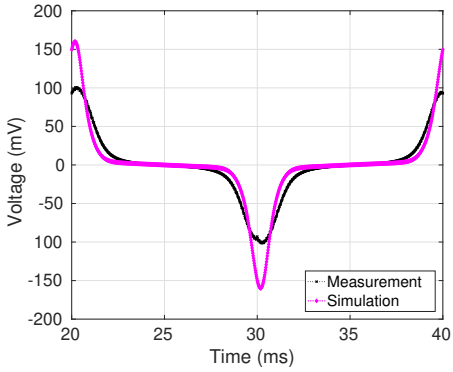

(b) HA.

Figure 4.7: Case 1 (series). Measured and simulated voltage in the central leg.

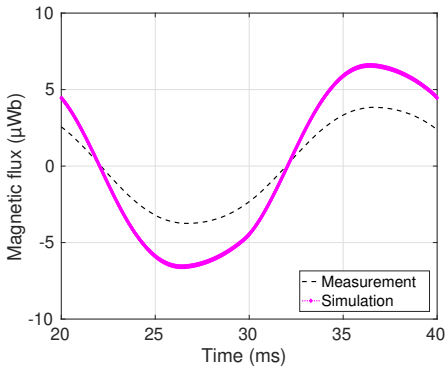

(a) LA.

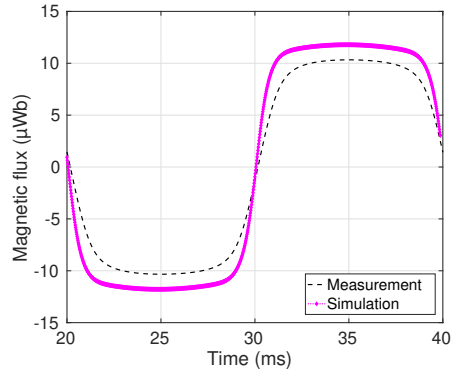

(b) HA.

Figure 4.8: Case 1 (series). Magnetic flux going in the central leg from the series-connected windings.

Different sub-cases are considered:

(a) The phase shift between the two excitation voltages is $\phi = 45°$.

(b) Two sinusoidal waveforms in quadrature: one winding is supplied by a sinusoidal voltage and the other by a cosinusoidal voltage (phase shift of $\phi = 90°$ between the two excitation voltages).

(c) The phase shift is $\phi = 315°$ between the two excitation voltages.

Below, it is shown the case for which the currents in windings N_3 and N_4 are shifted in quadrature. Hence, rotating fields are expected. Results for cases 2a-2c are depicted in Appendix C.

Case 2b: phase-shift $\phi = 90°$

In Figure 4.9 both experimental and simulated current waveforms are shown and it can be seen that there is a phase shift between them.

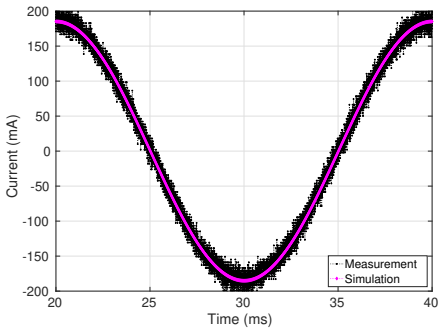

(a) LA: current in the winding N_3.

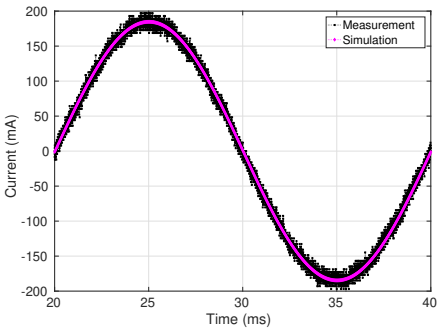

(b) LA: current in the winding N_4.

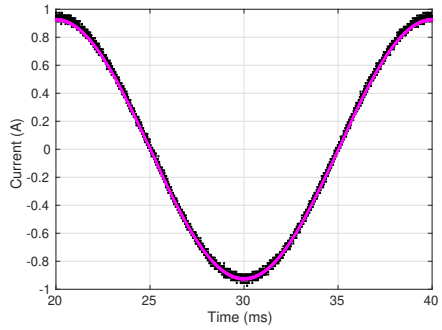

(c) HA: current in the winding N_4.

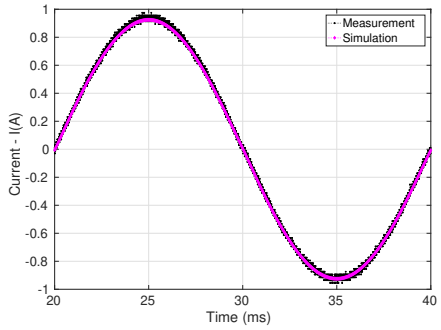

(d) HA: current in the winding N_4.

Figure 4.9: Case 2b. Comparison of simulations versus measured currents in the windings.

In this way, the phase-shift of 90° between the two excitation sources generate rotating fields in the T-joint region, as it can be seen in Figures 4.10-4.11, where the computed **b**-loci and **h**-loci obtained at point K and Y, respectively, are depicted for LA and HA.

Results for Case 2b are depicted in Figure 4.12 and show that the computational model is able to reproduce the experimental waveforms obtained in the measurement winding (N_1), for LA and HA, and the flux distributions in the T-region of the core. Even in this case, it is possible to observe the same tendency of Case 1, in which simulations overestimate measurements.

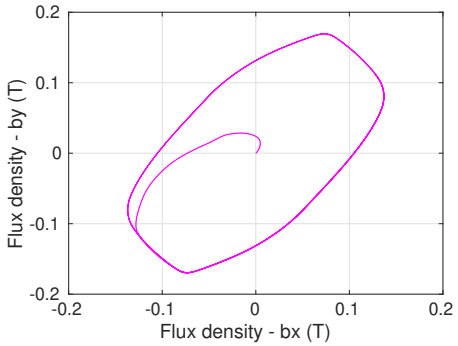

(a) **b**-loci (LA).

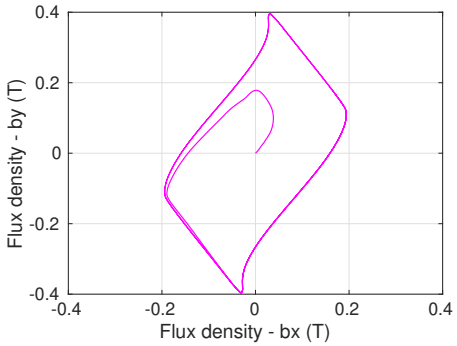

(b) **b**-loci (HA).

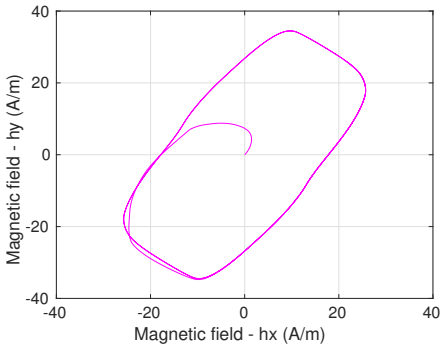

(c) **h**-loci (LA).

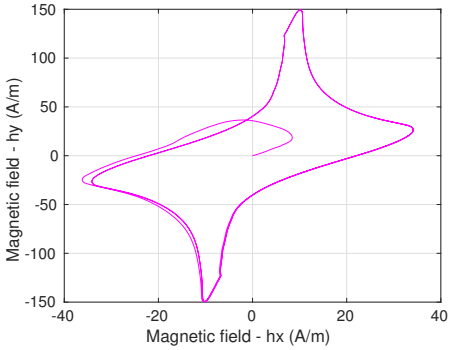

(d) **h**-loci (HA).

Figure 4.10: Case 2b (rotating fields): computed **b**-loci and **h**-loci at point K.

4.2.3 Case 3 (multi-harmonics)

In the configuration of Case 3, multiple harmonic signals have been taken into account. Windings are supplied by two independent voltage sources (9.2)-(9.3) at different frequencies and a phase-shift of ϕ, both with the same peak value v_p $(1-5$ V). Different sub-cases are considered:

(a) $f_1 = 3f_2 = 150$ Hz, $f_2 = 50$ Hz, $\phi = 0°$

(b) $f_1 = 3f_2 = 150$ Hz, $f_2 = 50$ Hz, $\phi = 90°$

(c) $f_1 = 5f_2 = 250$ Hz, $f_2 = 50$ Hz, $\phi = 0°$

(d) $f_1 = 5f_2 = 250$ Hz, $f_2 = 50$ Hz, $\phi = 90°$

In the followings, Case 3b (third harmonic and rotating fields) and Case 3c (fifth harmonic and unidirectional fields) are shown. Cases 3a-3d are depicted in Appendix C.

Case 3b (third harmonic - rotating fields)

The waveform of computed supply currents in the windings are compared to the measured ones in Figure 4.13. Calculated data of voltage and magnetic flux show a good agreement with the measured ones, as depicted in Figures 4.14.

Case 3c (fifth harmonic - unidirectional fields)

Computed and measured waveform of supply currents in the two windings are compared in Figure 4.16. Simulated currents reproduce adequately the measured ones. Figure

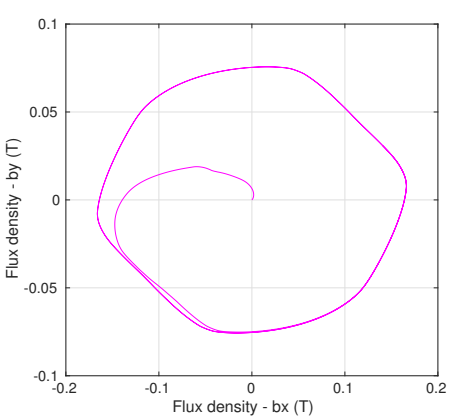

(a) **b**-loci (LA).

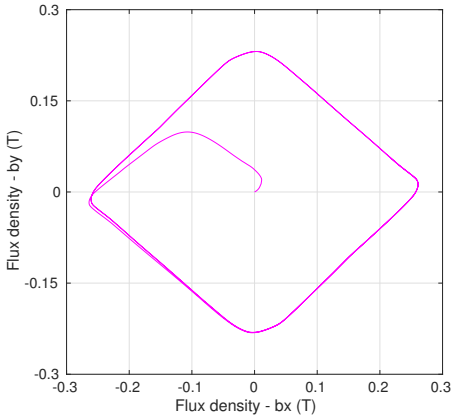

(b) **b**-loci (HA).

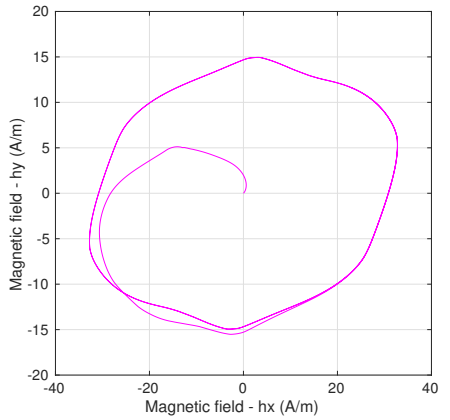

(c) **h**-loci (LA).

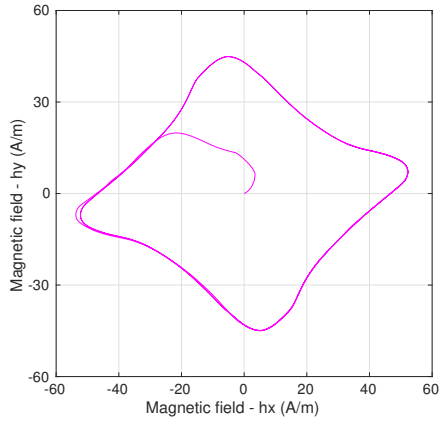

(d) **h**-loci (HA).

Figure 4.11: Case 2b (rotating fields): computed **b**-loci and **h**-loci at point Y.

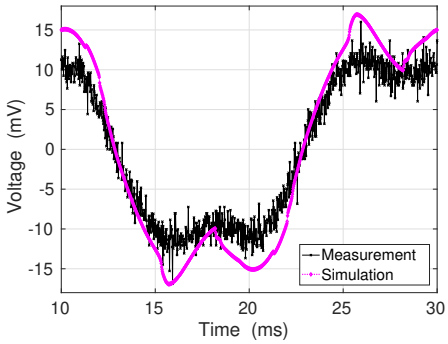

(a) Measured and simulated voltage in the central leg (LA).

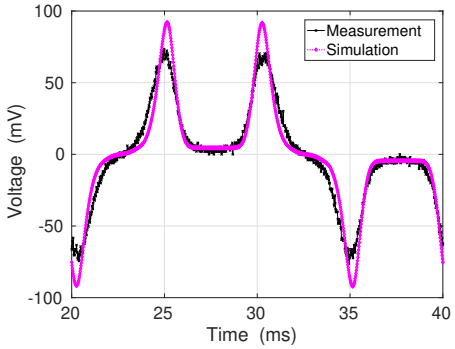

(b) Measured and simulated voltage in the central leg (HA).

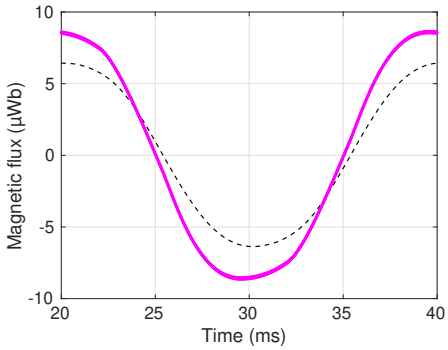

(c) Magnetic flux going in the central leg from winding N_3 (LA).

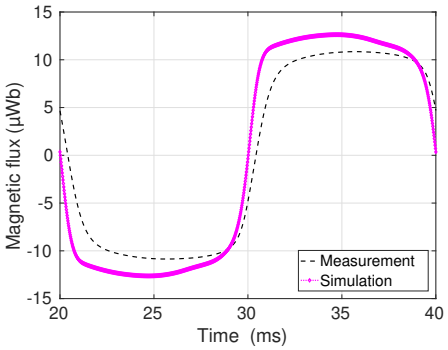

(d) Magnetic flux going in the central leg from winding N_3 (HA).

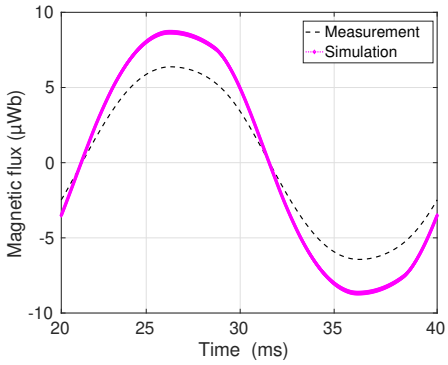

(e) Magnetic flux going in the central leg from winding N_4 (LA).

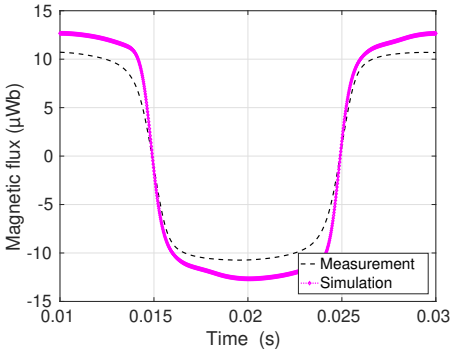

(f) Magnetic flux going in the central leg from winding N_4 (HA).

Figure 4.12: Case 2b (rotating fields).

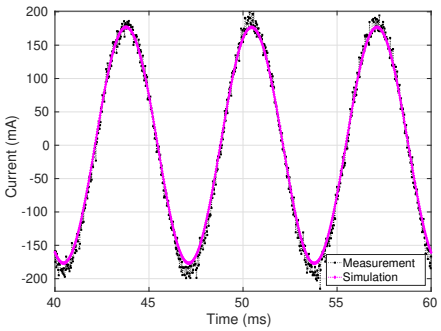

(a) LA: current in the winding N_3.

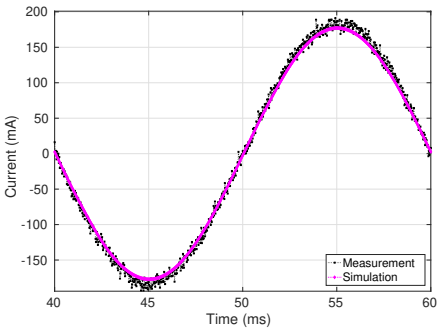

(b) LA: current in the winding N_4.

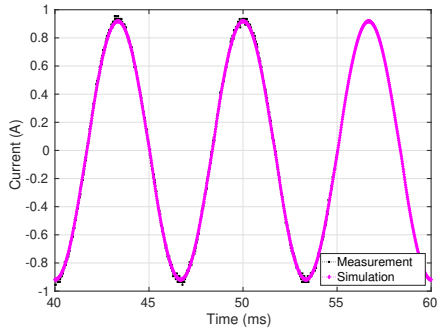

(c) HA: current in the winding N_3.

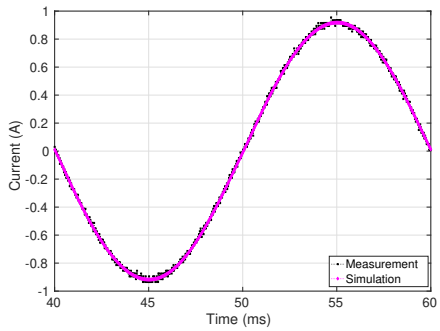

(d) HA: current in the winding N_4.

Figure 4.13: Case 3b (third harmonic-rotating fields). Comparison of simulations versus measured currents in the windings.

4.17 depicts the voltage in N_1, the magnetic flux from winding N_3 and N_4. Globally, predictions provide good representation of measurements for both LA and HA. However, as previously, simulated results slightly overestimate measured data.

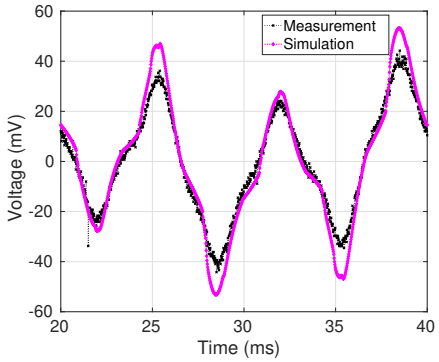

(a) Measured and simulated voltage in the central leg (LA).

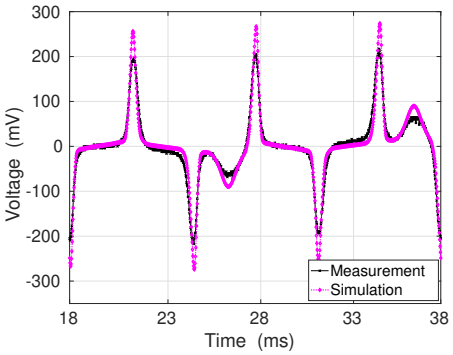

(b) Measured and simulated voltage in the central leg (HA).

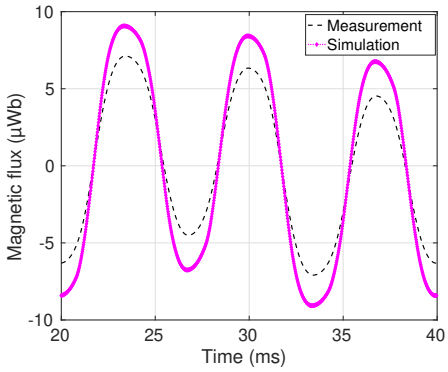

(c) Magnetic flux going in the central leg from winding N_3 (LA).

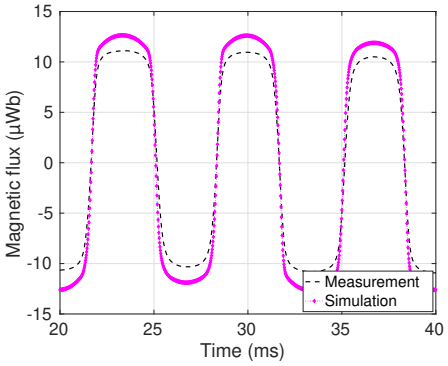

(d) Magnetic flux going in the central leg from winding N_3 (HA).

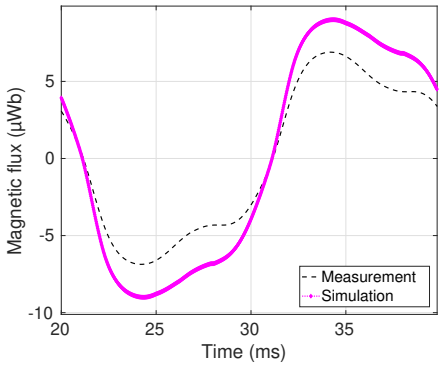

(e) Magnetic flux going in the central leg from winding N_4 (LA).

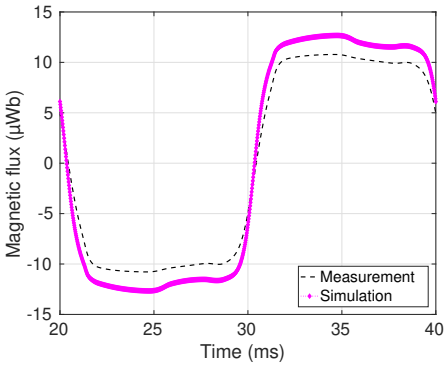

(f) Magnetic flux going in the central leg from winding N_4 (HA).

Figure 4.14: Case 3b (third harmonic-rotating fields).

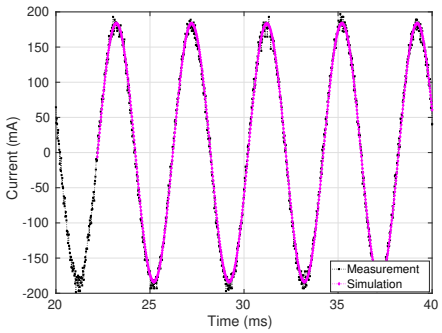

(a) LA: current in the winding N_3.

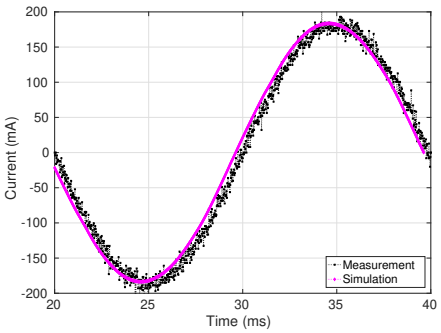

(b) LA: current in the winding N_4.

Figure 4.15: Case 3c (fifth harmonic-unidirectional fields). Comparison of simulations versus measured currents in the windings.

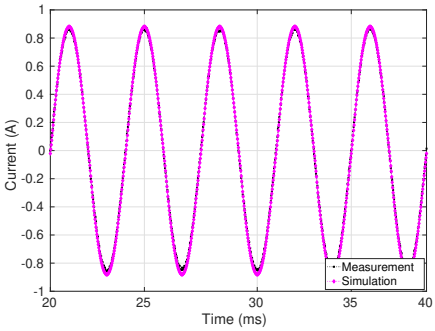

(a) HA: current in the winding N_3.

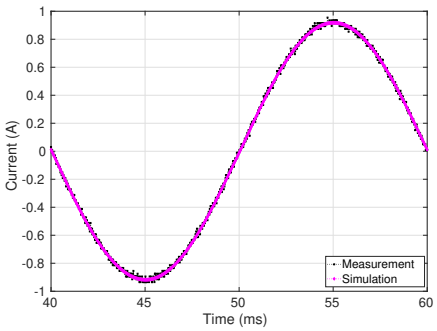

(b) HA: current in the winding N_4.

Figure 4.16: Case 3c (fifth harmonic-unidirectional fields). Comparison of simulations versus measured currents in the windings.

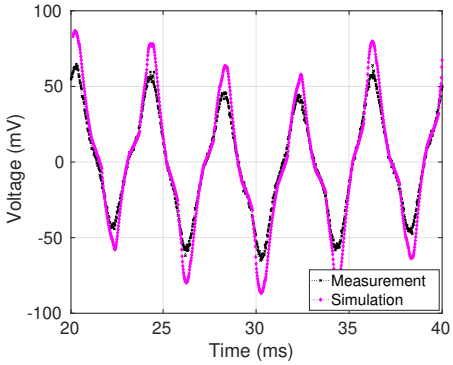

(a) Measured and simulated voltage in the central leg (LA).

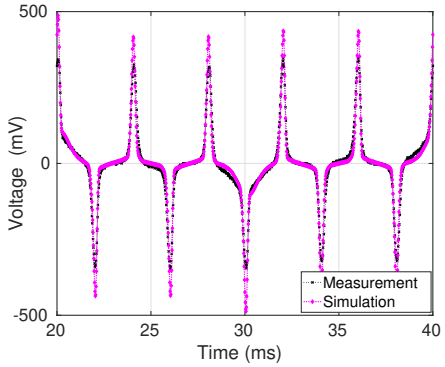

(b) Measured and simulated voltage in the central leg (HA).

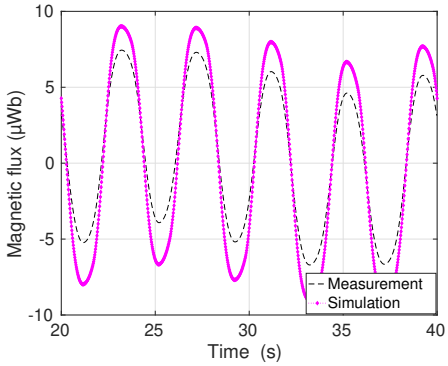

(c) Magnetic flux going in the central leg from winding N_3 (LA).

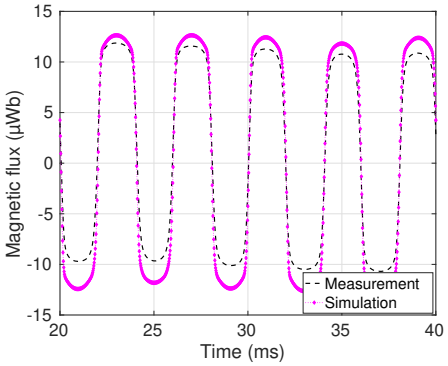

(d) Magnetic flux going in the central leg from winding N_3 (HA).

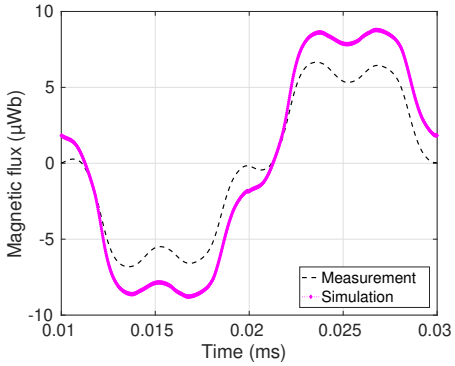

(e) Magnetic flux going in the central leg from winding N_4 (LA).

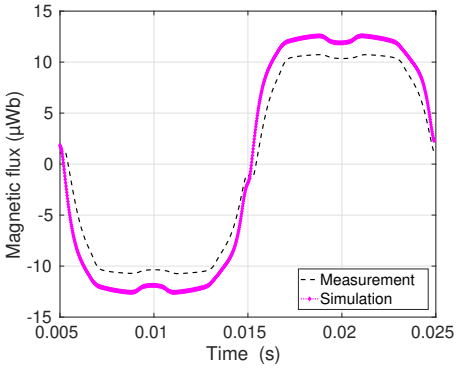

(f) Magnetic flux going in the central leg from winding N_4 (HA).

Figure 4.17: Case 3c (fifth harmonic-unidirectional fields). Magnetic flux going in the central leg from winding N_3 and N_4.

4.3 Discussion

At present, all the simulations carried out to represent several configurations for the E-cores transformer have shown that, with this choice of parameters, some differences exist between measurements and computed data.

Hence, in order to find the parameters influencing the obtained results, several simulations with different conditions have been performed, taking into consideration Case 3a (multi-harmonics) and Case 2b (phase-shift $\phi = 90°$).

Multi-harmonic signals

Let's consider Case 3a, endowed with multiple harmonics. Figure 4.18 illustrates the field distribution result displayed for a given time step ($n = 900$).

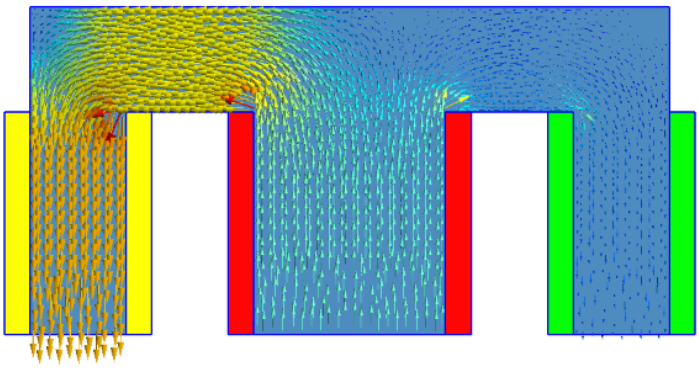

Figure 4.18: Case 3a: magnetic induction **b** distribution result displayed for a given time step ($n = 900$).

Firstly, a coarse mesh is adopted (MeshA), which consists of 2000 vertices and 4420 elements. Secondly, a finer mesh is taken (MeshB) with 12329 vertices and 25651 elements. Then, the approximation of the anhysteretic curves is modified, replacing the hyperbolic tangent (HypTang) with the Double Langevin (DLang) function (2.20). The four parameters have been fitted from measurements: $J_a = 0.4261$ T, $h_a = 20.2661$ A/m, $J_b = 0.0038$ T, $h_b = 18.8927$ A/m. Finally, a finer discretization of parameters is taken into account, simulating the model with $N = 40$ cells.

Table 4.3: Different conditions for simulations of Case 3a.

Simulation	**Mesh**	**Cells**	**Anhysteretic function**
Sim1	A	$N = 4$	Hyperbolic tangent
Sim2	B	$N = 4$	Hyperbolic tangent
Sim3	A	$N = 4$	Double Langevin
Sim4	A	$N = 40$	Hyperbolic tangent

Results of simulations are plotted in Figure 4.19 and compared to experimental data of the voltage in the measurement winding of the D.U.T.

Let's focus on Sim1 and Sim3, in which the only difference is the approximation chosen for the anhysteretic curve. In Sim1, a hyperbolic tangent function is used, whereas the double Langevin is employed in Sim3. Differences between the two functions are clearly observed in Figure 4.20. None of them respects exactly the evolution of the measured curve (in full lines), which itself is an approximation of the anhysteretic curve. In particular,

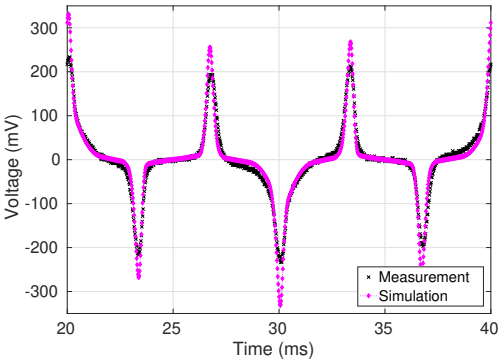

(a) **Sim1** (MeshA - 4 cells - HypTang).

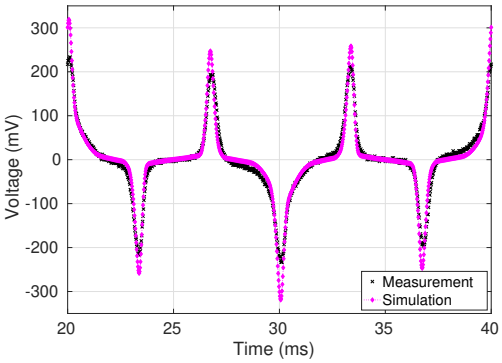

(b) **Sim2** (MeshB - 4 cells - HypTang).

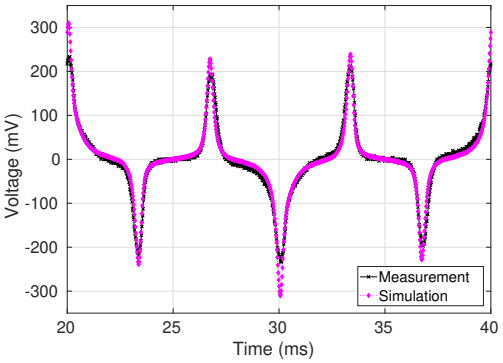

(c) **Sim3** (MeshA - 4 cells - DLang).

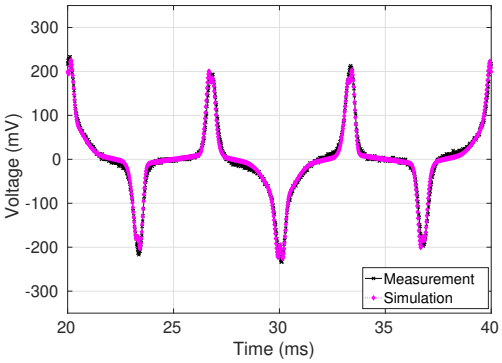

(d) **Sim4** (MeshA - 40 cells - HypTang).

Figure 4.19: Case 3a. Experimental and simulated voltage in the measurement winding in different conditions.

discrepancies between the measured curve and the Double Langevin function decrease in the saturation zone, whereas, the hyperbolic tangent shows a much lower value than the measured one. This is reflected on the comparison of voltages in the measurement winding of the E-cores transformer. In fact, differences are less evident for Sim3, since the Double Langevin function allows a better agreement between experimental and computed results.

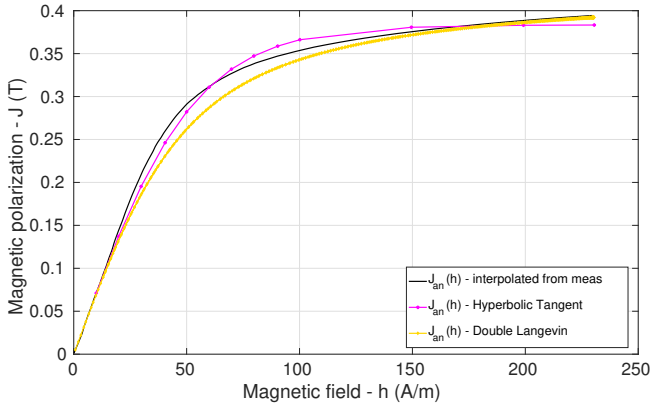

Figure 4.20: Anhysteretic curves $J_{an}(h)$.

It can be remarked that results are less accurate for MeshA, using a hyperbolic tangent function as approximation of $J_{an}(h)$. The deviation slighly decreases adopting a finer mesh, but it is clear that differences become less significative when the anhysteretic saturation law is represented with a Double Langevin function.

As can be seen, simulated results and measurements show good agreement when the EB model is simulated with $N = 40$ cells, as it can be seen in Figure 4.19d and in Figure 4.21 in further detail.

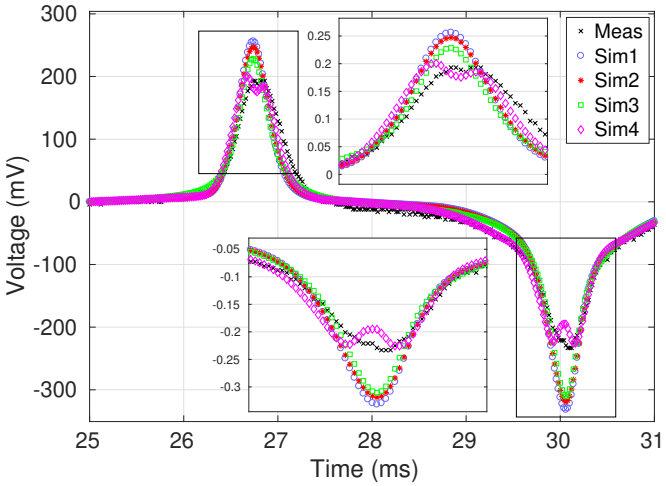

Figure 4.21: Simulations with different conditions compared to measured data for Case 3a.

Rotating fields

Let's focus our attention on Case 2b, where rotating fields are expected. Figure 4.22 shows measurement data compared to simulations performed with several number of cells and

Table 4.4: Different conditions for simulations of Case 2b.

Cells	Anhysteretic function
$N = 4$	Hyperbolic tangent
$N = 4$	Double Langevin
$N = 8$	Double Langevin
$N = 16$	Double Langevin

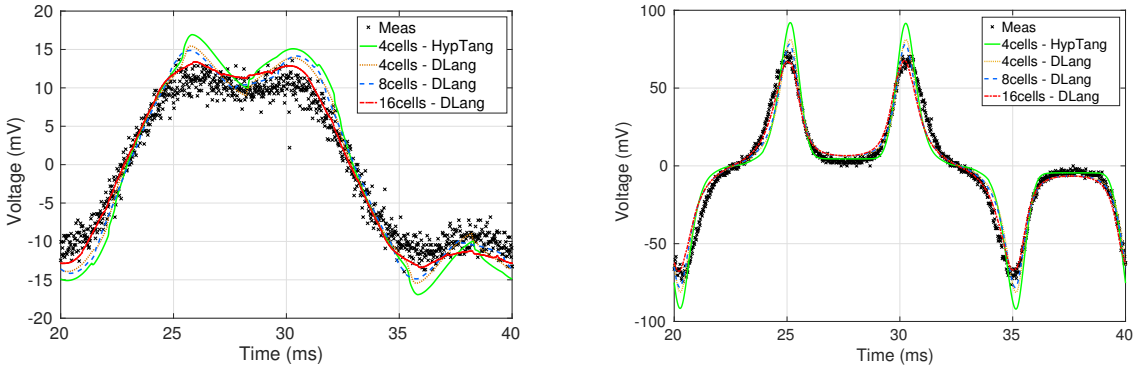

(a) LA. (b) HA.

Figure 4.22: Voltage in the measurement winding, measured and simulated in different conditions for Case 2b.

the introduction of the double Langevin function to approximate the anhysteretic function (cf. Table 4.4).

As can be seen in Figure 4.22, for simulations with 4 cells, the double Langevin function allows a better agreement with measured data points compared to the hyperbolic tangent function, in both cases of LA and HA. Then, the number of cells is increased up to 32 cells, but accuracy is not improved for $N > 16$ cells. With 16 cells, differences between simulated results and measurements appear less significant, showing satisfactory agreement.

Figure 4.23 depicts the discrete representation of pinning field distributions for different number of cells. EB model simulated with 16 cells provide a finer computation in the mean range values of magnetic fields ($h = 20 - 60$ A/m), comparing to 4 and 8 cells.

The refinement of the EB model outputs towards the measurement with an increase of the number of cells is clearly visible.

Time of simulations for waveforms produced by the EB model, with various number of cells $N = 2, 3, 4, 8, 16$ is displayed in Figure 4.24. If the number of cells varies, the number of internal variables change, and, during the simulation, each of them requires a processing time to describe its evolution. It appears that the complexity grows with the number of cells.

Overall, differences are probably due to the adopted approximations. First, a 2D analysis has been carried out in order to verify the model behaviour in a various range of excitation waveforms. However, the magnetic circuit shape is larger than deeper, so the effects in the depth direction (i.e. the presence of a leakage flux, the path of which surrounds the windings in the third dimension) may not be negligible.

Other hypothesis are linked to possible uncertainties in the geometry simplifications (see Table 7.1). In fact, the material characterisation has been carried out on a ring core. Indeed, in these simulations, we are allocating the same features of the ring core on the E geometry. Nevertheless, ferrites are well-known to have a wide dispersion. For example,

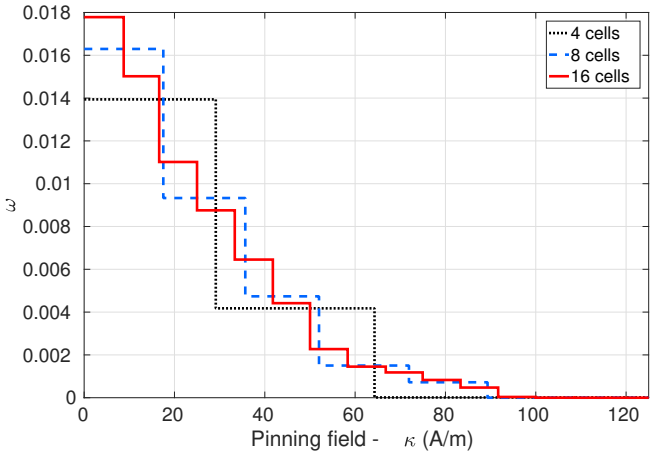

Figure 4.23: Discrete representation with 4, 8 and 16 cells (one of which is purely reversible) for the the pinning field distribution $\omega(\kappa)$ of 3C90 ferrite material.

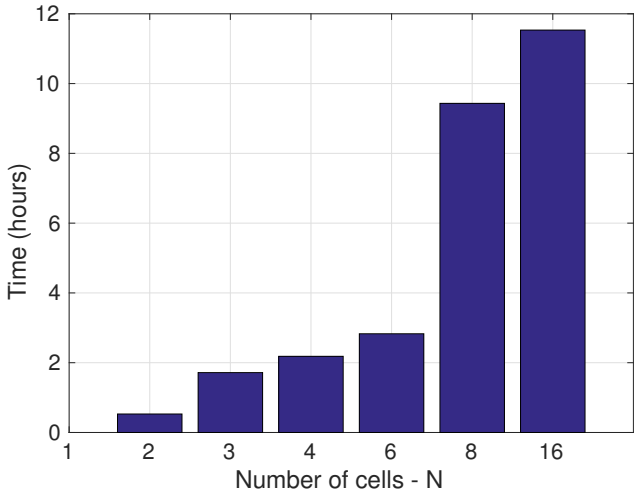

Figure 4.24: Time variation for simulations with various number of cells.

the amplitude permeability is given to ±25%, which could explain why differences seem more marked for low amplitude tests.

Finally, differences can be due to the material modelling. Indeed, this analysis has revealed that, computed data overestimate measurements, except when an higher number of parameters is used. So, in this particular case, 4 cell parameters are not enough to fully represent the complex material response, considering that good agreement is found when 16 cells are used to simulate the material behaviour. Actually, several works [69]-[74]- [117] have proven that the number of cells in which the model is discretized depends on the required accuracy: models with higher number of cells will provide an accurate representation of the material response, but they will be also more complex to handle from the computational point of view.

4.4 Conclusion

Several experimental tests and 2D FE simulations have been performed on a E-E core transformer built in the Ampère laboratory. The objective is to study the vectorial nature of the EB model in case of rotating flux and multiple harmonic signals at different amplitude levels. A 2D analysis has been carried out, showing various configurations. In most cases, the computed results overestimate the experimental ones. Nevertheless, satisfactory qualitative agreement is found in comparing the computed and measured results, considering the test-case approximation. Finally, a 2D assumption provides a useful insight into the real application, in order to firstly examine the hysteresis model behaviour. Future work will investigate the 3D FE analysis, so as to deeply consider the complex problematics related to the case-study.

Chapter 5

Conclusion and perspectives

This thesis deals with the issue of effectively modelling soft ferrite materials under arbitrary excitation waveforms by means of a valid hysteresis model.

Indeed, technological advances relies on an increasingly precise understanding of material physical laws. Whether it is mainstream application or advanced technology, every system must be conceived in accordance with its actual in-use conditions. This requires to take into consideration the external parameters, such as the temperature of the medium, as early as the design stage. Actually, certain properties deteriorate with increasing temperature. So, the objective is to be able to evaluate *a priori*, by numerical simulation, the performances of electromagnetic systems designed on the basis of particular magnetic materials, especially SMMs.

5.1 Contributions of this work

The EB hysteresis model has been chosen to describe the behaviour of the magnetic material under investigation, because it presents several advantages, together with mathematical and physical sophistication. Unlike the classical Preisach model and the original JA model, the EB model is intrinsically vectorial and energy-consistent, namely its foundation is based on thermodynamic principles. A parameters identification strategy allows to obtain the material parameters starting from standard magnetic measurements.

In Chapter 2, a specific protocol has been carried out to measure magnetic properties in static and dynamic conditions. At the same time, some static measurements were made under thermal stress. Thanks to these measurements, input data needed for the EB model parameters identification method could have been extracted.

In Chapter 3, the identification protocol is applied to the input data mentioned above. The simulated hysteresis loops are systematically compared to measured ones. Complex signals (with harmonics), which are not part of input data, have also been examined, in order to test the robustness of the identified parameters and the hypothesis of static hysteresis. After checking that simulated results were in good agreement with the measured ones, the same identification protocol has been applied to measurements at different temperatures in order to test its adaptability.

Because of the energy-consistency of the EB model, the identified material parameters are meant to be characteristic of the material, regardless of any particular experimental condition. Indeed, although the identification protocol is performed under specific conditions, e.g. sinusoidal in time with unidirectional field, the obtained parameters can be used in 2D models and in presence of distorted signals and higher harmonics. This has been confirmed through comparison with temperature-dependent measurements

under arbitrary loads at quasi-static excitations. Hence, the identification strategy is robust and stable, as the parameters identified by simple excitation waveforms can be used to accurately simulate hysteresis loops subject to complex magnetisation waveforms for different temperatures.

After identification, some first tendencies of the EB model parameters evolution with temperature could have been established. An accuracy analysis have been made regarding the number of cells for all temperatures. It has been shown that a number of 4 cells is enough to achieve a good accuracy for all temperatures.

Results show, that there is a strong correlation between the temperature and magnetic properties of 3C90 Mn-Zn ferrite material. This link cannot be neglected in technical applications. In the design of power electronic devices containing passive components made of Mn-Zn ferrite cores, it is very important issue to take into account the operating temperature range of the device and to assess whether such components will work adequately in such thermal conditions. Furthermore, methods able to predict the behaviour of materials as a function of temperature are valuable tools for engineers.

For this reason, an extension to the existing EB model has then been proposed, so as to take into account the effect of temperature with only a few measurements, based on a 2D interpolation. Furthermore, a first step concerning a scaling law of the model parameters (ω_k, κ^k) with the temperature has been suggested and partially validated. This first step will be useful in the future to predict hysteresis loops for complex signals and for any temperature falling in the range of available measurements.

In Chapter 4, the EB model is applied as a constitutive law of the E-cores in the FE simulation of a transformer for different excitation cases. Alternating, distorted and rotating fields have been studied and compared to measured data. FE simulations have been validated by means of experimental data of a self-made test-transformer application, with satisfactory agreement for global quantities considering the adopted assumptions and the actual nature of the EB model. In fact, FE simulations have been performed with the same parameters derived from the identification protocol, applied to measurement on a ring core. Indeed, we are allocating the same features of the ring core on the E geometry. Finally, the complexity of this case requires to adopt a higher number of cells to simulate the material response.

5.2 Perspectives

A certain number of perspectives that are, at the moment, more or less advanced, have also been investigated in this thesis. The following sections will present those and can be considered as a solid base for future work.

Hereafter, Section 5.2.1 deals with an attempt to take into account dynamic effects in the EB model. Section 5.2.2 presents a comparison of two different identification protocols concerning material parameters. Then, Section 5.2.3 investigates the possibility of a link between the materials parameters and the micro-structural features of such materials.

5.2.1 Dynamic modelling

In the aim of precise modelling of magnetic components, a complete model of the material composing the magnetic core is essential. In fact, in ferromagnetic materials, phenomena consist of both rate-dependent and rate-independent components. The rate-dependent effect includes classical eddy currents and excess currents, whereas the rate-independent part represents the static hysteresis effect. This material model should describe its

hysteresis behaviour under static operating conditions (static model) in addition to its dynamic behaviour due to eddy currents and wall motion effects (dynamic model). For this reason, the dynamical modelling of SMMs has been addressed in this work, with the possibility to extend the static version of the EB model to dynamics through its parameters.

Indeed, originally, the standard EB model is a rate-independent (static) hysteresis model. Authors of [72] introduced a viscosity term which could be added in the model so as to obtain a dynamical vector model. This additional contribution would correspond to the dynamic loss, which may potentially become the major contribution to the magnetic losses at high frequencies.

A first step consists in applying the same protocol used for the temperature dependence. In order to analyse the ability to reproduce dynamic curves, hysteresis loops in the frequency range $10 - 1000$ kHz are measured. As shown in Section 2.3, frequency-dependent measurements have been performed on the ferrite material under study. Figure 5.1 shows measurements at maximal flux density $b = 20$ mT for various frequencies.

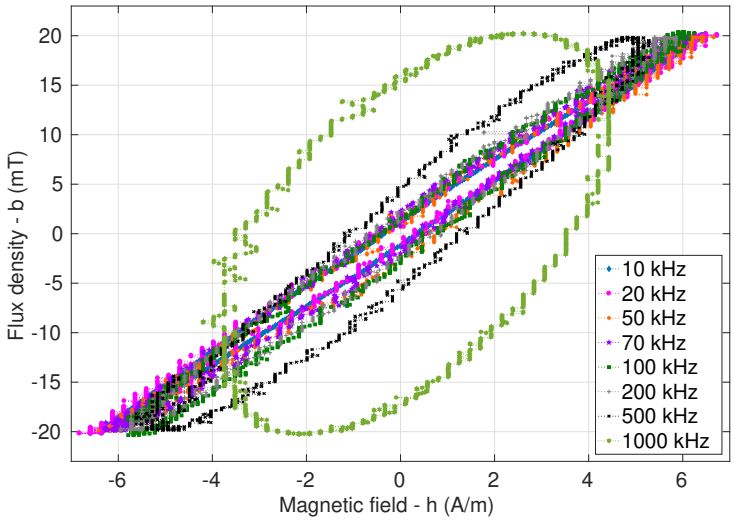

Figure 5.1: Measurements in the frequency range.

Sets of parameters $(\omega_k, \kappa^k)_{k=1,\dots,N}$ have to be identified in order to construct the EB model. Hence, the AUX method, previously applied to static measurements (cf. Section 3.2), has been applied to frequency-dependent measurements. The coercive field characteristic $h_c(h_p)$ is obtained from the measurement of a series of symmetric hysteresis loops of increasing amplitude for each frequency, as seen in Figure 5.2.

The $h_c(h_p)$ characteristic increases as frequency raises, highlighting the influence of frequency on hysteresis curves. Unfortunately the measurement equipment did not allow measurements at certain values of induction/frequency sets. It can be noted that saturation is not attained for measurements starting from $f = 200$ kHz, due to these limitations.

For this reason, Figures 5.3 shows the procedure steps, focusing only on measurements reaching saturation, namely the constructed auxiliary function $F(h)$ and the corresponding pinning field cumulative distribution function $\partial_h F(h)$ for frequencies from 10 kHz up to 100 kHz. In Figure 5.4 the continuous pinning field distributions are plotted for five different frequencies, $10 - 20 - 50 - 70 - 100$ kHz.

It can be noticed that the area subtended from distributions increases with increasing frequency. This appears coherent with the fact that pinning field κ is linked to the coercive

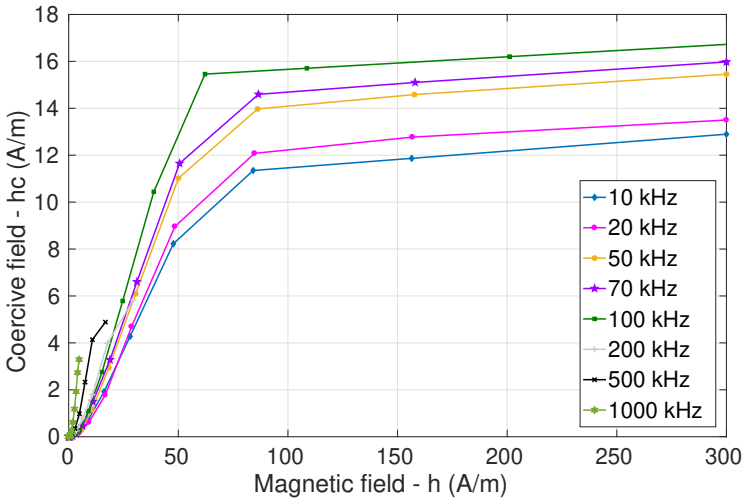

Figure 5.2: Coercive field $h_c(h_p)$ of symmetrical hysteresis loops measured for different frequencies.

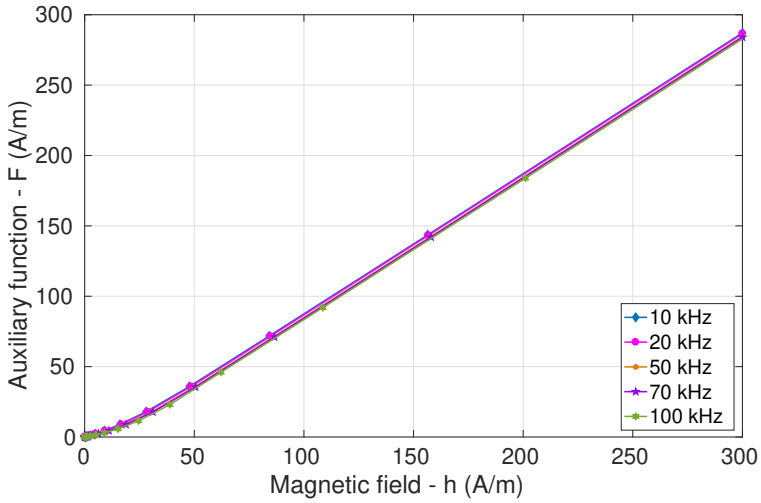

(a)

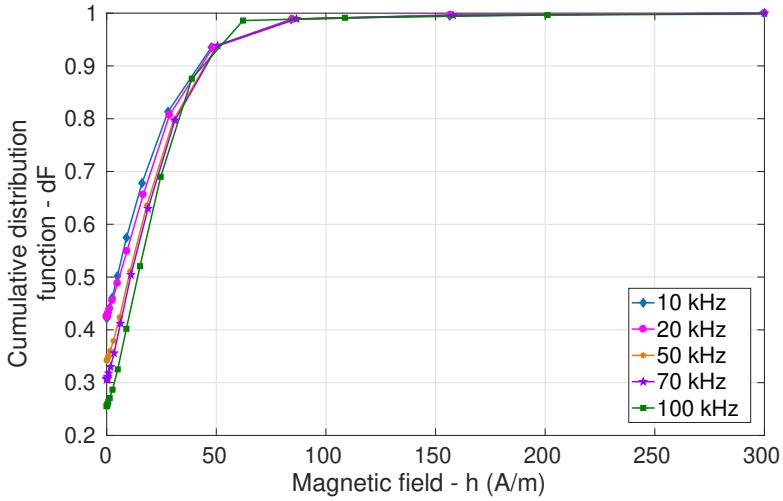

(b)

Figure 5.3: (a) Function $F(h)$ and (b) corresponding pinning field cumulative distribution function $\partial_h F(\kappa)$.

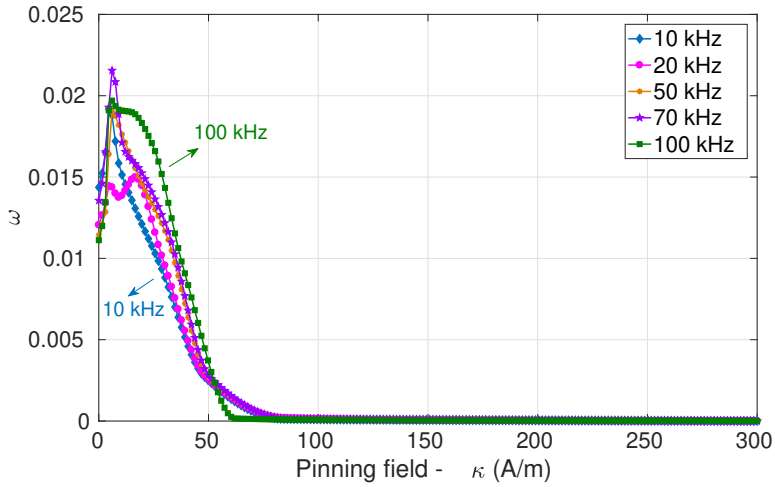

Figure 5.4: Identified pinning field probability density $\omega(\kappa)$ for five different frequencies.

field h_c, which raises as frequency increases. Whereas, the peak level does not seem to be clearly linked to the increment of frequency, e.g. the peak corresponding to 10 kHz is higher than the one at 20 kHz, where two peaks are present, or the peak level of 70 kHz is higher than the one at 100 kHz.

The continuous distributions $\omega(\kappa)$ are then discretised, from $N = 2$ to $N = 200$ cells, for the purposes of the numerical implementation. For verification, we simulated hysteresis curves to the diverse frequencies and the simulation results have been compared with measurement data of the material.

Hence, the NRMSE between measurements and simulations are plotted for $f = 10$ kHz (cf. Figure 5.5), 50 kHz (cf. Figure 5.6) and 100 kHz (cf. Figure 5.7).

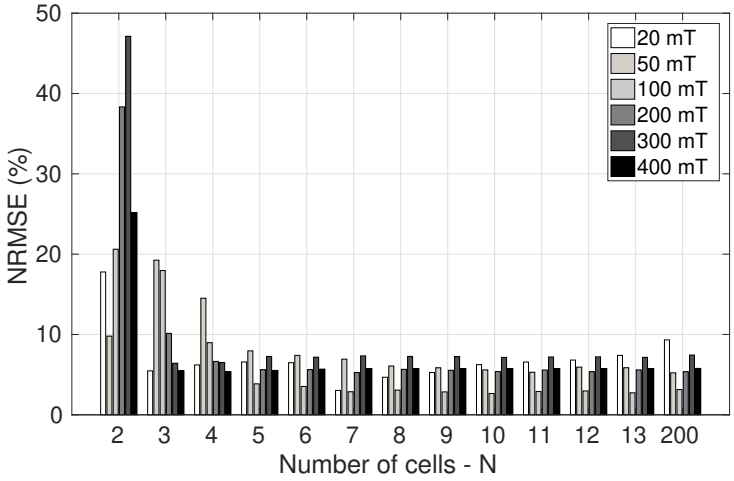

Figure 5.5: NRMSE for different flux density amplitudes at $f = 10$ kHz by varying the number of cells N.

At $f = 10$ kHz, increasing the number of cells to $N = 5$ significantly reduces the errors for all amplitude levels. The same tendency can be observed in the other cases, even if errors are more significant for $f = 100$ kHz (cf. Figure 5.8). Nevertheless, results are satisfactory and constitute a promising step, confirming that this technique is still valid in this frequency range.

Another perspective could take into account a dynamic hysteresis model based on Bertotti's work [121] and using the EB model for representation of the static hysteresis.

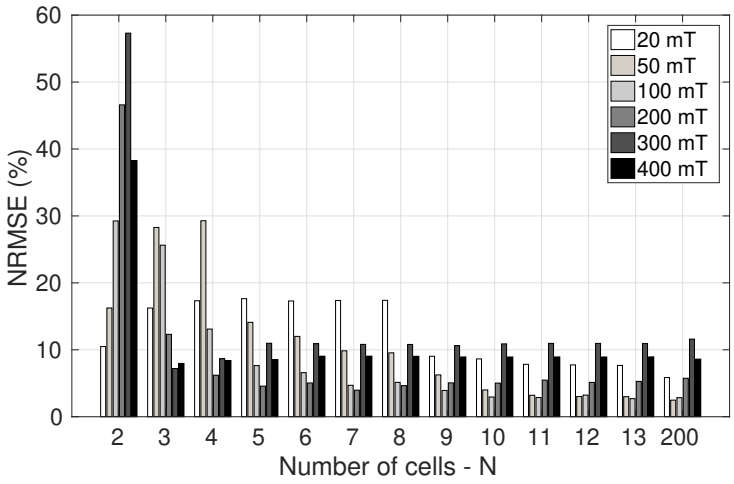

Figure 5.6: NRMSE for different flux density amplitudes at $f = 50$ kHz by varying the number of cells N.

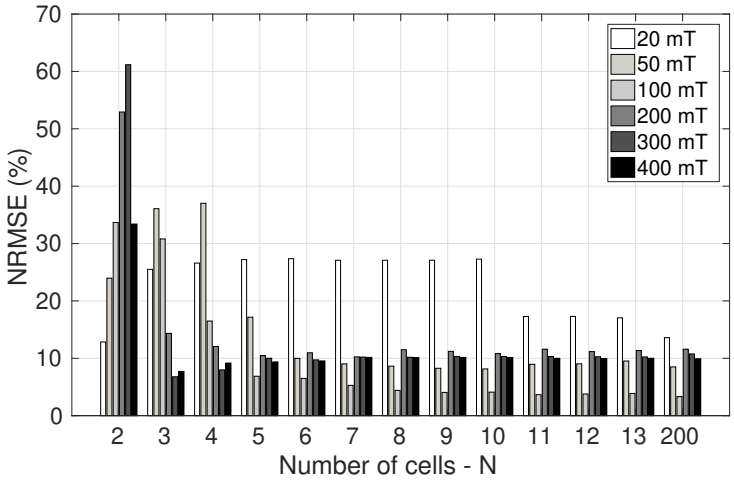

Figure 5.7: NRMSE for different flux density amplitudes at $f = 100$ kHz by varying the number of cells N.

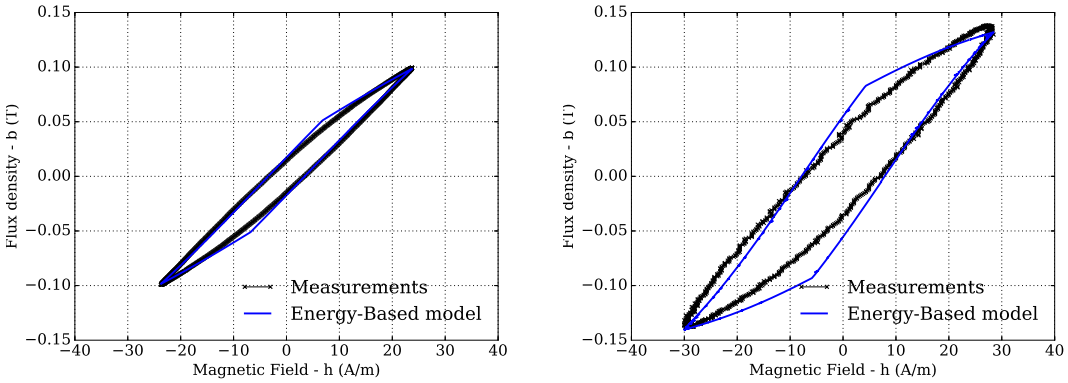

(a) $f = 10$ kHz. (b) $f = 100$ kHz

Figure 5.8: Measured and simulated loops with 5 cells.

Indeed, Bertotti shows an elegant way to add static hysteresis, classical eddy currents and excess eddy currents together to obtain a dynamic hysteresis model [121]. Besides, in his work, he proposed analytical expressions for the rate-dependent part. These expressions have been associated with the Preisach [122], JA [123] and Bergqvist [124] models for calculating the static contribution.

5.2.2 Identification protocols

From this study, it might be remarked that the identification strategy gives satisfactory results for the ferrite material under test, as it has been proven in previous sections. However, it possesses some limitations. Actually, it cannot always be applicable to all kind of unidirectional measurements, for example, it is not possible to obtain a complete $h_c(h_p)$ curve in measurements not attaining the saturation state, so undermining the following steps of the procedure. Future works will be dedicated to the improvement of the identification protocol on the basis of this additional aspect, in order to obtain a more refined EB hysteresis model. Ultimately, an alternative identification protocol based on optimisation, hereafter called OPT, has been detailed in [74] and recently compared to the AUX method in [125].
The OPT method relies on the identification of (ω_k, κ^k) sets such as:

$$\begin{cases} (\omega_k, \kappa^k) = \arg\min\limits_{Y,X} ||b_m(h) - b_s(h)||_2^2 \\ \omega_k \geq 0 \quad ; \quad \sum_{k=1}^{N} \omega_k = 1 \\ \kappa^1 = 0 \quad ; \quad \kappa^k \leq \kappa^{k+1} \end{cases} \tag{5.1}$$

where $\mathrm{K} = (\kappa^1 \dots \kappa^N)$, $Y = (\omega_1 \dots \omega_N)$ and $b_m(h)$ and $b_s(h)$ are measured (or reference) and simulated $b(h)$ responses respectively. It is proposed to solve (5.2) instead for reasons detailed after.

$$\begin{cases} \Delta\kappa^k = \arg\min\limits_{\Delta \mathrm{K}} ||b_m(h) - b_s(h)||_2^2 \\ \omega_k \equiv 1/N \\ \Delta\kappa^k \geq 0 \end{cases} \tag{5.2}$$

Where $\Delta\mathrm{K} = (\Delta\kappa^1 \dots \Delta\kappa^{N-1})$ and $\Delta\kappa^k = \kappa^{k+1} - \kappa^k$. With the formulation (5.2) the problem is "only" a non-negative least square problem. Moreover, (5.2) has a reduced number of unknowns than (5.1) ($N-1$ compared to $2N-1$). The major improvement is that ω_k is imposed and is no longer a degree of freedom. It is then much easier to solve and avoid of local minima. The price to pay is that a higher number of cells is in principle necessary to obtain a comparable accuracy. That's why, the identification protocol is actually made in two steps. The first step is to solve (5.2) with a "high" number of cells and then reduce it thanks to a packing cells algorithm. The basic concept is to search the smallest non-zero term, and to aggregate it with its bigger neighbour. Namely, assume that $\Delta\kappa^k$ is the smallest non-zero term of $\Delta\mathrm{K}$, and that $\Delta\kappa^{k+1} > \Delta\kappa^{k-1}$; then the algorithm will execute:

$$\begin{aligned} \Delta\kappa^{k+1} &\leftarrow \Delta\kappa^{k+1} + \Delta\kappa^k \\ \Delta\kappa^k &\leftarrow 0 \end{aligned}$$

This last operation is repeated until two non-zero, not too small, adjacent terms can be found in the vector $\Delta\mathrm{K}$. Note that, when aggregating p cells together, from a population of N, the weight of the aggregated cell is p/N.

In order to avoid any measurement problem, the methods have been tested firstly with a virtual material. The latter has a Langevin function $J_{an}(h)$ such as (2.19), with $J_a =$

1.2566 T and $h_a = 10$ A/m. The ω_k and κ^k values for the virtual material are reported in Table 5.1 as reference. With these parameters, the needed data for identification with the model (loops of various amplitudes) have been generated. The vectors of h and b of each loop are directly used for the OPT method, whereas, for the AUX method, it is necessary to extract both h_p and h_c from these loops to build the $h_c(h_p)$ curve. Finally, identified ω_k and κ^k of both methods are reported in Table 5.1.

Table 5.1: Reference and identified values of ω_k and κ^k sets for the virtual material.

Reference	ω_k	0.1	0.4	0.3	0.2
	κ^k	0	1	5	15
OPT	ω_k	0.1667	0.333	0.3333	0.1667
	κ^k	0	0.9865	4.8809	11.45
AUX	ω_k	0.22	0.521	0.226	0.04
	κ^k	0	3.17	13.83	63.32

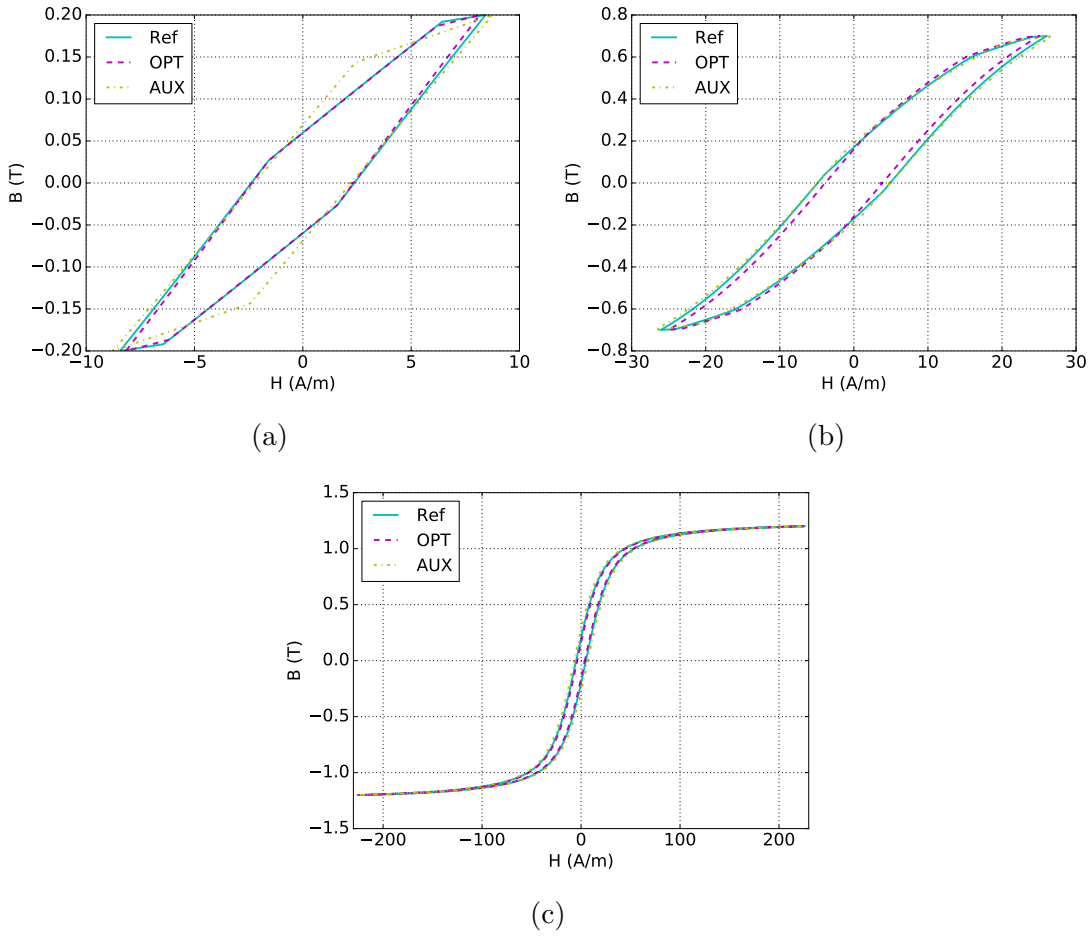

Figure 5.9: Loops at different amplitudes for the virtual material. Reference loop (solid line), loops simulated with parameters identified by OPT (dashed line) and loops simulated with parameters identified by AUX (dashdot line).

Figure 5.9 shows the reference loops and those calculated with parameters from both methods. It can be seen that computed loops with parameters given by OPT and AUX are in a good agreement with the reference ones (exception for the very low amplitude loops) despite the fact that both methods failed to retrieve exactly the parameters sets.

Indeed, the OPT method, retrieved quite well the κ^k values (exception for the last value), but the weights are relatively different. The AUX method failed to retrieve both κ^k and ω_k. Thus a better accuracy is achieved for loops simulated with parameters identified by OPT than with AUX, in the whole range of amplitudes, especially for low amplitude loops (see Figure 5.10).

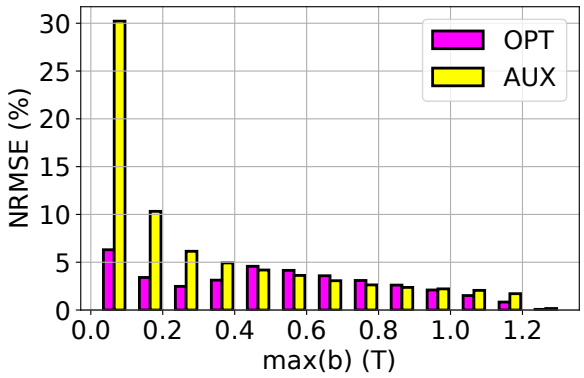

Figure 5.10: Normalized root mean square error versus flux density amplitudes of each loop for both models (virtual material).

To confirm these results, both methods have been tested on a real material, the 3C90 ferrite material (ring core). The same protocol, as for the virtual material, is employed. In order to achieve good accuracy in the models predictions, simulations have been performed with 5 cells. The anhysteretic function of this material is also modeled thanks to (2.19), with $J_a = 0.4319$ T and $h_a = 17.3971$ A/m. Identified values of ω_k and κ^k are reported in Table 5.2.

Table 5.2: Identified values of ω_k and κ^k sets for the 3C90 ferrite.

OPT	ω_k	0.1818	0.2727	0.1818	0.2727	0.0909
	κ^k	0	0.2	6.95	25.99	42.26
AUX	ω_k	0.42	0.278	0.197	0.098	0.007
	κ^k	0	7.43	23	43.86	126

Once again, the (ω_k, κ^k) sets given by both methods are relatively different in appearance. With a deeper analysis, some values of κ^k given by each identification method have similar values, but they are shifted of one cell (three last κ^k values given by OPT are quite the same as three intermediate values of κ^k values given by AUX). Measured and simulated loops are plotted in Figure 5.11 for different amplitudes. Simulated loops with parameters given by each method are very close to the measured ones, except again for the very low amplitudes loops. This is confirmed by the Figure 5.12, where one can see that the NRMSE is below 6% for all loops except the lowest amplitude one.

From the analyse of the continuous curves of the derivative dF of the auxiliary function F for the AUX method and the corresponding continuous curve OPT which is given by doing the cumulative sum of ΔK^k and ω_k before the packing phase. We added on the same graph the corresponding step function curves of the cumulative sum of ω_k versus κ^k of Table 5.1 including the reference case for comparison. All these curves are plotted for the virtual material in Figure 5.13. The same curves (except reference curve that doesn't exist in this case) are plotted for the 3C90 ferrite material in Figure 5.14.

By first looking closer to Figure 5.13, one can see that the both continuous curves given by each method intercepts more or less the reference step function approximately

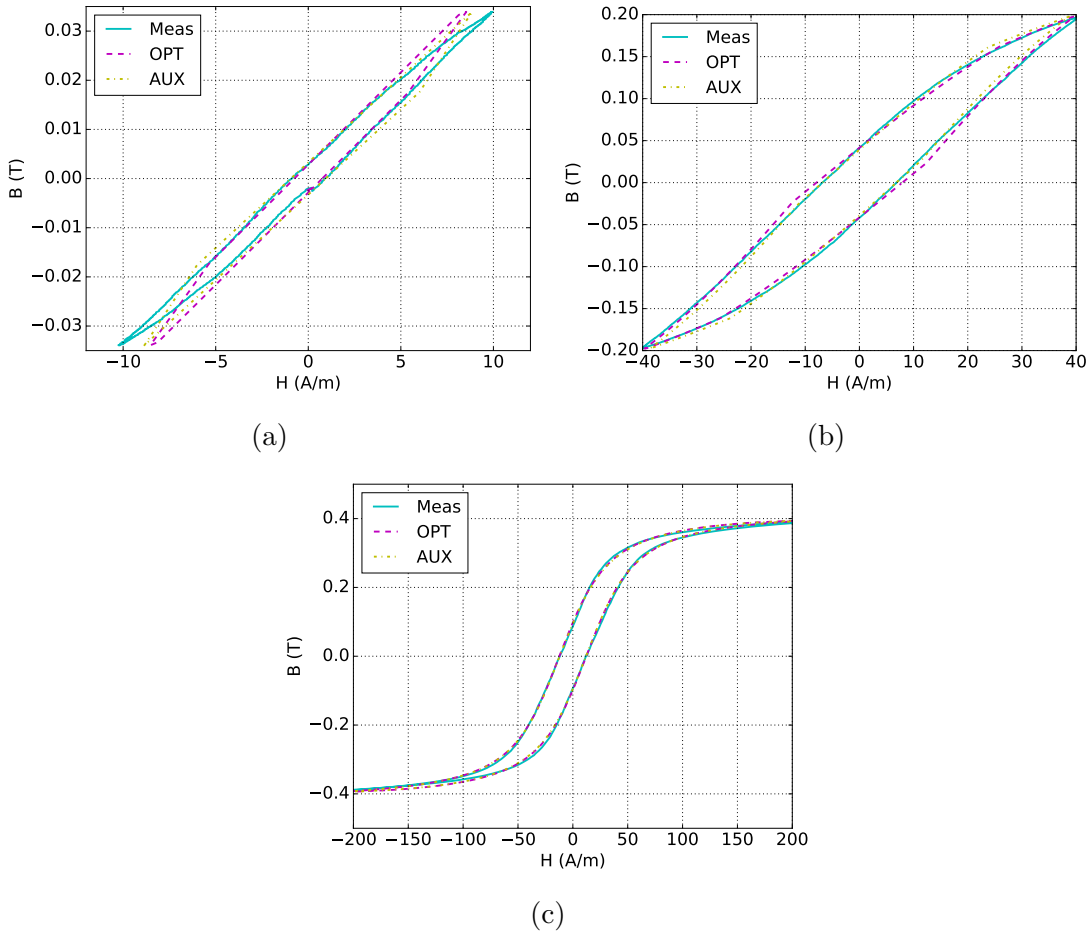

Figure 5.11: Loops at different amplitudes for the 3C90 ferrite material. Measured loop (solid line), loops simulated with parameters identified by OPT (dashed line) and loops simulated with parameters identified by AUX (dashdot line).

in the middle of each stairs except at the two extreme positions (low and high values of pining field). This explains why the global accuracy is correct for both methods. Now, at low field values the continuous and discrete curves of OPT are closer to the reference case than the AUX curves. This explains why a better accuracy is achieved with OPT than AUX in these regions. A possible reason would be that the auxiliary function is built thanks to the extrapolation of the $h_c(h_p)$ curve at low fields (see (7.9)). The extrapolation may be wrong in this particular case because the virtual material is not a real one and may not follow this law. Another possible reason would be that the numerical double derivation of F may induce a loss of information specifically in this sensitive region. For the high field values, differences also occur, but maybe for a different reason. Indeed the AUX continuous curve of dF is smoothly increasing until saturation $dF = 1$ whereas OPT continuous dF curve saturates sooner. It means that, at the end, AUX gives artificially a greater value to the last κ^k value due to this smooth saturation (see Table 5.1), whereas the OPT method found that it is unnecessary to increase the value of κ after a certain value. But this last case is less problematic, because these sets are only activated for very high fields (saturation approach) where anhysteretic approximation is responsible for higher inaccuracies. As the material is a virtual one and its saturation is perfectly represented, the error is very small for the full saturation amplitude ($b > 1.2$ T). One final observation is that two steps of the reference case are very well retrieved by "OPT discrete" even if the exact (ω_k,κ^k) are not the same. Therefore, this could define an affordable goal that should achieve any identification method in order to reach a good accuracy.

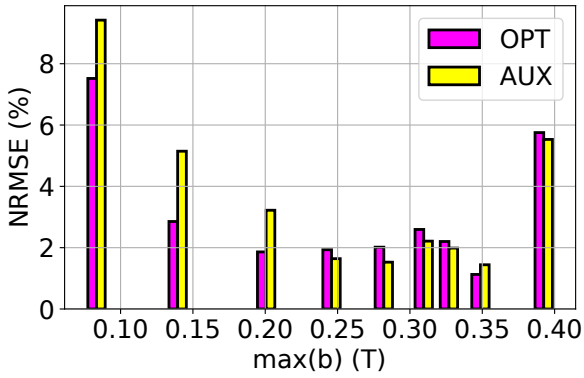

Figure 5.12: Normalized root mean square error versus flux density amplitudes of each loop for both models (3C90 ferrite material).

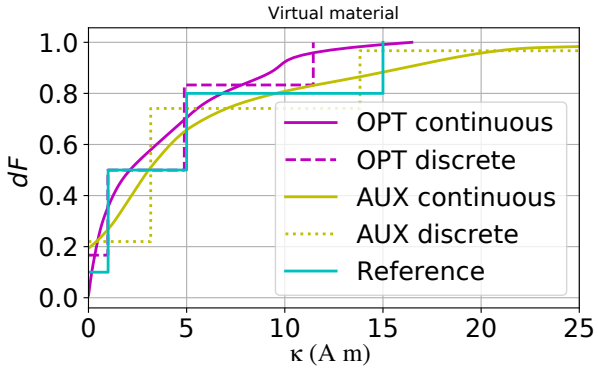

Figure 5.13: First derivative dF or cumulative weights versus κ for the virtual material.

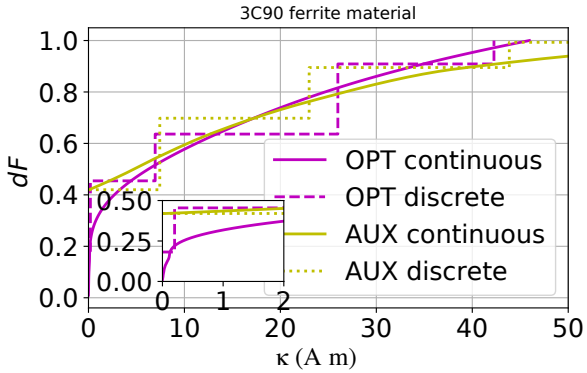

Figure 5.14: First derivative dF or cumulative weights versus κ of the 3C90 ferrite material.

Concerning the 3C90 ferrite material, as no reference case is available except measurements, it can be seen that the same observations can be made for this material. Last value of κ^k value given by AUX is particularly high but its weight is small, so this cell does not influence the accuracy. In this case, it is probably the Langevin function that influence the most the accuracy. Some steps of the discrete curves of OPT and AUX are very similar but as said before, the stairs are shifted of one cell. The first stair has been missed by AUX (see the inset of Figure 5.14). This is why the method OPT also achieves a better accuracy at very low fields in this case (see Figure 5.12).

Finally, it has been found that both methods can give parameters that allows to compute loops with a good accuracy in a large range. The method OPT gave better results than AUX in the very low field range. This has been explained by the extrapolation of the $h_c(h_p)$ curve at low fields (input data) and by the numerical double derivation [109] that can induce some errors. This study also showed that an affordable goal for any identification method to achieve a good accuracy would be to have a rather good continuous $dF(\kappa)$ trajectory and to cut it into (ω_k, κ^k) sets correctly.

Perspectives of this work would be to compare the methods for other materials and also when changing the temperature of one material and find an evolution of the parameters with temperature [117]. Improvements can also be made on both methods by changing the specific input data, for example using $b(h)$ virgin curve for [109] or by changing the optimization method for [74].

5.2.3 Link with microstructure

Prediction of magnetic domain structure is an essential part in the complete understanding of SMMs behaviour. The derivation of magnetic domain structure from structural information about the system in question is a complex issue. In literature, micromagnetics [126] is the main theoretical approach used to define the behaviour of magnetic materials at scale where atomic granularity is not resolved and the material is referred as a continuous medium, for which the magnetic state is described by the magnetisation vector as a function of position inside the body [27]. However, the difficulty of developing dedicated micromagnetic tools for the description of bulk magnetic materials is reflected by various hysteresis models proposed for the handling of bulk properties or in the power loss modelling, where losses are calculated by means of several assumptions about magnetisation processes. Nevertheless, micromagnetics suggest a deep connection existing between magnetisation processes and microstructural aspects, such as dislocations, grain size, texture, presence of secondary phases, anisotropy, etc...

In this context, results related to the identification protocol of parameters for the EB hysteresis model have proven to be correlated with material microstructure (e.g. grain size, uniformity, defects, ...) [109]. The identification strategy has been applied to five non-grain-oriented electrical steel grades, M235-35A (3.2wt% Si), M250-35A (3.2wt% Si), M330-35A (3.2wt% Si), M330-50A (3.2wt% Si) and M400-50A (3.2wt% Si). Experimental data of such materials, represented in Figure 5.15, are courtesy of authors of [109]. In particular, these materials have an average grain size d of about 100 μm, 109 μm, 87.5 μm, 122 μm and 70 μm, respectively, as reported in [109]. All these cases present a peak value of probability density for a specific pinning field, before getting to zero for higher pinning field values. The different behaviour of such curves could originate from the inner material nature.

The resulting trends for the five non-oriented steel grades point out the dependency of the coercive force on grain size, dislocation density and sheet thickness. For example, M235-35A and M250-35A have the same alloy but different grain sizes, resulting in a shift

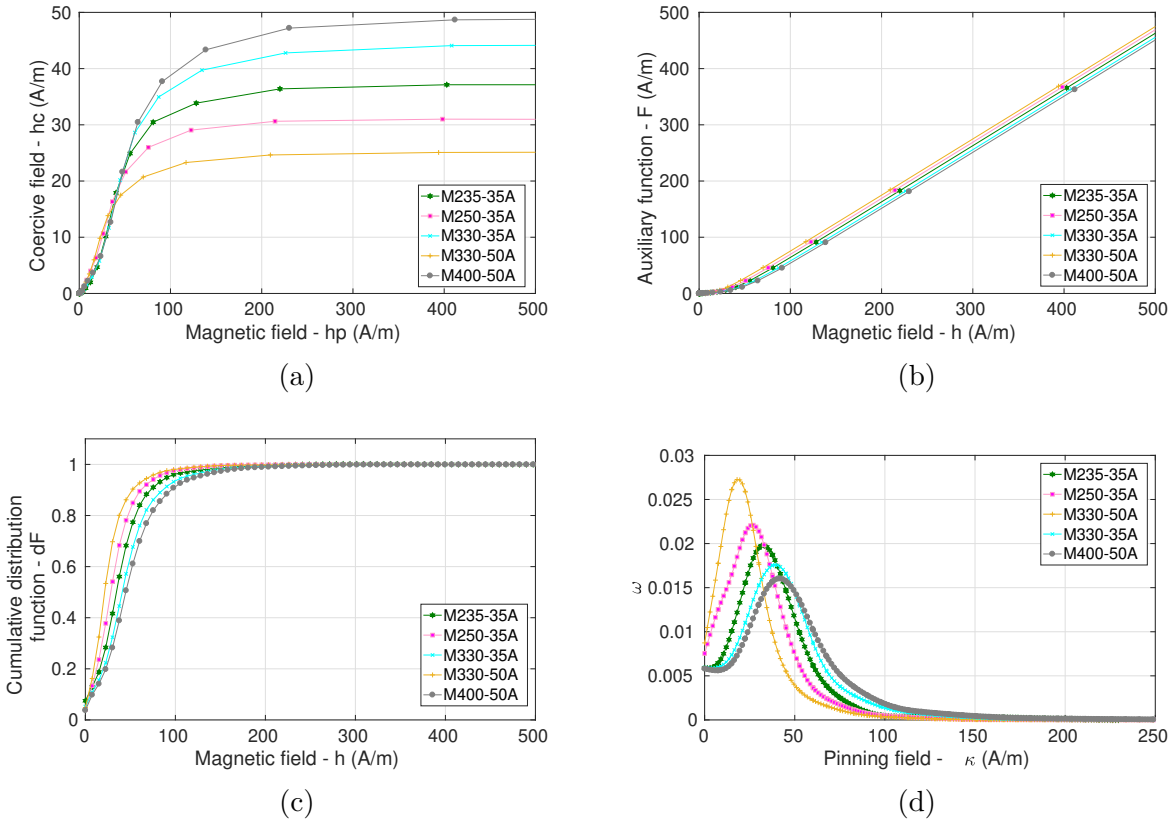

Figure 5.15: Procedure for the identification of the continuous distribution $\omega(\kappa)$ for five different steel grades.

of the peak value of the distribution towards higher value of pinning field for the material with a smaller grain size (M235-35A in this case). If one compares the M330-35A with M330-50A, having the same alloy but different thickness and grain size, one can state that a decrease in thickness, somehow correlating with dislocation densities, determines additional effects to the coercive field. In fact, the material properties can be determined by the grain size, the dislocation density in the material structure and defects at the microscopical level. A modification in the average grain size influences the domain wall movement and, as a result, the coercivity. In principle, the wide spectrum of grain size in the microstructure is correlated with the extension of the pinning field distribution.

To complete the previous study [109], the identification method has been applied to a FeSi 3%wt 0.5 mm thick non oriented (NO) material, commonly used in the manufacture of rotating machines. The material has been characterised on an Epstein yoke cutting strips along four different directions with respect to the rolling direction, as detailed in the TEAM 32 problem [119]. Hereafter, we will consider the comparison between the 0 degree cut strip, rolling direction (RD) and the 90 degree cut strip, transverse direction (TD).

It can be observed that if the angle between the magnetic field $\mathbf{h}$ and the rolling direction increases, the anisotropy effect becomes significative: the maximal value of probability density moves towards higher values of pinning field κ, resulting in a smoother curve $\omega(\kappa)$, as observed for TD. The same tendency has been also observed in [109].

To go further, this identification technique has been applied to three materials of different nature, to find out if previous results can be generalized [127]. The materials under test are soft ferrite Mn-Zn 3C90, FeSi grain-oriented steel (GO) and Phyterm260, an iron-nickel-copper-chromium soft magnetic alloy. Results of identification are plotted

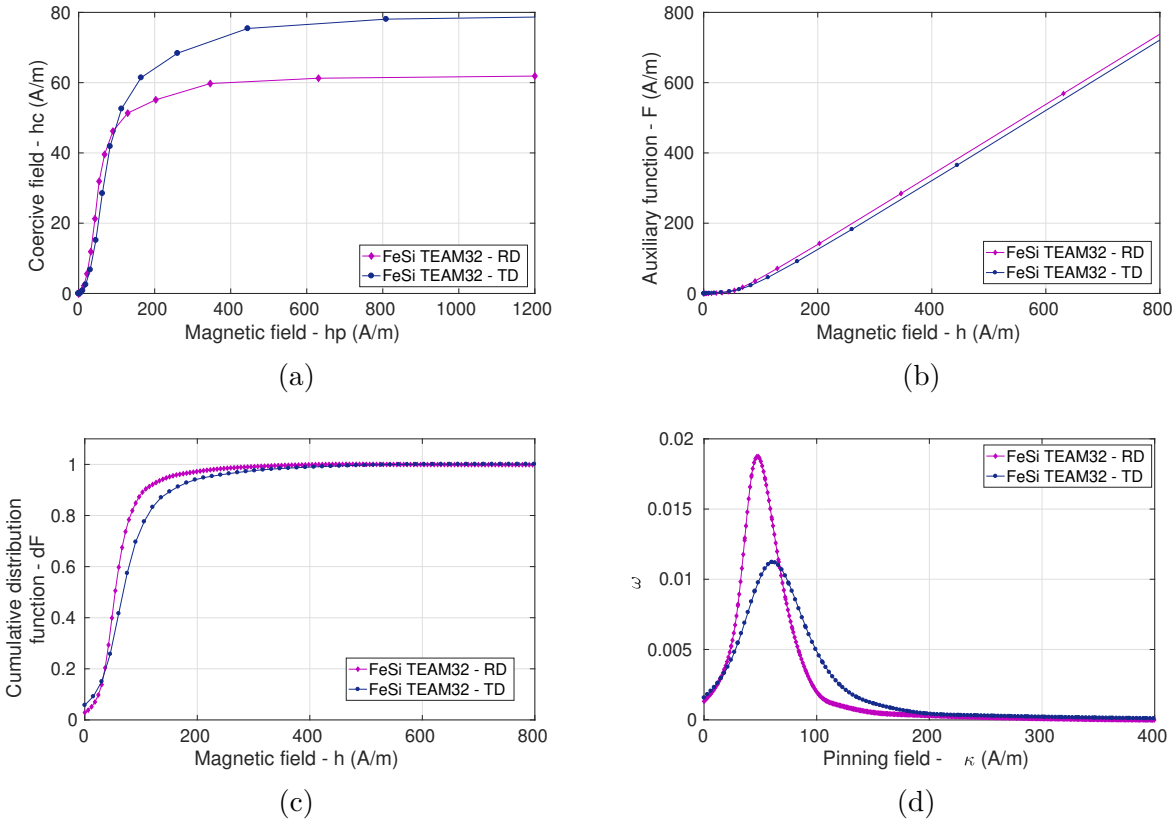

Figure 5.16: Procedure for the identification of the continuous distribution $\omega(\kappa)$ for FeSi NO material.

in Figure 5.17.

In order to determine the grain size of such materials, samples have been analysed with a Scanning Electron Microscopy (SEM) in the laboratory. Phyterm260 and FeSi GO samples have been embedded in a resin and polished, then by means of grinding, marks and levels are removed and the sample surface is cleaned. The artifacts of grinding are eliminated with very little material removal through polishing. Fixed abrasives composed of abrasive particles bonded to the paper or plates are used in the grinding process for fast material removal. As concerns ferrite material, a fracture surface of the sample has been analysed with SEM. Figures 5.18-5.19 show the microstructure of the investigated materials. The determination of the grain size has been performed by means of the line intercept method.

Figure 5.18 shows the SEM images for ferrite 3C90, where grains and grain-boundaries are clearly visible. The coercive force is about $h_c \approx 12$ A/m, the grain structure appears rather inhomogeneous and the measured average diameter grain size is approximately $d \approx 10.5$ μm, coherently with literature [128]- [129]- [130]. This kind of material possesses a relatively low peak in the continuous distribution, characterized by a flat shape, as it can be observed in Figure 5.17d.

Pinning field probability density curves $\omega(\kappa)$ may provide information about the material microstructure, particularly on grain size. A higher grain size involves a weaker coercive force, which results in a shift of the peak of $\omega(\kappa)$ curves towards lower values of pinning field and viceversa.

The other materials under test need further investigation for a clear measure of grain size, in order to verify the hypothesis that the probability density of pinning field $\omega(\kappa)$ represents a sort of *identity document* of the material. In Figure 5.17d, Phyterm260 and

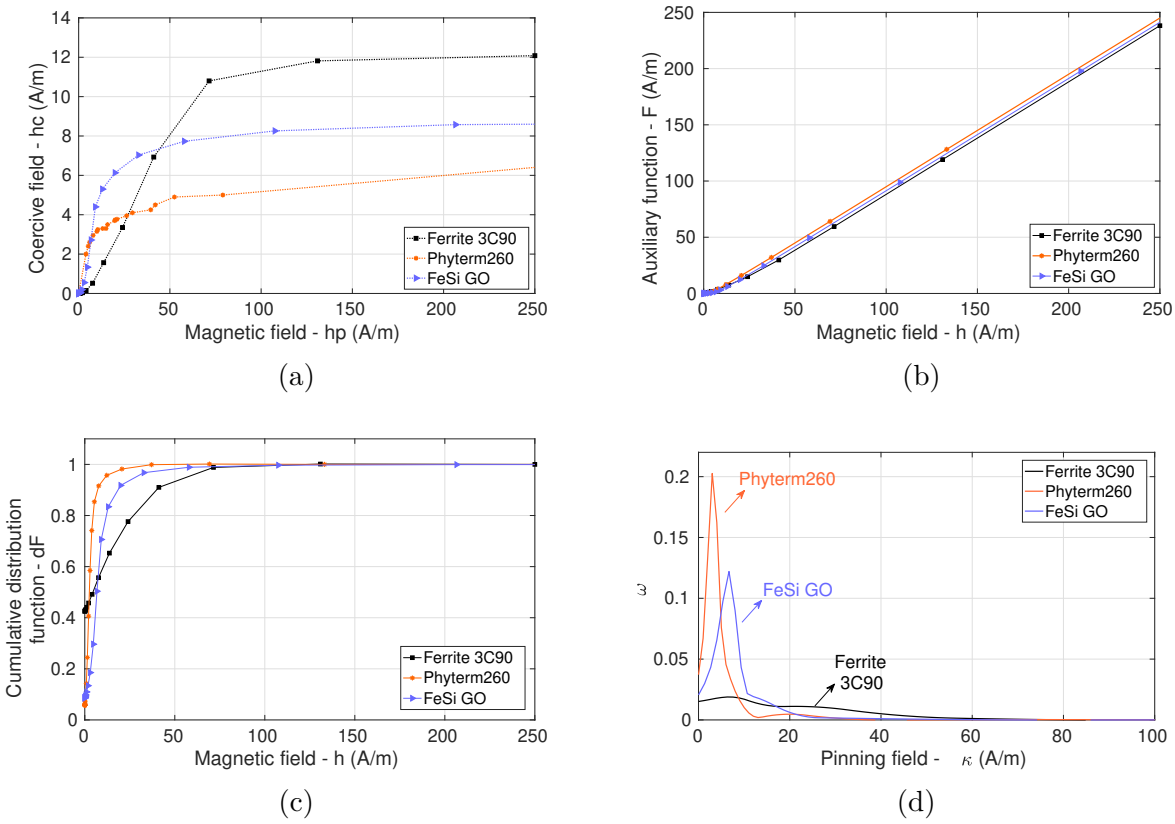

Figure 5.17: Procedure for the identification of the continuous distribution $\omega(\kappa)$ for three different materials: ferrite 3C90, FeSi GO and Phyterm260.

FeSi GO materials have a high and narrowed peak value and coercive fields of about $h_c \approx 6$ A/m and $h_c \approx 8$ A/m, respectively. So, it seems consistent that their peak values are in correspondence of low pinning fields in respect of ferrite curve tendency. Phyterm260 material has been subject to a heat treatment ($T = 300$°C/hour, decarburazing anneal in wet H_2 atmosphere at 1170°C/4hours). The average of grain size of Fe-Ni-Cr alloys is about $d \approx 380\ \mu$m for specimen underwent solution treatment at $T = 1200$°C/3hours [131]. Thus, it can be assumed that the grain size of such material is about of the same order of magnitude.

The basic concept is that the pinning field distribution is linked to irreversible nature (coercive field) of magnetic materials and reflects its internal structure. These macroscopic continuous curves could constitute a new macroscopic tool to observe some of the microscopical characteristics of soft magnetic materials. With more work it may provide information about microstructural features without the use of heavy hardware (SEM).

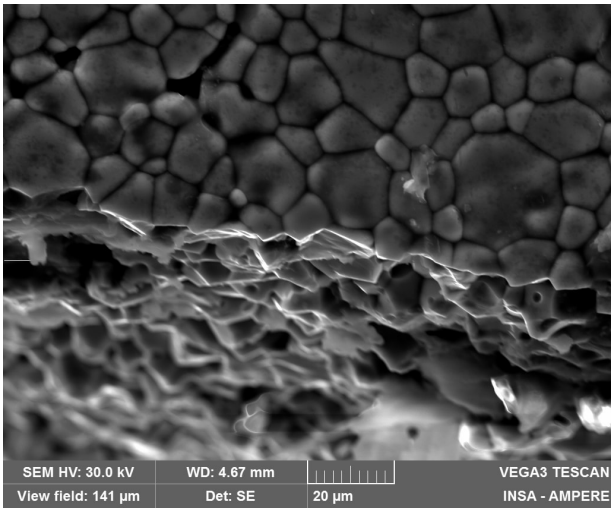

(a)

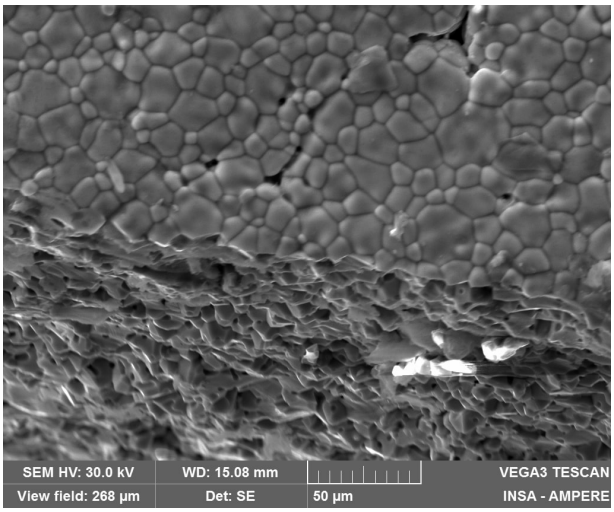

(b)

Figure 5.18: SEM images for ferrite 3C90.

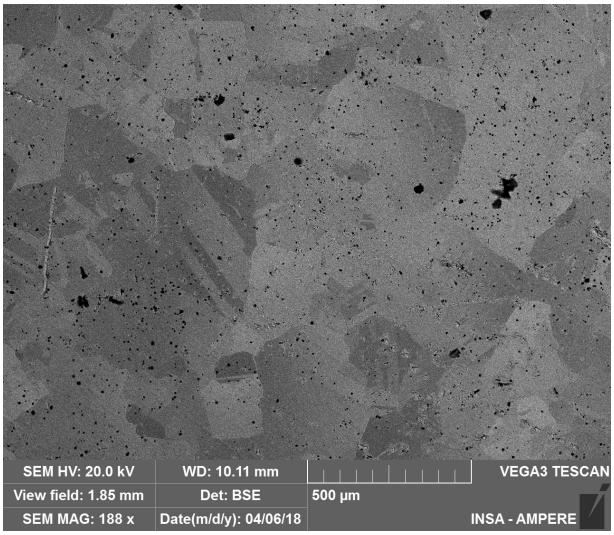

(a)

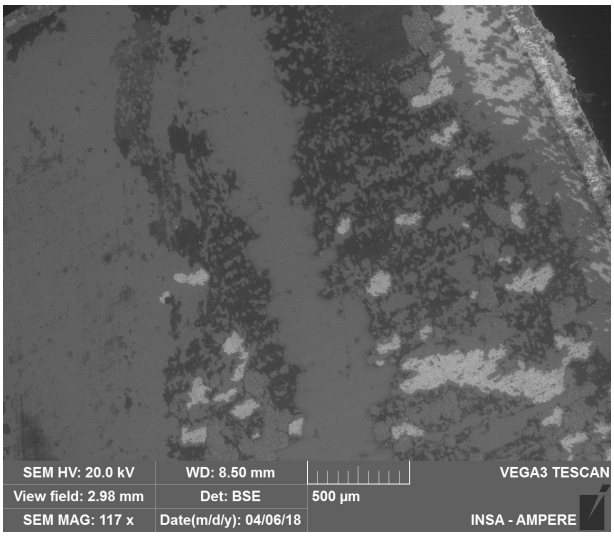

(b)

Figure 5.19: SEM images for (a) Phyterm260 and (b) Fe-Si GO materials.

Part II

Version française

Ce résumé étendu en français se limite à une présentation détaillée des contributions originales de la thèse, replacées dans le contexte de la recherche.

Contexte

Les matériaux magnétiques jouent un rôle central dans le développement actuel et future des applications liées à la conversion d'énergie électrique. On peut trouver des composants magnétiques dans une infinité d'applications : transports, système numériques, dispositifs biomédicaux, domotique, et encore beaucoup d'autres technologies de pointe.

Le développement de l'électronique de puissance est soumis à des contraintes liées à l'électromagnétismes. Dans ces applications on est en quête de puissances toujours plus élevée, avec des rendements plus élevées et un coût et un encombrement de plus ne plus faible. Cela passe par le développement de modèles de matériaux et composants magnétiques plus précis. En effet, avec les rapides progrès de l'électronique de puissance, la fréquence de fonctionnement s'étend désormais jusqu'au MHz. En particulier, les transformateurs sont considérés comme un élément-clef des circuits électroniques de puissance du future. Ils doivent avoir une grande fiabilité, et un moindre encombrement. D'après la loi de Faraday, la force électromotrice induite dans les bobinages est proportionnelle au flux magnétique et à la fréquence de travail. Ainsi, en élevant la fréquence de travail il est possible de baisser considérablement le flux magnétique – et donc le poids et la taille des transformateurs, en comparaison avec ceux qui travaillent en basse fréquence. Cette tendance vers des hautes fréquences et vers la miniaturisation des composants pousse le développement de matériaux magnétiques avec haute perméabilité et faibles pertes. Les matériaux magnétiques doux sont utilisés pour les noyaux des transformateurs et inductances ; ils jouent un rôle-clef dans la conception de systèmes électroniques de puissance à haut rendement. Ce groupe de matériaux comprends les ferrites doux, les alliages magnétiques spéciaux et les matériaux amorphes. A cause de la grande variété des applications, il est nécessaire de caractériser les matériaux magnétiques sur une grande plage de conditions de travail. Par exemple, à haute fréquence un certain nombre de facteurs, comme les pertes fer, l'effet de la température sur les propriétés magnétiques, l'effet de peau et de proximité dans le noyau magnétique et dans les bobinages, ainsi que le flux de fuite, deviennent non négligeables, et doivent nécessairement être pris en compte. Une partie de ces problématiques sont abordées tout le long des chapitres de cette thèse. Les paramètres les plus importants sont la température et la fréquence de travail, en relation avec l'influence qu'ils ont sur la taille et le rendement des systèmes électriques. La volonté des fabricants de pousser le développement de la connaissance scientifique dans ce domaine découle de l'impact qu'ont les matériaux sur les pertes, l'encombrement et la gestion de l'échauffement des dispositifs électroniques. Limiter ou diminuer cette influence sur la taille et le rendement repose sur la possibilité de repousser plus loin certains paramètres critiques des matériaux magnétiques, comme la température de travail maximale, le champ coercitif, l'effet des courants induits dans le matériau. De plus, les convertisseurs haute-fréquence utilisent rarement des courants strictement sinusoïdaux pour exciter les matériaux magnétiques. Très souvent la modulation de largeur d'impulsion (PWM) est utilisée, ce qui implique que les matériaux magnétiques doivent fonctionner sur une large plage de fréquences, et en régimes périodiques non sinusoïdaux. Ces facteurs devraient être pris en compte dès la conception

et la modélisation numérique de dispositifs électroniques. Dans ce contexte, l'estimation des pertes magnétiques (appelées aussi pertes fer) est un sujet difficile et de grande importance, en vu de la complexité du comportement des matériaux magnétiques, et en particulier de l'hystérésis. De plus, le riche contenu harmonique dans le flux magnétique, et les hauts niveaux d'induction dans les dispositifs électromagnétiques exacerbent le besoin d'outils de modélisation capables de prédire précisément les pertes. Actuellement, des modèles simplistes qui séparent les pertes fer en trois termes, sont utilisés dans la plupart des cas : soit dans la modélisation numérique, en phase post-processing à partir d'une répartition spatiale du champ magnétique, soit sur la base de courbes de perte établies à partir de tableaux de référence. Il est généralement admis que ces méthodes fournissent une précision acceptable ; toutefois, les limites d'applicabilité et les imprécisions liées à ces méthodes sont également connues.

La réponse des matériaux magnétiques, la complexité des phénomènes hystérétiques, la dépendance de la température ainsi que le comportement dynamiques ne sont pas pris en compte. Pour atteindre de meilleurs précisions, il est nécessaire d'intégrer dans les méthodes de simulation numérique des modèles de pertes fers plus fins, et en particulier des modèles d'hystérésis qui prennent en compte la température et la fréquence.

Dans cette optique, différents modèles d'hystérésis sont utilisés, parmi lesquels les plus célèbres sont ceux de Preisach et de Jiles-Atherton. Tous les deux ont des avantages, et aussi des inconvenients. En particulier, à la base il s'agit de modèles scalaires, statiques et indépendants de la température. De plus, leur interprétation du point de vue physique est parfois incomplète, en particulier en ce qui concerne le modèle de Preisach. Pour des applications pratiques, il est fondamental que ces modèles respectent les lois de la thermodynamiques, afin d'évaluer correctement les pertes. Le modèle énergétique de Henrotte [72] est un modèle quasi-statique cohérent avec les lois de la thermodynamique, et il est intrinsèquement vectoriel. Une caractéristique importante est que les cycles d'hystérésis sont construits à partir de la superposition de la contribution d'un certain nombre de cellules, donc le nombre peut être choisi de la sorte à obtenir la précision souhaitée.

L'objectif global de cette thèse est de développer des méthodes efficientes pour prédire avec précision le comportement de matériaux magnétiques doux, en prenant en compte l'influence de la température et de la fréquence sur les paramètres du modèle EB.

Chapter 6

État de l'art

6.1 Origines du magnétisme

En 1820, Hans Christian Œrsted ouvre la voie à l'électromagnétisme, pilier de la physique du XIX siècle. Il observe qu'un "conflit électrique" provoqué aux bornes d'un appareil voltaïque par un fil "conducteur ou conjonctif" provoque dans certaines conditions la déviation d'une aiguille aimantée placée à proximité. Il en déduit qu'il existe un lien entre phénomènes électriques et magnétiques. Dans les semaines qui suivent la publication du mémoire d'Œrsted, André Marie Ampère pose les bases théoriques de l'électrodynamique, avec notamment le concept novateur de "courant électrique" : le magnétisme résulte de la présence de courants électriques, c'est-à-dire du déplacement de charges électriques. Le premier électroaimant est réalisé en 1824 par William Sturgeon, il est à la base de l'électrotechnique moderne. On doit ensuite la découverte de l'induction électromagnétique à Michael Faraday. En 1831, il montre qu'un aimant en mouvement crée un courant électrique dans un fil conducteur placé à proximité.

Maxwell précise les concepts de champs électriques et magnétiques en introduisant en particulier le champ de déplacement électrique. Il publie sa théorie en 1864, et en déduit en 1865 l'existence théorique d'ondes électromagnétiques (dont la lumière est un cas particulier). Dans son célèbre "Traité" (1873), il a simplifié sa théorie mais l'écriture moderne sous forme de 4 équations seulement, connues aujourd'hui comme les "équations de Maxwell", est la contribution d'Heaviside. A partir de 1886, Hertz met expérimentalement en évidence les "ondes électromagnétiques", ce qui constitue une vérification des travaux théroriques de Maxwell.

Au niveau atomique, les propriétés magnétiques d'un matériau dépendent de la contribution du moment orbital due à la rotation des électrons autour du noyau, et du moment magnétique de spin qui se trouve en tant que tel dans chaque électron. La superposition de ces deux effets conduit au moment magnétique total $\mathbf{m}_0$ de l'atome. L'aimantation $\mathbf{M}$ est la grandeur macroscopique qui décrit le caractère magnétique d'un matériau. Cette grandeur correspond au moment magnétique total par unité de volume. La relation linéaire $\mathbf{b} = \mu_0\mathbf{h}$, dans le vide, associe les grandeurs vectorielles densité de flux ou induction magnétique $\mathbf{b}$ et champ d'excitation magnétique $\mathbf{h}$ avec $\mu_0 = 4\pi \cdot 10^{-7}$, perméabilité du vide [132]. La réaction d'un matériau à l'application d'un champ magnétique extérieur est caractérisée par l'induction magnétique, suivant la relation $\mathbf{b} = \mu_0(\mathbf{h} + \mathbf{M})$, avec $\mathbf{J} = \mu_0\mathbf{M}$ (polarisation magnétique). La caractéristique qui décrit la réponse des matériaux magnétiques face à un champ magnétique $\mathbf{h}$ est la susceptibilité magnétique χ, qui lie les grandeurs $\mathbf{M}$ et $\mathbf{h}$ et dépend de la nature du matériau ($\mathbf{M} = \chi\mathbf{h}$). Ainsi, on obtient la formulation générale du vecteur induction (μ_r :

perméabilité relative) :

$$\mathbf{b} = \mu_0(1+\chi)\mathbf{h} = \mu_0\mu_r\mathbf{h} = \mu\mathbf{h}$$

En fonction du matériau considéré, la perméabilité magnétique peut être constante pour des grandes groupes de valeurs du champ magnétique appliqué (i.e. matériaux diamagnétiques et paramagnétiques) ou varier significativamente avec le champ magnétique dans lequel ils sont entourés (i.e. ferromagnétiques et ferrimagnétiques) [133].

6.2 Classification de matériaux selon leurs propriétés magnétiques

Les matériaux magnétiques sont subdivisés en cinq familles sur la base des différents paramètres clés (perméabilité magnétique relative μ_r et la susceptibilité χ) : diamagnétisme, paramagnétisme, ferromagnétisme, antiferromagnétisme, ferrimagnétisme. Dans la suite, les caractéristiques de deux familles principales (para- et ferromagnétisme) seront décrites.

Les matériaux paramagnétiques, comme par exemple l'aluminium, le chrome et le sodium, sont caractérisés par des particules avec un moment magnétique spontané. Lorsque le champ magnétique est nul ($\mathbf{h} = 0$), les moments sont orientés de manière aléatoire et le matériau n'est pas aimanté. En présence d'un champ magnétique, les moments visent à s'orienter, dans une certaine mesure, dans la direction de ce champ et l'aimantation $\mathbf{M}$ du matériau est due à l'excès de moments magnétiques orientés dans le sens du champ appliqué. L'aimantation d'un matériau paramagnétique est faible et décroît avec la température à cause de l'agitation thermique. Il existe une température, appelée température de Curie T_C, au delà de laquelle le matériau perd son aimantation spontanée [133]. À ce propos, les propriétés thermiques des matériaux magnétiques ont été étudiées par Pierre Curie, qui a montré que, dans les matériaux magnétiques, l'aimantation diminue lorsque la température augmente. De plus, lorsqu'une certaine température est depassée (température de Curie), les matériaux magnétiques perdent leurs propriétés ferromagnétiques et agissent comme des substances paramagnétiques.

Pour le type d'applications industrielles visées par ce travail, seuls les matériaux ferromagnétiques sont intéressants, en raison des perméabilités très élevées qu'ils permettent d'atteindre : à courant d'excitation égal, ces matériaux (judicieusement disposés dans le système) permettent de générer des flux d'induction beaucoup plus importants.

Les principaux matériaux ferromagnétiques sont les cinq métaux de transition (le chrome (Cr), le manganèse (Mn), le fer (Fe), le cobalt (Co) et le nickel (Ni)), la plupart des lanthanides (métaux de transition communément appelés terres rares), plusieurs alliages, et les ferrites. Les valeurs de susceptibilité magnétique et perméabilité magnétique relative sont très élevées (10^1 à 10^6). La particularité des matériaux ferromagnétique est de présenter une aimantation spontanée même en l'absence d'un champ magnétique extérieur. Cette propriété est due à la présence des domaines magnétiques qui composent le matériau, appelés domaines de Weiss, séparés par des parois de Bloch, présentées en détail dans la section suivante.

6.2.1 Ferromagnétisme à différentes échelles

La complexité des phénomènes physiques au sein des matériaux ferromagnétiques doux amène à traiter le ferromagnétisme à différentes échelles [134]. Au niveau microscopique, on peut étudier le comportement magnétique de chaque atome et l' interaction dans

la structure cristallographique du matériau. À l'échelle mésoscopique, ces phénomènes microscopiques engendrent des zones qui contient une même direction d'aimantation. Il s'agit des domaines de Weiss, qui sont délimités par des parois. Au moment de l'application d'un champ extérieur, si les domaines ont la direction d'aimantation dans le même sens du champ appliqué, ceux-ci vont s'agrandir, ce qui provoque le déplacement des parois. La paroi est une zone limite entre deux différentes directions d'aimantation, dont le déplacement entraîne une variation de flux, qui créé des courants induits microscopiques. Plus en détail, un matériau ferromagnétique monocristallin s'organise en domaines qui correspondent à la minimisation des différentes énergies : l'énergie d'échange, qui tend à aligner les moments magnétiques microscopiques de chaque atome, l'*énergie d'anisotropie magnéto-cristalline*, qui oriente l'aimantation (moment magnétique localisés) le long de certains axes cristallographiques définis, appelés directions d'aimantation facile, l'*énergie magnéto-élastique*, qu'il faut fournir au matériau pour modifier les mise en commun d'électrons, l'*énergie magnétostatique*, correspondant à l'action des champs magnétiques créés par tous les atomes voisins sur chaque atome isolé.

Enfin, au niveau macroscopique, les phénomènes soulignés aux autres échelles ressortent durant la caractérisation du matériau, par un comportement hystérétique non-linéaire [134]. Dans un matériau, l'hystérésis magnétique est une effet direct de l'existence des domaines et des processus d'aimantation, par déplacement et déformation des parois de Bloch. Chaque point (h, b) (cf. Figure 1.17) à l'intérieur du cycle est une condition possible du matériau [135]. Son comportement dépend ainsi non seulement de la valeur courante de h mais aussi de l'histoire du matériau, c'est-à-dire de tous les états d'aimantation antérieurs. Le cycle est caractérisé par certaines grandeurs : induction à saturation b_{sat}, induction rémanente b_r, champ coercitif h_c, courbe anhystérétique (transformation réversible).

Le mécanisme d'aimantation, en fonction du champ appliqué, peut être réprésenté comme la succession de trois mécanismes, qui engendrent la "courbe de première aimantation" :

1. zone à faibles champs (processus réversible) : le déplacement des parois est assimilé à une déformation élastique. Si l'augmentation du champ extérieur n'est pas suffisante pour décrocher la paroi, celle-ci se déforme sans provoquer de variation brutale de l'aimantation.

2. l'intensité du champ magnétique extérieur atteint un niveau qui fait en sorte que les parois surmontent les sites d'ancrages. Si l'aimantation des domaines est dans la même direction proche de celle du champ magnétique appliqué, ces domaines augmentent leur volume par rapport aux autres.

3. l'intensité du champ magnétique est très grande. L'aimantation va vers saturation. Les parois de Bloch commencent à disparaître, il reste seulement une structure avec un seul domaine, avec des moments magnétiques qui s'alignent sur la direction du champ extérieur.

6.3 Vue d'ensemble des modèles de pertes fer

Il existe plusieurs modèles qui permettent d'avoir àcces aux pertes fer [134]- [24]. Ils sont fondés sur un ensemble quasiment limité de mesures sur le matériau magnétique.

6.3.1 Modèle de Steinmetz

Il s'agit d'un modèle empirique basé sur l'équation de Steinmetz (SE). Il permet le calcul des pertes en fonction de la fréquence et de la densité de flux crête $\hat{b}$. Les coefficients C_{SE}, α et β sont définis par des mesures en régime sinusoïdal.

$$p_{Fe} = C_{SE} \cdot f^{\alpha} \cdot \hat{b}^{\beta} \tag{6.1}$$

Toutefois, cette relation est restreinte seulement au régime sinusoïdal. Pour cette raison, une première modification de cette équation a été introduite, l'équation de Steinmetz modifiée (MSE, Modified Steinmetz Equation) :

$$p_{Fe} = C_{SE} \cdot f_{eq}^{\alpha-1} \cdot \hat{b}^{\beta} \cdot f_r \tag{6.2}$$

$$f_{eq} = \frac{2}{\Delta b^2 \cdot \pi^2} \int_0^T \left(\frac{db}{dt}\right)^2 dt \tag{6.3}$$

Avec $\Delta b = b_{max} - b_{min}$. La fréquence f_r correspond à la période nécessaire pour passer de b_{max} à b_{min}. Cependant cette approche est parfois inexacte pour des inductions non symétriques et de faibles amplitudes.

Un autre ajustement de SE consiste dans le *Generalized Steinmetz equation* (GSE) :

$$p_{Fe} = \frac{1}{T} \int_0^T C_{SE} \cdot \left|\frac{db}{dt}\right|^{\alpha} \cdot |b(t)|^{\beta-\alpha} \, dt \tag{6.4}$$

Dans ce cas, cette approche amène à de résultats satisfaisants pour les faibles inductions et prend également en considération la présence d'inductions non symètriques, sans l'ajout d'autres coefficients. Par contre, cette équation est moins précise dans la représentation des cycles mineurs engendrés par la présence d'harmoniques.

Une autre solution consiste dans le modèle GSE appelée «improved Generalized Steinmetz Equation » (iGSE) :

$$p_{Fe} = \frac{1}{T} \int_0^T C_{SE} \cdot \left|\frac{db}{dt}\right|^{\alpha} \cdot |\Delta b|^{\beta-\alpha} \, dt \tag{6.5}$$

Une autre exténsion est NSE *Natural Steinmetz Extension*, qui analyse l'influence de la forme d'onde rectangulaire de commutation, comme la modulation de largeur d'impulsion (MLI) :

$$p_{Fe} = \left(\frac{\Delta b}{2}\right)^{\beta-\alpha} \frac{C_{SE}}{T} \int_0^T \left|\frac{db}{dt}\right|^{\alpha} dt \tag{6.6}$$

6.3.2 Modèle de Bertotti

Une autre mèthode permet d'obtenir les pertes fer pour des formes d'induction non sinusoïdales, d'après Bertotti. Il a proposé une approche de décomposition, de nature dynamique [136]. L'hypothèse du modèle consiste en la séparation des pertes magnétiques en trois contributions : pertes par hystérésis statique, pertes par courants de Foucault et pertes par excès. Pour une sollicitation à $b(t)$ imposée, il est possible de prévoir le champ total pour n'importe quelle forme d'onde :

$$h_{tot}(t) = h_s(b(t)) + h_{class}(t) + h_{exc}(t) \tag{6.7}$$

où $h_s(b(t))$ est le champ statique ou quasi-statique, Le terme h_{class} est le champ dû aux courants de Foucault et considéré comme le produit d'une constante γ avec la dérivée

temporelle du champ d'induction magnétique. Le paramètre γ dépend de la conductivité σ et de la géométrie de l'échantillon (en cas de tôles magnétique avec épaisseur d):

$$h_{class} = \gamma \frac{\partial b}{\partial t} \qquad \gamma = \frac{\sigma d^2}{12} \tag{6.8}$$

Le terme h_{exc} serait le champ excédentaire dû aux mouvements de parois, où S_{est} la section du circuit magnétique, V_0 est un paramètre micro-structurel du matériau corrélé à la taille des gains et G définit le coefficient de friction d.

$$h_{exc} = \alpha\delta \left| \frac{\partial b}{\partial t} \right|^{1/2} \qquad \alpha = \sqrt{\sigma G V_0 S} \qquad \delta = \operatorname{sign}\left(\frac{\partial b}{\partial t} \right) \tag{6.9}$$

6.4 Les modèles d'hystérésis

Les modèles d'hystérésis représentent l'ensemble des phénomènes physiques engendrés au cours du processus de dissipation énergétique. Ces modèles essaient de rétablir le lien entre le cycle d'aimantation réel du matériau, et les pertes associées.

Actuellement, il y a un choix important de modèles de comportement statique des matériaux. Il existe des modèles basés sur des considérations phénoménologiques, adaptés à la représentation de l'historique de l'aimantation et intrinsèquement vectoriel, respectivement ceux de Preisach [30], Jiles–Atherton (JA) [55] et "Energy-Based" (EB) [137] or "Vector Play Model" (VPM). Nous allons détailler le dernier modèle cité, qui est celui que nous avons utilisé dans notre travail.

Modèle énergétique (EB)

Le modèle "Energy-Based" (EB) or VPM [68] [69] [70], inspiré par [10] est un modèle macroscopique proposé pour l'hystérésis ferromagnétique. Il est intrinsèquement vectoriel et, contrairement au modèle de JA, le nombre de paramètres n'est pas limité. Il se fonde sur une formulation thermodynamique consistante dans laquelle l'énergie magnétique stockée et l'énergie dissipée sont connues à tout instant.

À partir des première et deuxième principes de la thermodynamique, le champ magnétique appliqué $\mathbf{h}$ est décomposé en une partie réversible $\mathbf{h}_{re}$ et une irréversible $\mathbf{h}_{ir}$, telles que $\mathbf{h} = \mathbf{h}_{re} + \mathbf{h}_{ir}$, conduisant à l'équation aux dérivées partielles :

$$\mathbf{h} - \frac{\partial u^k(\left|\mathbf{J}^k\right|)}{\partial \mathbf{J}^k} - \chi^k \frac{\dot{\mathbf{j}}^k}{\left|\dot{\mathbf{j}}^k\right|} = \mathbf{0} \tag{6.10}$$

où $\mathbf{h}$: champ magnétique, $\mathbf{J} = \sum_k \mathbf{J}^k$: polarisation magnétique (le point au-dessus représente la dérivée temporelle), u^k : densité d'énergie magnétique stockée (composante réversible) et κ^k : champ de pinning (composante irréversible).

Le champ magnétique $\mathbf{h}$ est l'entrée du modèle, N est le nombre de cellules; chaque cellule est équivalente à un système mécanique composé d'un ressort en parallèle avec un amortisseur (Fig.**??**).

En considérant une approche différentielle, la simplification suggérée par [68] consiste à assumer que $\mathbf{J}^k$ est parallèle à $\mathbf{h}^k_{re}$.

Les termes

$$\mathbf{h}^k_{re} = \sum_{k=1}^{N} \omega_k \mathbf{h}^k_{re} \tag{6.11}$$

représentent l'état interne de chaque cellule, mis à jour en fonction du champ magnétique $\mathbf{h}$ et de la valeur actuelle $\mathbf{h}_{re0}^k$, suivant :

$$\mathbf{h}_{re}^k = \begin{cases} \mathbf{h}_{re0}^k & si\ \|\mathbf{h} - \mathbf{h}_{re0}^k\| < \kappa^k \\ \mathbf{h} - \kappa^k \cdot \frac{h - \mathbf{h}_{re0}^k}{\|h - \mathbf{h}_{re0}^k\|} & autrement \end{cases} \tag{6.12}$$

qui représente la solution approchée explicite de l'équation (6.12). Les poids ω_k sont associées aux cellules et χ^k est lié au champ coercitif. Les deux paramètres doivent vérifier les contraintes suivantes :

$$\omega_k \geq 0 \quad ; \quad \sum_{k=1}^{N} \omega_k = 1 \tag{6.13}$$

$$\kappa^1 = 0 \quad ; \quad \kappa^k \leq \kappa^{k+1} \tag{6.14}$$

L'aimantation M est calculée comme fonction de $\mathbf{h}_{re}$:

$$\mathbf{M} = M_{an}(\|\mathbf{h}_{re}\|) \cdot \frac{\mathbf{h}_{re}}{(\|\mathbf{h}_{re}\|)} \tag{6.15}$$

où $M_{an}(\|\mathbf{h}_{re}\|)$ est la fonction anhystérétique scalaire calculée avec la fonction de Langevin [138].

Enfin, la densité de flux magnétique est

$$\mathbf{b} = \mu_0(\mathbf{M} + \mathbf{h}) \tag{6.16}$$

Chapter 7

Moyens de mesure et caractérisation expérimentale

La caractérisation d'un matériau magnétique consiste à mesurer les cycles d'hystérésis $b(h)$. La manipulation peut être réalisée pour différents intensités d'excitation, pour des sollicitations dynamiques et dans des environnements contraints, à température variable [97]- [11].

L'échantillon, de forme toroïdale, est doté de longueur moyenne l_e et de section A_e. Ceci joue le rôle de noyau magnétique fermé dans un transformateur constitué d'un circuit primaire avec N_1 spires, parcouru par le courant i_1, et d'un circuit secondaire équipé de N_2 spires, avec une tension v_2 à ses bornes. Supposons un champ magnétique homogène dans le spécimen, une section de flux constante sur le parcours l_e, et des fuites magnétiques négligeables. Le théorème d'Ampère permet alors d'affirmer que

$$h(t) = \frac{N_1 i_1(t)}{l_e} \tag{7.1}$$

Si i_1 est variable dans le temps, alors la polarisation magnétique $J(h)$ l'est à son tour et crée une force électromotrice (f.e.m) induite, v_2, aux bornes du bobinage secondaire [11].

$$\oint_{\partial S_{mc}} \mathbf{e}(t) \cdot \mathrm{d}\mathbf{l} = -\frac{\partial}{\partial t} \int_{S_{mc}} \mathbf{B}(t) \cdot \mathrm{d}\mathbf{S} = -\frac{\partial}{\partial t} \Phi_{mc}(t) \tag{7.2}$$

où $\Phi_{mc}(t)$ est le flux dépendent du temps passant à travers S_{mc}, la section transversale de la bobine de mesure. La tension induite est donnée par

$$v_2(t) = -N_2 \frac{\partial \Phi_{mc}(t)}{\partial t} \tag{7.3}$$

Le flux magnétique Φ_{mc} à t_1 est déterminé par

$$\Phi_{mc}(t_1) = -\frac{1}{N_2} \int_0^{t_1} v_2(t) \mathrm{d}t \tag{7.4}$$

Le flux total est la somme de deux contributions [17]: le flux $\Phi_{mat}(t)$ dans le matériau, avec section transversale A_e et le flux dans l'air entourant l'échantillon $\Phi_{air}(t)$,

$$\Phi_{mc}(t) = \Phi_{mat}(t) + \Phi_{air}(t) = \int_{A_e} \mathbf{b}(t) \cdot \mathrm{d}\mathbf{S} + \int_{S_{mc}-A_e} \mu_0 \mathbf{h}(t) \cdot \mathrm{d}\mathbf{S} \tag{7.5}$$

Le deuxième terme (flux dans l'air) peut être négligé dans la plupart de cas pratiques [101], car la section d'air concernée est petite devant la section du matériau, et la valeur

de l'induction y est beaucoup plus faible (dans le rapport de la perméabilité relative). L'induction magnétique dans le matériau $b_{mat}(t_1)$ est déterminé par:

$$b_{mat}(t_1) = \frac{1}{A_e}\int_{A_e} \mathbf{b}(t_1)\cdot \mathrm{d}\mathbf{S} \approx \frac{\Phi_{mc}(t_1)}{A_e} = -\frac{1}{N_2 A_e}\int_0^{t_1} v_2(t)\mathrm{d}t \tag{7.6}$$

Toutefois, l'intégration pour obtenir b, surtout en basse fréquence, est compliqué en raison de faibles niveaux de v_2, du bruit et de la dérive des appareils . Une possible solution consiste dans l'utilisation de fluxmètres ou de l'intégration numérique réalisée sur les valeurs acquises de v_2 [11].

7.1 Mesures quasi-statiques en fonction de la température

Dans ce travail, la méthode de l'hystérésigraphe [101] est utilisée pour caractériser un noyau toroïdal, constitué de ferrite doux Mn-Zn 3C90, un matériau isotrope, dont les paramètres sont listés dans le Tableau 7.1.

La structure du système de mesure est présentée en Figure 2.2. Les cycles d'hystérésis ont été mesurés à différentes températures (Table 7.2) dans le cas de :

- **formes d'ondes d'excitation simples** (unidirectionnel), dont le schéma de principe du banc est donné en Figure 2.3.
- **formes d'ondes d'excitation complexes** (unidirectionnel avec ajout d'harmoniques) avec le banc expérimental présenté en Figure 2.4.

Table 7.1: Paramètres du noyau en ferrite doux 3C90.

Symbole	**Valeur**	**Description**	**Conditions**
μ_i	$2300 \pm 20\%$	perméabilité initiale	25 °C; $\leqslant$ 10 kHz; 0.25 mT
μ_a	$5500 \pm 25\%$	amplitude permeability	100 °C; $\leqslant$ 25 kHz; 200 mT
b	470 mT 380 mT	induction	25 °C; 10 kHz; 1200 A/m 100 °C; 10 kHz; 1200 A/m
ρ	4800 kg/m^3	masse volumique	
T_c	$\geqslant$ 220 °C	température de Curie	
l_e	73.2 mm	longueur effective	
S_e	36.9 mm^2	surface effective	
V_e	2700 mm^3	volume effectif	
OD	29 mm	diamètre externe	
ID	19 mm	diamètre interne	
HT	7.5 mm	hauteur	

Table 7.2: Gamme de températures mesurées (K).

Excitation simple	223	248	273	293	323	348	373	398	423	448
Excitation complexe				293	323		373			

7.1.1 Formes d'ondes d'excitation simples

Les mesures de cycles d'hystérésis ont été réalisées par le biais d'un hystérésigraphe (Laboratorio Elettrofisico Walker LDJ Scientific - Nerviano, Italie) [104]. Cela permet des mesures en courant continu ou en courant alternatif sur des noyaux toriques ou en lamelles, jusqu'à 1 MHz. Le banc expérimental [11] est détaillé dans la Figure 2.3. Un PC commande l'envoi d'un signal d'excitation, en V, au GBF. Ce signal est transmis au bobinage primaire, connecté en série au rhéostat et à une résistance de shunt, dont le rôle est de mesurer le courant qui y circule. Cette configuration permet de réaliser une pseudo source de courant pour accomplir des mesures à h imposé. Au niveau du bobinage secondaire, il y a un intégrateur analogique qui intègre la tension à ses bornes, pour obtenir b (7.6). En effet, les grandeurs h et b ne sont pas directement mesurables, donc leurs valeurs sont déduites sur la base de grandeurs électriques associées [11]. Le champ h est déterminé par un courant, image de la tension aux bornes de la résistance de shunt. La densité de flux b à partir de l'intégration de la tension aux bornes de l'enroulement secondaire. Ainsi, les formes d'onde « images » de h et b sont analysées par la carte d'acquisition, de manière synchrone. En dernier, le logiciel traite les signaux obtenus pour tracer le cycle d'hystérésis $b(h)$ mesuré.

7.1.2 Formes d'ondes d'excitation complexes

Compte tenu de l'impossibilité de prendre en considération des signaux plus complexes avec l'hystérésigraphe [104], un banc expérimental (Figure 2.4) a été conçu et réalisé au laboratoire, qui offre une large gamme de possibilités en termes de formes d'ondes, avec l'ajout d'harmoniques. Le noyau a été placé dans le four SNOL 30/1100, utilisé pour chauffer l'échantillon à différentes températures (Tableau 7.2). Le GBF est piloté par ordinateur à travers le logiciel Waveform Manager Plus, qui permet la création, la modification et la gestion de formes d'ondes arbitraires.

Table 7.3: Symboles et description de chaque grandeur.

Symbole	Signaux simples	Signaux complexes	Description
N_1	60	60	bobinage d'excitation
N_2	39	39	bobinage de mesure
R_{shunt}	1.795 Ω	2 Ω	résistance de shunt
$Rheostat$	60 Ω	176 Ω	rhéostat

7.2 Résultats

En détail, pour chaque cas, les tensions d'entrée sont :

1. *Signaux simples*: forme d'onde sinusoïdale ($f = 50$ Hz) à différent niveaux de champ

$$v(t) = v_p \cdot (\sin(2\pi f t)) \tag{7.7}$$

2. *Signaux complexes*:

   - forme d'onde sinusoïdale ($f = 50$ Hz) avec superposition de l'harmonique 3 ($3f = 150$ Hz), $T = 293$ K (cf. Figure 2.5):

$$v(t) = v_p \cdot (\sin(2\pi f t) + \sin(6\pi f t)) \tag{7.8}$$

- signal de modulation de largeur d'impulsions (MLI) (fondamental $f = 1$ kHz avec ajout d'harmoniques d'ordre 3 et 7) à $T = 323$ K (cf. Figure 2.6a) et $T = 373$ K (cf. Figure 2.6b).

Afin d'illustrer les résultats obtenus, les cycles d'hystérésis sont représentés en Figure 2.7 pour différentes formes d'onde et différentes températures. Pour ce qui concerne les signaux simples, plusieurs cycles à différents niveaux de champs ont été mesurés pour une même température. L'ajout d'harmoniques, pour les signaux complexes, donne lieu à de petits cycles mineurs au sein du cycle majeur. Globalement, on peut observer que l'induction à saturation et le champ coercitif décroissent avec l'augmentation de la température. La diminution du champ coercitif avec l'augmentation de la température résulte d'une réduction du couplage d'échange et de l'interaction spin-orbite. Nous reviendrons aux variations des propriétés avec la température plus en détail dans le Chapitre 3.

7.3 Mèthode d'identification des paramètres

La stratégie d'identification des paramètres pour le modèle EB [109] est basée sur la courbe expérimentale $h_c(h_p)$, mesurée à partir de points expérimentaux relevés sur des cycles à différentes amplitudes. h_c est le champ coercitif relevé sur un cycle dont l'amplitude du champ appliqué est h_p. Il est nécessaire d'interpoler et d'extrapoler la courbe pour les hautes valeurs de h_p, mais aussi pour les faibles valeurs (7.9) :

$$h_c(h_p) = \begin{cases} h_c = h_{c_{max}} & si\ h_p >_{p_{max}} \\ h_c = interpolation & si\ h_{p,min} < h_p < h_{p,seuil} \\ h_c = h_{c_{min}} \cdot \left(\frac{h_p}{h_{p_{min}}}\right)^2 & si\ h_p < h_{p_{min}} \end{cases} \tag{7.9}$$

Ensuite, nous procédons avec la construction d'une fonction récursive $F(h)$. On démarre avec un point $h > h_{p_{seuil}}$, de cette manière $F(h) = h - h_{c_{max}}$. Les points suivants sont ainsi calculés :

$$h^n = \frac{h^{n-1} + h_c(h^{n-1})}{2} \tag{7.10}$$

$$F(h) = \begin{cases} h^n - h_{c_{max}} & si \quad h^n > h_{p_{seuil}} \\ \frac{F(h^{n-1})}{2} & sinon \end{cases} \tag{7.11}$$

Il faut ensuite dériver la fonction F deux fois par rapport à h. La dérivée seconde de F représente la distribution continue des poids affectée à chaque cellule. Enfin, une fois discrétisée cette dernière, nous avons obtenu différents paramètres (ω_k, χ^k) en changeant le nombre de cellule.

Chapter 8

Modélisation statique

8.1 Effet de la température sur les propriétés magnétiques

Les mécanismes d'aimantation dans les matériaux ferromagnétiques dépendent de la température. L'influence de ce paramètre sur la caractéristique magnétique $b - h$ du ferrite doux 3C90 est bien visible, comme on peut le constater dans les Figures 2.7 - 3.1.

Pour un champ d'excitation suffisamment élevé pour saturer le matériau, une élévation de température a pour effet une diminution de la surface du cycle d'hystérésis du ferrite Mn-Zn.

Comme illustré en Figure 3.1, quelques grandeurs du cycle d'hystérésis, par exemple le champ coercitif, le champ rémanent et l'induction à saturation diminuent. En particulier, la variation du champ coercitif h_c avec la température est montrée à la Figure 5.8b : la coercivité diminue de façon exponentielle avec la température, comme attendu [111].

La variation mesurée de la polarisation magnétique relative $J_{sat}(T)/J_{sat0}$ en fonction de la température relative T/T_c est montrée en Figure **??** (points), ainsi que son extrapolation jusqu'au point théorique à la température de Curie (ligne). Lorsque $T = 0$ la polarisation est égale à l'induction de saturation J_{sat}, alors que pour $T = T_c$, J_{sat} vaut zéro.

8.2 Identification des paramètres en fonction de la température

La procédure précédemment décrite dans la Section 2.4 a été appliquée au matériau en question à différentes températures. La courbe $h_c(h_p)$ a été mesurée pour chaque série de cycles d'hystérésis avec h_p croissant, pour chaque température. La variation des courbes $h_c(h_p)$ en fonction de la température est montrée dans la Figure 3.4. Il est évident que le champ coercitif diminue lorsque la température augmente. Cela est cohérent avec les cycles présentés à la Figure 3.1. Ensuite, les figures 3.5 et 3.6 montrent la construction des fonctions auxiliaires $F(h)$ et les fonctions de distribution cumulative des champ de pinning $\partial_h F(h)$. Les distributions continues estimées $\omega(\kappa|T)$ sont illustrées par la Figure 3.7. La dernière étape consiste à discrétiser les distributions continues en N cellules, afin d'obtenir des ensembles discrets de paramètres $(\omega_k, \kappa^k)_{k=1,\dots,N}$.

Le champ d'accrochage (pinning field) moyen diminue, lorsque la température augmente. Cela pourrait être lié au fait que, à températures plus élevées, le bruit thermique permet de surmonter plus facilement les barrières d'énergie crées par le site d'ancrage, par conséquent le champ d'accrochage diminue. Par ailleurs, il est rapporté

dans la littérature [114], [115], [116] que, à hautes températures, la taille des grains croît. Ainsi, la croissance de la taille des grains augmente la distance des points d'accrochage dans le matériau et, en conséquence, le champ coercitif décroît.

8.3 Validation de mesures "standards"

Le modèle EB a été testé sur des mesures standards "simples", quasi-statiques, à plusieurs températures, en faisant varier le nombre de cellules de 2 à 8. Pour simuler avec N cellules, il est indispensable de représenter la courbe anhystérétique de manière à identifier entièrement le modèle. Elle est ici calculée en considérant la ligne médiane des courbes majeures mesurées. L'identification des paramètres peut être effectuée de deux manières : en réduisant au minimum l'erreur entre mesures et courbes d'hystérésis calculées ou à l'aide de la procédure d'identification décrite dans la Section 2.4.

La figure 3.8 compare les cycle d'hystérésis majeurs $b(h)$ mesurés et simulés à $h_p = 230$ A/m pour différentes températures (248 K, 348 K, 448 K) avec la même amplitude $h_p = 230$ A/m pour $N = 3$ cellules.

Les cycles mesurés et simulés avec $N = 4$ cellules à différentes amplitudes ($h_p = 40$ A/m, 80 A/m) pour la même température, i.e. $T = 323$ K, sont montrés à la Figure 3.10.

8.4 Modèle EB : analyses de précision et de robustesse

L'objectif de cette section est d'examiner la précision de la correspondance entre la réponse du modèle et les données de mesure. Un autre aspect consiste à vérifier si la précision peut être améliorée en augmentant le nombre de paramètres du modèle. Cette validation est délibérément réalisée avec des mesures "standards", autrement dit uniquement avec des champs alternatifs sinusoïdaux.

La précision du modèle peut être évaluée sur la base de l'erreur moyenne quadratique normalisée (NRMSE) entre les champ d'induction simulé et mesuré :

$$\text{NRMSE} = \frac{\sqrt{\sum_{n=1}^{N_{meas}} ||b_{sim,n} - b_{meas,n}||^2}}{\sqrt{\sum_{n=1}^{N_{meas}} ||b_{meas,n}||^2}} \times 100\% \tag{8.1}$$

où N_{meas} est le nombre des points mesurés.

Les figures suivantes résument quelques résultats de l'analyse de convergence, avec N allant de 2 à 8 cellules.

En particulier, la figure 3.12 montre les cycles d'hystérésis pour deux valeurs extrêmes du champ, representés avec $N = 3$ (Figure 3.12a) et 4 cellules (Figure 3.12b).

Il apparaît que la modélisation avec 3 cellules permet une représentation assez précise des cycles majeurs. Par contre, les cycles mineurs ressortent quasiment en forme de parallélogramme - notamment pour le cycle mineur à 40 A/m (cf. Figure 3.12a) - et sont donc mal décrits. L'augmentation du nombre de cellules à $N = 4$ (Figure 3.12b) réduit considérablement les différences de forme et de surface des cycles, et aussi le NRMSE (cf. Figure 3.13), y compris pour les cycles mineurs.

Par ailleurs, l'écart qui existe dans les cycles majeurs, particulièrement autour du coude de saturation, n'est pas corrigé.

La Figure 3.14 représente le NRMSE en fonction de la température, pour des cycles de même amplitude $h_p = 230$ A/m. Pour les cycles majeurs, une bonne représentation des cycles d'hystérésis (NRMSE $< 5\%$) est généralement obtenue à partir de 3 cellules.

8.5 Validation des mesures "complexes"

Les paramètres identifiés précédemment ont été utilisés tels quels pour simuler des configurations de magnétisation complexes. Les mesures ont été réalisées pour $T = 293$ K, 323 K et 373 K (cf. figure 2.7). La comparaison de ces mesures "non-standards" avec les simulations du modèle EB permet une évaluation plus complète de sa capacité prédictive.

Les cycles mesurés et simulés avec $N = 3$ et $N = 4$ cellules sont illustrées à la Figure 3.16, pour le signal avec troisième harmonique à $T = 293$ K.

En augmentant le nombre de cellules, on referme mieux les petits cycles de recul, ce qui est cohérent avec l'étude précédente sur la précision.

Le modèle montre son aptitude à simuler des signaux avec harmoniques à une température donnée. Il produit des cycles mineurs stables; plus précisément ces boucles sont correctement fermées (contrairement au modèle original de Jiles-Atherton [65], [61], [62]).

La performance du modèle EB pourrait être améliorée en utilisant une discrétisation plus fine, comme le montre la Figure 3.18, où le NRMSE pour chaque température mesurée contribue à l'évaluation de la prédiction du modèle EB. Soulignons que le modèle EB a été utilisé avec les paramètres identifiés précédemment à partir de signaux d'excitation simples (sinusoïdaux, sans harmonique).

Les résultats mesurés et simulés sont globalement en bon accord, ce qui indique que le modèle est capable de prédire des cycles complexes à toute température, au moins dans la plage mesurée. Pour conclure, le modèle EB, simulé avec des paramètres identifiés à partir de mesures standards, est apte à fournir des résultats d'une précision raisonnable aussi pour des cycles mesurés dans des conditions non-standards.

8.6 Extension du modèle : prise en compte des variations de température

A ce stade, la variation des propriétés magnétiques avec la température conduit à la nécessité d'identifier les paramètres du modèle EB pour chaque température de travail. Dans cette section, nous proposons de premières idées qui pourraient conduire à une extension du modèle permettant la prise en compte de la température directement dans le modèle EB. Cette partie originale de mon travail à fait l'objet d'une présentation à la Conférence internationale IGTE en 2018, puis d'un article publié en 2019 dans la revue COMPEL [117]. En effet, dans les applications pratiques, les ingénieurs doivent connaître les courbes de distribution continues $\omega(\kappa)$ à différentes températures, ou directement leurs approximations discrètes (ω_k, κ^k), pour pouvoir réaliser un prototypage virtuel adéquat. Dans la suite, nous détaillons deux méthodes, une continue et une discrète.

8.6.1 Interpolation des courbes $\omega(\kappa|T)$ continues

Pour évaluer la robustesse de notre approche, nous avons exécuté une validation croisée en comparant les fonctions originales $\omega(\kappa|T)$, obtenues pour toutes les températures disponibles, avec les courbes obtenues par interpolation (spline), en utilisant seulement

moitié de l'ensemble de données (T = 223 K, 273 K, 323 K, 373 K et 448 K). L'objectif est de reconstituer les cinq courbes manquantes (T = 248 K, 293 K, 348 K, 398 K, 423 K).

Les courbes originales (traits pleins), obtenues par la méthode d'identification, et les nouvelles issues de l'interpolation sont illustrées à la Figure 3.19. On peut remarquer que celles-ci sont en bon accord avec les courbes précédemment identifiées, suggérant que le modèle aurait pu être identifié en utilisant un ensemble réduit de mesures.

8.6.2 Paramètres discrets (ω_k, κ^k) en fonction de la température

Dans cette section, une première propriété de la loi de variation des paramètres avec la température est proposée. Les courbes de distribution continues $\omega(\kappa|T)$ ont été discrétisées avec $N = 3$ cellules, permettant ainsi d'obtenir les paramètres discrets $(\omega_k(T), \kappa^k(T))_{k=1,\dots,N}$ pour des températures T comprises entre 223 K et 448 K. En ce qui concerne les paramètres ω_k, la propriété $\sum_{k=1}^{N} \omega_k = 1$ doit être vérifiée à chaque température. Les paramètres κ^k sont liés à la force locale d'accrochage (ou au champ coercitif). On formule l'hypothèse que, à toute température, les produits $\omega_k(T) \cdot \kappa^k(T)$ sont mis à l'échelle comme :

$$\frac{\omega_k(T) \cdot \kappa^k(T)}{\omega_k(T_0) \cdot \kappa^k(T_0)} = \frac{h_c(T)}{h_c(T_0)} \tag{8.2}$$

où ce rapport est connu pour une température de référence T_0. On peut observer que cela est cohérent avec [74].

Par conséquent, les paramètres du modèle EB identifiés à une température de référence pourraient être utilisés pour simuler le comportement de matériaux magnétiques à d'autres températures. Mais à ce point de notre travail, nous n'avons pas encore réussi à séparer les variables ω et κ dont nous ne connaissons que le produit. Cette connaissance permet néanmoins de restreindre le nombre nécessaire des mesures pour une gamme de températures donnée.

8.7 Conclusion

Ce chapitre porte dans un premier temps sur la validation du modèle EB pour les ferrites Mn-Zn, à différentes températures, puis sur l'analyse des effets de la température sur les propriétés magnétiques mesurées, et sur les paramètres du modèle EB.

Le modèle a été validé avec des formes d'ondes de magnétisation sinusoïdale simples, et a montré sa capacité à prévoir le comportement du matériau pour des signaux d'excitation complexes.

La méthode d'identification proposée s'avère donc être efficace et robuste. Cette étude montre que l'erreur quadratique (NRMSE) diminue avec l'augmentation du nombre de cellules N. On peut remarquer que trois cellules sont généralement suffisantes pour obtenir un bon résultat pour des forme d'onde pas trop complexes, tandis qu'un nombre plus élevé est généralement nécessaire pour des harmoniques à faible amplitude.

Cette étude nous a permis d'assurer une opérabilité du modèle dans le cas de signaux complexes et dans une large gamme de températures, et ouvre la voie à une future extension du modèle à la température : la loi de variation des paramètres proposée semble cohérente avec la physique du modèle et représente un premier pas. La prochaine étape consistera à trouver un moyen de séparer les variables ω, κ, ce qui permettra de prédire séparément les variations avec la température de ces paramètres du modèle.

Chapter 9

Validation avec simulations aux éléments finis

Afin de vérifier la précision du modèle EB dans l'analyse par éléments finis, les résultats de simulation peuvent être validés à l'aide de mesures réalisées sur un cas-test. Il s'agit d'une application réaliste, un transformateur E-E, dans plusieurs configurations, conçu pour générer des formes d'onde sinusoïdales, déphasées ou non. Dans certains cas, avec ce montage on obtient des champs tournant au niveau de la jonction entre la colonne centrale et la culasse. Les données mesurées dans les différentes configurations sont détaillées dans les sections suivantes. Ce travail à fait l'objet d'une présentation à la Conférence internationale Compumag en 2019 [118].

9.1 Dispositif expérimental

La géométrie du transformateur est montrée dans la Figure 4.1. Les paramètres sont listés dans le Tableau 4.1. La mise en place a été conçue spécialement pour cet usage.

Le système se compose de deux noyaux E, ce qui permet d'obtenir un circuit magnétique sans entrefer (cf. Figure 4.2). Le noyau est constitué de ferrite doux Mn-Zn 3C90, Ferroxcube [103], préalablement caractérisé (chapitre 7) généralement utilisé en électronique de puissance. Deux bobinages de 15 spires sont placés sur les jambes externes. Ces enroulements peuvent être connectés en série ou alimentés par deux sources de tension commandées de manière indépendante. Des champs unidirectionnels ou tournants dans certaines parties sont alors possibles. Grâce à des supports appropriés construits à l'aide d'une imprimante 3D, les bobines de détection C_1 and C_2, composées de 20 spires chacune, sont utilisées pour estimer le flux allant dans la jambe centrale à partir de chaque enroulement (T-joint).

Différentes configurations sont définies sur la base des conditions d'alimentation des bobinages (cf. Figure 4.3), avec différents niveaux d'amplitude v_p ($v_p = 1$ - basse amplitude LA, 5 V - haute amplitude HA) et décalages de phase d'angle ϕ (0° ou 90°).

9.2 Simulations aux éléments finis

Cette section introduit les simulations construites sur la plateforme ONELAB (Gmsh/GetDP) à l'aide de la formulation de la magnéto-statique où le modèle EB a été implémenté [47]. Cela a été préalablement mis au point et testé sur des cas plus simples (par exemple, [120]). Le calcul est effectué par le biais de la formulation en potentiel vecteur magnétique $\mathbf{a} - v$ appliqué sur le cas-test du transformateur.

Les bobinages sont considérés comme inducteurs bobinés. Chacun d'entre eux est représenté, dans la section transversale, par des zones rectangulaires autour des jambes du noyau. Un couplage avec des circuits externes dans le logiciel aux élément finis permet l'imposition de sources commandées en tension. Pour le cas d'essai, on peut utiliser une approximation 2D, où **h** et **b** se trouvent dans le plan **xy** et la densité de courant **j** est supposée perpendiculaire au domaine. Le fait de considérer un cas 2D permet d'exprimer la formulation en termes d'un potentiel vecteur **a**, où seule la composante a_z selon l'axe z est non nulle, et constitue l'inconnue du problème. De plus, en raison de la symétrie, on peut se focaliser seulement sur moitié de la géométrie du transformateur, comme on peut le voir dans la Figure 4.4. Les simulations sont effectuées avec $N = 4$ cellules, avec (ω_k, κ^k) pour $T = 293$ K (cf. Tableau 9.1). La courbe anhystérétique est approximée par une fonction tangente hyperbolique (2.18) avec $J_a = 0.38$ T et $h_a = 53$ A/m.

Table 9.1: Paramètres pour ferrite 3C90.

ω	κ (A/m)
$\omega_1 = 0.43422$	$\kappa^1 = 0$
$\omega_2 = 0.41383$	$\kappa^2 = 13.53$
$\omega_3 = 0.14966$	$\kappa^3 = 42.37$
$\omega_4 = 0.00227$	$\kappa^4 = 115.61$

9.2.1 Cas 1 (série)

Dans le cas 1, les bobinages sur les jambes extérieures sont connectées en série avec une résistance $R_{add} = R_{series} + R_{shunt}$, de telle sorte à ce que les flux s'additionnent. Le circuit est alimenté avec une source de tension, avec des niveaux de tension différents et à la fréquence $f = 50$ Hz:

$$v_{AC} = v_p \cdot \sin(2\pi f t) \tag{9.1}$$

Les flux sont unidiretionnels, et on ne s'attend pas à obtenir des champs tournants. La figure 4.6 montre la comparaison entre les courants dans les bobinages simulés et mesurés.

9.2.2 Cas 2 (déphasage entre les sources de tension)

Dans le cas 2, les bobinages sur les jambes extérieures sont alimentés par deux sources de tensions indépendantes, de même amplitude et même fréquence $f_1 = f_2 = 50$ Hz (mais avec un déphasage ϕ):

$$v_{AC1} = v_p \cdot \sin(2\pi f_1 t + \phi) \tag{9.2}$$

$$v_{AC2} = v_p \cdot \sin(2\pi f_2 t) \tag{9.3}$$

Les deux signaux sont en quadrature ($\phi = 90°$). De cette manière on obtient un champ tournant dans le T-joint, comme on peut l'observer dans la Figure 4.10.

9.2.3 Cas 3 (signaux multi-harmoniques)

Dans le cas 3, les deux bobinages sont alimentés par deux sources de tensions indépendantes (9.2)-(9.3) avec duex fréquences différentes, et avec la même tension de pic v_p $(1 - 5$ V). Différents sous-cas ont été traités:

a) $f_1 = 3f_2 = 150$ Hz, $f_2 = 50$ Hz, $\phi = 0°$

b) $f_1 = 3f_2 = 150$ Hz, $f_2 = 50$ Hz, $\phi = 90°$

c) $f_1 = 5f_2 = 250$ Hz, $f_2 = 50$ Hz, $\phi = 0°$

d) $f_1 = 5f_2 = 250$ Hz, $f_2 = 50$ Hz, $\phi = 90°$

Dans la suite, on va focaliser l'attention aux Cas 1, 2b et Cas 3b-3c. Le Cas 1 est testé pour valider les formes d'onde unidirectionnelles, alors que Cas 2b est approprié pour vérifier la modélisation des effets d'hystérésis vectorielle, avec le champ tournant. Enfin, les Cas 3b-3c conviennent pour vérifier signaux multi-harmoniques, distordus, sous flux unidirectionnels ou tournants.

9.3 Discussion

Globalement, les données calculées par simulation de la tension et du flux magnétique sont en bon accord avec les mesures sur les cas d'essai, comme illustré dans la Figure 4.14. Toutefois, les résultats de simulation surestiment légèrement les données expérimentales.

Table 9.2: Different conditions for simulations of Case3a.

Simulation	**Mesh**	**Cells**	**Anhysteretic function**
Sim1	A	$N = 4$	Tangente hyperbolique
Sim2	B	$N = 4$	Tangente hyperbolique
Sim3	A	$N = 4$	Double Langevin
Sim4	A	$N = 40$	Tangente hyperbolique

Afin de trouver les paramètres influençant les résultats obtenus, plusieurs simulations dans différentes conditions ont été réalisées (cf. Tableau 9.2), en considérant le Cas 3a HA, à titre d'exemple, pour comparer les résultats.

D'abord, un maillage grossier a été adopté (MeshA), consistant en 2000 nœuds and 4420 éléments. Deuxièmement, un maillage plus fin est considéré avec 12329 nœuds and 25651 éléments (MeshB) . Ensuite, l'approximation de la courbe anhystérétique est modifiée, en considérant la Double fonction de Langevin (2.20). Les quatre paramètres de la fonction ont été ajustés à partir de mesures : $J_a = 0.4261$ T, $h_a = 20.2661$ A/m, $J_b = 0.0038$ T, $h_b = 18.8927$ A/m. Enfin, une discrétisation plus fine des paramètres est prise en compte, en effectuant la simulation du modèle avec $N = 40$ cellules.

On peut remarquer que les résultats sont moins précis pour le maillage grossier (MeshA) et lorsque la courbe anhystérétique $J_{an}(h)$ est representée par une fonction tangente hyperbolique. Les écarts diminuent légèrement avec un maillage plus fin (MeshB), mais il est évident que les différences se réduisent beaucoup si l'on remplace la fonction tangente hyperbolique avec la fonction double Langevin. Comme on peut le voir, les résultats simulés et expérimentaux sont en bon accord lorsqu'on augmente considérablement le nombre de cellules, $N = 40$ cells, Figures 4.19d et 4.21 (détail). Nous pouvons mettre ces écarts sur le compte des approximations adoptées:

- En premier lieu, une analyse 2D a été réalisée pour vérifier le comportement du modèle dans une gamme variée de formes d'onde d'excitation. Toutefois, au vu de la profondeur du système, cette hypothèse est facilement criticable. Le système est plus large que profond, donc les effets the effects dans la direction de profondeur peuvent être des facteurs non négligeables. La surestimation des résultats pourrait donc être causée par la présence d'un flux de fuite, dont la trajectoire entoure les enroulements dans la troisième dimension.

- D'autres sources d'erreurs possibles sont liées à la tolérance des côtes dans la géométrie du noyau (voir Tableau 7.1). Plus important, nous avons caractérisé les propriétés magnétiques du matériau sur un échantillon de forme torique, et nous affectons les mêmes caractéristiques à notre circuit en E. Or les ferrites sont bien connues pour avoir une large dispersion. Par exemple, la perméabilité d'amplitude est donnée à $\pm 25\%$. Ce qui pourrait expliquer le fait que les écarts sont plus marquées pour les essais à faible amplitude.

Cette analyse a révélé que les résultats de simulation surestiment les mesures, sauf lorsqu'un nombre plus élevé de paramètres est utilisé. Dans ce cas-test particulier, un nombre de 4 cellules n'est pas suffisant pour représenter pleinement les mécanismes complexes au sein du matériau. Cependant, on peut observer qu'un bon accord entre mesures et simulations est obtenu dans le cas où 40 cellules sont utilisées pour simuler le comportement du matériau. En fait, plusieurs travaux [69]- [74]- [117] ont démontré que le nombre de cellules dans lequel le modèle est discrétisé dépend de la précision requise : modèles avec un plus grand nombre de cellules permettront une représentation plus précise de la réponse du matériau, mais vont demander plus de temps de calcul de de mémoire pour réaliser les simulations.

À la lumière de ces approximations, il pourrait sembler utile de considérer un cas 3D, afin de vérifier les résultats obtenus. Toutefois, on trouve que déjà dans le cas 2D les formes d'onde des tensions sont bien reproduites, et que les résultats sont globalement en bon accord. Enfin, la modélisation 2D fournit une information utile et pertinente sur le comportement du modèle d'hystérésis.

Chapter 10

Conclusions et perspectives

Cette thèse porte sur la modélisation des dispositifs du génie électrique, avec une attention particulière pour les modèles de matériaux magnétiques.

Le Chapitre 6 introduit l'état de l'art de ce travail, notamment les modèles d'hystérésis présents dans la littérature. Particulièrement, le modèle EB est étudié en vertu de ces propriétés souhaitables. Il s'agit d'un modèle intrinsèquement vectoriel, dont le nombre de paramètres à identifier varie selon la précision souhaitée. Le modèle se fonde sur une interprétation énergétique consistante dans laquelle l'énergie magnétique stockée et l'énergie dissipée sont connues à tout instant. Pour cette raison, ce modèle a été choisi pour décrire le comportement du matériau magnétique sous test.

Dans le Chapitre 7, une procédure spécifique a été appliquée pour mesurer les propriétés magnétiques dans des conditions statiques et dynamiques. Dans le même temps, les mesures statiques ont été réalisées en faisant varier la température. Grâce à ces mesures, les données d'entrée nécessaires pour le protocole d'identification du modèle EB peuvent être extraites.

Le protocole d'identification est ensuite appliqué aux données mesurées mentionnées ci-dessus. Les cycles d'hystérésis simulés sont comparés systématiquement aux cycles expérimentaux dans le Chapitre 8. De plus, des signaux complexes (avec l'ajout d'harmoniques), qui ne font pas partie des données d'entrée du modèle ont été testés pour évaluer la robustesse des paramètres identifiés.

Après avoir vérifié que les résultats obtenus par simulation sont en bon accord avec les mesures, le même protocole d'identification a été appliqué à différentes températures pour évaluer sa capacité d'adaptation.

Une fois terminée la phase d'identification, de premières tendances sur l'évolution des paramètres du modèle EB avec la température ont pu être mises en évidence. L'analyse de précision a été conduite en faisant varier le nombre de paramètres pour toutes les températures de notre jeu de mesures. En conclusion, un nombre de cellules égal à 4 est suffisant pour obtenir un bonne précision pour chaque température, et pour différentes excitations. A ce stade, la variation des propriétés magnétiques avec la température conduit à la nécessité d'identifier les paramètres du modèle EB pour chaque température de travail. De premières idées qui pourraient conduire à une extension du modèle permettant la prise en compte de la température directement dans le modèle EB ont été testées. Il s'agit de construire des courbes de distribution continues, ou directement leurs approximations discrètes pour pouvoir réaliser un prototypage virtuel dans le logiciels aux éléments finis, qui prenne en compte les variations de température, si possible en partant de mesures à une seule température.

Dans le chapitre 9, nous vérifions la précision du modèle EB dans des analyses par éléments finis d'une structure plus complexe que celle qui a servi à la caractérisation

expérimentale du matériau utilisé : notamment, le champ n'y est pas uniforme, et la présence de plusieurs enroulements d'excitation permet d'y générer à certains endroits des variations de la direction du champ, voire un champ tournant. Cette structure est un transformateur E-E, qui a été conçu, construit et mesuré au laboratoire dans le cadre de cette thèse.

Les formes d'onde calculées des tensions dans le bobinage de mesure sont en bon accord avec les données expérimentales pour les différentes configurations d'excitation étudiées, même si des écarts existent à cause des approximations faites (notamment le passage en 2D).

Le relatif succès de ces modélisations montre que le comportement vectoriel du modèle EB est globalement bon.

Enfin, nous avons déjà commencé à creuser certaines des perspectives de ce travail, jusqu'à publier quelques résultats, notamment sur le comportement dynamique du modèle EB, sur l'étude d'autres protocoles d'identification de ses paramètres [125] et sur la relation entre la microstructure du matériau et les paramètres du modèle [127].

Appendices

Appendix A

Magnetic measurements

A.1 Static temperature-dependent measurements

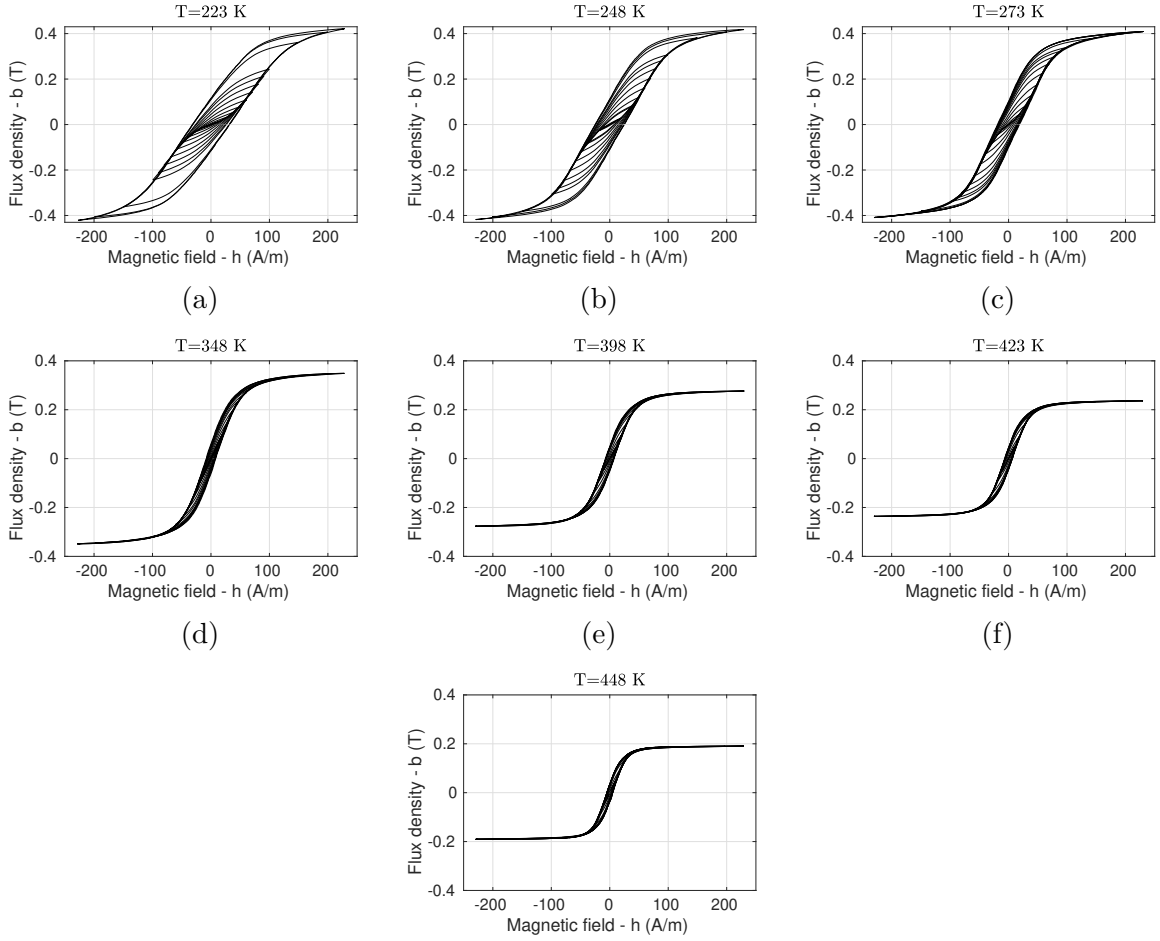

Figure A.1: Hysteresis cycles $b(h)$ measured at several temperatures in simple conditions.

A.2 HF measurements

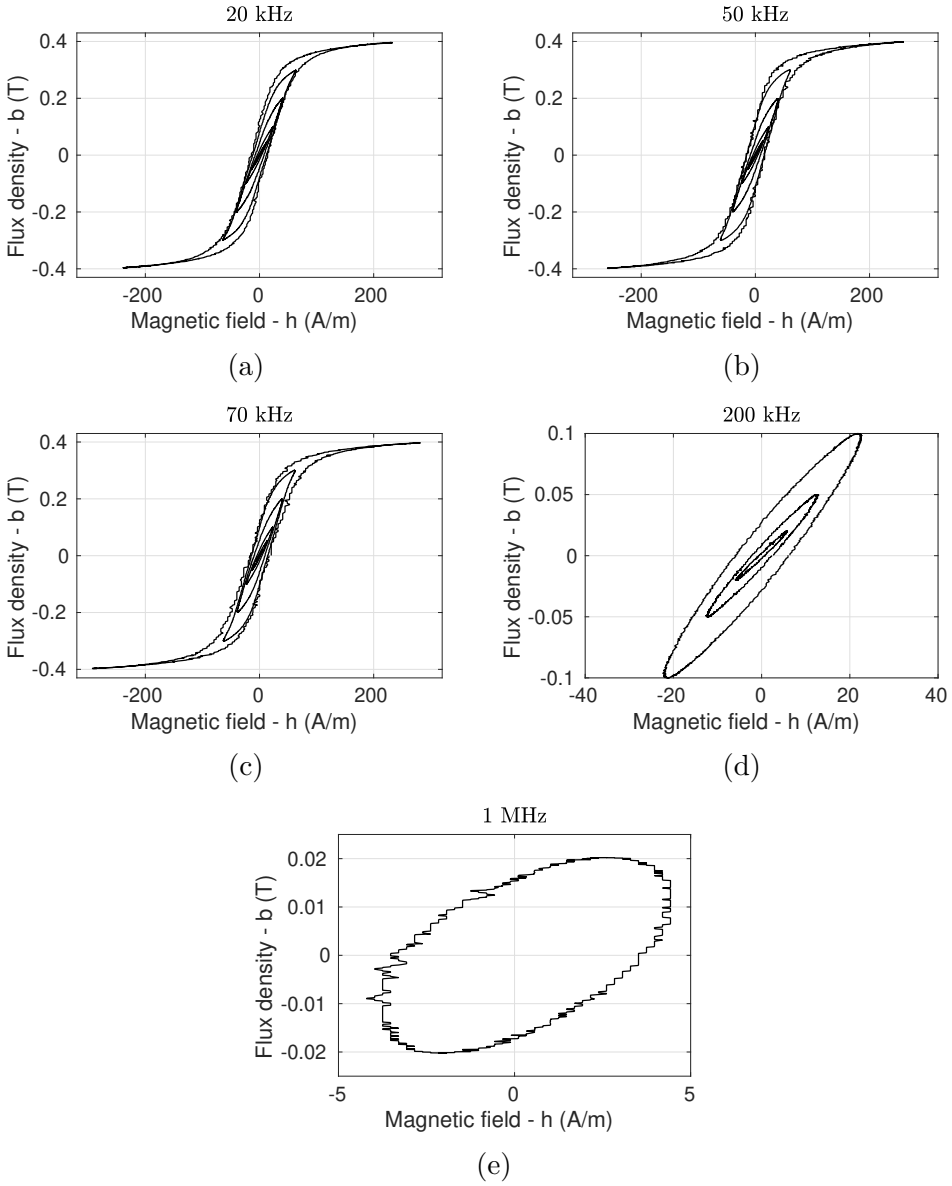

Figure A.2: Hysteresis cycles $b(h)$ measured at several frequencies.

Appendix B

Finite Element Formulations

B.1 Introduction

In the case of quasi-static magnetic applications, displacement currents are neglected and the Maxwell equations write:

$$\operatorname{curl} \mathbf{e} = -\partial_t \mathbf{b} \tag{B.1}$$

$$\operatorname{curl} \mathbf{h} = \mathbf{j} \tag{B.2}$$

$$\operatorname{div} \mathbf{b} = 0 \tag{B.3}$$

A magnetic vector potential $\mathbf{a}$ and an electric scalar potential v can be defined:

$$\mathbf{b} = \operatorname{curl} \mathbf{a} \qquad ; \qquad \mathbf{e} = -\partial_t \mathbf{a} - \operatorname{grad} v \tag{B.4}$$

The choice of these potential is not unique; in general a gauge has to be imposed, for instance $\operatorname{div} \mathbf{a} = 0$. However, in 2D plane modeling the magnetic vector potential $\mathbf{a}$ is perpendicular to the plain, so that this gauge is imposed by construction.

The problem is well posed when constitutive equations and appropriate boundary conditions are imposed. All these quantities fit into Tonti's diagram:

$$\begin{array}{ccccccc} v & \xrightarrow{\text{grad}} & \mathbf{e}, \mathbf{a} & \xrightarrow{\text{curl}} & \mathbf{b} & \xrightarrow{\text{div}} & 0 \\ & & \updownarrow \sigma, \epsilon & & \updownarrow \mu & & \\ 0 & \xleftarrow{\text{div}} & \mathbf{j} & \xleftarrow{\text{curl}} & \mathbf{h} & & \end{array} \tag{B.5}$$

This diagram is composed of two sequences of fields (the "**e**-row" and the "**h**-row"), which are represented horizontally. Constitutive laws are represented vertically, and represent the link between the **e**-row and the **h**-row.

In classical Finite Element modeling constitutive laws and one equation among (B.1) and (B.2) are imposed strongly, whereas the remaining equation is imposed weakly. In 2D is practical to strongly impose (B.1), which is done by imposing (B.4). The electric field $\mathbf{e}$ and the vector potential $\mathbf{a}$ *in conductive regions*[1] are both perpendicular to the plane xy, whereas the magnetic field $\mathbf{h}$ and flux density $\mathbf{b}$ lie in the plane xy. Observe that $\operatorname{grad} v$ is a perpendicular vector, and that it is uniform on each connected conductor.

[1] In 2D modeling the electric field is perpendicular to the plane in the coils and in massive conductors, but *not* in insulators. However the electric field is usually not computed in insulators, hence this fact is often forgotten.

B.2 Magnetodynamic $\mathbf{a} - v$ formulation

Ampère's law (B.2) is imposed in a weak sense by writing:

$$\iint_\Omega \mathbf{h} \cdot \operatorname{curl} \mathbf{a}' \, \partial\Omega + \int_{\partial\Omega} \mathbf{n} \times \mathbf{h} \cdot \mathbf{a}' \, d\partial\Omega - \iint_{\Omega_s} \mathbf{j} \cdot \mathbf{a}' \, \partial\Omega_s = 0 \tag{B.6}$$

$$- \iint_\Omega \mathbf{j} \cdot \operatorname{grad} v' \, \partial\Omega + \int_{\partial\Omega} \mathbf{n} \cdot \mathbf{j} v' \, d\partial\Omega = 0 \tag{B.7}$$

for any test function $\mathbf{a}'$ and v' belonging to an appropriate function space. The boundary terms vanish in the outer boundary (modeling the infinite or symmetry axes).

The current density writes:

$$\mathbf{j} = \mathbf{j}_s + \sigma \mathbf{e} = \mathbf{j}_s - \sigma(\partial_t \mathbf{a} + \operatorname{grad} v) \tag{B.8}$$

where $\mathbf{j}_s$ is the current in stranded coils. One observes that if no massive conductors are present, then $\sigma \equiv 0$ identically in the computational domain, hence the $\mathbf{a} - v$ formulation reduces to the magnetostatic $\mathbf{a}$ formulation.

B.2.1 Current-driven stranded coils

In stranded coils, eddy currents in the wires are neglected and the current density writes:

$$\mathbf{j}_s = \sum_n \frac{N_n I_n}{S_n} \hat{\mathbf{k}}_n = \sum_n I_n \mathbf{w}_n \tag{B.9}$$

where S_n is the section of the n-th coil, $\hat{\mathbf{k}}_n$ is the unitary vector oriented along the z direction, N_n is the number of turns and I_n is the current intensity, and $\mathbf{w}_n = N_n / S_n \hat{\mathbf{k}}_n$ is called the wire density vector. The orientation of $\mathbf{w}_n$ accounts for the direction of current. Current in stranded coils is imposed strongly. If all conductors excepted stranded coils are short-circuited, formulation can be simplified by imposing:

$$v = 0 \tag{B.10}$$

Therefore the electric field writes:

$$\mathbf{e} = -\partial_t \mathbf{a} \tag{B.11}$$

and (B.7) is unnecessary. Hence the magnetodynamic formulation reduces to (B.6) and writes:

$$\iint_\Omega \mathbf{h} \cdot \operatorname{curl} \mathbf{a}' \, \partial\Omega + \partial_t \iint_\Omega \sigma \mathbf{a} \cdot \mathbf{a}' \, \partial\Omega = \sum_n I_n \iint_\Omega \mathbf{w}_n \cdot \mathbf{a}' \, \partial\Omega \tag{B.12}$$

The boundary term usually vanishes due to natural (Neumann) boundary conditions.

B.2.2 Voltage-driven stranded coils

When voltages have to be imposed, the corresponding current is of course an unknown of the problem. Therefore we must add to the formulation a number of supplementary equations corresponding to the number of coils where the voltage is imposed. For each of these coils $\Omega_{s,n}$ the following equation must be imposed:

$$U_n = R_n I_n + \partial_t \Phi_n \tag{B.13}$$

where R_n is the resistance of the coil, which has to be known[2] and Φ_n is the magnetic flux linked with the coil. It can be demonstrated that this flux writes:

$$\Phi_n = \iint_{\Omega_{s,n}} \mathbf{a} \cdot \mathbf{w}_n \; \partial\Omega_{s,n} \tag{B.14}$$

Therefore, the problem can be formulated as:

$$\iint_{\Omega} \mathbf{h} \cdot \operatorname{curl} \mathbf{a}' \; \partial\Omega + \partial_t \iint_{\Omega} \sigma \mathbf{a} \cdot \mathbf{a}' \; \partial\Omega = \sum_n I_n \iint_{\Omega} \mathbf{w}_n \cdot \mathbf{a}' \; \partial\Omega \tag{B.15}$$

$$U_n = R_n I_n + \partial_t \iint_{\Omega_{s,n}} \mathbf{a} \cdot \mathbf{w}_n \; \partial\Omega_{s,n} \tag{B.16}$$

Remark that (B.16) can always be written:

- If the current I_n is imposed, it is used in post-processing to compute the voltage U_n,
- If the voltage U_n is imposed, the equation is part of the linear system to be solved so as to compute the current I_n, which is then an unknown of the problem.

Moreover, (B.16) allows to couple the Finite Element model with electric circuits. Circuits equations can be written by using the classical modified nodal analysis (other methods exist), and can be solved simultaneously with the Finite Element problem.

B.3 Time discretization

In order to solve numerically, (B.15)-(B.16) must be discretised both in space and time domain. As for time domain discretisation, the simplest approach is backward Euler scheme which writes:

$$\partial_t \mathbf{a}(t) \simeq \frac{\mathbf{a}(t_{i+1}) - \mathbf{a}(t_i)}{t_{i+1} - t_i} \tag{B.17}$$

By using this method, a linear system has to be solved at each time step. The solution of the previous time step becomes a source term (together with imposed voltages and currents) to compute the next one.

[2] In the case of massive coils, the conductivity σ allows to formulate the problem in such a way that the resistance R_n is computed in post-processing. The case of stranded coils is quite different: the resistance R_n has to be known.

Appendix C

Gallery of Finite Element simulations

C.1 Case 2

C.1.1 Case 2a: phase-shift $\phi = 45°$

Figures C.1 and C.2 show the currents in the windings obtained from the simulations compared to the measured ones. Predictions provide the same output and the simulated results are in agreement with the measured ones.

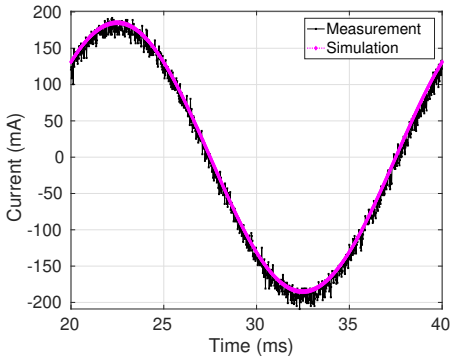

(a) Current in the winding N_3.

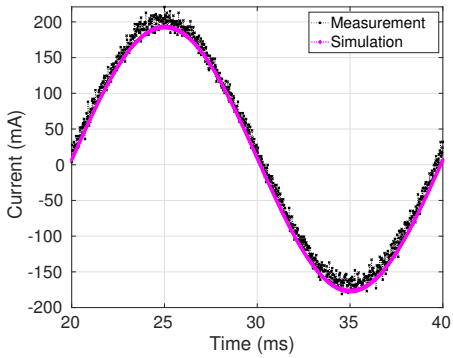

(b) Current in the winding N_4.

Figure C.1: Case 2a (low amplitude). Comparison of the measured currents in the windings with the simulation with the EB hysteresis model.

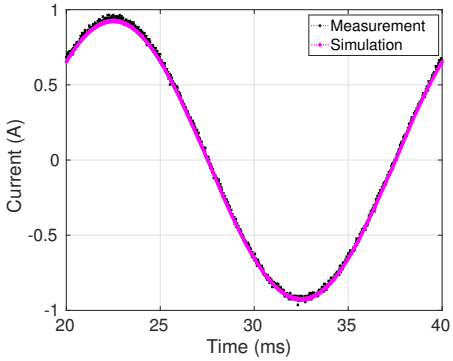

(a) Current in the winding N_3.

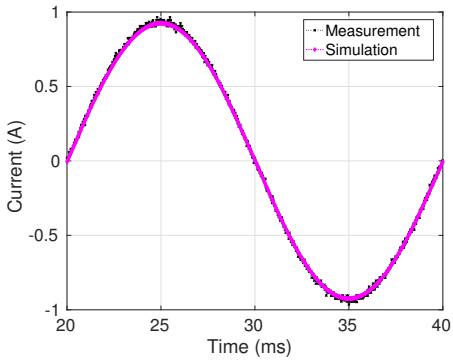

(b) Current in the winding N_4.

Figure C.2: Case 2a (high amplitude). Comparison of the measured currents in the windings with the simulation with the EB hysteresis model.

In Figure C.3 the computed voltages are compared to the measured data obtained in the measurement winding (N_1) for low and high amplitudes.

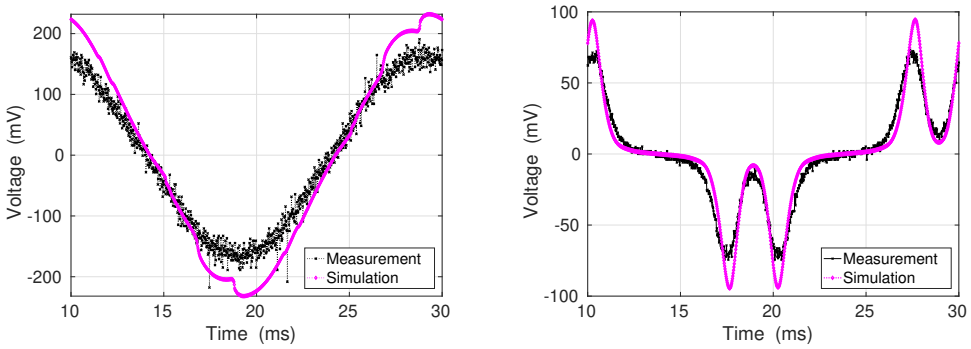

(a) Low amplitude ($V_p = 1$ V). (b) High amplitude ($V_p = 5$ V).

Figure C.3: Case 2a. Measured and simulated voltage in the central leg.

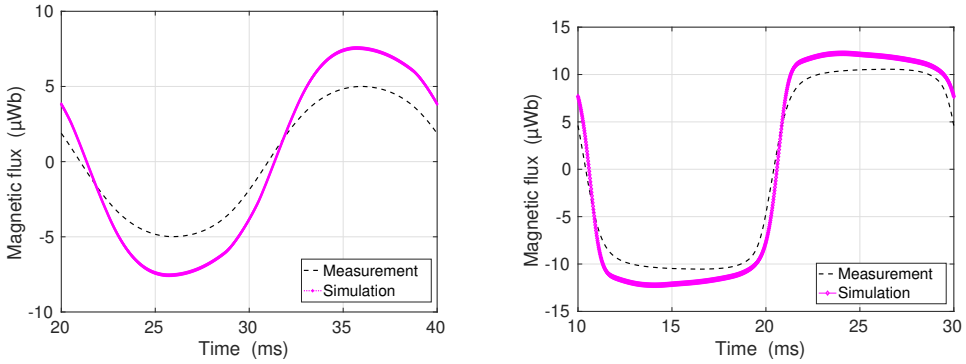

(a) Low amplitude ($V_p = 1$ V). (b) High amplitude ($V_p = 5$ V).

Figure C.4: Case 2a. Magnetic flux Φ_{12} going in the central leg from winding N_3.

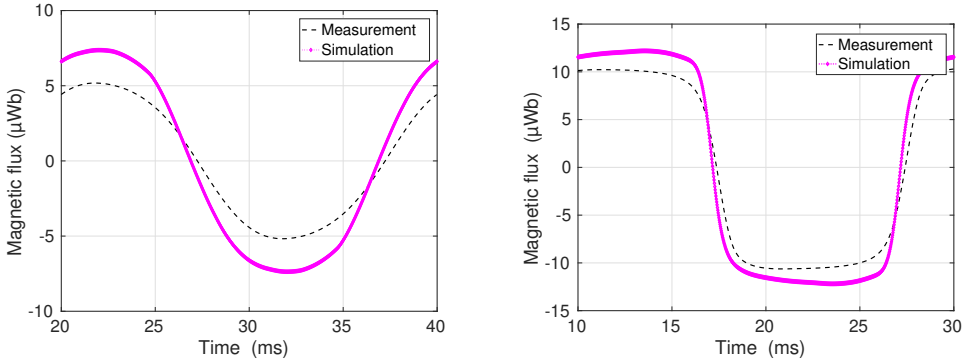

(a) Low amplitude ($V_p = 1$ V). (b) High amplitude ($V_p = 5$ V).

Figure C.5: Case 2a. Magnetic flux Φ_{34} going in the central leg from winding N_4.

C.1.2 Case 2c: phase-shift $\phi = 315°$

The waveform of computed and measured supply currents in the two windings are compared in Fig. 10.

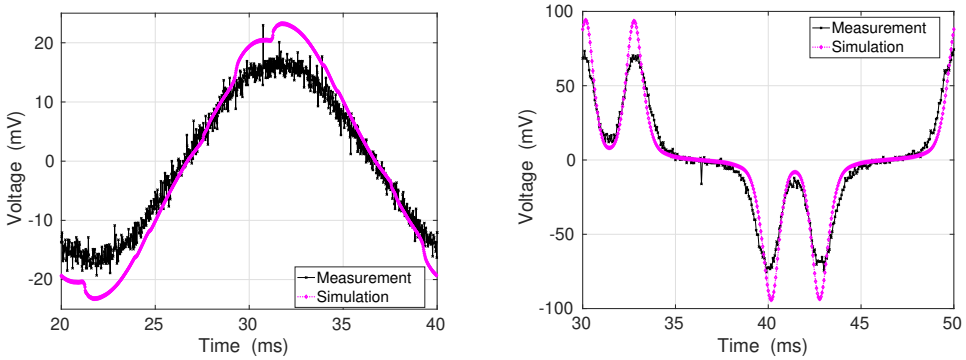

(a) Low amplitude ($V_p = 1$ V). (b) High amplitude ($V_p = 5$ V).

Figure C.6: Case 2c. Measured and simulated voltage in the central leg.

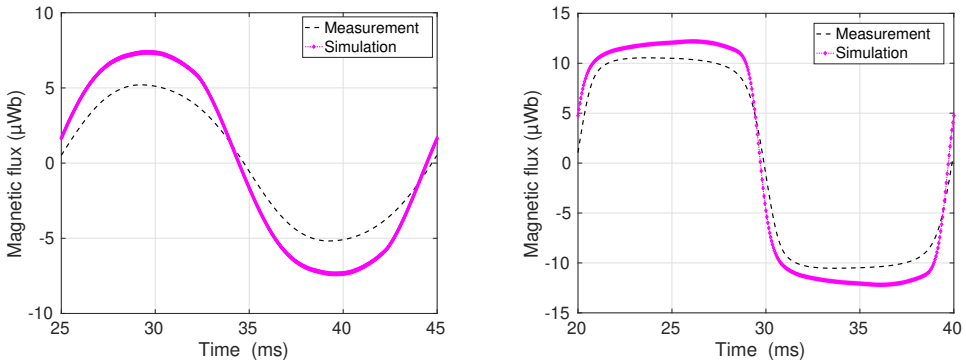

(a) Low amplitude ($V_p = 1$ V). (b) High amplitude ($V_p = 5$ V).

Figure C.7: Case 2c. Magnetic flux Φ going in the central leg from winding N_3.

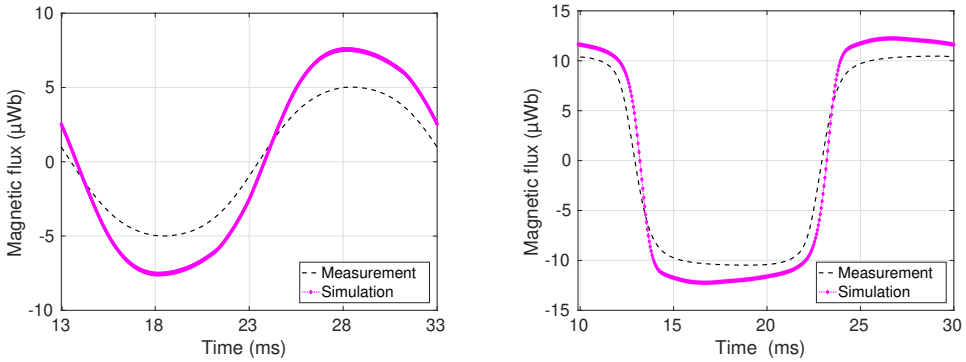

(a) Low amplitude ($V_p = 1$ V). (b) High amplitude ($V_p = 5$ V).

Figure C.8: Case 2c. Magnetic flux Φ going in the central leg from winding N_4.

C.2 Case 3

C.2.1 Case 3a: $f_1 = 3f$, $\phi = 0°$

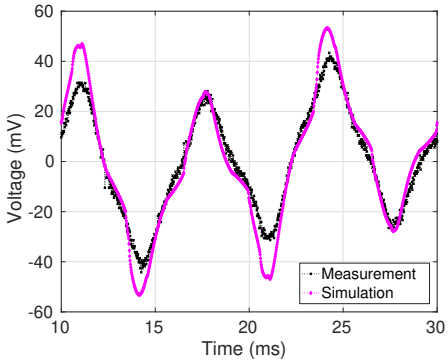

(a) $V_p = 1$ V.

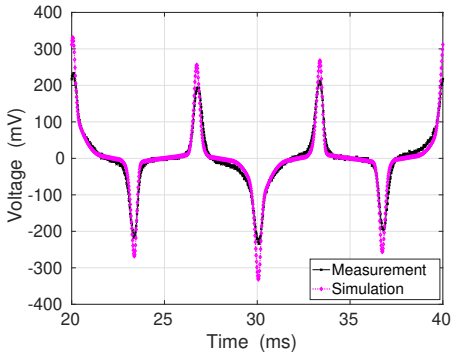

(b) $V_p = 5$ V.

Figure C.9: Case 3a. Measured and simulated voltage in the central leg.

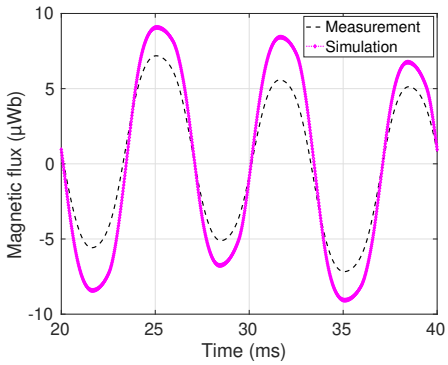

(a) Low amplitude ($V_p = 1$ V).

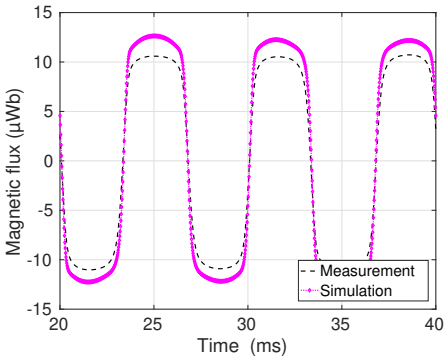

(b) High amplitude ($V_p = 5$ V).

Figure C.10: Case 3a. Magnetic flux Φ going in the central leg from winding N_3.

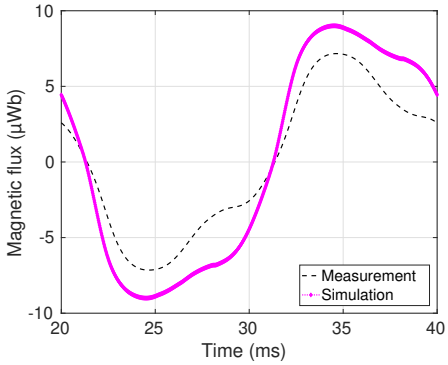

(a) Low amplitude ($V_p = 1$ V).

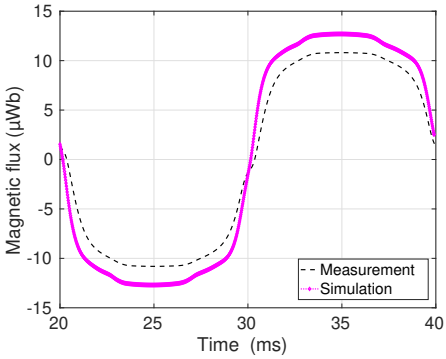

(b) High amplitude ($V_p = 5$ V).

Figure C.11: Case 3a. Magnetic flux Φ going in the central leg from winding N_4.

C.2.2 Case 3d: $f_1 = 5f$, $\phi = 90°$

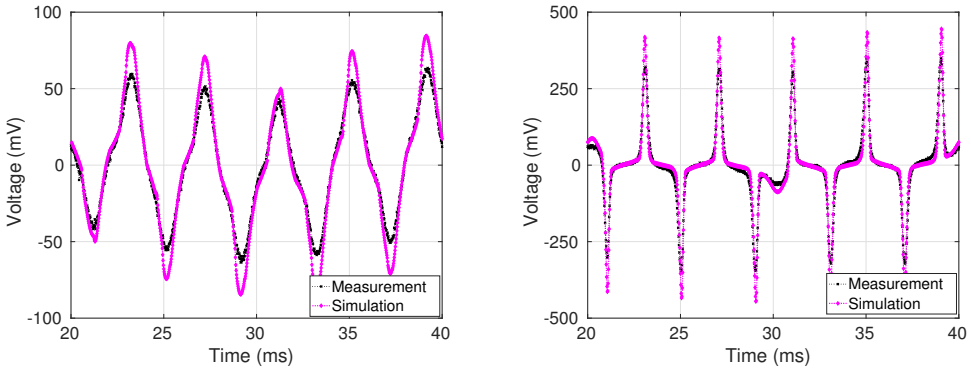

(a) Low amplitude ($V_p = 1$ V). (b) High amplitude ($V_p = 5$ V).

Figure C.12: Case 3d. Measured and simulated voltage in the central leg.

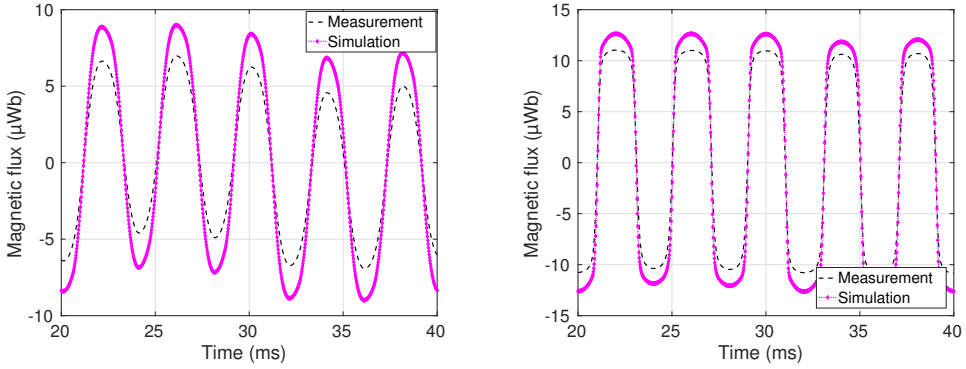

(a) Low amplitude ($V_p = 1$ V). (b) High amplitude ($V_p = 5$ V).

Figure C.13: Case 3d. Magnetic flux Φ going in the central leg from winding N_3.

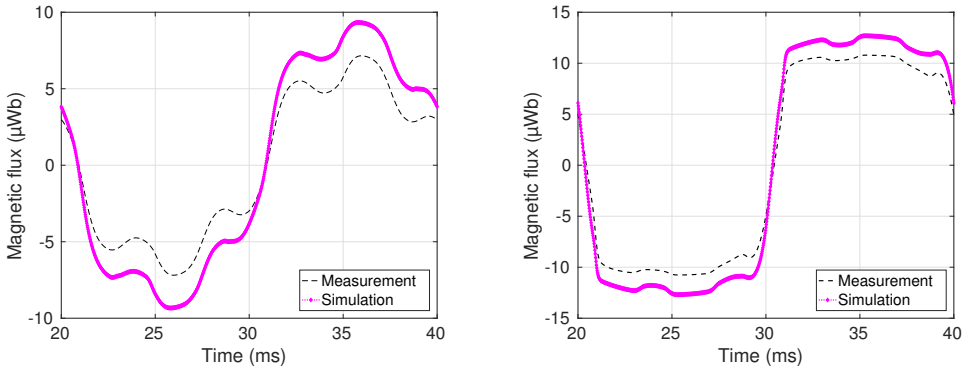

(a) Low amplitude ($V_p = 1$ V). (b) High amplitude ($V_p = 5$ V).

Figure C.14: Case 3d. Magnetic flux Φ going in the central leg from winding N_4.

Bibliography

[1] D. R. Askeland and W. J. Wright, The Science and Engineering of Materials, SI Edition. CL-Engineering, 7th ed., 2014.

[2] L. Daniel, Multi-scale modelling of the magneto-mechanical behaviour of ferromagnetic textured materials. PhD thesis, École normale supérieure de Cachan - ENS Cachan, 2003.

[3] P. Robert, Matériaux de l'électrotechnique. Traité de l'électricité. PPUR, 1999.

[4] A. Guennou, P. Queffelec, P. Gelin, and J. L. Mattei, "Coupled Magnetostatic/Electromagnetic Studies of Nonuniformly Biased Y-Junction Circulator: Application to Transmission Bandwidth Increase," IEEE Transactions on Magnetics, vol. 43, pp. 3645–3651, Sept. 2007.

[5] A. Hubert and R. Schäfer, Magnetic domains : the analysis of magnetic microstructures. Berlin: Springer, 1998.

[6] R. Becker and W. Döring, Ferromagnetismus. Berlin, Heidelberg: Springer Berlin Heidelberg, 1939.

[7] G. Bertotti, Hysteresis in Magnetism. San Diego: Academic Press, 1998.

[8] J. M. D. Coey, Magnetism and Magnetic Materials. Cambridge University Press, 2010.

[9] F. Fiorillo, G. Bertotti, C. Appino, and M. Pasquale, "Soft magnetic materials," Wiley Encyclopedia of Electrical and Electronics Engineering, Nov 2016.

[10] A. Bergqvist, "Magnetic vector hysteresis model with dry friction-like pinning," vol. Physica B, no. 233, pp. 342–347, 1997.

[11] O. Messal, Caractérisation et modélisation du comportement thermomagnétique d'alliages FeNi pour le prototypage virtuel. PhD thesis, Claude Bernard Lyon I, 2013.

[12] H. Lu, Y. Guo, J. Zhu, J. Zhong, and J. Jin, "Soft magnetic materials for high frequency high power density transformers in power electronic systems," 2007.

[13] A. Leary, P. Ohodnicki, and M. McHenry, "Soft magnetic materials in high-frequency, high-power conversion applications," JOM Journal of the Minerals, vol. 64, 07 2012.

[14] E. Cardelli, "Chapter 4 - Advances in Magnetic Hysteresis Modeling," vol. 24 of Handbook of Magnetic Materials, pp. 323 – 409, Elsevier, 2015.

[15] G. Fournet, Électromagnétisme à partir des équations locales. Masson, 1979.

[16] R. Hilzinger and W. Rodewald, Magnetic materials: fundamentals, products, properties, applications. Vacuumschmelze, 2013.

[17] S. Steentjes, Efficiently modeling soft magnetic materials for transformers, actuators and rotating electrical machines. Dissertation, RWTH Aachen University, Aachen, 2018.

[18] L. Rayleigh, "XXV. Notes on electricity and magnetism.— iii. On the behaviour of iron and steel under the operation of feeble magnetic forces," The London, Edinburgh, and Dublin Philosophical Magazine and Journal of Science, vol. 23, no. 142, pp. 225–245, 1887.

[19] BS EN 60404-1:2017 - Magnetic materials. Classification. 2017.

[20] S. Tumanski, Handbook of magnetic measurements / S Tumanski. Boca Raton: CRC Press, 2011.

[21] [Online]. Available: https://spectrum-magnetics.com/products/soft-magnetic-materials/.

[22] T. Waeckerlé, "Matériaux magnétiques doux cristallins magnétisme et métallurgie appliqués," Techniques de l'ingénieur Matériaux magnétiques en électrotechnique, vol. base documentaire : TIB259DUO., no. ref. article : d2121, 2010.

[23] A. Frias, Minimization of iron loss of traction electrical motors by modeling and optimization systems. PhD thesis, Claude Bernard Lyon I, 2015.

[24] A. Krings, Iron Losses in Electrical Machines - Influence of Material Properties, Manufacturing Processes, and Inverter Operation. PhD thesis, KTH, Electrical Energy Conversion, 2014.

[25] H. Jordan, "Die ferromagnetischen konstanten für schwache wechselfelder," Elektr. Nach. Techn, vol. 1, p. 8, 1924.

[26] R. H. Pry and C. P. Bean, "Calculation of the Energy Loss in Magnetic Sheet Materials Using a Domain Model," Journal of Applied Physics, vol. 29, pp. 532–533, Mar. 1958.

[27] G. Bertotti, "Connection between microstructure and magnetic properties of soft magnetic materials," Journal of Magnetism and Magnetic Materials, vol. 320, no. 20, pp. 2436 – 2442, 2008.

[28] G. Bertotti, G. Di Schino, A. Ferro Milone, and F. Fiorillo, "On the effect of grain size on magnetic losses of 3% non-oriented SiFe," J. Phys. Colloques, vol. 46, pp. C6–385–388, Sept. 1985.

[29] F. Preisach, "Über die magnetische Nachwirkung," vol. 94, no. 1, pp. 277–302, May 1935.

[30] F. Preisach, "On the Magnetic Aftereffect," IEEE Transactions on Magnetics, vol. 53, pp. 1–11, Mar. 2017.

[31] I. Mayergoyz, Mathematical models of hysteresis. Springer, 1991.

[32] I. Mayergoyz, G. Friedman, and C. Salling, "Comparison of the classical and generalized Preisach hysteresis models with experiments," IEEE Transactions on Magnetics, vol. 25, pp. 3925–3927, Sept. 1989.

[33] D. C. Jiles and D. L. Atherton, "Theory of ferromagnetic hysteresis," Journal of Magnetism and Magnetic Materials, vol. 61, pp. 48–60, Sept. 1986.

[34] A. Stancu and L. Spinu, "Temperature- and time-dependent Preisach model for a Stoner–Wohlfarth particle system," IEEE Transactions on Magnetics, vol. 34, pp. 3867–3875, Nov 1998.

[35] T. Song and R. Roshko, "Preisach model for systems of interacting superparamagnetic particles," IEEE Transactions on Magnetics, vol. 36, pp. 223–230, Jan. 2000.

[36] A. Raghunathan, Y. Melikhov, J. E. Snyder, and D. C. Jiles, "Theoretical Model of Temperature Dependence of Hysteresis Based on Mean Field Theory," IEEE Transactions on Magnetics, vol. 46, pp. 1507–1510, June 2010.

[37] L. Dupré, J. Gyselinck, and J. Melkebeek, "Complementary finite element methods in 2d magnetics taking into account a vector Preisach model," IEEE Transactions on Magnetics, vol. 34, pp. 3048–3051, Sept. 1998.

[38] G. Friedman and I. Mayergoyz, "Hysteretic energy losses in media described by vector Preisach model," IEEE Transactions on Magnetics, vol. 34, pp. 1270–1272, July 1998.

[39] J. Gyselinck, L. Vandevelde, D. Makaveev, and J. Melkebeek, "Calculation of no load losses in an induction motor using an inverse vector Preisach model and an eddy current loss model," IEEE Transactions on Magnetics, vol. 36, pp. 856–860, July 2000.

[40] J. Saitz, "Computation of the core loss in an induction motor using the vector Preisach hysteresis model incorporated in finite element analysis," IEEE Transactions on Magnetics, vol. 36, pp. 769–773, July 2000.

[41] I. Mayergoyz, Mathematical Models of Hysteresis and Their Applications. Electromagnetism, New York: Elsevier Science, 2003.

[42] A. Bergqvist, "A simple vector generalization of the Jiles-Atherton model of hysteresis," IEEE Transactions on Magnetics, vol. 32, pp. 4213–4215, Sept. 1996.

[43] J. Gyselinck, P. Dular, N. Sadowski, J. Leite, and J. Bastos, "Incorporation of a Jiles–Atherton vector hysteresis model in 2D FE magnetic field computations: Application of the Newton–Raphson method," COMPEL: The International Journal for Computation and Mathematics in Electrical and Electronic Engineering, vol. 23, pp. 685–693, 09 2004.

[44] J. Leite, N. Sadowski, P. Kuo-Peng, N. Batistela, J. Bastos, and A. de Espindola, "Inverse Jiles–Atherton Vector Hysteresis Model," IEEE Transactions on Magnetics, vol. 40, pp. 1769–1775, July 2004.

[45] J. V. Leite, M. V. Ferreira da Luz, N. Sadowski, and P. A. da Silva, "Modelling Dynamic Losses Under Rotational Magnetic Flux," IEEE Transactions on Magnetics, vol. 48, pp. 895–898, Feb. 2012.

[46] F. Henrotte and K. Hameyer, "A dynamical vector hysteresis model based on an energy approach," IEEE Transactions on Magnetics, vol. 42, pp. 899–902, Apr. 2006.

[47] K. Jacques, Energy-Based Magnetic Hysteresis Models - Theoretical Development and Finite Element Formulations. PhD thesis, Université de Liège, Belgique, 2018.

[48] T. Matsuo, D. Shimode, Y. Terada, and M. Shimasaki, "Application of stop and play models to the representation of magnetic characteristics of silicon steel sheet," IEEE Transactions on Magnetics, vol. 39, pp. 1361–1364, May 2003.

[49] T. Matsuo and M. Shimasaki, "Two Types of Isotropic Vector Play Models and Their Rotational Hysteresis Losses," IEEE Transactions on Magnetics, vol. 44, pp. 898–901, June 2008.

[50] M. Novak, J. Eichler, and M. Kosek, "Difficulty in identification of preisach hysteresis model weighting function using first order reversal curves method in soft magnetic materials," Applied Mathematics and Computation, vol. 319, pp. 469–485, 2018.

[51] A. Stancu, Analysis of the Identification Methodologies in Preisach Modeling, pp. 173–177. Dordrecht: Springer Netherlands, 1997.

[52] M. Tousignant, Modélisation de l'hystérésis et des courants de Foucault dans les circuits magnétiques par la méthode des éléments finis. PhD thesis, Communauté Université Grenoble Alpes, France, 2019.

[53] D. C. Jiles and D. L. Atherton, "Ferromagnetic hysteresis," IEEE Transactions on Magnetics, vol. MAG-19, Sept. 1983.

[54] D. C. Jiles and D. L. Atherton, "Theory of ferromagnetic hysteresis (invited)," Journal of Applied Physics, vol. 55, pp. 2115–2120, Mar. 1984.

[55] D. C. Jiles and D. L. Atherton, "Theory of ferromagnetic hysteresis," Journal of Magnetism and Magnetic Materials, vol. 61, no. 1–2, pp. 48 – 60, 1986.

[56] P. Weiss, "L'hypothèse du champ moléculaire et la propriété ferromagnétique," J. Phys. Theor. Appl., vol. 6, no. 1, pp. 661–690, 1907.

[57] J. Leite, S. Avila, N. Batistela, W. Carpes, N. Sadowski, P. Kuo-Peng, and J. Bastos, "Real Coded Genetic Algorithm for Jiles–Atherton Model Parameters Identification," IEEE Transactions on Magnetics, vol. 40, pp. 888–891, Mar. 2004.

[58] K. Chwastek and J. Szczyglowski, "Identification of a hysteresis model parameters with genetic algorithms," Mathematics and Computers in Simulation, vol. 71, pp. 206–211, May 2006.

[59] R. Marion, R. Scorretti, N. Siauve, M.-A. Raulet, and L. Krähenbühl, "Identification of Jiles–Atherton Model Parameters Using Particle Swarm Optimization," IEEE Transactions on Magnetics, vol. 44, pp. 894–897, June 2008.

[60] A. Benabou, S. Clénet, and F. Piriou, "Comparison of Preisach and Jiles–Atherton models to take into account hysteresis phenomenon for finite element analysis," Journal of Magnetism and Magnetic Materials, vol. 261, pp. 139–160, Apr. 2003.

[61] S. E. Zirka, Y. I. Moroz, R. G. Harrison, and K. Chwastek, "On physical aspects of the Jiles-Atherton hysteresis models," Journal of Applied Physics, vol. 112, no. 4, 2012.

[62] M. Petrun, S. Steentjes, K. Hameyer, and D. Dolinar, "Comparison of static hysteresis models subject to arbitrary magnetization waveforms," COMPEL - The International Journal of Computations and Mathematics in Electrical and Electronic Engineering, vol. 36, pp. 774–790, May 2017.

[63] K. Carpenter, "A differential equation approach to minor loops in the Jiles-Atherton hysteresis model," IEEE Transactions on Magnetics, vol. 27, pp. 4404–4406, Nov. 1991.

[64] D. Jiles, "A self consistent generalized model for the calculation of minor loop excursions in the theory of hysteresis," IEEE Transactions on Magnetics, vol. 28, pp. 2602–2604, Sept. 1992.

[65] A. Benabou, J. Leite, S. Clénet, C. Simão, and N. Sadowski, "Minor loops modelling with a modified Jiles–Atherton model and comparison with the Preisach model," Journal of Magnetism and Magnetic Materials, vol. 320, pp. e1034–e1038, Oct. 2008.

[66] D. Miljavec and B. Zidarič, "Introducing a domain flexing function in the Jiles–Atherton hysteresis model," Journal of Magnetism and Magnetic Materials, vol. 320, pp. 763–768, Mar. 2008.

[67] J. Leite, A. Benabou, and N. Sadowski, "Accurate minor loops calculation with a modified jiles-atherton hysteresis model," COMPEL: The International Journal for Computation and Mathematics in Electrical and Electronic Engineering, vol. 28, pp. 741–749, 05 2009.

[68] F. Henrotte, A. Nicolet, and K. Hameyer, "An energy-based vector hysteresis model for ferromagnetic materials," COMPEL - The International Journal of Computations and Mathematics in Electrical and Electronic Engineering, vol. 25, pp. 71–80, Jan. 2006.

[69] V. François-Lavet, F. Henrotte, L. Stainier, L. Noels, and C. Geuzaine, "Vectorial Incremental Nonconservative Consistent Hysteresis model," ACOMEN, Nov. 2011.

[70] F. Henrotte, S. Steentjes, K. Hameyer, and C. Geuzaine, "Iron Loss Calculation in Steel Laminations at High Frequencies," IEEE Transactions on Magnetics, vol. 50, pp. 333–336, Feb. 2014.

[71] S. Steentjes, F. Henrotte, C. Geuzaine, and K. Hameyer, "A dynamical energy-based hysteresis model for iron loss calculation in laminated cores," International Journal of Numerical Modelling: Electronic Networks, Devices and Fields, vol. 27, no. 3, pp. 433–443, 2014.

[72] F. Henrotte and K. Hameyer, "A dynamical vector hysteresis model based on an energy approach," IEEE Transactions on Magnetics, vol. 42, pp. 899–902, Apr. 2006.

[73] A. Bergqvist, A. Lundgren, and G. Engdahl, "Experimental testing of an anisotropic vector hysteresis model," IEEE Transactions on Magnetics, vol. 33, pp. 4152–4154, Sept. 1997.

[74] F. Sixdenier and R. Scorretti, "Numerical model of static hysteresis taking into account temperature: Static hysteresis taking into account temperature," International Journal of Numerical Modelling: Electronic Networks, Devices and Fields, vol. 31, p. e2221, Mar. 2018.

[75] O. Messal, F. Sixdenier, L. Morel, and N. Burais, "Temperature Dependent Extension of the Jiles-Atherton Model Study of the Variation of Microstructural Hysteresis Parameters," IEEE Transactions on Magnetics, vol. 48, pp. 2567–2572, Oct. 2012.

[76] P. D. Mitchler, E. D. Dahlberg, E. E. Wesseling, and R. M. Roshko, "Henkel plots in a temperature and time dependent preisach model," IEEE Transactions on Magnetics, vol. 32, pp. 3185–3194, July 1996.

[77] V. François-Lavet, F. Henrotte, L. Stainier, L. Noels, and C. Geuzaine, "An Energy-Based Variational Model of Ferromagnetic Hysteresis for Finite Element Computations," IEEE Transactions on Magnetics, vol. 49, May 2013.

[78] D. Lin, P. Zhou, and A. Bergqvist, "Improved vector play model and parameter identification for magnetic hysteresis materials," IEEE Transactions on Magnetics, vol. 50, pp. 357–360, Feb 2014.

[79] A. Bergqvist, D. Lin, and P. Zhou, "Temperature-dependent vector hysteresis model for permanent magnets," IEEE Transactions on Magnetics, vol. 50, no. 2, pp. 345–348, 2014.

[80] P. Weiss, "La constante du champ moléculaire. Equation d'état magnétique et calorimétrie," Journal de Physique, vol. 1, no. 5, pp. 163–175, 1930.

[81] R. Gersdorf, "Ferromagnetic properties of fe and ni in relation to their band structure," Journal De Physique Et Le Radium, vol. 23, no. 10, pp. 726–729, 1962.

[82] J. Hopkinson, "Magnetic and other physical properties of iron at a high temperature," Philosophical Transactions of the Royal Society of London. A, vol. 180, pp. 443–465, 1889.

[83] N. Duan, W. Xu, S. Wang, J. Zhu, R. Qu, and S. Jia, "A Temperature-Dependent Hysteresis Model for Soft Ferrites," IEEE Transactions on Magnetics, vol. 53, pp. 1–4, June 2017.

[84] G. Bertotti, "Dynamic generalization of the scalar Preisach model of hysteresis," IEEE Transactions on Magnetics, vol. 28, pp. 2599–2601, Sept. 1992.

[85] L. Dupre, R. Van Keer, and J. Melkebeek, "On a magnetodynamic model for the iron losses in non-oriented steel laminations," Journal of Physics D: Applied Physics, vol. 29, no. 3, p. 855, 1996.

[86] L. Dupré, G. Bertotti, V. Basso, F. Fiorillo, and J. Melkebeek, "Generalisation of the dynamic Preisach model toward grain oriented Fe–Si alloys," Physica B: Condensed Matter, vol. 275, pp. 202–206, Jan. 2000.

[87] L. Dupré, R. Van Keer, and J. Melkebeek, "Modelling the electromagnetic behaviour of sife alloys using the preisach theory and the principle of loss seperation," Mathematical Problems in Engineering, vol. 7, no. 2, pp. 113–128, 2001.

[88] D. Jiles, "Frequency dependence of hysteresis curves in 'non-conducting' magnetic materials," IEEE Transactions on Magnetics, vol. 29, pp. 3490–3492, Nov. 1993.

[89] K. Chwastek, "Modelling of dynamic hysteresis loops using the Jiles–Atherton approach," Mathematical and Computer Modelling of Dynamical Systems, vol. 15, pp. 95–105, Feb. 2009.

[90] D. Zhang and J. E. Fletcher, "Double-Frequency Method Using Differential Evolution for Identifying Parameters in the Dynamic Jiles–Atherton Model of Mn–Zn Ferrites," IEEE Transactions on Instrumentation and Measurement, vol. 62, pp. 460–466, Feb. 2013.

[91] Ruoyang Du and P. Robertson, "Dynamic Jiles–Atherton Model for Determining the Magnetic Power Loss at High Frequency in Permanent Magnet Machines," IEEE Transactions on Magnetics, vol. 51, pp. 1–10, June 2015.

[92] M. Raulet, B. Ducharne, J. Masson, and G. Bayada, "The Magnetic Field Diffusion Equation Including Dynamic Hysteresis: A Linear Formulation of the Problem," IEEE Transactions on Magnetics, vol. 40, pp. 872–875, Mar. 2004.

[93] M. Raulet, F. Sixdenier, B. Guinand, L. Morel, and R. Goyet, "Limits and rules of use of a dynamic flux tube model," COMPEL - The international journal for computation and mathematics in electrical and electronic engineering, vol. 27, pp. 256–265, Jan. 2008.

[94] M.-A. Raulet, "Contribution à la modélisation des matériaux magnétiques liés à leur environnement en génie électrique," HDR, Énergie électrique. Université Claude Bernard - Lyon I, 2011.

[95] T. Chevalier, A. Kedous-Lebouc, B. Cornut, and C. Cester, "A new dynamic hysteresis model for electrical steel sheet," Physica B: Condensed Matter, vol. 275, pp. 197–201, Jan. 2000.

[96] T. Gautreau, Iron losses prediction in electrical motors. Loss Surface hysteresis model and application to synchronous permanent magnet machines. Theses, Institut National Polytechnique de Grenoble - INPG, Dec. 2005.

[97] A. T. Bui, Caractérisation et modélisation du comportement des matériaux magnétiques doux sous contrainte thermique. PhD thesis, Université Claude Bernard Lyon 1, 2011.

[98] S. Yan, J. Kotulski, and J.-M. Jin, "Nonlinear multiphysics and multiscale modeling of dynamic ferromagnetic–thermal problems," Journal of Applied Physics, vol. 123, p. 105107, 03 2018.

[99] IEC 60404-4. Magnetic materials - part 4. Methods of measurement of the d.c. magnetic properties of magnetically soft materials. November 2008.

[100] IEC 60404-6. Magnetic materials - part 6. Methods of measurement of the magnetic properties of magnetically soft metallic and powder materials at frequencies in the range 20 Hz to 100 kHz by the use of ring specimens. November 2018.

[101] F. Fiorillo, Measurement and characterization of magnetic materials. Amsterdam: Elsevier, 2004.

[102] D. Gordon, Direct-Current Magnetic Hysteresigraphs. ASTM International, 1973.

[103] "Soft Ferrites and Accessories - Data Handbook," 2013. [Online]. Available: https://elnamagnetics.com/wp-content/uploads/catalogs/Ferroxcube/catalog.pdf.

[104] [Online]. Available: https://www.laboratorio.elettrofisico.com.

[105] T. Guillod, J. Huber, F. Krismer, and J. W. Kolar, "Litz wire losses: Effects of twisting imperfections," in 2017 IEEE 18th Workshop on Control and Modeling for Power Electronics (COMPEL), pp. 1–8, IEEE, 2017.

[106] S. Zhao, Q. Li, F. C. Lee, and B. Li, "High-frequency transformer design for modular power conversion from medium-voltage ac to 400 vdc," IEEE Transactions on Power Electronics, vol. 33, no. 9, pp. 7545–7557, 2018.

[107] M. Leibl, G. Ortiz, and J. W. Kolar, "Design and experimental analysis of a medium-frequency transformer for solid-state transformer applications," IEEE Journal of Emerging and Selected Topics in Power Electronics, vol. 5, no. 1, pp. 110–123, 2017.

[108] J. Acero, R. Alonso, J. M. Burdio, L. A. Barragan, and D. Puyal, "Frequency-dependent resistance in litz-wire planar windings for domestic induction heating appliances," IEEE Transactions on Power Electronics, vol. 21, no. 4, pp. 856–866, 2006.

[109] K. Jacques, S. Steentjes, F. Henrotte, C. Geuzaine, and K. Hameyer, "Representation of microstructural features and magnetic anisotropy of electrical steels in an energy-based vector hysteresis model," AIP Advances, vol. 8, p. 047602, Apr. 2018.

[110] L. Prigozhin, V. Sokolovsky, J. W. Barrett, and S. E. Zirka, "On the energy-based variational model for vector magnetic hysteresis," IEEE Transactions on Magnetics, vol. 52, no. 12, pp. 1–11, 2016.

[111] J. Hauschild, H. Fritzsche, S. Bonn, and Y. Liu, "Determination of the temperature dependence of the coercivity in Fe/Cr (110) multilayers," Applied Physics A, vol. 74, pp. s1541–s1543, Dec 2002.

[112] M. Kachniarz and R. Szewczyk, "Study on the Rayleigh Hysteresis Model and its Applicability in Modeling Magnetic Hysteresis Phenomenon in Ferromagnetic Materials," Acta Physica Polonica A, vol. 131, pp. 1244–1250, May 2017.

[113] A. Raghavender, K. Zadro, D. Pajic, Z. Skoko, and N. Biliškov, "Effect of grain size on the Néel temperature of nanocrystalline nickel ferrite," Materials Letters, vol. 64, pp. 1144–1146, May 2010.

[114] A. Mager, "About the influence of grain size on the coercivity," Ann. Phys. Leipzig, vol. 446, pp. 15–16, 1952.

[115] E. Adler and H. Pfeiffer, "The influence of grain size and impurities on the magnetic properties of the soft magnetic alloy 47.5% NiFe," IEEE Transactions on Magnetics, vol. 10, pp. 172–174, June 1974.

[116] F. J. G. Landgraf, J. R. F. da Silveira, and D. Rodrigues-Jr., "Determining the effect of grain size and maximum induction upon coercive field of electrical steels," Journal of Magnetism and Magnetic Materials, vol. 323, pp. 2335–2339, Oct. 2011.

[117] M. R. Longhitano, F. Sixdenier, R. Scorretti, L. Krähenbühl, and C. Geuzaine, "Temperature-dependent hysteresis model for soft magnetic materials," COMPEL - The International Journal of Computations and Mathematics in Electrical and Electronic Engineering, vol. 38, no. 5, 2019.

[118] M. R. Longhitano, F. Sixdenier, R. Scorretti, C. Geuzaine, and L. Krähenbühl, "Test-case transformer for the energy-based vector hysteresis model," in 2019 22nd International Conference on the Computation of Electromagnetic Fields (COMPUMAG), pp. 1–4, July 2019.

[119] O. Bottauscio, M. Chiampi, C. Ragusa, L. Rege, and M. Repetto, "A test case for validation of magnetic field analysis with vector hysteresis," IEEE Transactions on Magnetics, vol. 38, pp. 893–896, Mar. 2002.

[120] [Online]. Available: http://onelab.info/.

[121] G. Bertotti, Hysteresis in Magnetism. Electromagnetism, San Diego: Academic Press, 1998.

[122] E. Barbisio, F. Fiorillo, and C. Ragusa, "Predicting loss in magnetic steels under arbitrary induction waveform and with minor hysteresis loops," IEEE Transactions on Magnetics, vol. 40, no. 4, pp. 1810–1819, 2004.

[123] D. C. Jiles, "Modelling the effects of eddy current losses on frequency dependent hysteresis in electrically conducting media," IEEE Transactions on Magnetics, vol. 30, pp. 4326–4328, Nov 1994.

[124] D. Ribbenfjard and G. Engdahl, "Modeling of dynamic hysteresis with bergqvist's lag model," IEEE Transactions on Magnetics, vol. 42, pp. 3135–3137, Oct 2006.

[125] M. R. Longhitano, F. Sixdenier, R. Scorretti, C. Geuzaine, F. Henrotte, and L. Krähenbühl, "Comparison of identification protocols of a static hysteresis model," in 2019 22nd International Conference on the Computation of Electromagnetic Fields (COMPUMAG), pp. 1–4, July 2019.

[126] H. Kronmüller and M. Fähnle, "Micromagnetism and the microstructure of ferromagnetic solids," Micromagnetism and the Microstructure of Ferromagnetic Solids, Cambridge, UK: Cambridge University Press, 2009, Oct 2009.

[127] M. R. Longhitano, F. Sixdenier, R. Scorretti, and L. Krähenbühl, "Les paramètres d'un modèle d'hystérésis statique peuvent-ils renseigner sur la microstructure d'un matériau ?," in Symposium de Génie Electrique (SGE'18), (Nancy, France), July 2018.

[128] Y. Yamamoto and A. Makino, "Application of mn-zn ferrite with fine grain size to magnetic heads.," Journal of the Japan Society of Powder and Powder Metallurgy, vol. 40, pp. 881–885, Sept 1993.

[129] S. Zajac, B. Hutchinson, R. Lagneborg, and M. Korchynsky, "Ferrite grain refinement in seamless pipes through intragranular nucleation on vn," 3rd International Conference on Thermomechanical Processing of Steels, TMP 2008, vol. 101, Feb 2009.

[130] M. Sugimoto, "The past, present, and future of ferrites," Journal of the American Ceramic Society, vol. 82, no. 2, pp. 269–280, 1999.

[131] E. Hamzah, M. Mudang, and M. Khattak, "Effect of variation in grain size on high temperature creep test of fe-ni-cr alloy," Advanced Materials Research, vol. 845, pp. 51–55, 12 2013.

[132] A. Benabou, Contribution à la caractérisation et à la modélisation de matériaux magnétiques en vue d'une implantation dans un code de calcul de champ. PhD thesis, Université Lille I, 2002.

[133] C. Zorni, Eddy current non destructive testing of ferromagnetic materials : experimentation and modeling. PhD thesis, Université Paris Sud - Paris XI, 2012.

[134] M. Frăţilă, Contribution à la prise en compte des pertes fer dans la modélisation des machines électriques par éléments finis. PhD thesis, 2012.

[135] A. Mansri, Processus d'aimantation dans les matériaux doux à base de fer - Représentation des Pertes en régime dynamique. PhD thesis, Université Badji Mokhtar, Algerie, 2014.

[136] G. Bertotti, "General Properties of Power Losses in Soft Ferromagnetic Materials," IEEE Transactions on Magnetics, vol. 24, pp. 621–630, Jan. 1988.

[137] F. Henrotte, A. Nicolet, and K. Hameyer, "An energy-based vector hysteresis model for ferromagnetic materials," COMPEL - The International Journal of Computations and Mathematics in Electrical and Electronic Engineering, vol. 25, no. 1, pp. 71–80, 2006.

[138] K. Jacques, C. Geuzaine, F. Henrotte, and J. Gyselinck, "Comparison between differential and variational forms of an energy-based hysteresis model," in 2016 IEEE International Energy Conference (ENERGYCON), pp. 1–6, Apr. 2016.

Remerciements

Je n'aurais jamais pu réaliser ce travail sans le soutien d'un grand nombre de personnes, dont la générosité et la disponibilité m'ont permis de progresser dans cette phase délicate de mon doctorat.

In primis, je tiens à remercier mes promoteurs Laurent Krähenbühl, Fabien Sixdenier et Riccardo Scorretti de m'avoir fait confiance et donné l'opportunité de mener ce travail dans d'excellentes conditions, au sein de l'équipe de recherche du laboratoire Ampère. Je vous suis reconnaissante de m'avoir fait découvrir le monde de la recherche scientifique et de m'avoir guidé par vos conseils et votre soutien. Cela a été un plaisir de travailler avec vous durant ces trois années. Laurent, je suis particulièrement admirative de ton optimisme, de l'ambiance agréable pendant le travail, qui ont été des sources de motivation et d'avancement continuels. Fabien, tu avais l'habitude de souligner mes erreurs avec tes grands éclats de rire, je te remercie pour ta disponibilité, d'avoir partagé ton expertise technique et ta rigueur scientifique. Un merci tout spécial à toi, Riccardo, tu m'as suivi avec ton infinie disponibilité dans chaque étape de la réalisation de ma recherche, merci pour ton soutien, bonne humeur, pour m'avoir appris, en même temps, la rigueur et la précision.

Je remercie également les membres de mon comité de thèse, Ruth V. Sabariego, Ermanno Cardelli, Christophe Geuzaine, François Henrotte, Laurent Daniel, pour leur participation, l'intérêt porté sur mon travail et leurs conseils prodigués pour la révision du présent manuscrit.

Plus particulièrement, je tiens à remercier Christophe Geuzaine de m'avoir accueilli dans l'équipe ACE de l'Université de Liège en Belgique, pour son optimisme, ses idées intéressantes lors de discussions techniques ou philosophiques, qui m'ont été fructueuses dans mon travail. Pendant mon séjour à Liège, j'ai connu Kevin Jacques que je remercie sincèrement pour m'avoir donné sa précieuse aide pour le développement de modèles sur les supports Gmsh et GetDP. Je tiens également à remercier François Henrotte pour ses sages conseils. Je voudrais exprimer ma reconnaissance à Giacomo Di Benedetto, déclaré "il genio", qui souvent m'a illuminé avec ses brillantes idées, et à mon cher prof Umberto Morbiducci, pour avoir cru en moi. J'ai beaucoup appris de leur savoir et de leurs suggestions.

De plus, je tiens à remarquer l'agréable atmosphère de travail qui a régné au sein du laboratoire Ampère et à remercier chaleureusement tous les collègues et permanents, en particulière Laurent Morel, Christian Martin, Charles Joubert, Jean-Louis Augé et Noël Burais, pour tous leurs conseils. Un grand merci à tous les collègues-amis Aurèlien Chazotte-Leconte, Malorie Carpentier, Maxime Semard, Nagham El Ghossein, qui m'ont accueilli avec bienveillance, et puis tous ceux que j'ai connu et avec qui j'ai partagé mon parcours, notamment Lulu Viêt Phung, Rémy Caillaud, Etienne Foray, Sofia Benouakta, François Tavernier, Valery Nkemeni, Alexandre Eid, William Wheeler, Laetitia Bourgeat, Rania Saoudi, Camille Sonneville, Antoine El-Hayek, Mohamed Ben-Marzouk, Alfie Pena et Edgar Tournon.

Je souhaite adresser une pensée à toutes les personnes qui m'ont entouré et soutenu

au cours de cette aventure. Enfin, et surtout, un merci spécial, du fond du cœur, à Pierre Demumieux, l'ami le plus cher, avec qui j'ai partagé mon bureau au début de ma thèse, qui a su me supporter et réconforter dans les moments plus difficiles. Je remercie infiniment ma famille, qui a toujours cru en moi et sur qui j'ai pu compter en toutes circonstances, qui m'a soutenu et surtout supporté dans tout ce que j'ai entrepris.

Merci pour vos encouragements, votre soutien, et votre compréhension.